UNIVERSITÉ DE STRASBOURG

EDSC École Doctorale des Sciences Chimiques

ÉCOLE DOCTORALE CHIMIE

[I.S.I.S.]

Zeolites as key-components for electronics and biomedicine

présentée par :

[Henning LUELF]

soutenue le : **13 Decembre 2013**

pour obtenir le grade de : **Docteur de l'université de Strasbourg**

Discipline/ Spécialité : Chimie

Zeolites as key-components for electronics and biomedicine

THÈSE dirigée par :

DE COLA Luisa	Professor, Université de Strasbourg, I.S.I.S.

RAPPORTEURS :

LIZ-MARZAN Luis	Professor, CIC biomaGUNE, Paseo de Miramón 182, 20009 Donostia – San Sebastian, Spain
WÖLL Christof	Professor, Karlsruhe Institute of Technology (KIT), Institute of Functional Interfaces

---

AUTRES MEMBRES DU JURY :

DECHER Gero	Professor, CNRS Institut Charles Sadron (UPR 22), Campus Cronenbourg

Table of contents

Résumé 1

1. Introduction 22
- 1.1. Nanotechnology and biomedicine 23
- 1.2. Nanocontainers and biomedicine 25
- 1.3. Zeolite-L 25
- 1.4. Microporous and mesoporous materials in biomedicine 28
- 1.5. Self-assembly of zeolites into monolayers 37
- 1.6. Further functionalization of zeolite-L monolayers 38
- 1.7. Scope of the thesis 39

2. Zeolite-L synthesis, functionalization and assembly into functional materials 49
- 2.1. Introduction 50
- 2.2. Cation exchange 54
- 2.3. Insertion of guest molecules 54
- 2.4. Functionalization of the external surface 57
- 2.5. Zeolite-L monolayer preparation 57
- 2.6. Soft litography 59
- 2.7. Experimental part 62

3. Growth of primary neurons on zeolite-L monolayers 69
- 3.1. Introduction 70
- 3.2. Neurons 72
- 3.3. Neuron growth on zeolite-L monolayers 75
- 3.4. Conclusion 78
- 3.5. Experimental part 80

4. Zeolites as key-components for electronics – Ultrahigh Magnetoresistance in One-Dimensional Molecular Wires 86
- 4.1. Introduction 87
- 4.2. Electrical conductivity in zeolites. State of the art. 89

4.3. Electrical conductivity in dye loaded single zeolite crystals 90
4.4. Magnetoresistance 95
4.5. Organic Magnetoresistance 96
4.6. The bipolaron model 97
4.7. Ultrahigh Magnetoresistance in one-dimensional molecular wires 99
4.8. Conclusion 105
4.9. Experimental part 107

5. Self-assembly from the gas phase – A new facile towards highly ordered structures 115
5.1. Introduction 116
5.2. Synthesis and characterization of the perylene monoimides 119
5.3. Solution vs. gas phase self-assembly 120
5.3.1. Morphology of the self-assemblies from solution 121
5.3.2. Morphology of the self-assemblies from the gas phase 122
5.4. Photophysics in solution and in different solid-state morphologies 126
5.5. Packing of PMI-1, PMI-2 and PMI-3 129
5.6. Conclusion 134
5.7. Experimental part 135

6. Zeolites as key-components for biomedicine – Zeolite-L as a multifunctional DNA and drug delivery system 141
6.1. Introduction 142
6.1.1. Transfection 142
6.1.2. Artificial transfection systems 143
6.1.3. Nanoparticles for transfection 144
6.2. Particle preparation and analysis 145
6.3. Microzeolite preparation and functionalization 147
6.4. DAPI release from DNA functionalized zeolite-L 148

6.5. Intracellular DNA and DAPI release from microzeolite-L 151
6.6. Nanozeolite preparation and functionalization 152
6.7. Intracellular DNA and DAPI release from nanozeolite-L 153
6.8. Fate of the particles and the DNA after uptake 159
6.9. Conclusion 159
6.10. Experimental part 161

7. Zeolites as key-components for biomedicine – Zeolite-L as a multifunctional PNA and drug delivery system 170
7.1. Introduction 171
7.2. Peptide Nucleic Acids in Gene Therapy 172
7.3. Material preparation and characterization 174
7.4. In vitro experiments with PNA functionalized zeolite-L 177
7.5. In vitro experiments with PLL coated and PNA functionalized zeolite-L 181
7.6. Multifunctional PNA and model drug delivery to living cells 183
7.7. Conclusion 184
7.8. Experimental part 186

8. Experimental and Instrumental Methods 194
8.1. Zeolite-L synthesis 195
8.2. Scanning electron microscopy (SEM) 195
8.3. Transmission electron microscopy (TEM) 198
8.4. Dynamic light scattering (DLS) 200
8.5. Zeta potential 201
8.6. UV/Vis spectroscopy 203
8.7. Steady state emission spectroscopy 204
8.8. Confocal microscopy 205

9. Summary 208

Résumé

La nanotechnologie est un domaine de recherche qui a pour objectif le développement de matériaux fonctionnels à l'échelle nanométrique (de 1 à 100 nm) présentant des propriétés électroniques, optiques, magnétiques ou biologiques uniques[1, 2, 3].
Le contrôle de la taille, la morphologie, la composition chimique et l'organisation à l'échelle nanométrique est un facteur crucial pour pouvoir contrôler et optimiser les propriétés des matériaux étudiés ainsi que leur réponse à leur environnement proche. Les nanomatériaux sont composés d'une grande variété de matériaux différents tels que les métaux, oxydes métalliques, polymères, lipides ou autres molécules organiques. Ils sont généralement synthétisés selon une approche « bottom-up » (approche ascendante) suivie par l'introduction des fonctionnalités désirées en modifiant la surface externe ou interne. Leur taille étant du même ordre que celle d'un grand nombre de molécules biologiques importantes, les nanoparticules sont particulièrement intéressantes pour des applications biomédicales. Les nanoparticules sont quelques ordres de grandeur plus petites que les cellules eucaryotes, ce qui permet des interactions spécifiques entre elles ou même l'absorption cellulaire.
Un paramètre clé qui rend les nanoparticules très intéressantes pour des applications biomédicales est la possibilité de combiner plusieurs fonctionnalités différentes sur une même nanoparticule, ce qui permet de concevoir des nanomatériaux multifonctionnels pour des applications très spécifiques.

De nombreux types de nanoparticules ont été conçus et étudiés au cours des dernières années.
La possibilité de piéger un grand nombre de molécules hôtes et de concevoir facilement des nanoparticules multifonctionnelles rend les « **nanocontainers** » (nanoconteneurs) particulièrement prometteurs dans le cadre d'applications biomédicales.
Tout d'abord, l'encapsulation protège les molécules hôtes des interactions avec leur environnement, ce qui peut conduire à des stabilités plus importantes, ou empêche des réactions secondaires indésirables avec l'environnement. En outre, la faible absorption cellulaire, la nature insoluble dans l'eau ou l'instabilité de certains médicaments peuvent être résolus par l'utilisation de « nanocontainers ». Ces médicaments peuvent être incorporés à l'intérieur des « nanocontainers » et la surface externe de la particule peut être fonctionnalisée avec des groupes fonctionnels capables de pénétrer ou solubiliser les cellules. De plus, la surface externe peut être fonctionnalisée avec des récepteurs afin de cibler de manière spécifique certains types de cellules ou de guider le devenir du « nanocontainer » après son absorption cellulaire[4, 5].

Une représentation schématique d'un « nanocontainer » adapté à des applications biomédicales est présentée en figure 1.

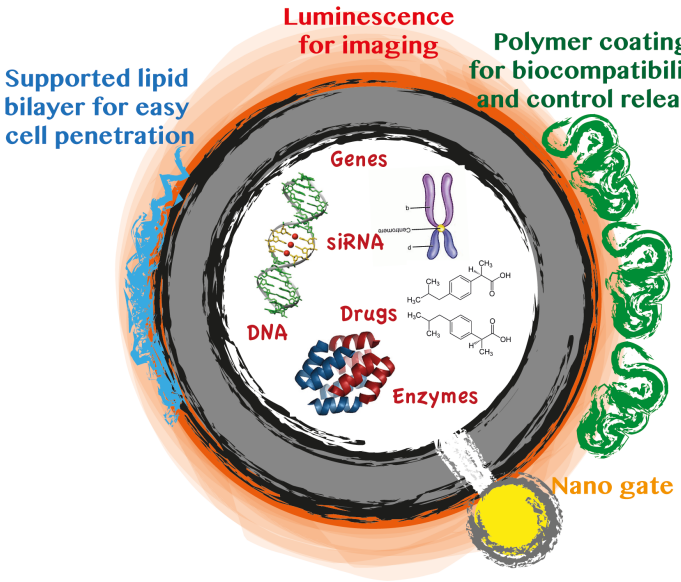

Figure 1. Représentation schématique de nanomatériau poreux adapté aux applications biomédicales. Les cavités sont remplies de molécules hôtes. La surface est modifiée afin d'optimiser la biocompatibilité. Les pores peuvent être conçus de telle sorte que la libération de la charge utile se produit de manière contrôlée. (Image provenant de : **H. Luelf**, A. Devaux, E. Prasetyanto, L. De Cola, *Organic Nanomaterials Synthesis, Characterization, and Device Applications*, T. Torres, B. Bottari, Wiley 2013).

Un type très particulier de « nanocontainers » sont les particules de zéolithe-L. La Zéolithe-L fait partie d'une classe de matériaux poreux à base d'aluminosilicate, appelés zéolithes. A ce jour, plus de 200 types de structures zéolithiques différentes ont été identifiées et elles sont principalement utilisées comme absorbants dans de nombreuses applications industrielles.
La Zéolithe-L est une zéolithe synthétique présentant une symétrie hexagonale. La structure se constitue de cages cancrinites, qui sont interconnectées pour former un système de canaux unidimensionnels. L'ouverture des pores, ainsi que le plus petit diamètre de canal, est de 0,71 nm. Le plus grand diamètre de canal est de 1,26 nm, et la longueur d'une unité de maille est de 0,75 nm. Les canaux sont arrangés de façon hexagonale et la distance de centre-à-centre entre deux canaux adjacents est de 1,8 nm.
En raison de la présence d'atomes d'aluminium dans le réseau zéolithique, les canaux présentent une charge négative, compensée par des cations équilibreurs de charge faiblement liés dans la structure. Ces cations peuvent être facilement remplacés par d'autres cations ou même par des molécules cationiques, telles que des molécules de colorant organique ou des molécules biologiquement actives[6]. Des cristaux de Zéolithe-L de différentes tailles ont été utilisés pour de nombreuses applications au cours des dernières années.
Les applications des zéolithes-L sont nombreuses et variées, allant de la conception de systèmes d'antennes photoniques artificielles[7], de l'utilisation de

zéolithe-L comme matériaux fonctionnels dans des systèmes auto-assemblés[1, 8] à des applications biomédicales[9, 10, 11, 12, 13].

Une approche très intéressante pour l'application des zéolithes-L, ou des zéolithes en général, est leur auto-assemblage en monocouches[14, 15], ce qui peut conduire à une orientation perpendiculaire au substrat de tous les canaux zéolithiques. Cela peut être utilisé pour concevoir des systèmes où la libération de molécules hôtes hors des pores de la zéolite est très orientée puisque l'un des côté des pores est bloqué par le substrat. D'autre part, les canaux fortement orientés peuvent être remplis avec des molécules électro-actives, comme des semi-conducteurs, afin d'étudier leurs propriétés électroniques dans cette unique orientation précise.
Pour certaines applications spécifiques, comme des applications biomédicales, une fonctionnalisation supplémentaire de la monocouche est souvent nécessaire. Par exemple, si la monocouche est utilisée comme substrat pour de la croissance cellulaire, la surface peut être rendue biocompatible en la recouvrant de certaines biomolécules. Ce revêtement peut généralement être effectué de plusieurs manières : par « drop-casting » (déposition de gouttes), « dip coating » (trempage-retrait), « spin-coating » (dépôt centrifuge) ou "layer-by-layer assembly » (assemblage couche par couche)[16], et il a été démontré que l'impression par micro-contact (« microcontact-printing », MCP) est une méthode très efficace pour fonctionnaliser et façonner les surfaces[17]. Le principe de fonctionnement général du MCP est illustré en figure 2.

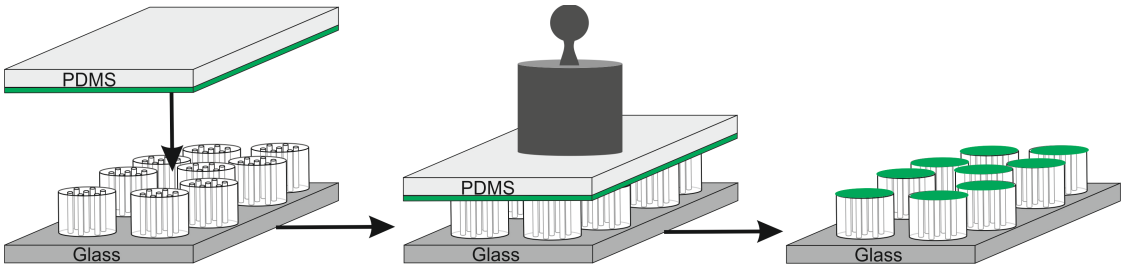

Figure 2. Schéma du principe d'impression par micro-contact. L'encre est représentée par la couche verte.

Il a également été montré qu'il est possible d'utiliser une technique d'impression par micro-contact modifiée, appelée impression micro-contact par transfert (« microcontact transfer printing ») [18], pour effectuer le transfert d'une monocouche sur une grande variété de substrats, par exemple des polymères conducteurs. Cela permet la préparation de monocouches dans des conditions bien définies et leur transfert ultérieur sur un substrat choisi.
Cette thèse a pour objectif l'utilisation de nanoparticules de zéolithe-L comme composants clés en électronique et biomédecine.
En particulier, nous cherchons à suivre la croissance, la multiplication et la communication synaptique des neurones primaires avec comme objectif final de suivre les manifestations synaptiques individuelles déclenchées par stimu-

lation électrique. Les zéolithes seront donc utilisées comme un site présynaptique artificiel pour amorcer des manifestations synaptiques, comme le montre la figure 3.

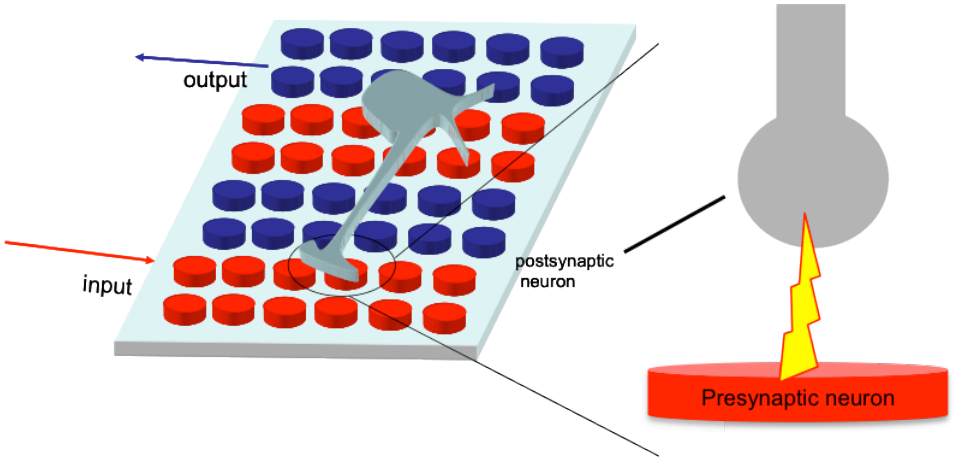

Figure 3. Représentation schématique de l'expérience. La conductivité électrique des zéolithes permet l'excitation électrique des neurones.

La culture de neurones primaires hippocampiques sur des zéolites-L sera discutée dans le chapitre 3. Ce projet avait pour but de développer les neurones primaires hippocamiques de souris sur des monocouches de zéolites-L. Le choix des zéolites a été dicté par le fait que les canaux des cristaux peuvent être remplis avec des petites molécules, et lorsque les zéolites sont assemblées en formant une monocouche les canaux sont perpendiculaires à la surface. Cette observation est de la plus grande importance dans la mesure ou le challenge de ce projet est de diriger les molécules dans les canaux dans le but d'induire soit un transport de charge (voir chapitre 4), soit la libération d'un composé chimique depuis les pores ou les surfaces de la particule. Dans ces deux conditions, les neurones peuvent être stimulés près du signal électrique, ou la molécule libérée est générée. La première étape est donc la préparation et la fonctionnalisation de la monocouche et la formation de la synapse. Dans le but de permettre la formation des synapses, une culture de neurones de plus de sept jours était désirée, car il a été montré que l'évolution in vitro des synapses ne se réalise pas pour une durée inférieure à sept jours.[19]

Dans un premier temps, les monocouches ont été fonctionnalisées avec un tripeptide arginine-glycine-acide aspartique (Arg-Gly-Asp, ou RGD selon l'appellation anglo-saxonne). Il a en effet été montré que les neurones présentent des intégrines qui se lient au tripeptide RGD, ce qui permet une bonne adhésion à la cellule et bonne culture cellulaire[20]. La culture des neurones a été réalisée en absence de cellules gliales pour permettre un contact direct des neurones à la surface, ce qui conduit à une stimulation efficace des neurones. Il est intéressant de noter que les cellules n'adhèrent pas aux surfaces et qu'aucune cellule n'est présente après quelques jours. Ce compor-

tement inattendu n'est pas encore totalement compris et de plus amples recherches seront réalisées prochainement.
Puis nous avons étudié la culture des neurones sur des monocouches fonctionnalisées par des groupements amines, car les neurones ont une affinité pour les surfaces chargées positivement[21]. Les groupements amine primaire sur la monocouche sont partiellement protonés en milieu physiologique (pH=7,4) ce qui est supposé favoriser l'adhésion et la croissance de la cellule. Il est à rappeler que la culture de cellule a été favorisée en absence de cellule gliale. En effet, nous avons obtenu une bonne adhésion cellulaire après deux jours. Cependant, la situation devient considérablement différente pour des temps d'incubation plus élevés. Après trois jours, le nombre de cellules décroit considérablement et après quatre jours, aucune cellule n'a été trouvée sur la surface.
Enfin, nous avons décidé d'utiliser une co-culture de neurones et de cellules gliales ; et de couvrir les monocouches de la zéolite avec un mélange de collagène et d'ornithine, comme il est souvent utilisé pour les cultures primaires de neurones.

Le chapitre 4 présente d'importantes expériences réalisées pour prouver la possibilité d'une stimulation directe de neurones sur une monocouche de zéolites.
En détail, notre but est d'interférer les neurones avec un transistor à effet de champ organique (OFET) pour permettre une stimulation directe des synapses, comme il est monté figure 4.

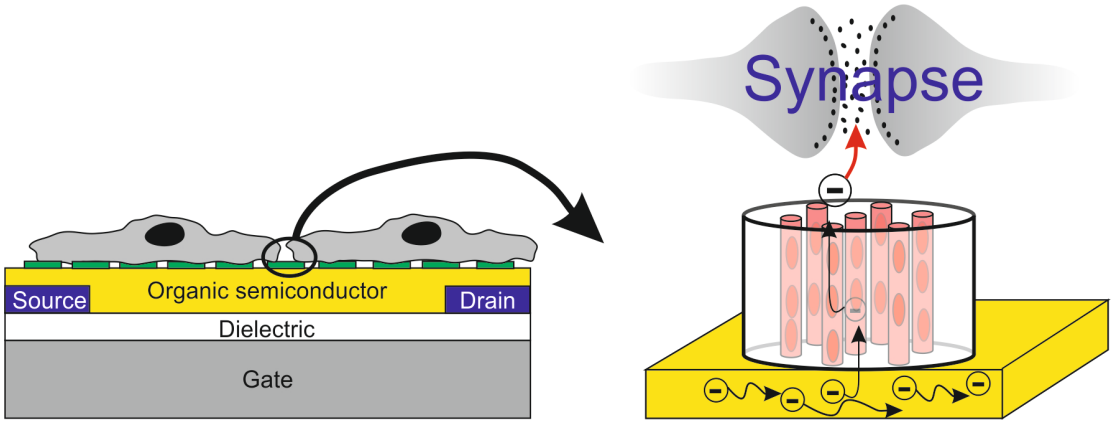

Figure 4. Représentation schématique d'adressage de neurones en les combinant avec des appareils électroniques organiques (OFETs).

L'interfaçage d'appareils électroniques avec des systèmes biologiques ont suscité un grand intérêt durant plusieurs années[22, 23] et certains exemples récents montrant la capacité de ces systèmes à distribué des neurotransmetteurs in vivo[24], de contrôler l'adhésion cellulaire[25, 26] ainsi que la migration[27], de mesurer l'activité neurale in vivo[28, 29] mais également d'évaluer l'integrité

de la barrière cellulaire[30]. Plusieurs exemples montrent la réussite de l'interface neurones/OFETs[31, 32, 33].

Pour permettre une stimulation électrique directe, la monocouche doit être électriquement conductrice, ce qui impliquerait un transport d'électrons de la surface de l'OFET vers les neurones ou les synapses. Cependant, il ne s'agit pas d'une tâche aisée car les zéolites sont par nature électriquement isolantes, ce qui empêche le transport d'électron vers les cellules. Nous avons donc l'intention de rendre la zéolite conductrice en remplissant les pores avec un matériau conducteur d'électron, capable de transporter les électrons de l'OFET aux cellules (voir figure 4).

Nous avons rempli les pores avec de grandes quantités de semi-conducteurs de type perylène diimide DXP car il a été montré que le DXP présente un recouvrement orbitalaire lorsqu'il sont introduits à l'intérieur des pores des zéolites-L à de fortes concentrations[34], ce qui devrait permettre à l'électron le passage d'une molécule à une autre de manière efficace. Nous avons prouvé que le DXP demeure intact après l'insertion, et mesuré la conductivité dans ces particules en utilisant un microscope de type CPAFM (Conductive Probe Atomic Force Microscope), comme nous pouvons le voir figure 5. Le CPAFM était équipé d'un électro-aimant, ce qui nous a permis d'étudier l'influence d'un champ magnétique externe sur la conductivité (magnétoconductance MC).

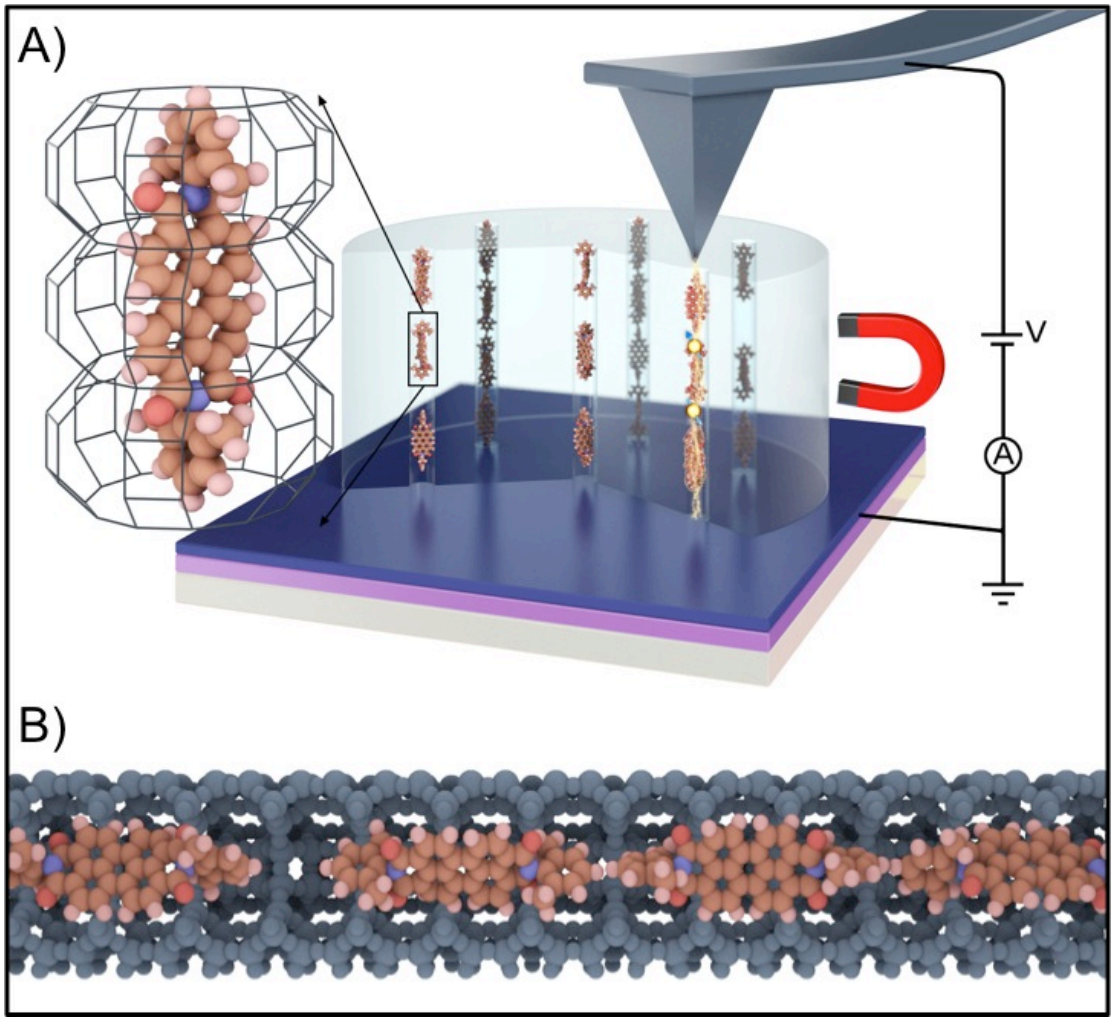

Figure 5. A) Représentation schématique de l'installation expérimentale pour étudier la dépendance de la conductivité électrique sur le champ magnétique à travers des chaînes 1D de DXP à l'intérieure d'une zéolite. B) Illustration de la molécule DXP à l'intérieur d'un canal de zéolite-L. Pour des raisons stériques, les molécules peuvent uniquement s'orienter selon leur longueur, parallèlement au canal.

Nous avons mesuré la longueur des cristaux avec des hauteurs entre 30 et 10 nm et obtenu de très petits courants qui dépendent de la hauteur de la zéolite (voir figure 6). La résistance croît avec l'augmentation de la longueur des canaux de manière exponentielle pour les bas voltages et de manière linéaire pour les hauts voltages. Le fait que le comportement de la résistance dépende clairement de la longueur des canaux est une preuve plus avancée que la conductivité est limitée par le transport à travers les chaines moléculaires plutôt que par le contact. Pour prouver que le conductivité est en effet due aux DXP à l'intérieur des pores, la conductivité a également été mesurée dans un échantillon de contrôle. Le contrôle a été traité de la même manière que les échantillons de DXP avec une seule différence : aucun DXP n'a été inséré dans les zéolites. Les caractéristiques des zéolites vides et des substrats de I à V (voir figure 6) ont été mesurées par CPAFM. Les mesures de I à V montrent un comportement isolant pour les zéolites vides. Même à 9 V, le

courant à travers les cristaux de zéolites-L était inférieur à la limite de détection du système. En plaçant le CPAFM sur le substrat ITO/PEDOT :PSS, un comportement ohmique a été observé avec une résistance typique de 10 Ohms, ce qui signifie une magnitude inférieure à la résistance de cristaux de zéolites-L pleins (jusqu'à 86%) avec des molécules de DXP.

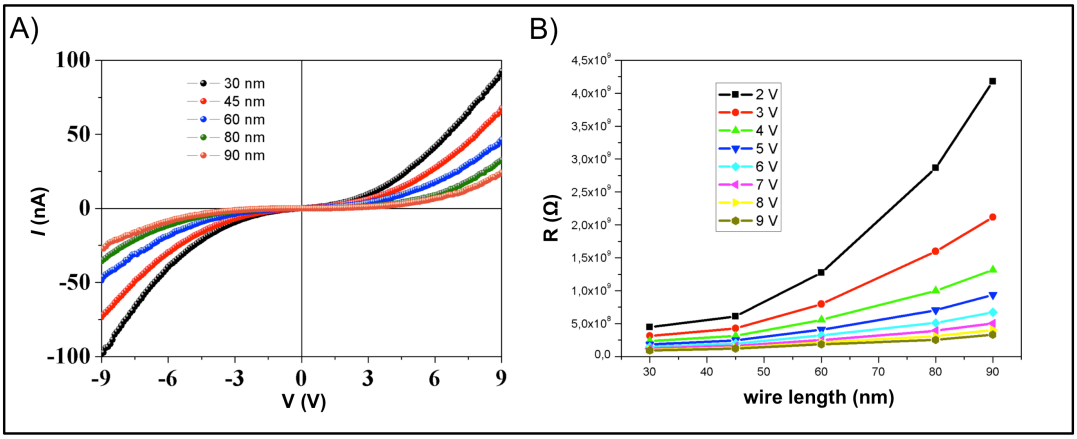

Figure 6. A) Courbes de I à V de chaînes 1-D de DXP dans un hôte de type zéolite-L montrant l'influence de la longueur de la chaîne sur le courant. B) Résistance dans des chaînes 1-D de DXP dans une zéolite en fonction de la longueur d'onde sur la longueur de chaîne et le voltage.

Ces résultats montrent déjà que l'introduction de grandes quantités de semi-conducteurs organiques peut être utilisée pour rendre la zéolite conductrice.
Par la suite, a été étudiée l'influence d'un faible champ magnétique (jusqu'à 14 mT) sur la conductivité électrique. Exceptionnellement, des valeurs de MC approchant 100% ont été observées. La tendance générale montre des valeurs de MCs négatives qui augmentent lorsqu'on diminue la tension. Nos données peuvent être ajustées par une fonction non lorentzienne. Les valeurs de B_0 varient entre 2 et 6 mT, ce qui est comparable aux valeurs obtenues pour l'essentiel des magnetoresistances organiques (OMAR) .De plus, les valeurs de B_0 ne montrent pas de nette dépendance à la tension ou à la longueur. Comme il a été montré figure 4.8, la plus grosse MC, de presque 100%, est obtenue pour une longueur de chaîne de 60 nm et une tension de 2 V (figure 7).

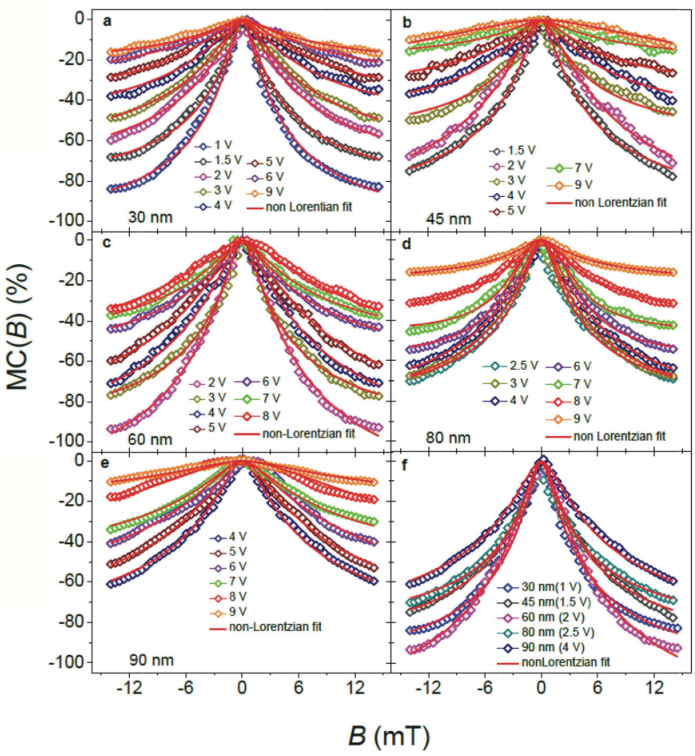

Figure 7. Magnetoconductance en fonction du champ magnétique pour différentes longueur de chaînes, f montre la valeur maximale pour chaque longueur de chaîne sur un même graphique. Les données on été mises en place avec un ajustement de type non lorentzien.

La dépendance à la tension est encore plus prononcée si la magnétoconductance MC est convertie en magnétorésistance MR. Cette dernière croît lorsqu'on décroît la tension et atteint un maximum (plus de 2000%) pour une longueur de 60 nm. La MR pour 0 V n'a pas pu être déterminée car le niveau de courant était inférieur au niveau de bruit du système. Les résultats sont résumés figure 8.

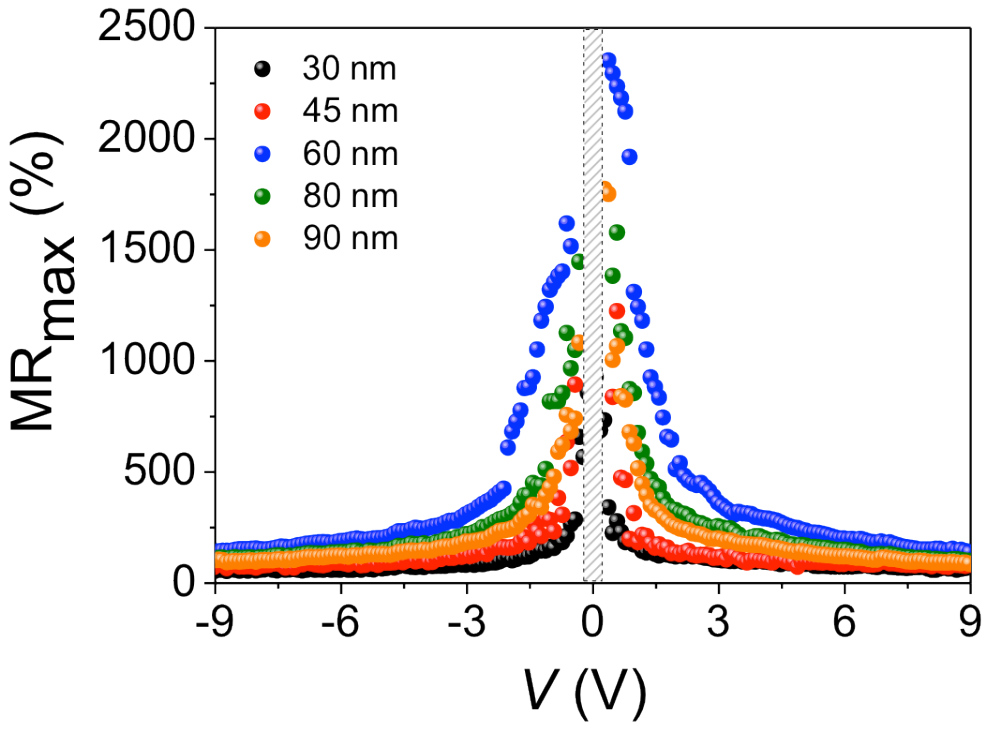

Figure 8. Magnétorésistance en fonction de la tension dans des chaînes de différentes longueurs.

Nous attribuons la très forte MR obtenue aux propriétés uniques des fils unidimensionnels incorporés dans une zéolite-L hôte. Du DXP libre avec une hauteur comparable de l'ordre de 40 nm montre uniquement une magnétorésistance d'environ -20% lorsque la même pointe PtSi-CP-AFM est utilisée. Lorsque la pointe est remplacée par un fil de platine (diamètre 250 µm), la MR descend en outre à environ -5%. Ces résultats s'orientent fortement dans le sens que le confinement et la formation des fils de DXP unidimensionnels sont à l'origine des très fortes valeurs obtenues. Nous expliquons les résultats en prenant le modèle bipolaire en tant que base et nous avons stimulé la MC en utilisant la méthode Monte Carlo. Nous obtenons une MC très similaire aux résultats expérimentaux quand les contre-cations (potassium) sont pris en compte dans la stimulation.

Le chapitre 5 décrit une voie plutôt inexplorée d'auto-assemblage de molécules organiques fonctionnelles, de dérivés de pérylène monoimide – par un auto-assemblage direct à partir de la phase gazeuse. Une série de pérylènes monoimides (voir figure 9) a été synthétisée, caractérisée par spectroscopie RMN ^{1}H, spectroscopie de masse et diffraction de rayons X sur monocristal et leur auto-assemblage en solution et en phase gazeuse a été étudié.

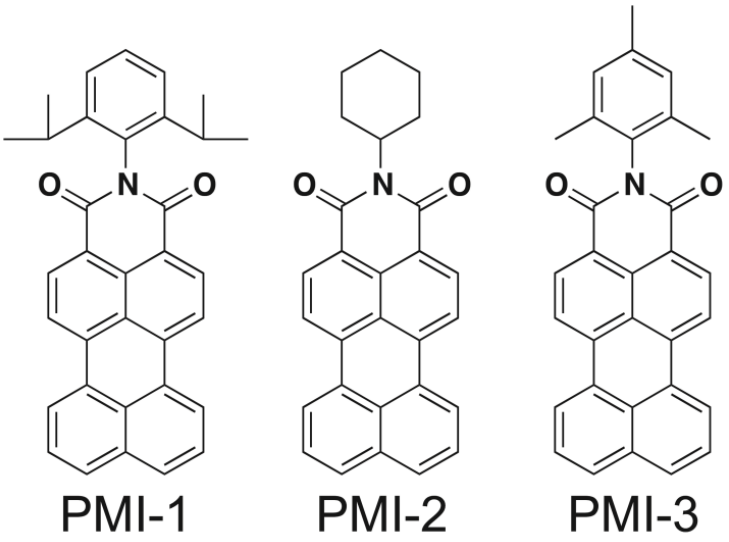

Figure 9. Structures moléculaires des trois perylènes monoimides utilisés dans cette étude

L'assemblage a ensuite été effectué par largage ou par sublimation directe sur un substrat (verre ou or).
Alors qu'un assemblage par largage conduit à des structures sans aucun ordre de gamme de longueur, l'auto-assemblage en phase gazeuse conduit, quant à lui, à des structures hautement ordonnées. Tous les pérylènes monoimides forment des structures unidimensionnelles avec leur long axe orienté perpendiculairement au substrat. Dépendant du groupe-tête, des morphologies légèrement différentes et des ratios d'aspects peuvent être obtenus.
L'empaquetage moléculaire a ensuite été examiné en utilisant la diffraction de rayons X sur monocristal combinée aux SAXS et WAXS et tous les composés montrent une forte tendance vis-à-vis du π-π-stacking et de la formation de dimère à l'état solide.
Les chapitres 6 et 7 traitent ensuite de l'application intracellulaire de cristaux de zéolites-L en tant que plateforme pour un nucléotide multifonctionnel et la délivrance de médicaments à des cellules vivantes.
La délivrance et la libération d'oligonucléotides d'ADN et un médicament modèle (DAPI) sont décrits dans le chapitre 6.
La voie synthétique est indiquée dans la figure 10. Des cristaux de zéolite de deux tailles différentes, 50 nm (nanozéolite-L) et environ 1000 nm (microzéolite-L), ont été synthétisés et caractérisés par MEB, MET, DLS et mesures de potentiel zeta. Dans une étape suivante, les pores des zéolites ont été remplies avec les molécules convives[35], comme le DXP ou la teinte nucléaire 4',6-diamidino-2-phenylindole (DAPI). Le chargement du DAPI a été déterminé par analyse thermogravimétrique (ATG) et il en résultait des chargements de 1,55 wt% pour les nanozéolites-L et de 0,9 wt% pour les particules de microzéolites-L.

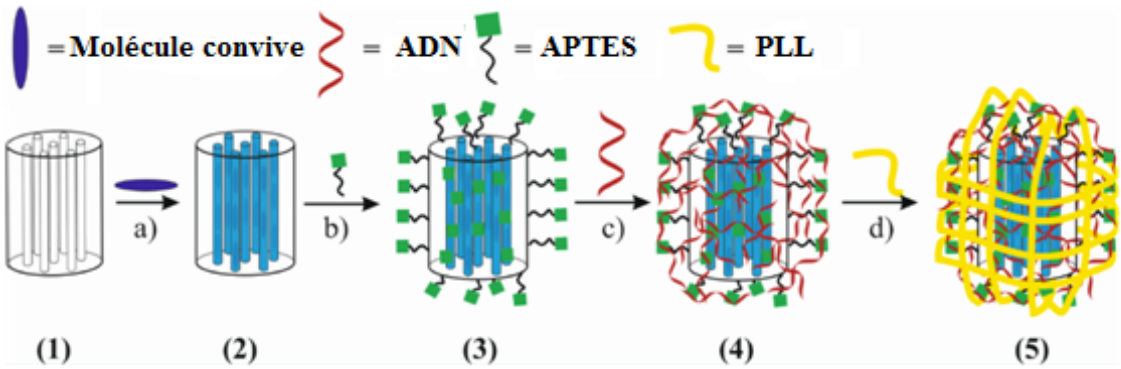

Figure 10. Préparation des particules réalisées. (1) zéolites vides, (2) = pores remplies avec des convives, (3) = fonctionnalisation en NH_2 des zéolites remplis, (4) liaison ADN électrostatique, (5) emballage des PLL sur l'ADN.

Après avoir rempli les zéolites-L, nous pouvons lier électrostatiquement l'ADN aux zéolites en les fonctionnalisant avec du (3-Aminopropyl)triethoxysilane (APTES). En effet, les groupements NH_2 sont partiellement protonnés dans des conditions physiologiques, ce qui conduit à une surface de particule positivement chargée.
L'ancrage électrostatique de l'ADN à des cristaux conduit à une fermeture quasi-complète des pores ayant pour conséquence une inhibition de la libération du DAPI, qui a récemment été démontrée pour des nanoparticules de silice mésoporeuse, où l'ADN agit comme un motif fermeture de pore/ouverture de pore à réponse stimuli-dépendante[36]. Que ce concept fonctionne aussi pour notre système est démontré dans ce chapitre.

Nous avons ensuite étudié les libérations intracellulaires d'ADN et de DAPI à partir de particules fonctionnalisées à l'aide d'ADN.
Nous avons d'abord utilisé les particules de microzéolites et les avons enveloppés avec de la PLL pour favoriser l'adduction au niveau de la cellule. L'incubation a été réalisée pour 1, 4 et 24 heures en utilisant une concentration en particules de 0,01 mg de zéolites par mL de milieux de culture.
Nous constatons que l'adduction est généralement très faible et seulement une très faible concentration en particule peut être trouvée dans les cellules. Après 1 heure, seulement très peu de particules sont prises par les cellules.
Après 4 heures, une quantité légèrement supérieure de particules est internalisée mais le nombre total est toujours très petit et l'ADN et le DAPI se localisent seulement dans les particules et ne se détachent pas sensiblement.
Le nombre de particules prises par les cellules augmente après 24 heures et une teinte fortement rouge pâle du cytoplasme est observée, ce qui est assigné au détachement de très petites quantités d'ADN à partir des zéolites. Puisqu'aucun ADN associé n'est présent dans le cytoplasme, on suppose que le détachement lent de l'ADN vis-à-vis de la surface est dû à un échange lent avec des protéines et des ions venant des milieux impliqués. Une quantité suffisante de DAPI est à présent libérée à partir des pores, ce qui conduit à

une teinture du noyau. Cependant, la majorité du DAPI est toujours présente à l'intérieur des zéolites et la majorité de l'ADN est liée aux cristaux.

Nous avons ensuite décidé de diminuer la taille des particules afin d'obtenir une meilleure inclusion dans la cellule et d'étudier plus en détail les cinétiques de libération de l'ADN et du DAPI. La préparation des particules est présentée en figure 10. Nous avons pu constater que ces particules sont bien captées par les cellules et que l'on en retrouve une grande concentration à l'intérieur des cellules. En outre, l'ADN et le DAPI sont relargué depuis les particules après 4 heures.
Nous avons donc pu étudier les cinétiques de libération de l'ADN et du DAPI et déterminer le devenir des particules et le détachement de l'ADN à l'intérieur des cellules.
Dans l'optique de déterminer les cinétiques de libération de l'ADN et du DAPI depuis les particules de type nanozéolites-L, les conditions expérimentales d'incubation des cellules ont été modifiées. En effet, afin de protéger l'ADN et le DAPI d'une libération trop rapide et afin d'améliorer l'incorporation dans les cellules en changeant la charge totale de la zéolite de négative à positive, nous avons couvert le dessus de l'oligonucléotide avec du PLL. Une concentration en zéolites de 0.01 mg/mL a été utilisée et le temps d'incubation a ainsi été réduit d'une heure. Après l'incubation, les cellules ont été abondamment lavées avec un tampon PBS dans le but d'enlever les zéolites trop faiblement attachées de la surface des cellules. Nous avons ensuite fait croître les cellules et l'imagerie a été effectuée directement après incubation, puis après 1, 2, 4, 6, 24, 48 et 72 heures afin de suivre le signal de l'ADN et du DAPI.
Pour évaluer l'influence de la couche de PLL sur la libération d'ADN et de DAPI, nous avons ensuite utilisé des particules sans PLL et incubé les cellules avec une concentration en particule dix fois supérieur pour permettre une inclusion suffisante.
Les résultats sont présentés sur les figures 11 et 12. Nous avons constaté une inclusion suffisante afin d'étudier les cinétiques. Notons que l'utilisation de particules couvertes de PLL fournis des résultats similaire voir meilleur qu'avec une concentration en particules dix fois supérieur.

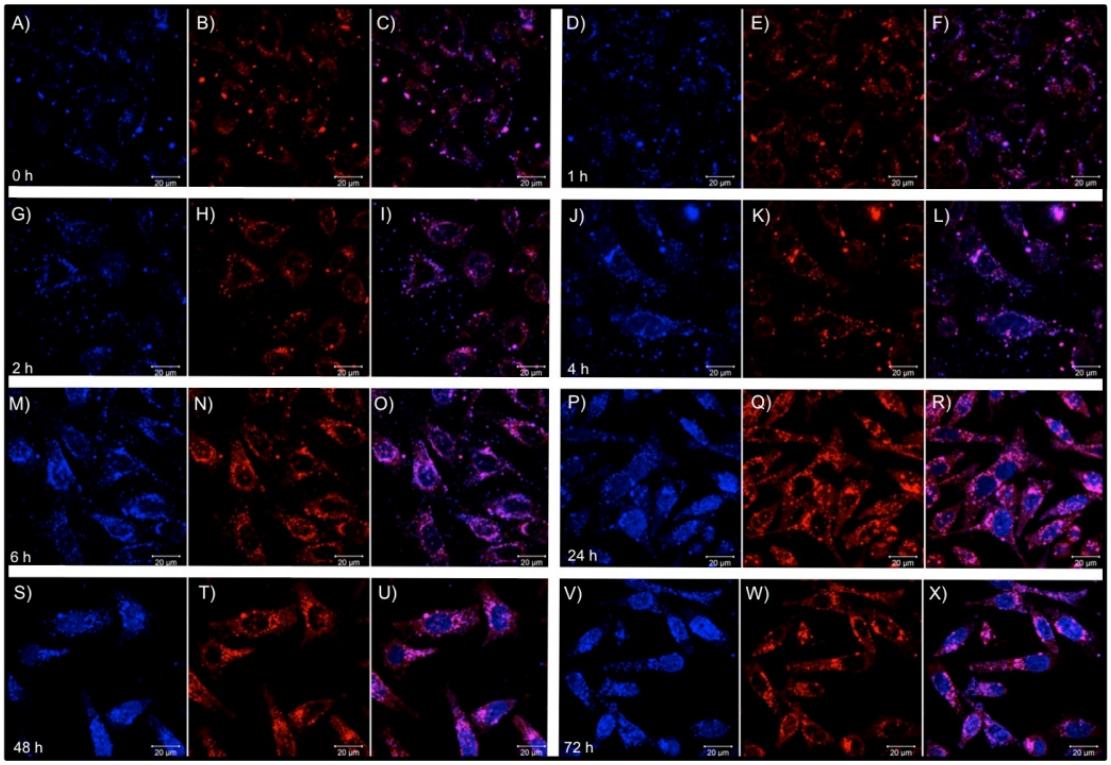

Figure 11. Microscopie confocale montrant les cinétiques de libération d'ADN et de DAPI à partir des nanozéolites-L couvertes par du PLL. L'incubation a été effectuée durant une heure et suivie par un lavage abondant avec du tampon PBS afin de retirer les particules adsorbées à la surface. Les cellules ont été incubées et les images ont été prisent directement après incubation (A, B, C); après 1 heures (D, E, F); après 2 heures (G, H, I); après 4 heures (J, K, L); après 6 heures (M, N, O); après 24 heures (P, Q, R); après 48 heures (S, T, U); après 72 heures (V, W, X). Image de gauche: fluorescence du DAPI. Image centrale: émission de Cy5. Image de droite: superposition. Excitation = 405 nm et 633 nm respectivement pour DAPI et Cy5. Les émissions ont été enregistrées avec un filtre pour DAPI et un autre pour Cy5.

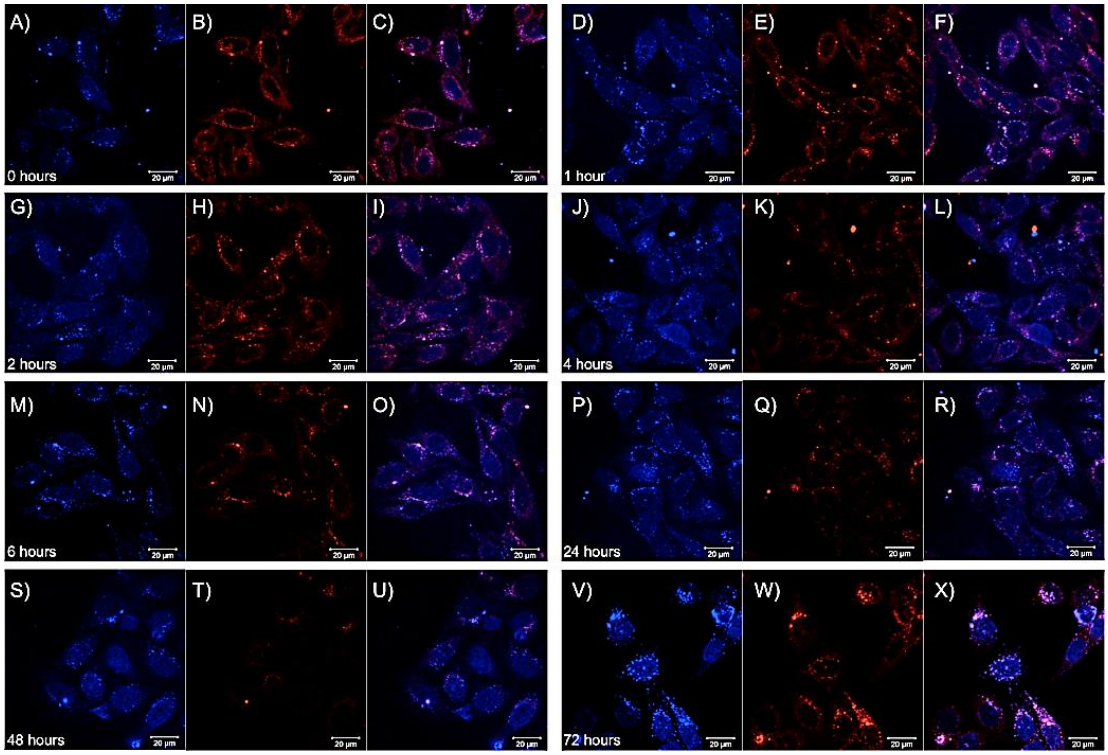

Figure 12. . Microscopie confocale montrant les cinétiques de libération d'ADN et de DAPI à partir des nanozéolites-L non couvertes par du PLL. L'incubation a été effectuée durant une heure et suivie par un lavage abondant avec du tampon PBS afin de retirer les particules adsorbées à la surface. Les cellules ont été incubées et les images ont été prisent directement après incubation (A, B, C); après 1 heures (D, E, F); après 2 heures (G, H, I); après 4 heures (J, K, L); après 6 heures (M, N, O); après 24 heures (P, Q, R); après 48 heures (S, T, U); après 72 heures (V, W, X). Image de gauche: fluorescence du DAPI. Image centrale: émission de Cy5. Image de droite: superposition. Excitation = 405 nm et 633 nm respectivement pour DAPI et Cy5. Les émissions ont été enregistrées avec un filtre pour DAPI et un autre pour Cy5.

Les deux échantillons montrent une libération d'ADN et du DAPI à partir des zéolites ainsi qu'une forte intensité d'émission de DAPI (dans le noyau) et d'ADN (dans le cytoplasme) après 24, 48 et 72 heures. Sachant que la division cellulaire se produit après 24 heures, une diminution de moitié du nombre de zéolites est attendue pour chaque division. Les principales différences entre ces deux expériences sont le nombre de particules incluses dans les cellules et le fait que la libération de DAPI avec les particules couvertes de PLL se produit après au moins 4 heures. Concernant les particules non couvertes, nous avons pu observer de faibles tâches dans le noyau après seulement une heure d'incubation. Ce délai vient du temps que prend le PLL à se dégrader permettant ainsi au DAPI et à l'ADN de pénétrer la cellule.
D'après ce que nous avons vu dans la littérature, les particules sont supposées s'accumuler dans le lysosome des cellules[37, 38], et l'ADN détaché est supposé s'accumuler dans les mitochondries.
Afin de fournir une preuve de cela, nous avons incubé des nanozéolites couvertes de PLL dans les conditions habituelles et nous avons marqué les lysosomes et les mitochondries avec des fluorophores. Nous avons ensuite utilisé

le microscope confocal pour prouver la localisation des particules dans les lysosomes et de l'ADN détaché dans les mitochondries.

La libération d'acides nucléo-peptidique (PNAs) et d'un médicament modèle (DAPI) est enfin présenté dans le chapitre 7.
La stratégie générale, décrite en figure 7.2, a été effectuée de manière à ce que la sonde PNA a été covalemment liée à la surface des cristaux de nano-zéolites-L dont les canaux ont été remplis par une molécule fonctionnelle. Cette molécule peut être soit fluorescente, soit suivre et localiser les particules après inclusion, soit un médicament modèle, dont la libération intracellulaire peut être surveillée après inclusion. Afin d'améliorer l'inclusion cellulaire, le système peut être couvert avec du PLL qui agis en tant que composé biodégradable augmentant l'inclusion cellulaire. Après dégradation de celui-ci, il laisse derrière lui le système actif PNA/zéolite-L. La préparation du matériau est présenté en figure 13.

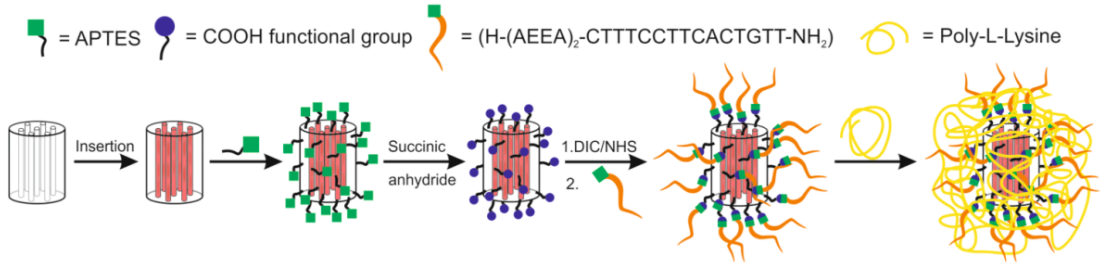

Figure 13. Schéma de fonctionnalisation pour obtenir les zéolites-L fonctionnalisées PNA.

Le nombre de sondes PNA qui se lie à un cristal seul est d'environ 145.
Avant ces expériences sur cellules, nous avons prouvé que le PNA conserve son action biologique antisense, bien que lié à une particule.
De plus, nous avons prouvé que les particules zéolite-L/PNA sont stables à l'intérieur des cellules et que le PNA ne se détache pas des particules après inclusion.
Nous avons ensuite effectué des expériences cellulaires en utilisant des concentrations de particules de 0,01 mg/mL et un temps d'incubation de 1, 4 et 24 heures. Les particules non couvertes sont alors très peu incluses dans la cellule et il faudrait un temps d'incubation trop long pour obtenir une inclusion suffisante.
Couvrir les particules avec du PLL permet alors d'outrepasser ce problème d'inclusion et nous montrons en figure 14 qu'un médicament modèle (DAPI) peut être libéré depuis les cellules après inclusion.

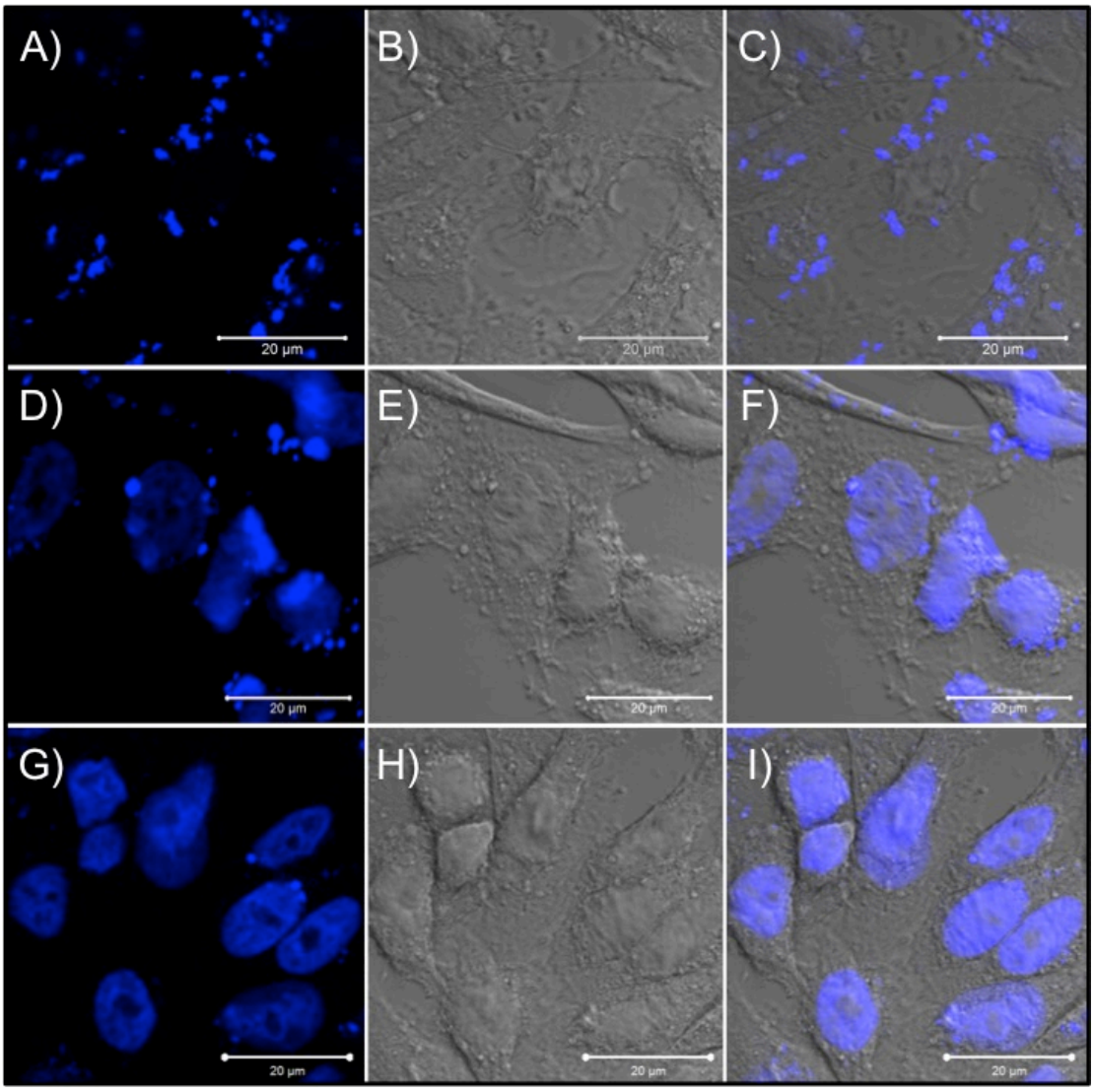

Figure 14. Microscopie confocale de cellule HeLa incubées avec 0,01 mg/mL de PLL-PNA-DAPI-zéolites fonctionnalisées après 1 heure (A-C), 4 heures (D-F), 24 heures (G-I). A, D, G) Images de la fluorescence du signal de DAPI; B, E, H) Image fond claire; C, F, I) superposition des deux images.

Après 4 heures, la quantité de particules dans la cellule est déjà augmentée et la tâche bleu du noyau est visible, ce qui est dû à une fuite de DAPI à travers les pores.

Une incubation prolongée à 24 heures conduit à une autre augmentation des particules incluses. Pendant ce temps, une quantité plus importante de DAPI est libérée, ce qui se traduit par une tâche bleue intense venant du noyau cellulaire.

D'autres applications telles que la bio-imagerie, la libération de médicament ou la thérapie génique sélectionnant des séquences cibles spécifiques du PNA seront testées en utilisant ces nanoparticules hybrides.

Références

[1] Eustis,S. and El-Sayed, M.A., *Chem. Soc. Rev.*, **35**, 209-217, **2006**.

[2] Lu, A.H., Salabas, E.L. and Schuth, F., *Angew. Chem. Int. Ed.*, **46**, 1222-1244, **2007**.

[3] Smith, A.M. and Nie, S.M., *Acc. Chem. Res.*, **43**, 190-200, **2010**.

[4] Buck, S.M., Koo, Y.E.L., Park, E., Xu, H., Philbert, M.A., Brausel, M.A., and Kopelmann, R., *Curr. Opin. Chem. Biol.*, **8**, 540-546, **2004**.

[5] Sukhorukov, G.B., Rogach, A.L., Zebli, B., Skirtach, A.G., Kohler, K., Antipov, A.A., Gaponik, N., Susha, A.S., Winterhalter,M., and Parak, W.J., *Small*, **1**, 194-200, **2005**.

[6] Calzaferri, G., Huber, S., Maas, H., and Minkowski, C., Angew. Chem. Int. Ed., 42, 3732-3758, 2003.

[7] Calzaferri, G., Meallet-Renault, R., Bruehwiler, D., Pansu, R., Dolamic, I., Dienel, T., Adler, P., Li, H., Kunzmann, A., *ChemPhysChem*, 12, 580-594, **2011**.

[8] Becker, M., De Cola, L., Studer, A., J. Mater. Chem. C., 1, 3287-3290, 2013

[9] Schulte, B., Tsotsalas, M., Becker, M., Studer, A., De Cola, L., *Angew. Chem. Int. Ed.*, 49, 6881-6884, **2010**.

[10] El-Gindi, J., Benson, K., De Cola, L., Galla, H.-J., and Kehr, N.S., *Angew. Chem. Int. Ed.*, 51, 3716-3720, **2012**.

[11] Tsotsalas, M.M., Kopka, K., Luppi, G., Wagner, S., Law, M.P., Schaefers, M., and De Cola, L., *ACS Nano*, 4, 342-348, **2010**.

[12] Tsotsalas, M.M., Busbu, M., Gianolo, E., Aime, S., and De Cola, L., *Chem. Mater*, 20, 5888-5893, **2008**.

[13] Strassert, C.A., Otter, M., Albuquerque, R.Q., Hone, A., Vida, Y., Maier, B., and De Cola, L., *Angew. Chem. Int. Ed*, 48, 7928-7931, **2009**.

[14] Lee, J.S., Ha, K., Lee, Y.J., and Yoon, K.B., Adv. Mater., 17, 837-841, 2005.

[15] Li, H., Devaux, A., Popovic, Z., De Cola, L., and Calzaferri, G., Microporous Mesoporous Mater., 95, 112-117, 2005.

[16] Decher, G., *Science* 277, 1232, 1997.

[17] Decher, G., *Science* 277, 1232, 1997.

[18] Cucinotta, F., Popovic, Z., Weiss, E.A., Whitesides, G.M., and De Cola, L., *Adv. Mater.*, 21, 1142-1145, **2009**.

[19] Dotti, C. G., Sullivan, C. A., Banker, G. A., *J. Neurosci.*, **8**, 1454-1468, **1988**.

[20] Johansson, P., Carlberg, P., Danielsen, N., Montelius, L., and Kanje, M., *Biomaterials*, **27**, 1251-1258, **2006**.

[21] Yavin, E., and Yavin, Z., J. Cell Biol., **62**, 540-546, **19**74.

[22] Simon, D.T., Larsson, K.C., Berggren, M., and Richter-Dahlfors, A., *J. Biomedical Science and Engineering*, **3**, 208-217, **2010**.

[23] Bink, H., Lai, Y., Saudari, S.R., Helfer, B., Viventi, J., Van der Speigel, J., Litt, B., and Kagan, C., *Conf. Proc. IEEE Eng. Med. Biol. Soc*., 5400-5403, **2011**.
[24] Simon, D. T. et al., *Nat. Mater*., **8**, 742, **2009**.
[25] Bolin, M. H. et al., *Adv. Mater*., **21**, 4379, **2009**.
[26] Wan, A. M. D., Brooks, D. J., Gumus, A., Fischbach, C. Malliaras, G. G., *Chem. Commun*., 5278, **2009**.
[27] Gumus, A., Califano, J. P., Wan, A. M. D., Huynh, J, Reinhart-King, C. A., Malliaras, G. G., *Soft Matter*, **6**, 5138, **2010**.
[28] Abidian, M. R. et al., *Adv. Mater*., **21**, 3764, **2009**
[29] Khodagholy, D. et al., *Adv. Mater*., **23**, 268, **2011**.
[30] Jimison, L. H. et al., *Adv. Mater*., **24**, 5919-5923, **2012**.
[31] Bystrenova, E. et al., *Adv. Funct. Mater*., **18**, 1751-1756.
[32] Toffanin, S. et al., *J. Mater. Chem. B*, **1**, 3850-3859, **2013**.
[33] Cramer, T. et al., *J. Mater. Chem. B*, **1**, 3728-3741, **2013**
[34] Busby, M., Devaux, A., Blum, C., Subramaniam, V., Calzaferri, G., and De Cola, L., *J. Phys. Chem. C*, **115**, 5974-5988, **2011**
[35] Calzaferri, G., Huber, S., Maas, H., Minkowski, C., *Angew. Chem. Int. Ed.* **42**, 3732-3758, **2003**.
[36] Climent, E. et al., *Angew. Chem. Int. Ed*., **122**, 7439-7441, **2010**.
[37] Wang, F. et al., *Nanomedicine* **2013**, doi: 10.1016/j.nano.2013.04.010
[38] Laskar, A., Ghosh, M. Khattak, S. I., Li, W., Yuan, X.-Y., *Nanomedicine* **7**, 705-717, **2012**.

Introduction

Abstract

This chapter will introduce general concepts, which then will be used throughout this thesis. In the beginning an overview about nanotechnology and biomedicine will be given. After that a special kind of nanoparticles, nanocontainers, will be introduced and their applications in biomedicine will be discussed. The zeolite-L nanocontainer will then be introduced for the first time and several examples of applying them in biomedicine will be given. Finally, their self-assembly into monolayers and possible applications of these substrates will be introduced.

The aim of this thesis is pointed out at the end of this chapter.

H. Luelf, A. Devaux, E. Prasetyanto, L. De Cola in *Organic Nanomaterials. Synthesis, Characterization, and Device Applications*, T. Torres, B. Bottari, Wiley 2013.

1.1 Nanotechnology and biomedicine

Nanotechnology is a research field that focuses on the development of functional materials in the nanometer scale (1 to 100 nm) with unique electronic, optical, magnetic or biological properties[1, 2, 3].

Control over the size, shape, chemical composition and the organization at the nanometer scale is a crucial factor for controlling and tuning the materials' properties as well as the response around them. Nanomaterials can be built up from a variety of different materials such as metals, metal oxides, polymers, lipids or other organic molecules and they are generally synthesized in a bottom up approach followed by a post-synthetic introduction of desired functionalities by modifying their outer or inner surfaces.

Nanoparticles are particularly interesting for biomedical applications since their size is in the same range as a variety of important biomolecules[4, 5, 6, 7, 8, 9]. Compared to eukaryotic cells, nanoparticles are a few orders of magnitude smaller, which allows for specific interactions between them or even for cell uptake[10].

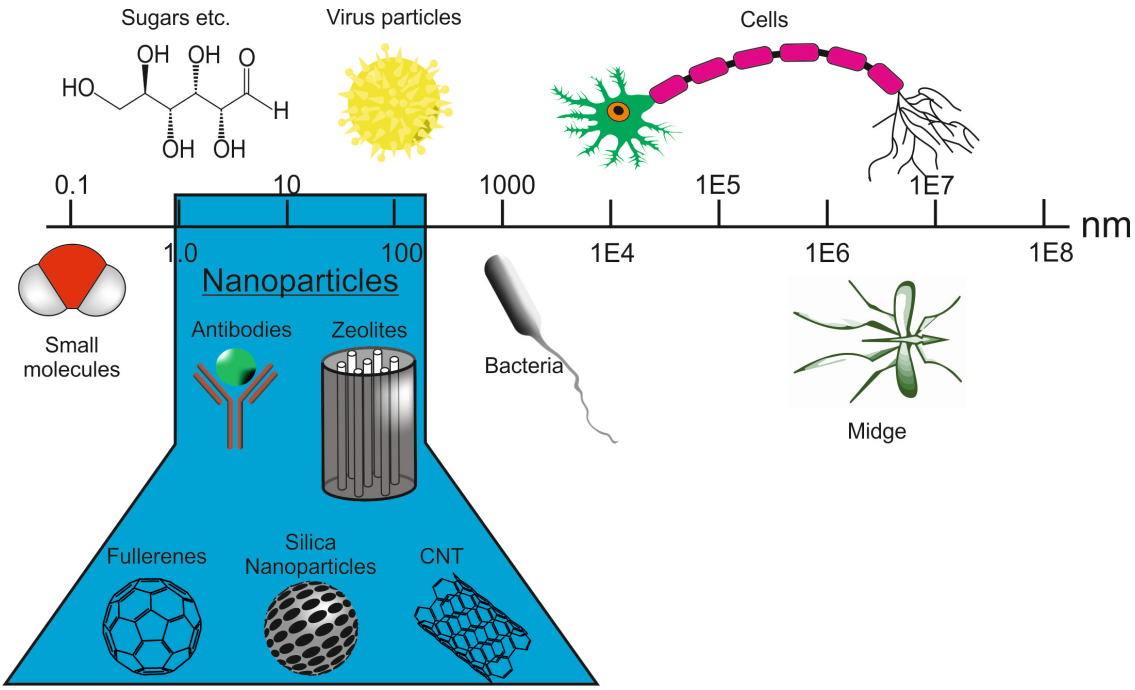

Figure 1.1. Size range of nanoparticles compared to biologically important molecules and living matter.

Nanoparticles for biomedical applications can be directly built up from biocompatible components and therefore nanoparticles have become very interesting in cell biology[11, 12], pharmaceutics and biotechnology[13, 14, 15, 16] molecular or cellular labeling, high contrast medical imaging[17], detection and tracking, or drug delivery[18].

A key factor that makes nanoparticles very interesting for biomedical applications is the possibility to combine several different functions on a single nano-

particle. A schematic view of a nanomaterial designed for biomedical applications is given in Figure 1.2.

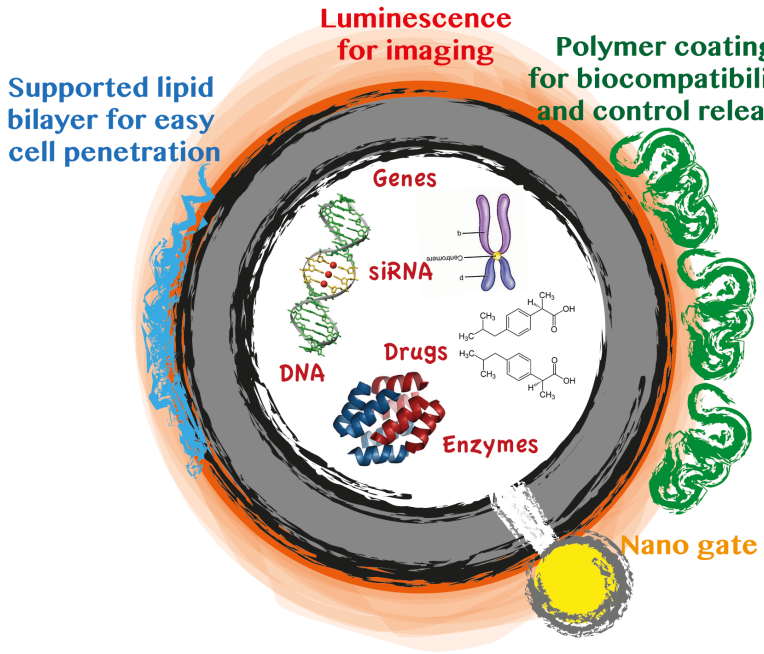

Figure 1.2. Schematic representation of a porous nanomaterial suitable for biomedical applications. The cavities are filled with guest molecules. The surface is modified to improve the biocompatibility. The pores can be engineered in such a way that the payload release occurs in a controlled manner. (Image taken from: **H. Luelf**, A. Devaux, E. Prasetyanto, L. De Cola in *Organic Nanomaterials Synthesis, Characterization, and Device Applications*, T. Torres, B. Bottari, Wiley 2013)

In addition to the design and synthesis of functional nanomaterials, their interaction with living systems, like cells, is a mayor issue when going *in vitro* or even *in vivo*. It has been shown that the particle-cell-interaction does not only depend on the material composition, but also on the size and shape. In this context Huang *et al.* have recently shown that the *in vivo* biodistribution and clearance of silica nanoparticles strongly depends on these factors[19]. Furthermore it has been shown that the toxicity of asbestos can be ascribed to their special needle-like geometry, which can cause apoptosis, inflammations or cancer[20].

In general, the determination of a materials' cytotoxicity is a very import and active research field, but one often finds contradicting results whether a material is toxic or not. Even the same type of nanoparticle can show very different toxicities depending on the particle size and morphology[21, 22, 23] and therefore systematic studies to evaluate a materials' cytotoxicity have to be performed for every variation in composition, size and shape.

Another very import challenge is the uptake of nanoparticles into cells or bacteria[24, 25, 26]. Depending on the composition, size and shape, the particles are internalized following different mechanisms like endocytosis, macropinocytosis or phagocytosis. The uptake mechanism has been shown to depend not only on the particle composition but also on their size and shape. This makes

an accurate forecast of the particle-cell interaction very difficult on the one hand, but on the other hand this allows for controlling and fine-tuning the internalization process and the final fate of the particle to a certain degree[27].

1.2. Nanocontainers and biomedicine

Many different types of nanoparticles have been designed and studied throughout the years.

Due to the possibility to entrap a large number of guest molecules and to easily tailor design multifunctional nanoparticles, the so-called **nanocontainers** are particularly promising for biomedical applications. A variety of biologically relevant biomolecules, like proteins, enzymes, hormones, metabolites, DNA, RNA or other molecules, have been entrapped into nanocontainers so far and their properties have been investigated in detail[28, 29, 30, 31, 32, 33, 34].

The encapsulation of guest molecules inside nanocontainers is very interesting for different reasons. First of all, the encapsulation protects the guests from interactions with their environment, which can lead to increased stabilities or prevents unwanted side reactions with the environment. Furthermore, the poor cellular uptake, the water insoluble nature or the instability of certain drugs can be tackled by using nanocontainers. These drugs can be incorporated inside the nanocontainers and the outer particle surface can be functionalized with cell penetrating or solubilizing functional groups. Above that, the outer surface can be functionalized with receptor entities to specifically target certain cell types or to guide the fate of the nanocontainer after it is taken up inside the cell[35, 36, 37, 38].

Many types of nanocontainers have been described in the literature, such as polymer based micelles or vesicles[39, 40], liposomes[41], metal-organic frameworks (MOFs)[42, 43], carbon nanotubes[44], porous crystals composed of complex salts[45], classical zeolites or zeolite-like materials[28], mesoporous silica or organosilicates[46, 47, 48]. This list should by no means be taken as exhaustive. This thesis will focus on zeolite-L nanocontainer featuring micropores in a unique one-dimensional geometry.

1.3. Zeolite-L

Zeolite-L is one representative of a class of porous aluminosilicate materials, which are called zeolites. Up to date there are more than 200 different zeolite framework-types identified and they are mostly used as absorbents in a variety of industrial applications.

Zeolite-L is a synthetic zeolite with hexagonal symmetry. The framework is built up from cancrinite cages (figure 1.3A), which form columns in the c-direction (figure 1.3B). These columns are connected by oxygen bridges in the a, b plane and thus give rise to 12-membered rings with a free diameter of

0.71 nm (figure 1.3C). Consequently, the zeolite-L consists of a one-dimensional channel system with a largest free diameter of 1.26 nm and a unit cell length of 0.75 nm (figure 1.3B). The channels are oriented in a hexagonal manner and the center-to-center distance of two adjacent channels is 1.8 nm (See figure 1.3D).

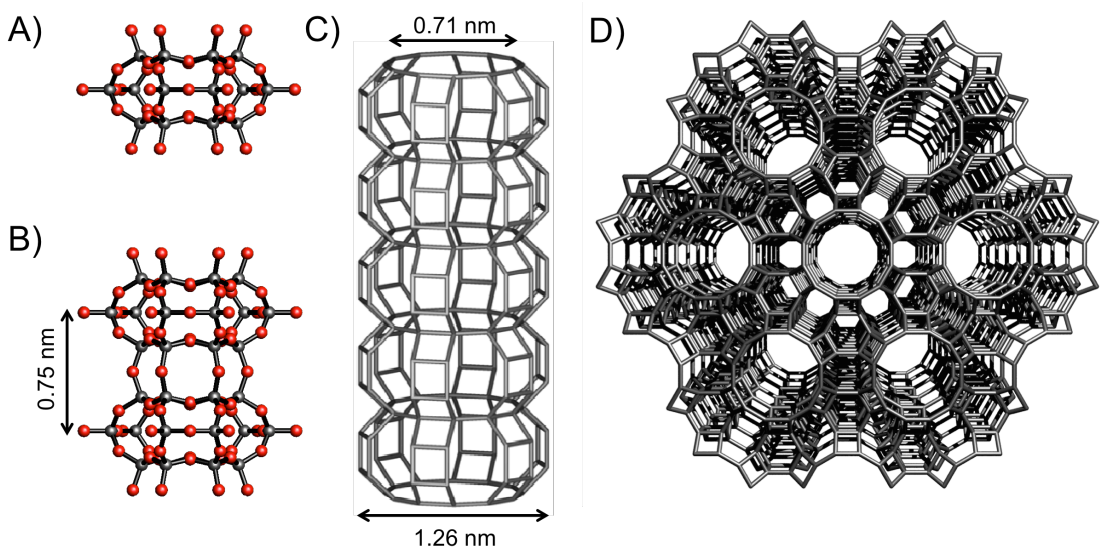

Figure 1.3. Zeolite framework. A) Cancrinite cages. B) Stack of nancrinite cages. C) These stacks are interconnected to form the channels. D) View on a zeolite-L framework along the c-axis. Channels are oriented in a hexagonal manner.

Due to the presence of aluminum atoms in the zeolite framework, the channels show a net negative charge, which is compensated by loosely bound charge-balancing cations. These cations can easily be replaced by other cations or even by cationic molecules, such as dye molecules or biologically active molecules[49].

The general stoichiometric formula of a zeolite-L is $M^{n+}{}_{y/n}[(SiO_2)_x (AlO_2)_y]$ zH_2O, where M are the charge-balancing cations and the water is due to absorbed water in the channels. The stoichiometric formula for a potassium exchanged zeolite-L is $K_9[(SiO_2)_{27} (AlO_2)_9]$ $21H_2O$. After the synthesis of zeolite-L was first reported in 1958[50], the nowadays accepted framework structure was finally reported by Barrer and Villiger in 1969[51]. Zeolite-L crystals are usually synthesized in hydrothermal conditions from synthesis gels containing an aluminium source and a silicon source (See chapter 2).

In order to use zeolite-L crystals as key components in functional materials, the crystals can be tailor functionalized by introducing different functional groups to different parts of the crystals.

To allow a systematic description of the possibilities to functionalize a zeolite-L crystal, the crystal is considered to be built up from three components: 1) the internal channel system; 2) the pore openings and 3) the external surface.

It has been shown, that each of these components can be functionalized independently from each other[52], which can be used to tailor design very specific crystals for every application.

The **internal channel system** of a zeolite-L is capable of hosting a variety of guest molecules. This avoids direct contact between the guests and the environment, which can lead to increased thermal or chemical stabilities and can be used to prevent undesired reactions or interactions between the guest molecules and the environment. It has been shown that guests incorporated into the one-dimensional channel system of zeolite-L can form unique one-dimensional arrangements with very special properties that can not be seen in solution or solid state[29, 53, 54]. These unique orientation of dye-molecules in zeolite-L and applications of such systems has been studied in detail throughout the years[55]. Depending on the guest molecule, it has been shown that those can behave as monomers or that they can show a significant overlap and formation of aggregates inside a zeolite-L host. For further details about the insertion of dye molecules in zeolite-L see chapter 2.
A second important component of a zeolite-L crystal is the **pore opening**. Since the pore openings are the interface between the interior and the exterior of a crystal, they play a very important role in the loading and release of guest molecules and controlling their chemical nature is of importance for applications like drug delivery[56, 57].
One concept to easily tune the properties of the pore openings are the so-called stopper molecules, which have been developed first for zeolite-L[58]. Stopper molecules consist of a long tail, which shows a high affinity for the pore system, and a bulky head group, which is not able to enter the pore system and thus blocks the pore. Stopper molecules can be bound to the zeolite crystal by different interactions such as physisorption, electrostatic interaction, hydrogen bonds or by covalent bond. The stopper molecules can be used to prevent guest molecules from leaking out of the pores as well as preventing molecules from the surrounding entering the pores. It has been shown that even very small molecules such as water or even oxygen are not able to enter into the pores after the stopper molecules are in place. Functional stopper molecules can be used as molecular valves that open and close the pores under certain conditions[59, 60, 61]. However, a selective functionalization of the pore opening is not trivial, since any chemistry must be highly specific and well controlled. Otherwise the molecules will be attached uncontrolled all over the crystal.
The third component, which will be discussed, is the **external surface**. This plays a key role for biological applications since it is in direct contact with the surrounding and determines how the materials can interact with it. The external surface can be tailor designed and functionalized by grafting functional molecules onto it. Depending on the final aim, different molecules for improving the biocompatibility or dispersability[62, 63], for enabling targeting of bio-

molecules, bacteria or cells[64], or to introduce labels such as chemical, luminescent, magnetic or radioactive[7], can be attached to the surface.
Finally, the surface can also be used to promote self-assembly on various supports[65, 66, 67]. For a detailed description of different surface modifications see chapter 2.
A key factor that makes zeolite-L crystal particular interesting for all kinds of different applications is the possibility to functionalize the different parts (pore system, pore openings and external surface) independently from each other.

1.4. Microporous and mesoporous materials in biomedicine

Since the most common hard meso- and micoroporous materials are inorganic in nature, their biocompatibility must be implemented on their outer surfaces and a strong research effort devoted on the adsorption or covalent binding of proteins, enzymes or other biomolecules is necessary to translate this abiotic system for *in vitro* and *in vivo* applications.
Depending on the final aim, adsorption of biological molecules can have desired (biosensors, immunoassays or protein purification systems) or undesired (deposition of biomaterial on contact lenses or dialysis membranes) effects and the development of a method to predict the adsorption properties on different substrates is a big step towards new materials in bio-engineering.
Since most of the mesoporous and microporous nanomaterials discussed in this chapter are silica based, their surface is strongly polar and their total charge is negative, which leads to unspecific binding of polar molecules, but also to a masking effect on the real surface functionalization in solutions containing serum or proteins, which compensate the overall charge[68].
Biocompatible nanocontainers can be used for very different possible applications, like imaging[20, 69, 70, 71, 72], drug delivery[73, 74, 75, 76], and combination of therapy and diagnostics (theranostics). Also antibacterial applications[77, 78, 79, 80], applications for sensing[81], and applications in biotechnology in general[82, 83, 84, 85, 86], where nanocontainers are usually used as supports to immobilize active molecules (like proteins or enzymes), have been reported. The immobilization of antibodies on zeolites has been reported in order to create a more specific receptor on the surface of the nanomaterials. This specificity is important if we wish to target a type of cell, bacteria or virus.
However, the interactions between nanoparticles and biomolecules or even more complex systems such as cells depends on many factors, which in part have been rationalized. Intuitively factors like hydrophilicity and hydrophobicity, electrostatic and structural interactions, size and shape of the nanomaterials and of course their chemical compositions play an important role. Talking about proteins also the change in conformation may complicate the prediction of their adsorption[87]. Mitchell *et al.* studied the uptake of different lipase enzymes onto zeolites and mesoporous silica particles for catalytic ap-

plications[88]. They have shown that the enzyme uptake strongly depends on the mesoporous surface. Furthermore Hu *et al.* studied the influence of the crystal plane and size of zeolite-L nanoparticles on the protein absorption behaviors[89]. Due to their larger surface areas, smaller crystals show larger protein adsorption capacities. In addition, a larger protein adsorption was observed at the (001) crystals plane, which can be explained by abundant exposed pore openings. Tavolaro *et al.* investigated the influence of a series of different factors on the immobilization of cytochrome c on zeolites and have shown that the electrostatic interaction seems to be the most important factor that governs the immobilization[90]. The adsorption could also be used to enrich a solution with sequestering a desired protein. Cao *et al.* presented an elegant example showing that it is possible to use nanozeolites for carrying out such a challenging task[91]. In contrast to mesoporous silica materials[92, 93], nanozeolites exhibit a multilayer protein adsorption mechanism on their surface[94], which endows nanozeolite particles with larger protein adsorption capacity. In addition, high chemical and environmental stability of zeolite materials favor their supplication under harsher conditions compared to other nanomaterials[69].

When going from protein or enzyme adsorption to cell adsorption on zeolite surfaces, the mechanisms of adsorption become much more complicated due to the complex constitution of cellular surfaces, where a variety of different active sites, such as proteins, polysaccharides or lipids, is present.

Kubota *et al.* have tried to simplify the complex interactions between cells and zeolite surfaces, by approximating them to colloidal particles interactions, where van der Waals and electric double layer interactions are taken into account[95].

Modification of the zeolite surface with surfactants can also be used to enhance cellular adhesion[96].

With this knowledge, a better design of hybrid systems can be achieved in order to facilitate the uptake or the adhesion on cells. However, we must remember that size matter and that shape is also relevant for cell uptake and their toxicity[97, 98].

In vitro studies: Interaction of zeolites with cells

One of the most crucial factors for applying nanoparticles in biomedicine and biotechnology is their biocompatibility. It is obvious that a material, which is designed to be applied in biomedicine, must not show any undesired toxicity or side effects when applied *in vitro* or even *in vivo*.

That zeolites, in particular discs-shaped zeolite-L particles, are indeed biocompatible and non-toxic, has been recently shown by *Li et al.*[99] They have shown, that disc-shaped zeolite-L particles show very little cytotoxicity in low concentration and independently of their surface functionalization. However, in high concentrations these particles show surface functionalization depend cytotoxicity, where positively functionalized particles show generally higher

toxicities compared to neutral or negatively charged particles. Also the uptake is strongly dependent on the surface functionalization. It has been shown that the particles are considerably internalized independently of their surface functionalization after 24 hours, but that the surface functionalization plays a very important role when shorter incubation times (around 2 hours) are applied. In this case it has been shown that even the uptake mechanism depends strongly on their surface functionalization.
The very good biocompatibility of zeolites already led to the development of commercially available products, which are widely applied in humans nowadays - some of them will be discussed later in this chapter.

A very elegant way of applying zeolite-L particles in biotechnology has been shown by Popovic *et al.* They have shown that zeolite nanocrystals can be used as an external tool to self-assemble living systems, like bacteria[100]. The self-assembly was achieved by using nonpathogenic *E. coli* (strain JM 109) and zeolite-L crystals with a mean length and mean diameter of 1.0 x 1.0 μm^2, which was filled with a fluorescent dye. The outer membrane of *E. coli* is blistered with lipopolysaccharides that are phosphorylated at multiple locations, which leads to a negatively charged outer membrane. The zeolite-L crystals were amino functionalized only at the channel entrances, which were protonated under the used conditions. This led to a positively charged system, which can bind electrostatically to the negatively charged bacteria membrane. Furthermore it has been shown that by using this setup and the right amounts of bacteria and nanocrystals it is possible to self assemble two bacteria with a nanocontainer junction (See Figure 1.4).

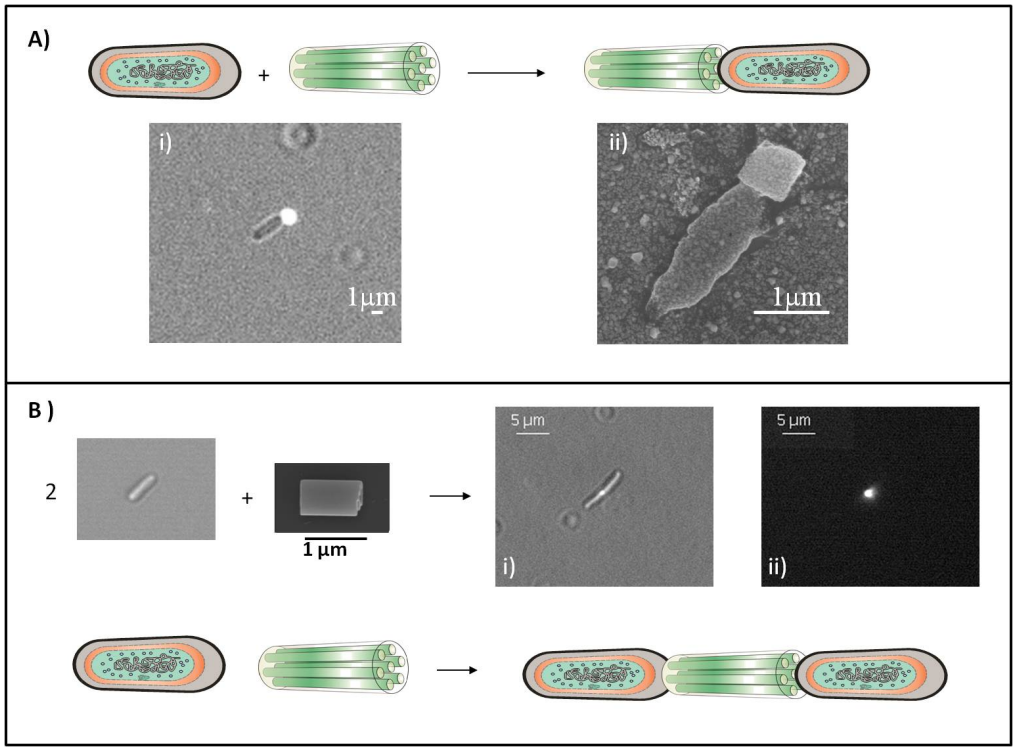

Figure 1.4. A) Illustration of a 1:1 zeolite-L/bacteria assembly. i) Optical microscope image taken upon irradiation with white and blue light. ii) SEM image of the assembly taken upon evaporation of the solvent and coating with silver (5 nm). **B)** Self assembly of two bacteria by using a zeolite L crystal as junction. i) Optical image taken upon white and blue light irradiation. ii) Irradiation of the same sample with blue light. The fluorescence of the dye filled junction is observed. (Image and figure caption taken from: **H. Luelf**, A. Devaux, E. Prasetyanto, L. De Cola in *Organic Nanomaterials Synthesis, Characterization, and Device Applications*, T. Torres, B. Bottari, Wiley 2013).

Such background was then exploited for theranostic applications using smaller zeolites and different functionalities able to target, label and photoinactivate pathogenic and antiobiotic-resistant bacteria (Neisseria gonorrhoeae and *E. coli*)[101]. In detail, a highly green luminescent perylene diimide dye (DXP) was inserted into pores of zeolite-L nanocrystals to label the cells. The outer surface was then functionalized with a silicon phthalocyanine photosensitizer that produces toxic singlet oxygen upon irradiation with red light. Additionally, the outer surface was functionalized with amine groups, which are protonated in physiological conditions and bind electrostatically to the negatively charged membrane of the bacteria. A pictorial view of the trifunctional nanomaterial and their components is given in figure 1.5. After the binding of the particles to the bacteria is confirmed by using the green fluorescent label inside the zeolites, the particles can be irradiated with red light to trigger the production of singlet oxygen, which then efficiently kills the bacteria.

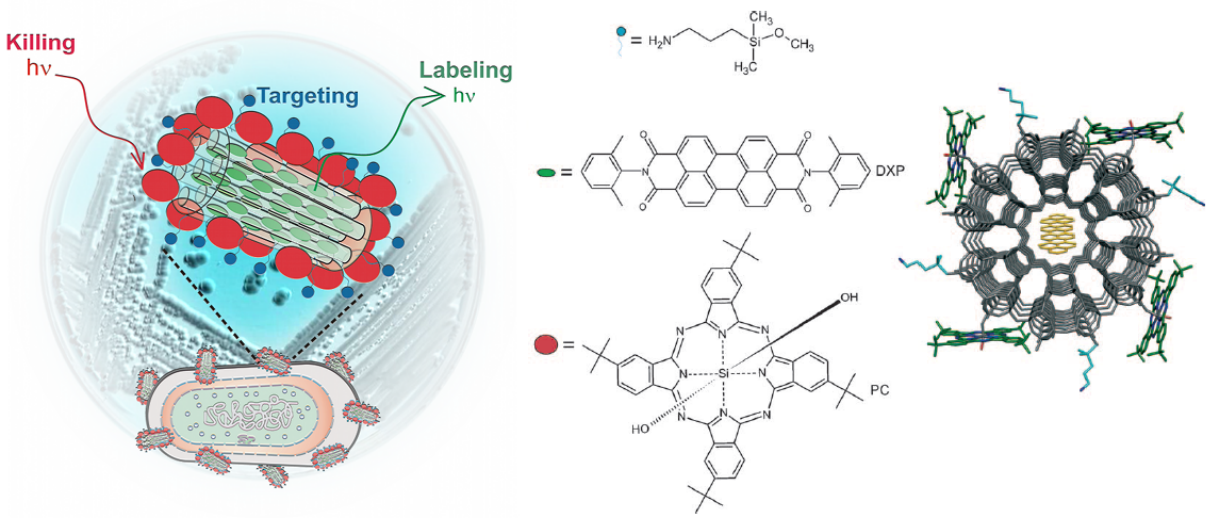

Figure 1.5. Pictorial representation of the designed trifunctional nanomaterial based on zeolite-L. (Image and figure caption taken from: **H. Luelf**, A. Devaux, E. Prasetyanto, L. De Cola in *Organic Nanomaterials Synthesis, Characterization, and Device Applications*, T. Torres, B. Bottari, Wiley 2013).

Another example of using nanomaterials for photodynamic therapy (PDT) applications was given by Hocine *et al.*[102], where crystalline silicalite, MCM-41 and nanoparticles with radial porosity were used. This time the porous materials have been internalized by cancer cells. Therefore water soluble porphyrins were encapsulated covalently inside the nanoparticles and PDT experiments were performed on MDA-MB-231 breast cancer cells. It has been shown that the reported nanoparticles show significant cell death after irradiation, which was however not correlated with the quantum yield of singlet oxygen production and therefore other parameters, like endocytosis, or membrane damage due to the size of the particles must play an important role on cell death.
Even though recently many studies have focused on the uptake of particles inside cells, not much is known on the mechanism of internalization and on the cytotoxicity of such materials.
The shape, the surface properties and functionalization play an important role for the particle-cell interaction, as shown by Huang et al[78] for mesoporous silica nanoparticles. It has been reported that particles without further functionalization are mediated by a clathrin-pitted mechanism[103], amino-functionalized nanoparticles are uptaken via a caveolae dependent mechanism[104], which is clathrin independent, and the uptake of mannose functionalized nanoparticles is mediated by mannose receptors[105]. However, such behavior has been tested only for one cell line and in specific conditions.

A typical application for nanocontainer particles is in the field of drug release. Therefore the pores are usually applied to encapsulate the drugs, which can optimally be released in a controlled way.

The most prominent inorganic systems studied for drug release are mesoporous silica particles[106, 107, 108, 109, 110, 111], but zeolites are very rarely studied for this purpose.

To the best of my knowledge only a few reports dealing with drug release from zeolite pores are published so far.
Rivera and Farís studied the potential application of clinoptilite-surfactant composites as supports for bio-active molecules[112]. Therefore the antibiotic sulfamethoxazole (see figure 1.6) was incorporated in a clinoptilite-benzalkonium chloride composite and it has been shown that 80% of the drug can be released from the system in aqueous medium in 24 hour.

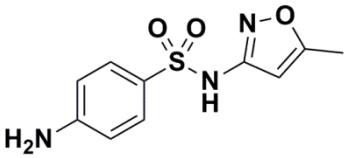

Figure 1.6. Structure of sulfamethoxazole. (Image and figure caption taken from: **H. Luelf**, A. Devaux, E. Prasetyanto, L. De Cola in *Organic Nanomaterials Synthesis, Characterization, and Device Applications*, T. Torres, B. Bottari, Wiley 2013).

Arruebo *et al.* reported a magnetic triggered drug delivery system based on magnetite and FAU zeolites and containing doxorubicin, an antitumor drug. *In vitro* experiments have shown that this system is able to store and release remarkable amounts of the drug[113].
A slightly different approach of investigating drug-release properties of a zeolite-drug system was reported by Fatouros *et al.* in 2011[114]. They have applied a combination of experiments and theory in order to assess the potential use of zeolite BEA as drug delivery agent. Molecular dynamics have been used to examine the diffusion of the two drugs salbutamol and theophylline (See image 1.7).

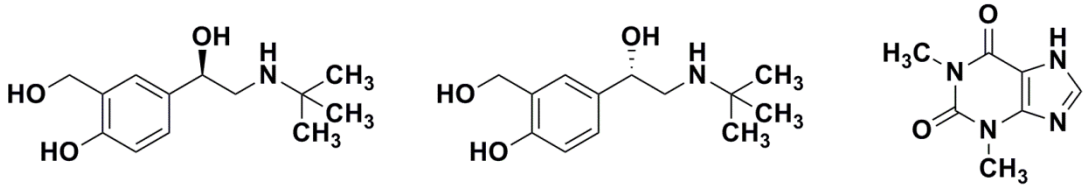

Figure 1.7. Structures of Salbutamol and Theophyllin. The active form of Salbutamol is (R)-Salbutamol. (Image and figure caption taken from: **H. Luelf**, A. Devaux, E. Prasetyanto, L. De Cola in *Organic Nanomaterials Synthesis, Characterization, and Device Applications*, T. Torres, B. Bottari, Wiley 2013).

Experimental studies regarding the loading and release of these drug molecules were done and support the results obtained by molecular dynamics.

These results suggest that modeling has an important role in screening zeolite-drug combinations for their drug-release applications.

***In vivo* studies: imaging and drug delivery**

As already mentioned before, the use of mesoporous materials for imaging and theranostic is potentially very interesting due to the high density of labels and / or drugs as well as the multimodality which can be implemented on these systems.

In 2008 the first example of using zeolite crystals as a dual-probe optical and magnetic imaging system was reported[7]. The channels of zeolite-L crystals with a length of just 30 nm were therefore loaded with a fluorescent dye (pyronine), which can be used as an optical imaging unit. In a second step, the outer surface is modified with a highly stable gadolinium(III) complex acting as the magnetic imaging unit. A pictorial view of the system and the 1/T1 NMRD profile is shown in figure 1.8.

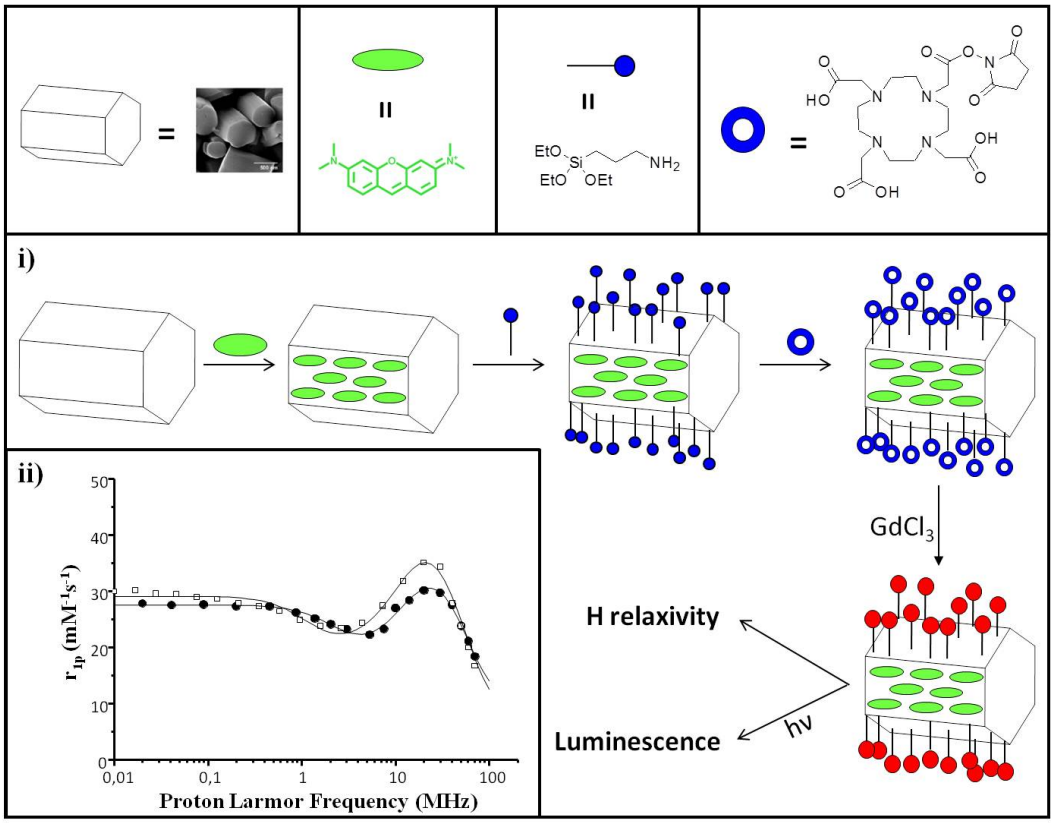

Figure 1.8. i) Synthesis of Gd-DOTA functionalized zeolite L crystals. In the first step pyronine molecules are introduced into the channels via ion exchange. In the second step a linker (APTES) is bound to the entire surface of the zeolite-L crystals. In the third step the chelating ligand (DOTA) is covalently attached to the back side of the linker. The final step involves complexation of the Gd(III) to the surface of the zeolite L crystals. The Gd(III)- DOTA complexes are represented as red balls. ii) 1/T! NMRD profile of a 1 mM solution of Gd-DOTA-zeolite L measured at 25 °C (●) and 37 °C (□). (Image and figure caption taken from: **H. Luelf**, A. Devaux, E. Prasetyanto, L. De Cola in *Organic Nanomaterials Synthesis, Characterization, and Device Applications*, T. Torres, B. Bottari, Wiley 2013).

Imaging can also be done using radioisotopes by scintillation methods (PET, Positron Emission Tomography). Therefore the zeolite-L crystals can be filled with the positively charged γ-emitter $^{111}In^{3+}$. In order to avoid leakage of the indium into the media, the channels were closed with stopcock molecules. The zeolite crystals have then been coated with PEG chains to render them biocompatible. The designed system is shown in figure **1.9.**

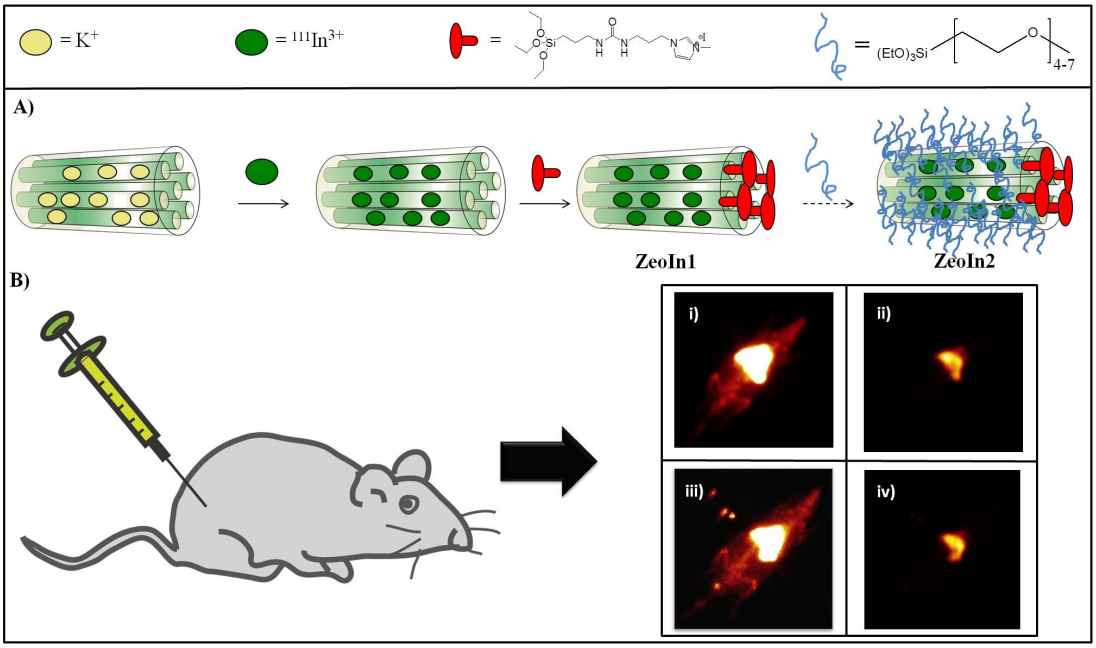

Figure 1.9. A) Schematic functionalization of the zeolite L crystals. B) Two-dimensional static scintigraphic images are obtained 70 min after injection of the zeolites. ZeoIn1 injected into rat 1 in i) high and ii) low contrast. ZeoIn2 injected into rat 2 in iii) high and iv) low contrast. (Image and figure caption taken from: **H. Luelf**, A. Devaux, E. Prasetyanto, L. De Cola in *Organic Nanomaterials Synthesis, Characterization, and Device Applications*, T. Torres, B. Bottari, Wiley 2013)

The zeolites were injected into rats and two-dimensional static scintigraphic images were recorded (See figure 1.9 B)). The biodistribution of the particles after 24 hours was monitored but the fate of the zeolites is still unknown.
In vivo studies related to the toxicity of inorganic nanomaterials are still a controversial field. Regarding mesoporous materials the early studies of Langer *et al.* showed that the "naked" mesoporous systems were very toxic even at rather low concentrations. However we should mention that the size of the materials employed was larger than 150 nm and the toxicity was found only when the materials were injected into the blood stream. Other studies indicated that the toxicity of the materials is very much related to their dose[115, 116, 117, 118, 119]. Tamori *et al.* showed that mesoporous systems with a diameter of 100 – 120 nm and covered with folic acid are toxic in mice after several days of treatment with a dose of 100 mg / kg[85]. On the other hand, decreasing the dose to 1 mg per mouse did not show significant toxicity.

The cytotoxicity of nanozeolites has only been studied *in vitro*. It has been shown, that their toxicity depends on the size, composition and shape. The pure-silica zeolite silicalite-1 shows no cytotoxicity, whereas aluminum-containing zeolites like ZSM-5, zeolite-L, and LTA show dose dependent toxic effects[120].
However, many more studies are necessary since the fate of the porous materials in the body is still not known. There are some interesting studies related to the biodegradation and excretion of silica nanoparticles[88]. In fact, it has been demonstrated that for mesoporous silicon degradation is completed within 20 hours[121, 122]. Indeed, so far most of the studies have been carried out with particles larger than 30 nm which would be problematic for passing the liver and renal barriers.

As already mentioned before, due to their good biocompatibility, zeolites are already used for medical purposes in humans and commercially available products are already on the market.
Amongst the earlier examples the use of zeolite Y in combination with the well known paramagnetism of Gd(III) has been investigated by Bresinka et al. in 1994[71]. They have shown that Gd(III) can be exchanged with sodium in NaY-zeolites. The GdNaY zeolites are reasonably stable to low pH and *in vivo* studies were done by Young *et al*. in order to evaluate the efficiency and safety of the system[70]. They found that the Gd-zeolites significantly improved the efficiency scores, that it is not absorbed from the gastrointestinal tract and thus it is not toxic. A company started on this discovery (Pharmacyclics) and the product is marketed under the name Gadolite®.
The presence of the Al and Si in the same material triggered some studies of the effect of Al on the magnetic response of Gd(III)[72].

Another application for zeolites, in particular clinoptilolite, is using them as food additives.
It has been shown that clinoptilolite has various positive effects when fed to animals, which is attributed to the ability of adsorbing a variety of toxins from the gut allowing for their removal from the body[123, 124]. This behavior has previously been found and applied for removing metal contaminations from soil[125] and water[126]. Feeding pigs with a diet supplemented with zeolites, has been shown to lead to an improved growth[127, 128] as well as an enhanced reproductive performance of sows[129]. These positive effects occur in the absence of any negative side effects, like a possible decrease in serum electrolyte concentration[130].
The ability of using zeolites to remove heavy metals from the human body has been studied by Flowers *et al* in 2009[131]. They evaluated the concentration of a variety of heavy metals (aluminium, anitimony, arsenic, bismuth cadmium, lead, mercury, nickel, and tin) in the urine of male healthy patients after taking a clinoptilolite suspension (Natural Cellular Defense®) for seven or 30 days.

They show that a daily dose of a clinoptilolite suspension is a very safe and efficient way of removing various heavy metals from the body. They also show that this treatment does not influence the serum electrolyte concentrations. The clinoptilolite suspension is nowadays commercially available as Natural Cellular Defense® marketed by Waiora.
Above that, a study from 2004 shows that using zeolites as food additives can lead to an accelerated recovery in human burn trauma victims[132].

1.5. Self-assembly of zeolites into monolayers

Self-assembly is a process in which a disordered system assembles themselves into an ordered structure[133, 134, 135].
The first examples of self-assembly are reported at the molecular level[136, 137, 138] and numerous examples are known in the literature about the self-assembly of molecules[124, 139, 140]. In the last years more and more attention was concentrated on the self-assembly of all kinds of nano-objects[141 142 143 144], like nanoparticles[122], nanorods[123], and plates[124].
Analogue to the self-assembly of molecules, the nanoobjects were assembled into one-dimensional and two-dimensional arrays using the well-established concepts of supramolecular chemistry. Although several examples are known in the literature, self assembly of nanostructures is much more difficult than self assembly of molecules, which is due the larger size, shape, and often lack of specificity and recognition sites. The situation becomes different when nanoobjects are assembled on a solid substrate since the nature or functionalization of the substrate can favor the deposition of the nanoparticles and can lead to high coverage and the formation of very homogenous monolayers[101, 145, 146, 147, 148, 149].
Most of the reported self-assembled nanoparticle monolayers concern with spherical shaped objects and just a very few examples were reported in which the assembly involves non-spherical porous systems. Amongst them, very relevant to this chapter are the reports by Cazaferri *et al.*[150] and Lee *et al.*[148] who described facile and straight forward ways to prepare self assembled monolayer from different zeolite crystals.
For a detailed description of zeolite-L monolayer preparation and functionalization see chapter 2 of this thesis.
The motivation to organize these materials in ordered monolayers rely on different properties of the outside materials and of the channels, as well as the possibility to trigger the release of molecules entrapped into the pores with an external stimulus.
Indeed the presence of thousands of molecules inside each nano-container and the fact that each of them could be addressed as a single object is very appealing and has been almost unexplored so far. The orientation of the channels is of critical importance since the surface will block one side if the

channels are oriented perpendicularly to it and the release could then be directional. On the other hand, if the materials are oriented randomly a control of a triggered release is difficult.
In this respect materials with one-dimensional channels are the best choice and the shape of the nanocontainer can be used to favor an arrangement on the surface *vs* an interparticle arrangement.
Amongst several applications, which can be envisaged with such organized layers, the biomedical, such as cell growth and eventually cell communication, and electrical, where the nanocontainers are used to form highly oriented molecular wires, are the most relevant for this chapter.

1.6. Further functionalization of zeolite-L monolayers

A further functionalization of the monolayer surface is often required for certain applications, especially in tissue engineering or biotechnology.
In order to use zeolite monolayers as a substrate for cellular growth, biocompatibility of the surface is crucial and can be provided by coating the zeolite-L surfaces with adhesive molecules, which can be done in different ways, each of them showing certain advantages and disadvantages.
A very simple and straightforward way is a functionalization by physisorption or non-covalent interactions such as hydrogen- or electrostatic bonds, which can be achieved in different ways, like drop-casting, spin-coating or layer-by-layer deposition[151]. The advantage of these methods is their very high versatility and their easy and fast producability. However, these methods often show low stabilities or they lack orientation of the biomolecules in respect to the surface. Above that, a structuring of the coating is often very difficult.
Another, but often more challenging way is the covalent functionalization of the monolayer surface. To functionalize the monolayer covalently, the functional groups on the monolayer must be chosen in that way that they can react with the coating molecules. This often restricts the choice of possible coatings, or special functional groups must be attached to either the monolayer or the coating beforehand. If this requirement is fulfilled, the coating can be attached in different ways. In a first approach the monolayer can just be added to a solution of the coating molecules. In this way, the whole surface can be easily functionalized, but a special control of the functionalization is not possible.
Spatial control can be achieved by using the concept of soft lithography[152]. Especially in cell biology soft lithography is used with increasing frequency due to its simplicity, low cost and compatibility with cells[153, 154]. The chemical modification is called microcontact printing (MCP) and it is used worldwide. The material, which is mostly used for soft lithography in combination with microbiology or biology, is polydimethylsiloxane (PDMS). This choice is dictated by the soft, flexible, biocompatible, insulating, unreactive, transparent to

UV/vis light, permeable to gases and only moderately permeable to water properties of PDMS[152, 153]. For further details about microcontact printing, see chapter 2.

1.7. Scope of the thesis

This thesis applies zeolite-L nanoparticles as key-components for electronics and biomedicine.

Depending on the application, zeolite-L crystals in different sizes and shapes are used, ranging from nanozeolite crystals with a length of just a few tenths of nanometers up to microzeolite particles with a size of about 1000 nm.

Chapter 2 introduces general concepts and experimental techniques, which have been used throughout this thesis. The zeolite synthesis, functionalization and self-assembly into monolayers is discussed in detail.

Chapters 3 and 4 then show first very important experiments that allow for the growth and stimulation of neuron cells on zeolite monolayers.

In particular we aim to monitor the growth, multiplication and synaptic communication of primary neurons with the final goal to monitor single synaptic events triggered by electrical stimulation. The zeolites are therefore be used as an artificial presynaptic site for initiating the signal cascade, as illustrated in figure 1.10.

In order to achieve this final goal, the optimal conditions for the neurons to grow and proliferate on zeolite-L monolayers are developed in chapter 3.

Once the optimal conditions are found, chapter 4 presents first experiments to allow for an electrical stimulation of these cells. This chapter describes how the per-se insulation zeolite material can be rendered electrical conductive by introducing semiconductor molecules in the pores.

These materials show extraordinary electrical properties allowing for applications even in the field of organic electronics.

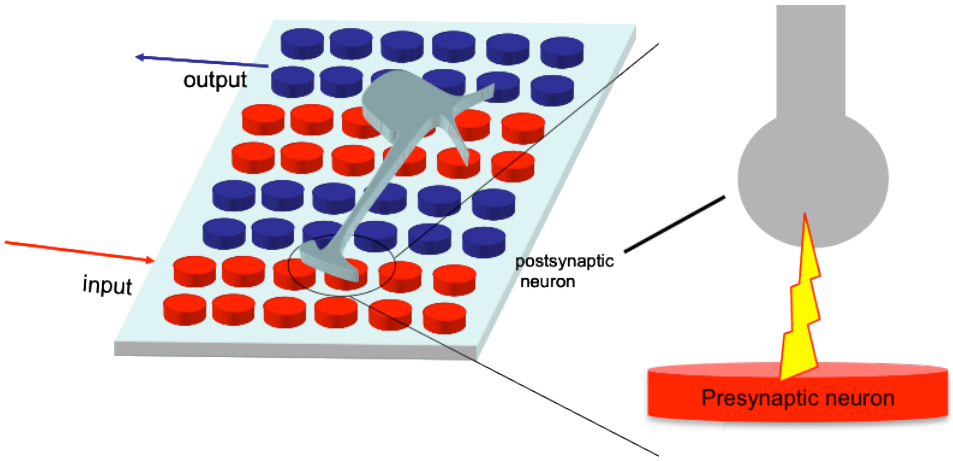

Figure 1.10. Schematic representation oft he experiment. Rendering the zeolites electrical conductive allows for an electrical excitation of the neurons.

Chapter 5 then presents another approach to assemble organic semiconductor molecules into highly ordered one-dimensional structures. The molecules are therefore assembled directly from the gas phase onto a substrate and weak intermolecular interactions then trigger the formation the assemblies.
Chapters 6 and 7 investigate the possibility of using zeolite-L nanoparticles as oligonucleotide carriers for a simultaneous release of the oligonucleotide and a model drug, which has been incorporated in the zeolite pores.
In detail, chapter 6 describes the delivery of DNA oligonucleotides for which 2 different types of zeolites (nanozeolite-L and microzeolite-L) are used.
Chapter 7 then shows the multifunctional delivery of peptide nucleic acids (PNAs) and a model drug to living cells.
Finally, chapter 8 describes experimental techniques that are used throughout this thesis.

References

[1] Eustis,S. and El-Sayed, M.A., *Chem. Soc. Rev.*, **35**, 209-217, **2006**.
[2] Lu, A.H., Salabas, E.L. and Schuth, F., *Angew. Chem. Int. Ed.*, **46**, 1222-1244, **2007**.
[3] Smith, A.M. and Nie, S.M., *Acc. Chem. Res.*, **43**, 190-200, **2010**.
[4] Dreaden, E. C., Alkilany, A. M., Huang, X., Murphy, C. J., El-Sayed, M. A., *Chem. Soc. Rev*. **41**, 2740-2779, **2012**.
[5] Kanasty, R., Dorkin, J. R., Vegas, A., Anderson, D., *Nat. Mater*. **12**, 967-977, **2013**.
[6] Mura, S., Nicolas, J., Couvreur, P., *Nat. Mater.*, **12**, 991-1003, **2013**.
[7] Tonga, G. Y., Saha, K., Rotello, V. M., *Adv. Mater*. 1-11, **2013**.
[8] Steinmetz, N. F., Manchester, M., *Viral Nanoparticles: Tools for Material Science and Biomedicine*, Pan Stanford Publishing, **2011**.
[9] Bulte, J. W. M., and Modo, M. M. J., *Nanoparticles in Biomedical Imaging*, Springer, **2008**.
[10] Mailänder, V., Landfester, K., *Biomacromolecules* **10**, 2379-2400, **2009**.
[11] Wang, E. C., Wang, A. Z., *Integr. Biol*. **2013**.
[12] Chakraborty , C., Pal, S., Doss, G. P., Wen, Z. H., Lin, C. S., *Front. Biosci*. **18**, 1030-1050, **2013**.
[13] Chopra, N., Gavalas, V.G., Hindis, B.J. and Bachas, L.G., *Anal. Lett.*, **40**, 2067-2096, **2007**.
[14] Corchero, J.L. and Villaverde, A., *Trends in biotechnol.*, **27**, 468-476, **2009**.
[15] Wang, Z. and Lu, Y., *J. Mater. Chem.*, **19**, 1788-1798, **2009**.
[16] Pelaz, B. et al., *ACS Nano* **6**, 8468-8483, **2012**.
[17] Tsotsalas, M., Busby, M., Gianolo, E., Aime, S., and De Cola, L.,*Chem. Mater.*, **20**, 5888-5893, **2008**.
[18] Cai, W., and Chen, X., *Small*, **11**, 1840-1854, **2007**.
[19] Huang, X., Li, L., Liu, T., Hao, N., Liu, H., Chen, D., and Tang, F., *ACS Nano*, **5**, 5390-5399, **2011**.
[20] Shi, X., von dem Bussche, A., Hurt, R.H., Kane, A.B., and Gao, H., *Nat. Nanotechn.*, **6**, 714-719, **2011**.
[21] Cauda, V., Argyo, C., and Bein, T., *J. Mater. Chem.*, **20**, 8693-8699, **2010**.
[22] Sauer, A.M., Schlossbauer, A., Ruthardt, N., Cauda, V., Bein, T., and Brauchle, C., *Nano Lett.*, **10**, 3684-3691, **2010**.
[23] Suteewong, T., Sai, H., Cohen, R., Wang, S.T., Bradbury, M., Baird, B., Gruner, S.M., and Wiesner, U., *J. Am. Chem. Soc.*, **133**, 172-175, **2011**.
[24] Liu, X., Chen, Y., Li, H., Huang, N., Jin, Q., Ren, K., Ji, J., *ACS Nano* **7**, 6244-6257, **2013**.
[25] Treuel, L., Jiang, X., Nienhaus, G. U., *J. R. Soc. Interface*, **10**, **2013**.
[26] Kim, J. A., Aberg, C., Salvati, A., Dawson, K. A., *Nature Nanotech*. **7**, 62-68, **2012**.
[27] Chou, L.Y.T., Ming, K., and Chan, W.C.W., *Chem. Soc. Rev.*, **40**, 233-245, **2011**.
[28] Calzaferri, G., and Devaux, A. John Wiley & Sons, Inc. New Jersey, **2011**.
[29] Moller, S.M., and Bein, T., *Science*, **333**, 297-298, **2011**.
[30] Mackowiak, S., Schmidt, A., Weiss, V., Argyo, C., von Schirnding, C., Bein, T., Bräuchle, C., *Nano Lett.* **13**, 2576-2583, **2013**.

[31] Dobay, M., Schmidt, A., Mendoza, E., Bein, T., Rädler, J., *Nano Lett*. **13**,1047-1052, **2013**.
[32] Schloßbauer, A., Sauer, A., Cauda, V., Schmidt, A., Engelke, H., Rothbauer, U., Zolghadr, K., Leonhardt, H., Bräuchle, C., Bein, T., *Adv. Healthcare Mater.* **1**, 316-320, **2012**.
[33] Colilla, M., González, B., Vallet-Regí, M., *Biomater. Sci*. **1**, 114-134, **2013**.
[34] Knezevic, N., Ruiz-Hernández, E., Hennink, W. and Vallet-Regi, M., *RSC Advances* **3**, 9584-9593, **2013**.
[35] Buck, S.M., Koo, Y.E.L., Park, E., Xu, H., Philbert, M.A., Brausel, M.A., and Kopelmann, R., *Curr. Opin. Chem. Biol*., **8**, 540-546, **2004**.
[36] Sukhorukov, G.B., Rogach, A.L., Zebli, B., Skirtach, A.G., Kohler, K., Antipov, A.A., Gaponik, N., Susha, A.S., Winterhalter,M., and Parak, W.J., *Small*, **1**, 194-200, **2005**.
[37] Kickhoefer, V. A. *et al*., *ACS Nano* **3**, 27-36, **2009**.
[38] Kularatne, S. A., Low. P. S., *Methods Mol. Biol*. **624**, 249-265, **2010**.
[39] Blanazs, A., Armes, S.P., and Ryan, A.J., *Macromol. Rapid Commun*., **30**, 267-277, **2009**.
[40] Rijcken, C.J.F., Soga, O., Henink, W.E., and von Nostrum, C.F., *J. Controlled Release*, **120**, 131-148, **2007**.
[41] Andresen, T.L., Jensen, S.S., and Jorgensen, K., Prog. *Lipid Res*., **44**. 69-97, **2005**.
[42] Muller, M., Devaux, A., Yang, C., De Cola, L., and Fischer, R.A., Abstracts of Papers, 239th ACA National Meeting, San Francisco, CA, United States, March 21-25, **2010**, INOR-370.
[43] Yaghi, O.M., O'Keeffe, M., Ockwig, N.W., Chae, H.K., Nature, 423, 705-714, 2003
[44] Lu, F., Gu, L., Meziani, M.J., Wang, X., Luo, P.G., Veca, L.M., Cao, L., and Sun, Y.P., Adv. Mater., 21, 139-152, 2009.
[45] Mauro, M., Schuermann, K.C., Pretot, R. Hafner, A., Mercandelli, P., Sironi, A., and De Cola, L., Angew. Chem. Int. Ed., 49, 1222, 2010.
[46] Corma, A., and Garcia, H., Eur. J. Inorg. Chem., 6, 1143-1164, 2004.
[47] Inagaki, S., Ohtani, O., Goto, Y., Okamoto, K., Ikai, M., Yanabaka, K.I., Tani, T., and Okada, T., Angew. Chem. Int. Ed., 48, 4042-4046, 2009.
[48] Schulz-Ekloff, G., Wohrle, D., van Duffel, B., and Schoonheydt, R.A., Micropor. Mesopor. Mater., 51, 91-138, 2002.
[49] Calzaferri, G., Huber, S., Maas, H., and Minkowski, C., Angew. Chem. Int. Ed., 42, 3732-3758, 2003.
[50] Breck, D.E.W., US Pat 3216789, 1965.
[51] Barrer, R.M., Villiger, H., Zeitschrift fuer Kristallographie – Crystalline Materials, 128, 352-370, 1969.
[52] Busby, M., Kerschbaumer, H., Calzaferri, G., Adv. Mater., 20, 1614-1618, 2008.
[53] Busby, M, Devaux, A., Blum, C, Subramaniam, V., Calzaferri, G., and De Cola, L., J. Phys. Chem. C, 115, 5974-5988, 2011.
[54] Mahato, R. N., Luelf, H., Siekmann, M. H., Kersten, S. P., Bobbert, P. A., de Jong, M. P., De Cola, L., van der Wiel, W. G., *Science*, **2013**
[55] Calzaferri, G., Lutkouskaya, K., Photochem. Photobiol. Sci., 7, 879-910, 2008.

[56] Fisher, K.A., Huddersman, K.D., and Taylor, M.J., Chem. Eur. J., 9, 5873-5878, 2003.
[57] Pearce, M.E., Mai, H.Q., Lee, N., Larsen, S.C., and Salem, A.K., nanotechnology, 19, 175103-175109, 2008.
[58] Calzaferri, G., Maas, H., Pauchard, M., Pfenniger, M., Megelski, S., Devaux, A., in Advances in Photochemistry, 2002
[59] Meng, H., Xue, M., Xia, T., Zhao, Y.L., Tamanoi, F., Stoddart, J.F., Zink, J.I., and Nel, A.E. J. Am. Chem. Soc., 132, 12690-12697, 2010.
[60] Thomas, C.R., Ferris, D.P., Lee, J.H., Choi, E., Cho, M.C., Kim, E.S., Stoddart, J.F., Shin, J.S., Cheon, J., and Zink, J.I., J. Am. Chem. Soc., 132, 10623-10625, 2010.
[61] Vallet-Regi, M., Balas, F., and Arcos, D., Angew. Chem. Int. Ed., 46, 7548-7558, 2007.
[62] Bruns, A.A., Vider, J., Ow, H., Herz, E., Penate-Medina, O., Baumgart, M., Larson, S.M., Wiesner, U., and Bradbury, M., Nano Lett., 18, 442-448, 2009.
[63] Suarez, S., Devaux, A., banuelos, J., Bossart, O., Kunzmann, A., and Calzaferri, G., Adv. Funct. Mater., 17, 2298-2306, 2006.
[64] Rosenholm, J.M., Meinander, A., Peuhu, E., Niemi, R., Eriksson, J.E., Sahlgren, C., and Linden, M., ACS Nano, 3, 197-206, 2009.
[65] Choi, J., Ghosh, S., Lai, Z., and Tsapatsis, M., Angew. Chem. Int. Ed., 45, 1154-1158, 2006.
[66] Cucinotta, F., Popovic, Z., Weiss, E.A., Whitesides, G.M., and De Cola, L., Adv. Mater, 21, 1142-1145, 2009.
[67] Hashimoto, S., Samata, K., Shoji, T., Taira, N., Tomita, T., and Matsuo, S., Micropor. Mesopor. Mater., 117, 220-227, 2009.
[68] Monopoli, M.P., Walczyk, D., Campbell, A., Elia, G., Lynch, I., Bombelli, F.B., Dawson, K.A., J. Am. Chem. Soc., 133, 2525-2534, 2011.
[69] Norek, M., Neves, I.C., and Peters, J.A., Inorg. CHem., 46, 6190-6196, 2007.
[70] Young, S.W., Qing, F., Rubin, D., Balkus, K.J., Engel, J.S., Lang, J., Dow, W.C., Mutch, J.D., and Miller, R.A., JMRI-J. Magn. Reson. Imaging, 5, 499-508, 1995.
[71] Bresinka, I., and Balkus, K.J., J. Phys. Chem., 98, 12989-12994, 1994.
[72] Csajbok, E., Banyai, I., Vancer Elst, L., Muller, R.N., Zhou, W.Z., and Peters, J.A., Chem. Eur. J., 11, 4799-4807, 2005.
[73] Dahm, A., and Eriksson, H., J. Biotechnol., 111, 279-290, 2004.
[74] Andersson, L.I.M., and Eriksson, H., Scand. J. Immunol., 66, 52-61, 2007.
[75] Perez, L.M., Lalueza, P., Monzon, M., Puertolas, J.A., Arruebo, M., and Santamaria, J., Int. J. Pharm., 409, 1-8, 2011.
[76] Horcajada, P., Ramila, A., PerezpPariente, J., and Vallet-Regi, M., Micropor. Mesopor. Mater., 68, 105-109, 2004.
[77] Chen, G., Beving, D.E., Bedi, R.S., Yan, Y.S., and Walker, S.L., Langmuir, 25, 1620-1626, 2009.
[78] Marambio-Jones, C., and Hoek, E., J. Nanopart. Res., 12, 1531-1551, 2010.
[79] Lalueza,P., Manoacuten, M., Arruebo, M., and Santamaria, J., Mater. Res. Bull., 2011.
[80] Lalueza, P., Monzon, M., Arruebo, M., and Santamaria, J., Chem. Commun., 47, 680-682, 2010.

[81] Mintova, S., Mo, S.Y., and Bein, T., Chem. Mater., 13, 901-905, 2001.
[82] Zhang, Y.H., Wang, X.Y., Shan, W., Wu, B.Y., Fan, H.Z., Yu, X.J., Tang, Y., and Yang, P.Y., Angew. CHem. Int. Ed., 44, 615-617, 2005.
[83] Zhang, D., Chen, Y., Chen, H.Y., and Xia, X.H., Anal. Bioanal. Chem., 379, 1025-1030, 2004.
[84] Corma, A., Fornes, V., and Rey, F., Adv. Mater., 14, 71-74, 2002.
[85] Platas-Iglesias, C., Vander Elst, L., Zhou, W.Z., Muller, R.N., Geraldes, C., Machmeyer, T., and Peters, J.A., Chem. Eur. J., 8, 5121-5131, 2002.
[86] Wu, F., Wang, Y.J., Wang, X.D., Zhang, Y.H., Tang, Y., and Yang, P.Y., Adv. Mater., 15, 1751-+, 2003.
[87] Walczyk, D., Bombelli, F.B., Monopoli, M.P., Lynch, I., and Dawson, K.A., J. Am. Chem. Soc., 132, 5761-5768, 2010.
[88] Mitchell, S., and Perez-Ramirez, J., Catal. Today, 168, 28-37, 2011.
[89] Hu, Y.Y., Zhang, Y.H., Ren, N., and Tan, T., J. Phys. Chem. C, 113, 18040-18046, 2009.
[90] Tavaloro, P., Tavaloro, A., and Martino, G., Colloids and Surfaces B: Biointerfaces, 70, 98-107, 2009.
[91] Cao, J., Hu, Y., Shen, C., Yao, J., Wei, L., Yang, F., Nie, A., Wang, H., Shen, H., Liu, Y., Zhang, Y., Tang, Y., and Yang, P., Proteomics, 9, 4881-4888, 2009.
[92] Vinu, A., Murugesan, V., and Hartmann, M., J. Phys. Chem. B, 108, 7323-7330, 2004.
[93] Hudson, S., Magner, E., Cooney, J., and Hodnett, B.K., J. Phys. Chem. B, 109, 19496-19506, 2005.
[94] Zhang, Y., Liu, Y., Kong, J., Yang, P., Tang, Y., and Liu, B., Small, 2, 1170-1173, 2006.
[95] Kubota, M., Nakabayashi, T., Matsumoto, Y., Shiomi, T., Yamada, Y., Ino, K., Yamanokuchi, H., Matsui, M., Tsunoda, T., Mizukami, F., and Sakaguchi, K., Colloids and Surfaces B: Biointerfaces, 64, 88-97, 2008.
[96] Joshi, P., Rayalu, S., Bansiwal, A., and Juwarkar, A.A., Plant and Soil, 296, 151-158, 2007.
[97] Meng, H., Yang, S., Li, Z., Xia, T., Chen, J., Ji, Z., Zhang, H., Wang, X., Lin, S., Huang, C., Zhou, Z.H., Zink, J.I., and Nel, A.E., ACS Nano, 5, 4434-4447, 2011.
[98] Huang, X., Teng, X., Chen, D., Tang, F., and He, J., Biomaterials, 31, 438-448, 2010.
[99] Li, Z., Hüve, J., Krampe, C., Luppi, G., Tsotsalas, M., Klingauf, J., De Cola, L., and Riehemann, K., Small, 9, 1809-1820, 2013.
[100] Popovic, Z., Busby, M., Huber, S., Calzaferri, G., and De Cola, L., Angew. Chem. Int. Ed., 46, 8898-8902,2006.
[101] Strassert, C.A., Otter, M., Albuquerque, R.Q., Hoene, A., Vida, Y., Maier, B., and De Cola, L., Angew. Chem. Int. Ed., 48, 7928-7931, 2009.
[102] Hocine, O., Gary-Bobo, M., Brevet, D., Maynadier, M., Fontanel, S., Raehm, L., Richeter, S., Loock, B., Couleaud, P., Frochot, C.I., Charnay, C., Derrien, G.I., Smaihi, M., Sahmoune, A., Morere, A., Maillard, P., Garcia, M., and Durand, J.-O., Int. J. Pharm., 402, 221-230, 2010.
[103] Huang, D.M., Hung, Y., Ko, B.S., Hsu, S.C., Chen, W.H., Chien, C.L., Tsai, C.P., Kuo, C.T., Kang, J.C., yang, C.S., Mou, C.Y., and Chen, Y.C., FASEB J., 19, 2014-2016, 2005.

[104] Slowing, I., Trewyn, B.G., and Lin, V.S.Y., J. Am. Chem. Soc., 128, 14792-14793, 2006.
[105] Brevet, D., Gary-Bobo, M., Raehm, L., Richeter, S., Hocine, O., Amro, K., Loock, B., Couleaud, P., Frochot, C., Morere, A., Maillard, P., Garcia, M., and Durand, J.-O., Chem. Commun., 1475-1477, 2009.
[106] Schlossbauer, A., Dohmen, C., Schaffert, D., Wagner, E., Bein, T., *Angew. Chem. Int. Ed.*, 50, 6828-6830, **2011**
[107] Liong, M., *et al.*, *ACS Nano*, 2, 889-896, **2008**
[108] Mamaeva, V., *et al.*, *Mol. Ther.***,** 19, 1538-1546, **2011**
[109] Manzano, M., Vallet-Regi, M., *J. Mater. Chem.*, 20, 5593-5604, **2010**
[110] Meng, H., Xue, M., Xia, T., Zhao, Y. L., Tamanoi, F., Stoddart, J. F., Zink, J. I., Nel, A. E., *J. Am. Chem. Soc.*, 132, 12690-12697, **2010**
[111] Tang, F., Li, L., Chen, D., *Adv. Mater.*, 12, 1504-1534,**2012**
[112] Rivera, A., and Farias, T., Micropor. Mesopor. Mater., 80, 337-346, 2005.
[113] Arruebo, M., Fernandez-Pacheco, R., Irusta, S., Arbiol, J., Ibarra, M.R., and Santamaria, J., Nanotechnology, 17, 4057-4064, 2006.
[114] Fatouros, D.G., Douroumis, D., Nikolakis, V., Ntais, S., Moschovi, A.M., Trivedi, V., Khima, B., Roldo, M., Nazar, H., and Cox, P.A., J. Mater. Chem., 21, 7789-7794, 2011.
[115] Lu, J., Liong, M., Li, Z., Zink, J.L., and Tamanoi, F., Small, 6, 1794-1805, 2010.
[116] Radu, D.R., Lai, C.-Y., Jeftinija, K., Rowe, E.W., Jeftinija, S., and Lin, V.S.Y., J. Am. Chem. Soc., 126, 13216-13217, 2004.
[117] Trewyn, B.G., Nieweg, J.A., Zhao, Y., and Lin, V.S.Y., Chem. Eng. J., 137, 23-29, 2008.
[118] Lu, J., Liong, M., Zink, J.L., and Tamanoi, F., Small, 3, 1341, 1364, 2007.
[119] Roy, I., Ohulchanskyy, T.Y., Pudavar, H.E., Bergey, E.J., Oseroff, A.R., Morgan, J., Dougherty, T.J., and Prasad, P.N., J. Am. Chem. Soc., 125, 7860-7865, 2003.
[120] Kihara, T., Zhang, Y., Hu, Y., Iviao, Q., Tang, Y., and Miyake, J., Journal of Bioscience and Bioengineering, 111, 725-730, 2011.
[121] Tasciotti, E., Liu, X., Bhavane, R., Plant, K., Leonard, A.D., Price, B.K., Cheng, M.M.-C., Decuzzi, P., Tour, J.M., Robertson, F., and Ferrari, M., Nat Nano, 3, 151-157, 2008.
[122] Godin, B., Gu, J., Serda, R.E., Bhavane, R., Tasciotti, E., Chiappini, C., Liu, X., Tanaka, T., Decuzzi, P., and Ferrari, M., J. Biomed. Mater. Res., 94A, 1236-1243, 2010.
[123] Spotti, M., et al., Vet. Res. Commun., 29, 507-515, 2005.
[124] Kransnoperova, A. P., Radiats. Biol. Radiocol., 39, 471-474, 1999.
[125] Oste, L. A., Lexmond, T. M., Van Reimsdijk, W. H., J. Environ. Qual., 31, 813-821, 2002.
[126] Pitcher, S. K., Slade, R. C., Ward, N. I., Sci. Total. Environ., 134, 161-166, 2004.
[127] Pong, W. G., Yen, J. T., Varel, V. H., Bull. Environ. Contam. Toxicol., 37, 795-803, 1988.
[128] Coffey, M. T., Picklington, D. W., J. Animal Sci., 67, 36, 1989.
[129] Mumpton, F. A., Fishman, P. H., J. Animal Sci., 45, 1188-1203, 1989.
[130] Papaioannou, S. C. et al. Res. Vet. Sci., 72, 61-68, 2002.

[131] Flowers, J. L., Lonky, S. A., Deitsch, E. J., Nutrition and Dietary Supplements, 1, 11-18, 2009.
[132] Maiankaia, N. N. et al., Vapr. Pitan., 73, 61-68, 2002.
[133] Huck, W.T.S.e. Nanoscale assembly techniques. Springer, 217.
[134] Whitesides, G.M., and Boncheva, M. Proc. Natl. Acad. Sci. U.S.A., 99, 4769-4774, 2002.
[135] Whitesides, G.M., and Grzybowski, B., Science, 295, 2418-2421, 2002.
[136] Whitesides, G.M., Kriebel, J.K., and Love, J.C., Sci. Prog., 88, 17-48, 2005.
[137] Mrksich, M., and Whitesides, G.M., Trends Biotechnol., 13, 228-235, 1995.
[138] Whitesides, G.M., Mathias, J.P., and Seto, C.T., Science, 254, 1312-1319, 1991.
[139] Badijc, J.D., Nelson, A., Cantrill, S.J., Turnbull, W.B., and Stoddart, J.F., Acc. Chem. Res., 38, 723-732, 2005.
[140] Lehn, J-M., Angew. Chem. Int. Ed., 27, 89-112, 1988 (Nobel Lecture).
[141] Yoon, K.B., Acc. Chem. Res., 40, 29-40, 2007.
[142] Daniel, M.C., and Astruc, D., Chem. Rev., 104, 293-346, 2004.
[143] Hurst, S.J., Payne, E.K., Qin, L.D., and Mirkin, C.A., Angew. Chem. Int. Ed., 45, 2672-2692, 2006.
[144] Clark, T.D., Tien, J., Duffy, D.C., Paul, K.E., and Whitesides, G.M., J. Am. Chem. Soc., 123, 7677-7682, 2001.
[145] Zabala-Ruiz, A., Li, H, and Calzaferii, G., Angew. Chem. Int. Ed., 45, 5282-5287, 2006.
[146] Ha, K., Park, J.S., Oh, K.S., Zhou, Y.S., Chun, Y.S., Chun, Y.S., Lee, Y.J., and Yoon, K.B., Microporous Mesoporous Mater., 72, 91-98, 2004.
[147] Lee, J.S., Lim, H., Ha, K., Cheong, H., and Yoon, K.B., Angew. Chem. Int. Ed., 45, 5288-5292, 2006.
[148] Lee, J.S., Ha, K., Lee, Y.J., and Yoon, K.B., Adv. Mater., 17, 837-841, 2005.
[149] Leiggener, C., and Calzaferri, G., CHemphyschem, 5, 1593-1596, 2004.
[150] Li, H., Devaux, A., Popovic, Z., De Cola, L., and Calzaferri, G., Microporous Mesoporous Mater., 95, 112-117, 2005.
[151] Decher, G., *Science* 277, 1232, 1997.
[152] Xia, Y.N., and Whitesides, G.M., Angew. Chem. Int. Ed., 37, 551-575, 1998.
[153] Whitesides, G.M., Ostuni, E., Takayama, S., Jiang, X.Y., and Ingber, D.E., Annual Review of Biomedical Engineering, 3, 335-373, 2001.
[154] Weibel, D.B., Di Luzio, W.R., and Whitesides, G.M., Nature Reviews Microbiology, 5, 209-218, 2007.

Zeolite-L synthesis, functionalization and assembly into functional materials

Abstract

This chapter describes the synthesis of zeolite L in different sizes and aspect ratios. In particular the synthesis of disc shaped zeolite L crystals (200 nm in diameter and about 50 nm in height) and zeolite L nanocrystals (length about 40 nm) is presented. Different methods to functionalize with desired groups and to obtain specific properties of the crystals are reported. In detail the exchange with different counter cations, the insertion of guest molecules and the functionalization of the external crystal surface are reported. Finally the assembly into monolayers and their further functionalization by soft lithography is discussed.

2.1. Introduction

Zeolite-L crystals in different sizes have been used for a variety of application throughout the years.

The applications vary from designing artificial photonic antenna systems[1] over applying zeolite-L crystals as functional materials in self assembled systems[1, 2] up to biomedical applications[3, 4, 5, 6, 7]. In order to use zeolite L crystals for such a variety of applications some initial work has been done in order to develop methods for tuning the size and shape of zeolite-L crystals.

By changing the synthesis parameters (composition of the synthesis gel, temperature or time, dynamic or static conditions) the crystal morphology (from cylindrical to disc-shaped) or the size (from 30 nm to about 10000 nm) can be tuned (See figure 2.1.)[8].

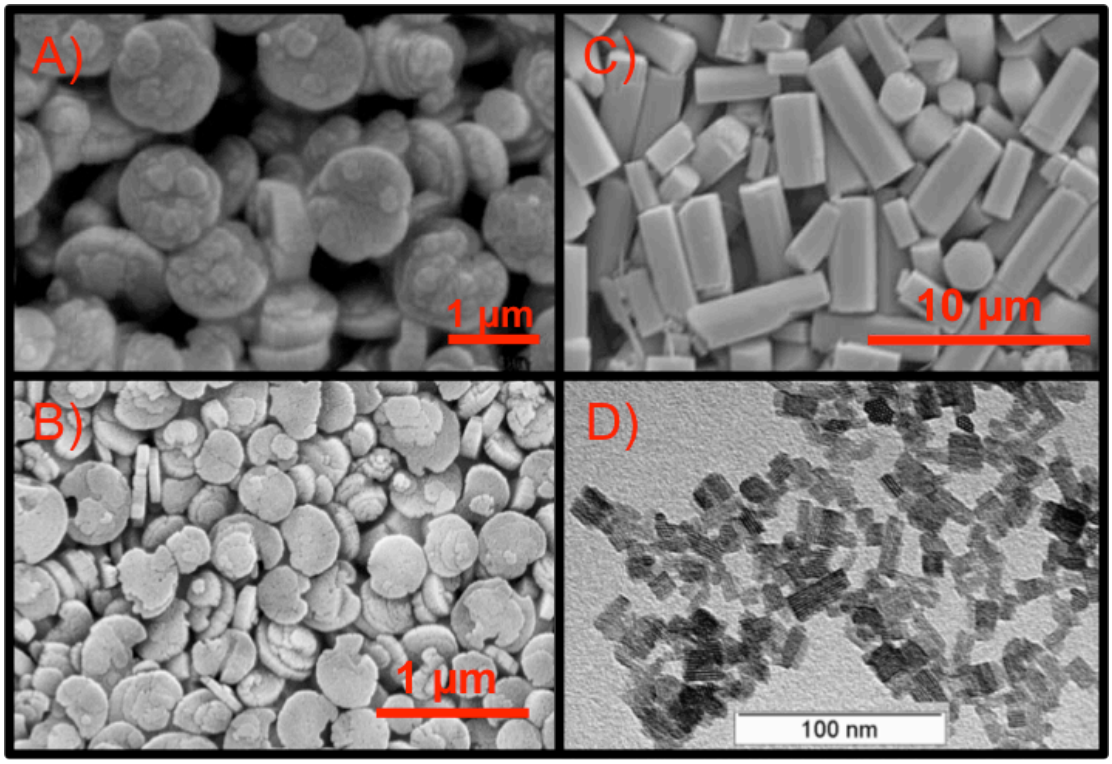

Figure 2.1. Zeolite-L crystals in different sized and morphologies. A) and B) show disc shaped crystals of different sizes. C) shows cylindrical zeolite-L crystals and D) depicts zeolite-L crystals of only a few nanometers in dimension.

Usually, zeolite-L crystals are synthesized using hydrothermal conditions from gels containing an aluminum source and a silicon source (see figure 2.2.). After combining these two gels, the hydrothermal synthesis is carried out at elevated temperatures in either static or dynamic conditions using custom made Teflon vessels and an oven equipped with a rotating unit.

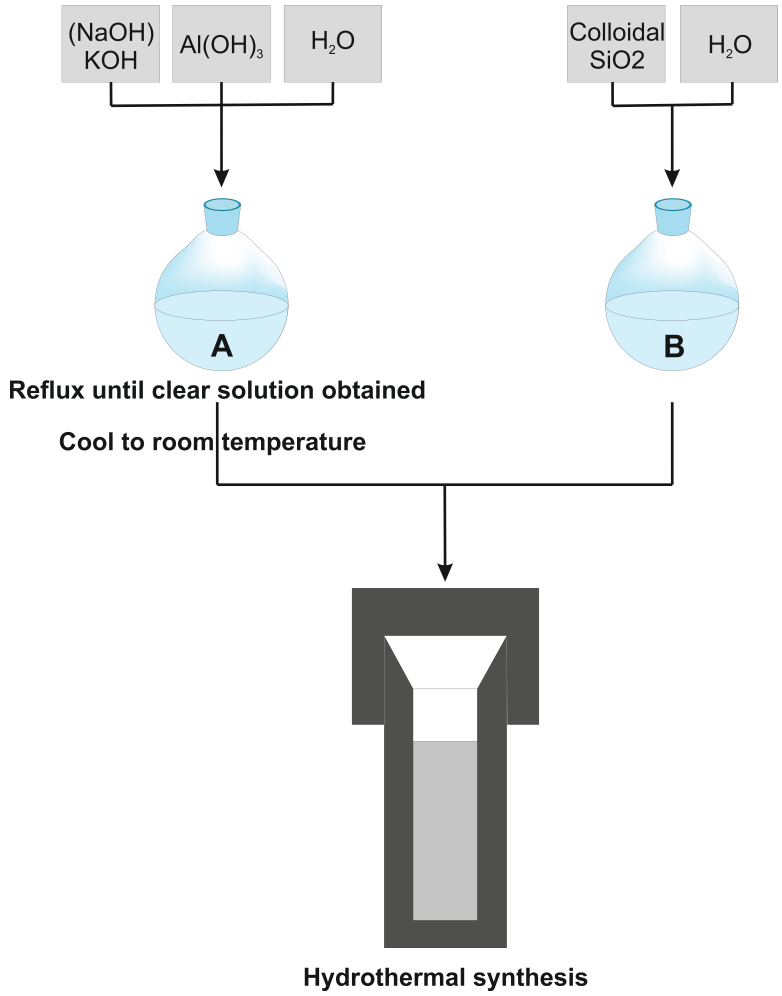

Figure 2.2. Schematic representation of zeolite L synthesis.

After 48 hours at 160 °C (for disc shaped zeolites) the synthesis of the zeolites is completed. The crystals are washed several times with deionized water and the success of the preparation is generally proven by means of powder x-ray diffraction, or by zeta potential measurements in combination with scanning electron microscopy, transmission electron microscopy for the nanozeolites, dynamic light scattering, nitrogen adsorption and the so-called thionine test.

The zeta potential gives a very good indication if the obtained material is in fact zeolitic. Due to the presence of free hydroxyl-groups on the outer crystal surface, the crystals show a net negative charge and the zeta potential of non-functionalized zeolite-L crystals is typically around -33 mV.

The thionine test is used to prove the presence of the pore system. Therefore a few milligram of zeolites are dispersed in an aqueous solution of thionine. Upon heating, the thionine enters in the pore system and a color change from violet to blue can be observed. The porosity can also be measured using nitrogen adsorption measurements. Therefore the amount of nitrogen adsorbed inside the pores is measured to determine the pore volume, the pore size, or the surface area of the crystals.

Dynamic light scattering in combination with scanning electron microscopy is then used to investigate the size distribution and the surface structure of the obtained zeolite crystals. Finally, to prove the crystallinity of the material, powder x-ray diffraction (XRD) is performed. A typical diffractogram in comparison with a simulated XRD diffractogram is shown in figure 2.3.

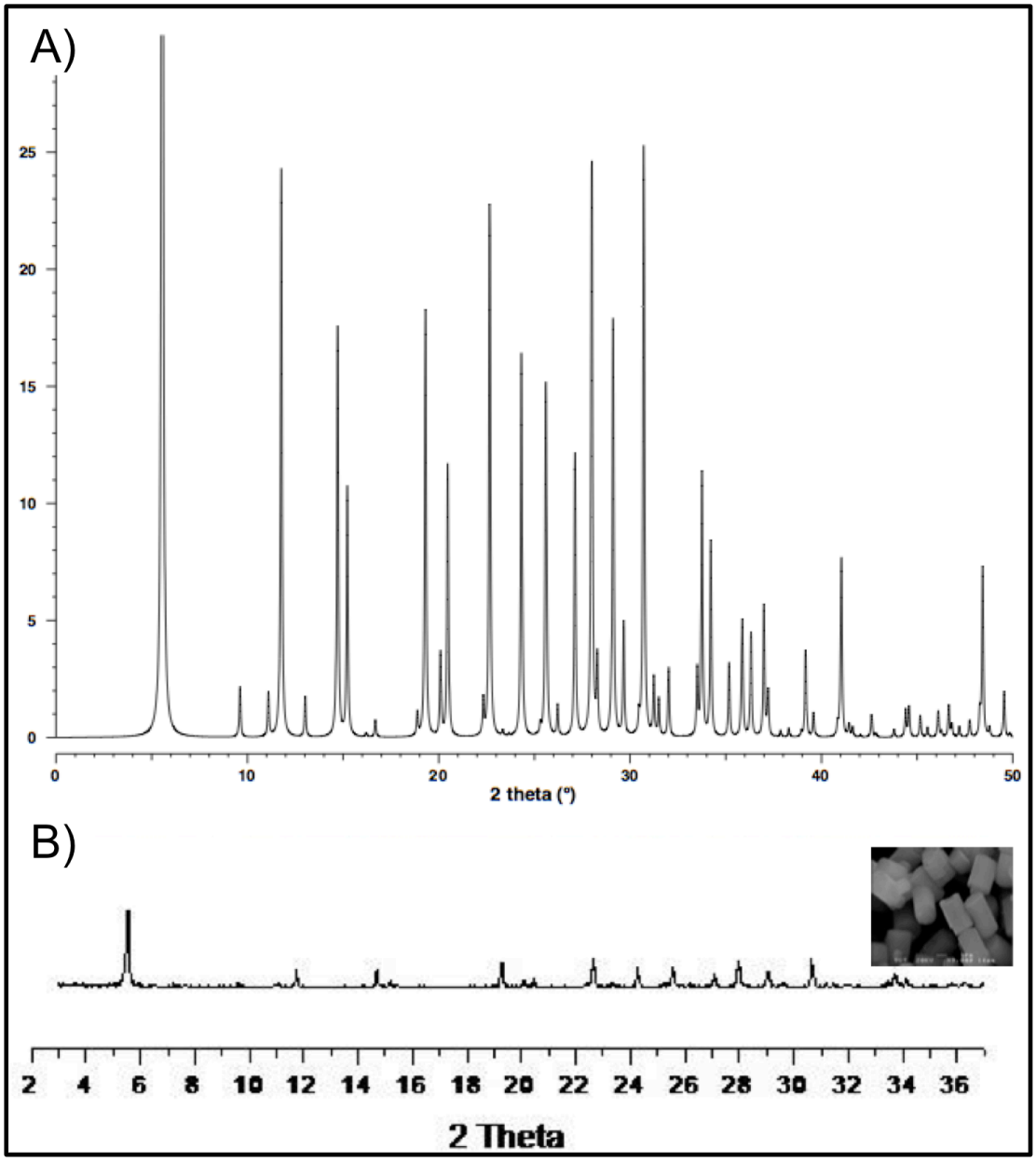

Figure 2.3. Powder x-ray diffraction of zeolite-L. A) shows a simulated XRD powder spectrum[9], B) Shown a measured XRD powder spectrum of cylindrical zeolite-L[10].

The main peaks are located at 2 Θ = 5.5, 19.4, 22.7, 28.0, 29.1, and 30.7. These peaks can be assigned to the crystallographic planes (100), (220), (221), (500), (302), (222). The assignment of all peaks to crystallographic planes is shown in table 2.1.

Table 2.1. Crystallographic data of zeoliteL[9].

h	k	l	2θ	d	M	I_{rel}	h	k	l	2θ	d	M	I_{rel}	h	k	l	2θ	d	M	I_{rel}
1	0	0	5.55	15.935	6	100.0	5	0	1	30.46	2.934	12	0.8	3	1	3	41.41	2.180	24	0.1
1	1	0	9.61	9.200	6	2.2	2	2	2	30.71	2.911	12	25.2	5	3	1	41.44	2.179	24	0.4
2	0	0	11.10	7.967	6	1.9	3	1	2	31.23	2.864	24	2.3	6	0	2	41.63	2.169	12	0.4
0	0	1	11.77	7.520	2	24.3	5	1	0	31.25	2.862	12	0.2	4	0	3	42.61	2.122	12	0.8
1	0	1	13.02	6.801	12	1.7	3	3	1	31.50	2.840	12	1.6	6	2	1	42.64	2.120	24	0.2
2	1	0	14.71	6.023	12	17.5	4	2	1	32.01	2.796	24	2.9	7	1	0	42.85	2.111	12	0.1
1	1	1	15.22	5.822	12	10.6	5	1	1	33.50	2.675	24	2.8	3	2	3	43.79	2.067	24	0.4
2	0	1	16.21	5.469	12	0.2	6	0	0	33.75	2.656	6	11.3	6	1	2	44.39	2.041	24	1.1
3	0	0	16.69	5.312	6	0.7	3	2	2	34.21	2.621	24	8.3	4	1	3	44.56	2.033	24	0.9
2	1	1	18.88	4.701	24	1.0	4	1	2	35.15	2.553	24	0.1	7	1	1	44.59	2.032	24	0.5
2	2	0	19.30	4.600	6	18.3	5	2	0	35.17	2.552	12	3.1	6	3	0	45.16	2.008	12	0.9
3	1	0	20.09	4.420	12	3.5	0	0	3	35.82	2.507	2	0.8	8	0	0	45.54	1.992	6	0.4
3	0	1	20.47	4.339	12	11.6	6	0	1	35.86	2.504	12	4.6	5	0	3	46.07	1.970	12	0.4
4	0	0	22.32	3.984	6	1.5	1	0	3	36.28	2.476	12	0.1	5	4	1	46.10	1.969	24	0.9
2	2	1	22.66	3.924	12	22.7	4	3	1	36.31	2.474	24	4.4	4	4	2	46.27	1.962	12	0.2
3	1	1	23.35	3.810	24	0.3	5	0	2	36.97	2.431	12	0.1	5	3	2	46.64	1.947	24	0.7
1	0	2	24.32	3.660	12	16.1	6	1	0	36.99	2.430	12	5.5	7	0	2	46.64	1.947	12	0.2
3	2	0	24.35	3.656	12	0.5	1	1	3	37.17	2.419	12	0.3	7	2	0	46.66	1.947	12	0.6
4	0	1	25.30	3.520	12	0.4	5	2	1	37.21	2.416	24	1.8	3	3	3	46.81	1.941	12	0.5
1	1	2	25.59	3.481	12	11.5	3	3	2	37.86	2.376	12	0.3	8	0	1	47.20	1.925	12	0.4
4	1	0	25.62	3.477	12	5.3	4	2	2	38.29	2.350	24	0.4	6	2	2	47.74	1.905	24	0.7
2	0	2	26.21	3.400	12	1.3	6	1	1	38.95	2.312	24	0.2	5	1	3	48.26	1.886	24	0.8
3	2	1	27.12	3.288	24	12.1	4	4	0	39.17	2.300	6	3.7	7	2	1	48.29	1.885	24	0.3
2	1	2	27.97	3.189	24	5.7	5	1	2	39.57	2.277	24	0.5	0	0	4	48.42	1.880	2	7.2
5	0	0	28.00	3.187	6	20.9	7	0	0	39.59	2.276	6	0.2	1	0	4	48.77	1.867	12	0.4
4	1	1	28.28	3.156	24	3.2	5	3	0	39.59	2.276	12	0.4	1	1	4	49.48	1.842	12	0.1
3	0	2	29.10	3.069	12	15.4	6	2	0	40.84	2.210	12	0.4	7	1	2	49.52	1.840	24	0.2
3	3	0	29.12	3.067	6	3.0	2	2	3	41.00	2.201	12	2.0	5	5	0	49.54	1.840	6	1.7
4	2	0	29.66	3.011	12	4.8	4	4	1	41.04	2.199	12	6.7	2	0	4	49.84	1.830	12	0.1

Representative scanning electron microscopy images and dynamic light scattering measurement of zeolite-L nanocrystals, disc-shaped zeolite-L crystals (diameter 200 nm) and zeolite-L microcrystals are shown in figure 2.4.

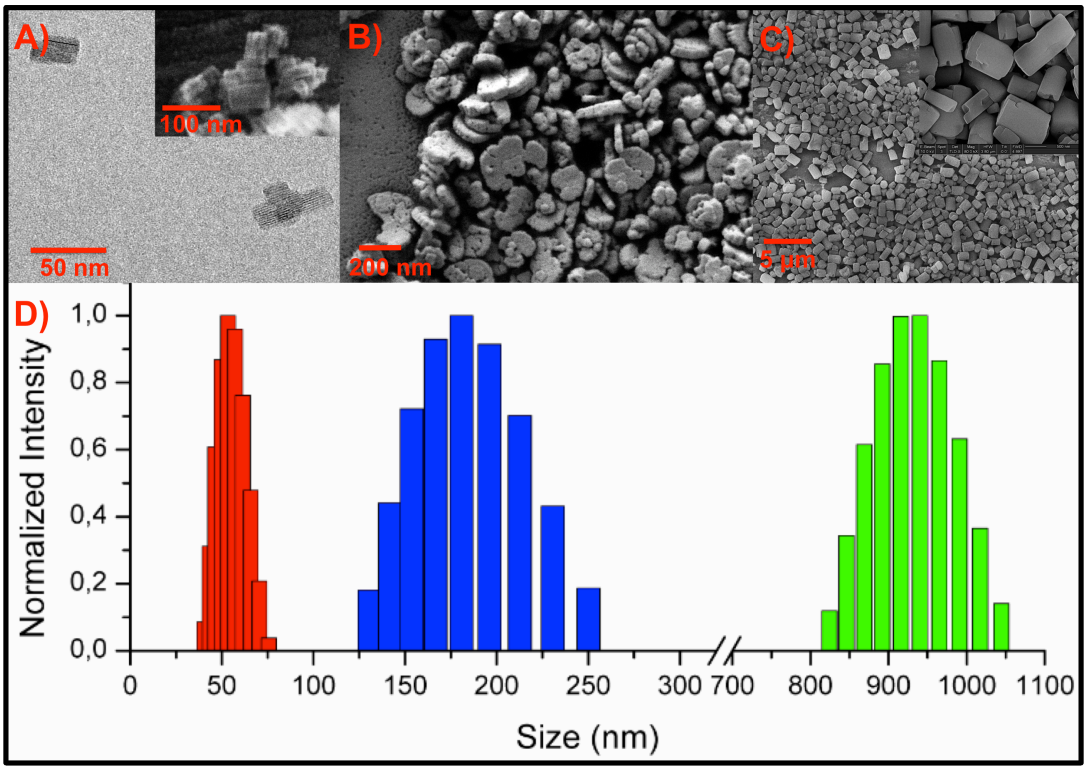

Figure 2.4. A) Transmission electron micrograph of nanozeolite-L crystals; B) Scanning electron microscopy images of disc-shaped zeolites; C) Scanning electron microscopy images of microzeolites. D) Size distribution of these zeolites by DLS. The values have been normalized for a better representation.

2.2. Cation exchange

A first parameter, which can be tuned depending on the application, is the nature of the counter cations in the channels to balance the negatively charged alumina sites. In a fully hydrated form, zeolite-L presents four different sets of counter cations, located at sites A, B, C, and D[11].

Site A cations are located in the center of a hexagonal prism surrounded by six oxygen atoms at a distance of 0.3 nm and 12 oxygen atoms at a distance of 0.365 nm. Site B cations are located in the centre of a cancrinite cage and are surrounded by 12 oxygen atoms. Site C counter cations are located in the middle of two adjacent cancrinite cages and are also surrounded by 12 oxygen atoms. Site D cations are those, which can be exchanged. They are located near to the wall of the channels and are bound to two water molecules and six framework oxygen atoms.

The exchange of site D cations can be done by heating a zeolite dispersion in a solution of the counter cation, which has to be inserted[12].

In a standard procedure all zeolites are potassium exchanged after synthesis and used in this form.

2.3. Insertion of guest molecules

For applications where special guest molecules are required in the pore system (in this thesis usually dye molecules are used), insertion can be done after cation exchange[13].

The loading with guest molecules can be done in different ways: by ion exchange (for cationic guest molecules), by insertion from the gas phase (if the guest molecules is sublimable), from solution, by crystallization inclusion or by in situ synthesis in the channel system[13].

This thesis just focuses on the insertion either by cation exchange or by sublimation from the gas phase.

Insertion via cation exchange is done by replacing the counter cations (K^+) by the desired guest molecules. Therefore the zeolites are dispersed in a guest molecule solution (usually in water). Due to a gain in entropy the counter cations are then slowly replaced by the guest molecules. Varying the insertion time, the temperature or the guest concentration in solution, can vary the degree of loading. For a faster insertion, the dispersion is usually heated.

For inserting neutral and sublimable molecules, a slightly different approach is chosen for insertion. In this approach, the adsorbed water molecules in the channels are replaced by the guests. Therefore the zeolites are mixed together with the guest molecules in a custom made glass ampule and the sample is dried at high vacuum (1E-6 mbar). Then the glass ampule is sealed and insertion is done at high temperatures, determined by the sublimation temperature of the molecule to be inserted, for usually 2-3 days. After insertion, surface

adsorbed guest molecules are removed by several washing steps. The general representation of both procedures is depicted in figure 2.5.

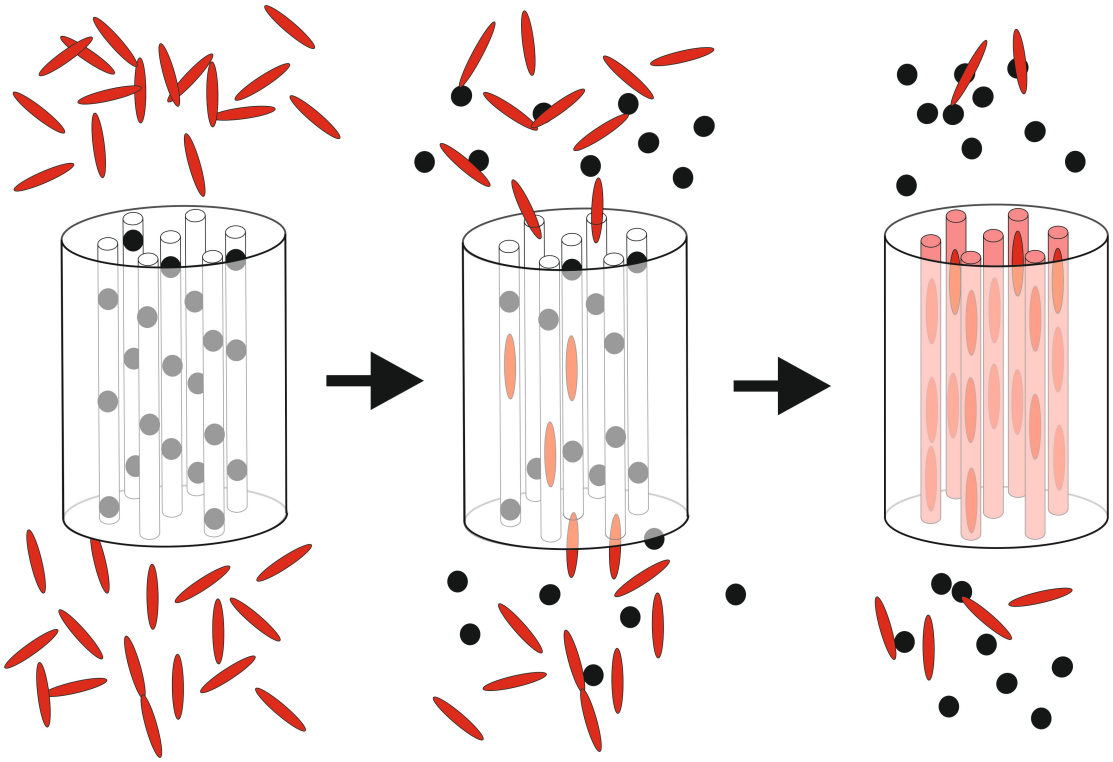

Figure 2.5. Schematic representation of a guest insertion into the channels of zeolite L. For cation exchange the black spheres represent charge balancing cations from the framework; for gas phase insertion the black spheres represent water molecules adsorbed in the channels.

A very important parameter is the amount of guests, which is inserted in the channels, also defined as loading of the zeolite. This number can be given as milligram guest molecules per gram zeolite or, which is more common in the zeolite-L community, as a loading parameter p, which is defined as the number of molecules per site and lies between 0 and 1. The number of sites is defined as the number of unit cells in a given amount of zeolite-L divided by the number of unit cells one guest molecule occupies (See equation 2.1.[12])

$$N_s = \frac{m_z}{2880\,\frac{g}{mol}} * \frac{1}{s} \qquad \text{Eq. 2.1.}$$

with m_z as the amount of zeolite-L in gram, 2880 g/mol is the molecular weight of one unit cell and s is the number of unit cells that one guest molecule occupies.
The loading parameter is finally defined as the ratio between the sites occupied (N_D) by guest molecules and the total number of sites available (N_S) as described in equation 2.2.

$$p = \frac{N_D}{N_S}$$ Eq. 2.2.

The loading parameter p can be determined experimentally by means of thermogravimetric analysis (TGA) determining first the percentage (mass) of loading and then calculating to the loading parameter p.
A typical thermogram for DXP loaded zeolite-L crystals is shown in figure 2.6. The black curve shows the mass loss upon heating in an N_2/O_2 atmosphere and the blue curve shows the temperature gradient, which is typically used. The slight weight loss at low temperatures is due to desorption of water molecules from the zeolite-L surface and channels. At higher temperatures (around 300 °C) a fast weight loss can be observed, which stabilizes when all guest molecules are removed from the zeolite-L channels.

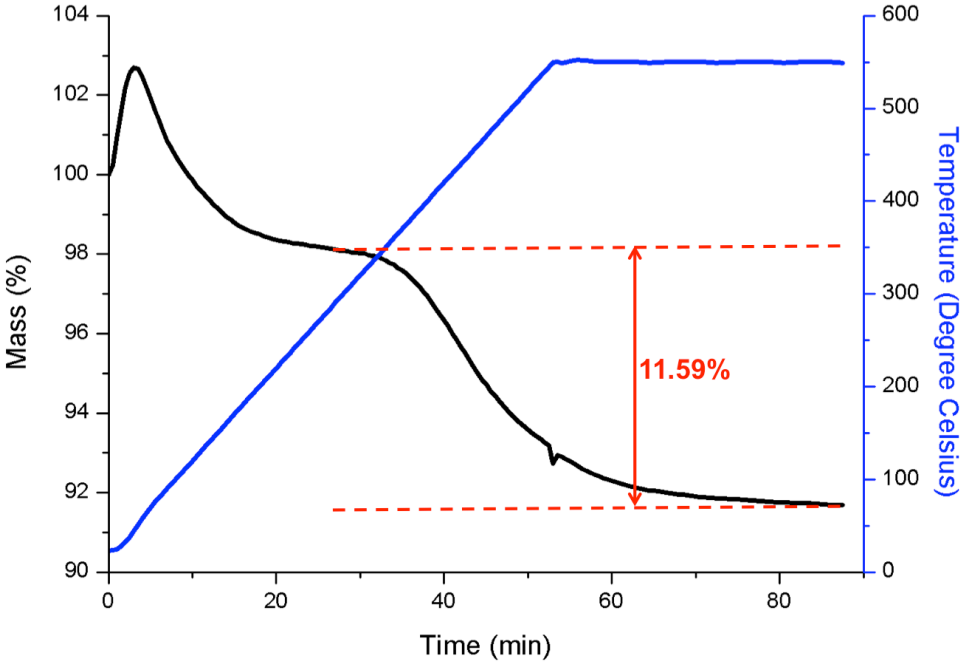

Figure 2.6. A typical thermogravimetric analysis curve of dye loaded zeolite-L crystals to determine the loading parameter. Black curve: Mass%; Blue curve: Temperature gradient.

For cationic molecules and small loading parameters the determination of the loading level by TGA can lead to uncertainties due to incomplete removal of the guests. In this case an analysis by the so-called HF test is suggested[14]. Therefore the zeolite matrix is dissolved in hydrofluoric acid and the guest concentration in solution is usually determined by means of UV/Vis absorption spectroscopy using typical absorption bands of the guest.
The etching of silicate materials is an autocatalytic reaction, which occurs according to the following mechanism:

$$6\ HF + 3\ H_20 \rightarrow 3\ HF_2^- + 3\ H_3O^+$$ Eq. 2.3.

$$SiO_2 + 3\ HF_2^- + 3\ H_3O^+ \rightarrow 2\ HF + SiF_4 + 5\ H_2O$$ Eq. 2.4.

2.4. Functionalization of the external surface

The modification of the external surface is often the most important functionalization, since the external surface is the part of a zeolite crystal, which is in direct contact to the surrounding media.

Functionalization of the external surface can be done either by electrostatic interaction with the net negatively charged zeolite-L surface or by covalently grafting functional groups to the surface, which is usually done by means of standard silane chemistry[15].

To functionalize the external surface by electrostatic interactions, either the net negatively charged zeolite-L crystals can be functionalized with molecules possessing positive charges or, if negatively charged functional groups should be introduced, the surface can be functionalized with positively charged groups in a first step and then functionalized with the negative guest in a second step. However, the drawback of electrostatic functionalization is the lack of control on the number of adsorbed groups, and the lack of orientation.

A more directed and controlled functionalization can be done by grafting functional groups covalently to the surface. In this case the zeolites are mostly dispersed in water, an alcohol, or toluene. When a good dispersion is obtained, the silane compound and a catalyst, mostly triethylamine, is added and the dispersion is gently heated to about 50 °C. The silane is covalently bound to the free hydroxyl groups on the zeolite surfaces by forming silicon-oxygen bonds. Purification is then done by washing the zeolites a few times with a good solvent for the silane. The number of groups attached to the surface can be done in different ways depending on the nature of the surface functionalization. If the functional groups are accessible by UV/Vis spectroscopy, quantification can be done by HF test[14]. If the functional groups are accessible by other methods, e.g. ninhydrin test for amine groups, quantification can be done in this way. Finally quantification can also be done by thermogravimetric analysis recording the weight loss due to the decomposition of the organic compounds.

2.5. Zeolite-L monolayer preparation

The external functionalization of the zeolites has several aims: i) it can give a certain dispersability or solubility to the crystals; ii) it can facilitate the recognition of a certain biomolecule; iii) it can be used to self-assemble the zeolites into larger structures[16, 17, 18, 19, 20]. More recently the functionalization of the zeolites has been used to create monolayers on different surfaces.

In this thesis the assembly of zeolites into monolayers plays a key role and will be described in detail in the following section.

In order to form a zeolite monolayer a covalent bond between the zeolite crystals and the substrate, usually glass, is formed. Therefore the substrate is

functionalized with molecules acting as covalent linkers (see Figure 2.7.) to the zeolite crystals. A variety of linker molecules are known in the literature and several different linkers were studied in detail by Yoon et al[21, 22, 23]. In dependence of the target substrate, different reagents have to be employed to functionalize the zeolites or the substrate itself. The most common substrates used for SAMs of zeolites are glass or quartz, which are then typically functionalized with alkoxysilanes bearing reactive head groups to form covalent bonds to the zeolites. The binding proceeds via nucleophilic substitution reactions between the head group of the linker and the hydroxyl groups on the zeolite surface[24, 25, 26, 27]. In order to obtain high quality monolayers, it is important that the interaction between the substrate and the bases of the zeolites must be stronger than with the coat and of any interactions between the crystals.

The highest packing densities of zeolite L monolayers are achieved by using disc shape zeolite-L crystals and using the sonication method[28]. The formation of such high packing densities can be explained with a phenomenon called surface migration. During the formation of a highly dense packed monolayer, the zeolites undergo dynamic cycles of bond forming/bond breaking reactions until the crystals are packed very close to each other, which allows the formation of inter-crystal hydrogen bonds.

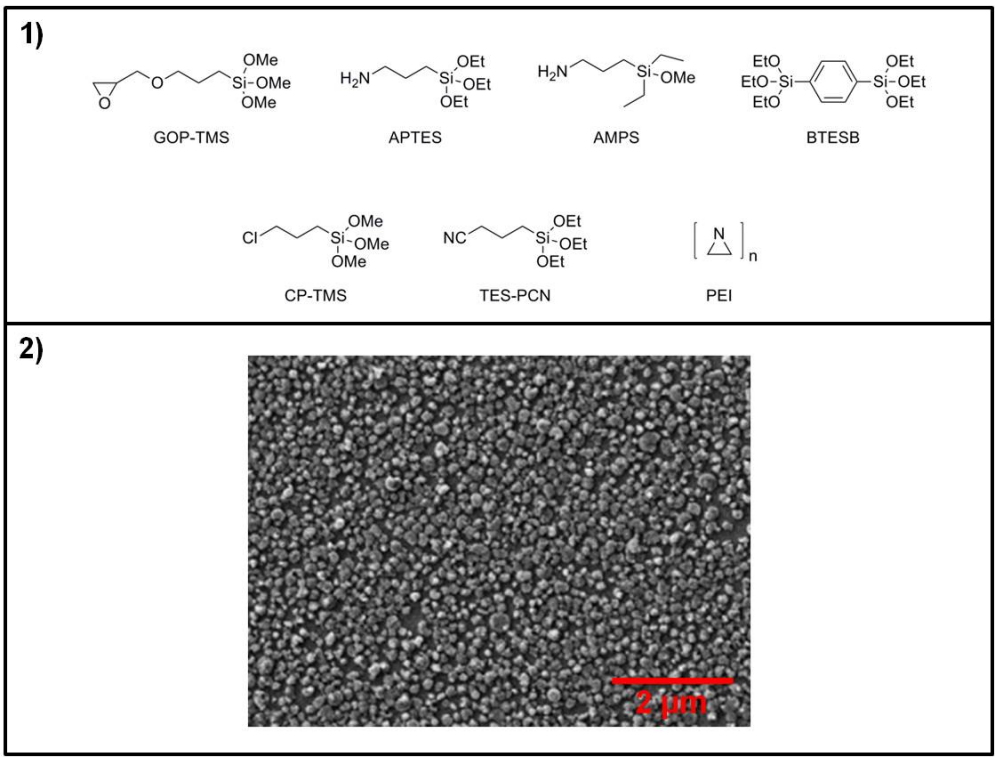

Figure 2.7. a) A selection of commonly used linker molecules for zeolite monolayer preparation. b) SEM image of a zeolite-L monolayer made by our group from small disc shaped crystals (150 - 230 nm) applying the sonication method. (Image taken from: H. Luelf, A. Devaux, E. Prasetyanto, L. De Cola in *Organic Nanomaterials Synthesis, Characterization, and Device Applications*, T. Torres, B. Bottari, Wiley 2013).

In the last years many authors reported several methods to prepare monolayers from a variety of different kinds of zeolites (e.g. Zeolite A, ZSM-5, Zeolite-L)[13, 14, 16, 29] and even of mesoporous materials.
The motivation to organize these materials in ordered monolayers rely on the interest to use such small containers as patterning motive and in the possibility to orient the channels perpendicular to the surfaces. This well-defined orientation can then be exploited to trigger the release of molecules entrapped into the pores with an external stimulus.

2.6. Soft litography

After the monolayer has been assembled on a substrate the upper surface is available for further functionalization.
An elegant approach for functionalizing the surface of a monolayer is soft lithography, more exactly microcontact printing, which has been developed by George Whitesides and Amit Kumar in 1993[30]. The schematic working principle of MCP is shown in figure 2.8. To functionalize a zeolite-L monolayer with a desired chemical functionalization, the channel entrances are functionalized using a silane derivative with a reactive group such as NH_2, COOH, or azides. The choice of the functionalization is dictated by the fact that a chemical reaction must occur by simple mechanical force and must have high yields, and occur at room temperature. Indeed, reactions such as click chemistry or peptide bond formation are most suitable for the MCP method. The complementary group to which the desired molecule is attached is then used as *ink* for a stamp usually made of Polydimethylsiloxane (PDMS) that is then pressed moderately to the functionalized zeolite surface, the monolayer. After a certain reaction time (usually few minutes), the PDMS stamp is lifted off from the monolayer and the monolayer is washed several times to remove loosely adsorbed molecules from the surface. The success of functionalization can be proved by typical surface analysis methods like contact angle measurements, FTIR, surface zeta potential, XPS or EDX analysis.

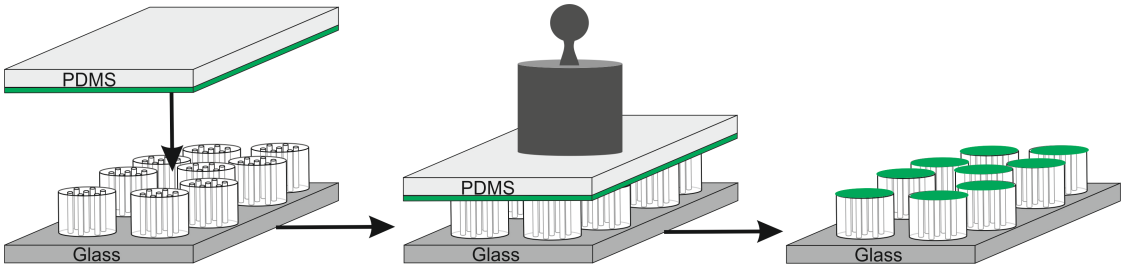

Figure 2.8. Schematic principle of microcontact printing. The *ink* is represented as a green layer.

As it has been shown by our group in cooperation with George Whitesides in 2009, soft lithography can also be used to transfer a zeolite monolayer almost

quantitatively from glass to almost every kind of substrate, like conductive polymers[31].
For this scope, the PDMS stamp is therefore pressed strongly on the monolayer surface for about 30 seconds and then peeled off quickly. This leads to a transfer of the monolayer to the PDMS stamp. In a second step the same PDMS is pressed against the acceptor surface for again 30 seconds and then peeled off slowly, which results in a transfer of the zeolites from the PDMs stamp to the acceptor surface, see figure 2.9. We have also shown by using polarized fluorescent microscopy that the zeolites are still highly ordered on the new substrate[20].

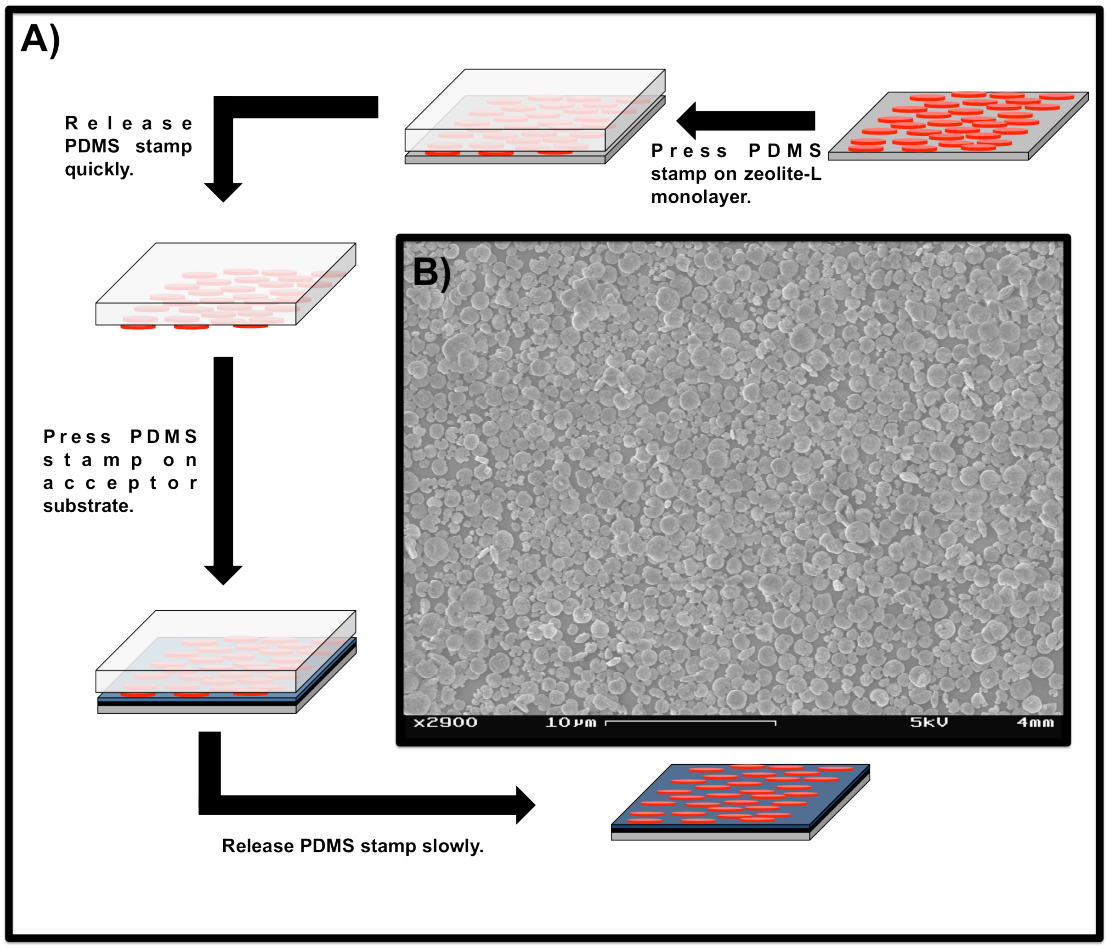

Figure 2.9. A) shows the schematic principle of microcontact printing transfer of a zeolite-L monolayer. B) shows a scanning electron microscope image of a transferred zeolite-L monolayer on a ITO PEDOT:PSS substrate.

In the context of this thesis the transfer has always been checked via SEM measurements. Figure 2.8 B shows a transferred monolayer on a ITO PEDOT:PSS substrate. It can be seen that the monolayer has been transferred almost quantitatively. Also the monolayers are highly stable after transfer, which makes it very useful for application in devices (See chapter 4 of this thesis[32])

In conclusion this chapter summarizes different procedures for manufacturing tailor made nanoparticles, starting from the synthesis in different shapes and sizes. These particles can then be functionalized very specifically in dependence of the application and used as single particles or they can be assembled into very organized monolayer structures. Finally these monolayers can be further functionalized or even transferred almost quantitatively to other substrates, both by using microcontact-printing techniques.

2.7. Experimental part

Zeolite Synthesis

1. Synthesis of disc-shaped zeolite-L

Zeolite-L crystals (length = 30-100 nm, diameter = 200-500 nm) were synthesized according to a literature protocol[8]. 5.52 g KOH and 3.48 g NaOH were added to 34.80 g doubly distilled water and fully dissolved. Then, 1.24 g $Al(OH)_3$ was added to the solution, and the solution was refluxed until the $Al(OH)_3$ was fully dissolved. After cooling to room temperature the amount of lost water was added. Then this solution was added quickly to 35.34 g of Ludox HS-40 and stirred strongly for about 2 minutes. Finally, the highly viscous suspension was transferred to a Teflon vessel, aged for 18 h at room temperature and then rotated with 40 rpm at 160 °C for 48 h. Then, the vessel was cooled to room temperature and zeolites were washed with doubly distilled water until the supernatant showed a neutral pH.

2. Synthesis of nanozeolite-L

Preparation of the silica dispersion: 15.00 g Aerosil OX-50 were added slowly to 35.00 g doubly distilled water and dispersed 8 minutes by using an Ultra Turrax disperser (IKA T18 Basic, 18000 rpm). After that the dispersion is kept for 1 hour at room temperature and redispersed for 8 minutes before use. Preparation of the aluminium solution (Solution A): 4.84 g KOH were dissolved in 20.00 g doubly distilled water. Then 1.56 g $Al(OH)_3$ were added to the solution and it was refluxed until a clear solution was obtained. Preparation of solution B: 7.23 g KOH were dissolved in 21.68 g doubly distilled water and 40.06 g of the silica dispersion were added. Finally, solution A was quickly added to solution B it was stirred at room temperature until the solution became turbid. Crystallization was then done at 170 °C for 6 hours at 40 rpm.

Synthesis of microzeolite-L

6.22 g KOH were added to 44.00 g doubly distilled water and fully dissolved. Then, 1.16 g Al was added to the solution, and the solution was refluxed until the Al was fully dissolved. After cooling to room temperature the amount of lost water was added. Then this solution was added quickly to 28.68 g of Ludox HS-40 and stirred strongly for about 2 minutes. Finally, the highly viscous suspension was transferred to a Teflon vessel and synthesis was done for 3 days at 175 °C for 48 h. Then, the vessel was cooled to room temperature and zeolites were washed with doubly distilled water until the supernatant showed a neutral pH.

Cation exchange

In order to exchange the cations, 50 mg zeolites were added to 100 mL of a 0.1 M aqueous cation solution, dispersed by sonication and refluxed for 18 hours. After cooling to room temperature the zeolites were washed with dou-

bly distilled water (5 x 20 mL) and this procedure was repeated for 3 times. Finally the zeolites were dried in vacuum.

Dye insertion

1. Insertion of DXP by sublimation

DXP was inserted from the gas phase at 300 °C[13]. Therefore DXP is mixed with zeolite-L in a glass ampoule. The amount of DXP loading is calculated by considering that one DXP molecule occupies 3 unit cells and a loading of 100% corresponds to the highest loading possible). The ampoule was dehydrated at about 4.0×10^{-6} mbar for 12 hours and sealed. The dye was then inserted at 300 °C for 72 hours. Afterwards the zeolite-L crystals were washed with n-butanol until the supernatant showed no absorbance anymore and the zeolites were finally dried in vacuum. The amount of inserted dye molecules was determined by TG-analysis.

2. Insertion of cationic dye molecules

Cationic dye molecules were inserted by cation exchange from aqueous solutions. Therefore the zeolites were dispersed in a 0.01 M dye solution (100 mg zeolite-L per 5 mL) and heated to 70 °C over night. The zeolites were washed several times until the supernatant did not show any fluorescence and then dried in vacuum. The loading parameter was determined by means of TGA.

Surface functionalization of zeolite L

1. Covalent functionalization

Functional groups are attached covalently to the surface of zeolite-L by means of silane chemistry. Therefore the zeolite-L crystals are dispersed in dry toluene (about 10 mg zeolite-L per mL) in a nitrogen atmosphere. Then the silane (e.g. APTES) and triethylamine (catalyst) are added to the dispersion and after sonication for about 10 minutes the dispersion is heated to 70 °C over night. Finally the zeolites are washed several times and dried in vacuum. The functionalization was analyzed by DLS and zeta potential.

2. Functionalization by electrostatic interactions

In the context of this thesis functionalization by electrostatic interaction was solely done with poly-L-lysine (PLL). Therefore the zeolite-L crystals showing an overall negative surface charge are dispersed in an aqueous solution of PLL (1% wt/wt). The dispersion was stirred for 1 hour at room temperature and then washed with deionized water.

Monolayer preparation

The zeolite monolayers were prepared by sonication method as previously reported[17]. Therefore the zeolite-L crystals were amino-functionalized using APTES and the glass slides were chloro-functionalized using CPTMS. In order to functionalize the zeolite crystals, 100 mg zeolites were dispersed in tol-

uene (10 mL) and sonicated for 5 minutes. Then 50 µL of APTES and triethylamine were added and the dispersion was sonicated for 40 minutes at 40 °C. The zeolites were finally washed with ethanol (5 x 12 mL) and dried in vacuum. The glass slides were first cleaned by heating them to 100 °C in a piranha-solution for 1 hour following washing with copious amounts of bidistilled water. The cleaned glass-slides were functionalized with CPTMS by fixing them in a self-made teflon rack to avoid overlap and adding toluene until the glass slides are completely covered. 2 mL of CPTMS were added and heated to 110 °C for 18 hours. Finally the glass slides were rinsed with ethanol and dried in a nitrogen flow. The monolayers were prepared by sonicating the glass slides for 15 minutes in a dispersion of the amino-functionalized zeolites in toluene (1 mg / mL). The quality of each monolayer was determined by means of scanning electron microscopy.

Zeolite monolayer transfer

The ITO substrates were first rinsed with several solvents (water, acetone and isopropanol) and finally cleaned in an UV/ozone cleaner for about 1 minute. Deposition of PEDOT:PSS and the monolayer transfer was done via spin coating at 2000 rpm for 10 seconds[20]. The transfer was performed by first pushing a PDMS stamp with the thumb against the monolayer for 30 seconds followed by a fast peeling of the stamp. In the transfer step the PDMS stamp was pushed against the ITO-PEDOT:PSS surface strongly with the thumb for 30 seconds followed by a slow peeling of the stamp[20]. The success and degree of monolayer transfer was checked via SEM measurements.

References

[1] Calzaferri, G., Meallet-Renault, R., Bruehwiler, D., Pansu, R., Dolamic, I., Dienel, T., Adler, P., Li, H., Kunzmann, A., *ChemPhysChem*, 12, 580-594, **2011**.

[2] Becker, M., De Cola, L., Studer, A., J. Mater. Chem. C., 1, 3287-3290, 2013

[3] Schulte, B., Tsotsalas, M., Becker, M., Studer, A., De Cola, L., *Angew. Chem. Int. Ed.*, 49, 6881-6884, **2010**.

[4] El-Gindi, J., Benson, K., De Cola, L., Galla, H.-J., and Kehr, N.S., *Angew. Chem. Int. Ed.*, 51, 3716-3720, **2012**.

[5] Tsotsalas, M.M., Kopka, K., Luppi, G., Wagner, S., Law, M.P., Schaefers, M., and De Cola, L., *ACS Nano*, 4, 342-348, **2010**.

[6] Tsotsalas, M.M., Busbu, M., Gianolo, E., Aime, S., and De Cola, L., *Chem. Mater*, 20, 5888-5893, **2008**.

[7] Strassert, C.A., Otter, M., Albuquerque, R.Q., Hone, A., Vida, Y., Maier, B., and De Cola, L., *Angew. Chem. Int. Ed*, 48, 7928-7931, **2009**.

[8] Zabala Ruiz, A., Bruehwiler, D., Ban, T., Calzaferri, G., *Monatshefte fuer Chemie*, 136, 77-89, **2005**.

[9] Treacy, M. M. J., Higgins, J. B., Collection of Simulated XRD Powder Patterns for Zeolites, Elsevier, **2001**.

[10] Insulan, W., Rangsriwatananon, K., *Engineering Journal*, 16, **2011**.

[11] Newell, P.A., Lovat, V.C.R., Zeolites, 3, 22-27, **1983**.

[12] Hennessy, B., Megelski, S., Marcolli, C., Shklover, V., Baerlocher, C., Calzaferri, G., *J. Phys. Chem. B*, 103, 3340-3351, **1999**

[13] Calzaferri, S. Huber, H. Mass, C. Minkowski, *Angew. Chem. Int. Ed*. 42, 3732, **2003**.

[14] Johnson, S. A., Brigham, E. S., Ollivier, P. J., and Mallouk, T. E., *Chem. Mater*, 9, 2448-2458, **1997**.

[15] Witucki, G. L. (Dow Corning Corporation), “A Silane Primer: Chemistry and Applications of Alkoxy Silanes” in A Journal of Coatings Technology Reprint, 1992

[16] Schulte, B., Tsotsalas, M., Becker, M., Studer, A., De Cola, L. *Angew. Chem. Int. Ed.*, 49, 6881-6884, **2010**.

[17] Popovic, Z., Busby, M., Huber, S., Calzaferri, G., De Cola, L., *Angew. Chem. Int. Ed.*, 46, 8898-8902, **2007**.

[18] Becker, M., De Cola, L., and Studer, A., J. Mater. Chem. C, 1, 3287, **2013**.

[19] Veiga-Gutirrez, M., Woerdemann, M., Prasetyanto, E., Denz, C., and De Cola, L., *Optics and Photonic news*, 23, 47-47, **2012**.

[20] Veiga-Gutirrez, M., Woerdemann, M. Prasetyanto, E., Denz, C., De Cola, L., *Adv. Mater.*, 24, 5199-5204, **2012**.

[21] Choi, S.Y., Lee, Y.J., Park, Y.S., and Yoon, K.B., *J. Am. Chem. Soc.*, 122, 5201-5209, **2000**.

[22] Kulak, A., Lee, Y.J., Lee, J.S., Kim, H.S., Park, Y.S., and Yoon, K.B., *Angew. Chem. Int. Ed.*, 39, 950-953, **2000**.

[23] Chun, Y.S., Ha, K., Lee, Y.J., Lee, J.S., Kim, H.S., Park, Y.S., and Yoon, K.B., *Chem. Commun.*, 1846-1847, **2002**.

[24] Zabala-Ruiz, A., Li, H, and Calzaferii, G., *Angew. Chem. Int. Ed.*, 45, 5282-5287, **2006**.
[25] Leiggener, C., and Calzaferri, G., *ChemPhysChem*, 5, 1593-1596, 2004.
[26] Calzaferri, G., Maas, H., Pauchard, M., Pfenniger, M., Megelski, S., Devaux, A., in *Advances in Photochemistry*, **2002**.
[27] Lee, J.S., Lim, H., Ha, K., Cheong, H., and Yoon, K.B., *Angew. Chem. Int. Ed.*, 45, 5288-5292, **2006**.
[28] Lee, J.S., Ha, K., Lee, Y.J., and Yoon, K.B., *Adv. Mater.*, 17, 837-841, **2005**.
[29] Ha, K., Park, J.S., Oh, K.S., Zhou, Y.S., Chun, Y.S., Chun, Y.S., Lee, Y.J., and Yoon, K.B., *Microporous Mesoporous Mater.*, 72, 91-98, **2004**.
[30] Kumar, A., and Whitesides, G.M., Abstracts of Papers of the American Chemical Society, 206, 172, **1993**.
[31] Cucinotta, F., Popovic, Z., Weiss, E.A., Whitesides, G.M., and De Cola, L., *Adv. Mater.*, 21, 1142-1145, **2009**.
[32] Mahato, R. N., Luelf, H., Siekmann, M. H., Kersten, S. P., Bobbert, P. A., de Jong, M. P., De Cola, L., van der Wiel, W. G., *Science*, **2013**.

Growth of primary neurons on zeolite-L monolayers

Abstract

This chapter deals with the growth of neuron cells on zeolite-L monolayers. The long-term goal is to pattern the surface with nanocontainers in order to address the cells in specific nanometer areas and to monitor the cell response (see also figure 1.10).

In order to form the pattern, nanoparticles and self-assembled monolayers have been used in combination with proteins, as a kind of extracellular matrix mimics. The patterned surfaces has been generated on glass and neuron growth has been followed for several days in order to realize the formation of synapses.

3.1. Introduction

In vivo cell growth and behavior are influenced and guided by a variety of very complex interactions with their environment, the extracellular matrix (ECM). ECM is a complex mixture of non-living material that surrounds the cell and determines the physical properties, intercellular communication or the dynamic behavior of cells.

However, a precise reproduction of the very complex ECM is very difficult to achieve *in vitro*, and therefore nanoparticles and self-assembled nanoparticle monolayers (SAMs) have been applied as a model system to mimic the natural ECM and to control cell behavior. To do so, the physical properties, like the stiffness or surface structure can be used to control the behavior. Above that, functional groups or molecules can be easily anchored to the surface, which altogether allows a physical and chemical guidance of cellular properties[1, 2, 3, 4, 5, 6, 7, 8, 9, 10].

Cell adhesion and their response to synthetic surfaces plays a very important role in the fields of biotechnology, for example for implantable sensors, microdevice development, cell culture, tissue engineering and many more[11, 12, 13]. The development of biocompatible substrates that allow a precise control over the growth and response of cells or living organisms is of great importance with the final goal to apply those surfaces in biomedicine and biotechnology. A fundamental understanding about how cells react to different nanotopographies is crucial in order to be able to tailor design those surfaces for different applications. Fabrication of such platforms can be done either by top-down approaches, like lithography, and, more interestingly, by bottom-up approaches like the direct formation of SAMs from molecules or even nanoparticles[14]. Due to their small size, easy functionalization and unique physical properties, SAMs built up from nanoparticles have been widely used in the fields of cell biology and tissue engineering[15, 16].

In general, self-assembled nanoparticle monolayers that are functionalized with bioactive molecules offer advantages over SAMs of molecules, which is due to the larger surface area and therefore higher local concentrations of the desired molecules. Recently, also the use of SAM built from nanoporous particles has attracted much attention due to the possibility to add new properties and functionalities to the system by entrapping and/or releasing functional molecules in/from the pores[17,18]. In particular, zeolite-L nanoparticle monolayers have been shown to offer great potential for applications in cell culture or biotechnology[9, 10, 19].

Neurons are a particular important cell type that forms, together with glia cells, the nervous system in an animal's body. The control of neuron adhesion and the guidance of neurite outgrowth on solid artificial surfaces are of growing interest due to different possible applications such as neurogenesis and neural development.

Neurite outgrowth and path-finding behaviors are governed by two structures, filopodia and lamellopodia, which have sizes between 100 and 300 nm[20] and act as sensing units to recognize the surrounding environment at the nanometer scale. Based on these recognitions the neurons are modifying their cytoskeletal structures[21, 22, 23].

Neuron adhesion and their guidance on artificial surfaces is also a key element of biotechnological- and biomedical neuroscience[24, 25, 26], where the patterning and alignment of neurons and/or neurites can be used to achieve a precise interfacing between the cells and artificial systems, like electronic devices[27, 28, 29]. Therefore the long-term adhesion of neurons to artificial surfaces is one of the major demands, but still one of the mayor issues that has to be solved in order to allow for real world applications[30, 31]. A basic understanding of the behavior and response of the neurons towards solid surfaces is required to tackle these issues.

It has been shown that the surface chemistry, the elasticity and topography of the surface influence the adhesion, migration, differentiation and guidance of neurons[24].

Cell adhesion, growth and guidance is often achieved by functionalizing the solid surface with certain adhesion-facilitating molecules such as polypetides, biopolymers, extracellular matrix proteins or oligopeptides[32, 33, 34, 35, 36]. It has been shown, that particularly positively charged peptide domains favor the adhesion of neurons[37] and that even partially positively charged amine groups can promote the growth and adhesion of neurons[38, 39, 40, 41, 42], which is attributed to electrostatic attractions with the negatively charged cell membrane, which then promotes cell adhesion and neurite outgrowth[43]. Very popular peptides that have shown to favor *in vitro* cell adhesion and growth are arginylglycylaspartic acid (RGD)[44], polylysine[45], polyornithin[46], collagen type IV[56], fibronection[47, 48] or laminin[58]. Additionally to electrostic interactions, these proteins favor cell adhesion due to a specific binding of integrins, which are expressed also on the axons of neurons, to the RGD sequence that is present in fibronectin, laminin or collagen type IV. RGD is indeed one of the most studied and very well known adhesion motifs[49].

The structures of RGD, poly-L-lysine (PLL) and poly-L-ornithine are shown in figure 3.1.

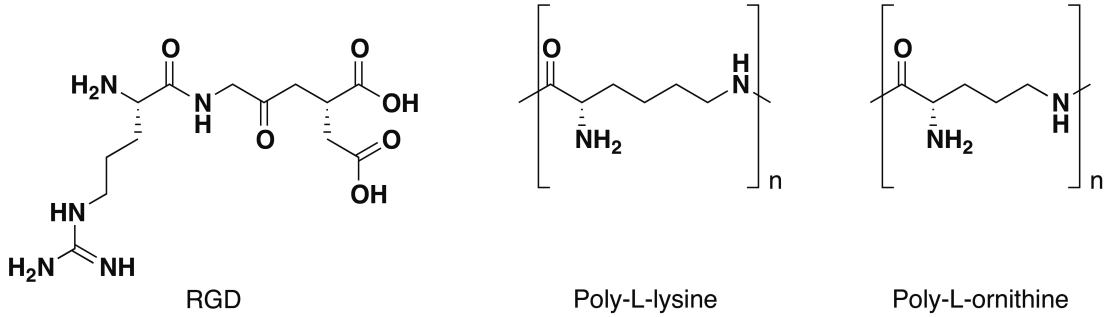

Figure 3.1. Molecular structures of RGD (left), Poly-L-lysine (middle) and Poly-L-ornithine (right)

In addition to chemical cues, surface topography can also influence and guide neuron adhesion and neurite growth and guidance on surfaces[50]. Surface roughness is known to influence the attachment and survival[51, 52, 53], axonal guidance[54, 55, 56, 57] and neurite outgrowth[58]. Furthermore it has been shown that surface structures less than 100 nm in size can influence neuron growth and adhesion[52, 59, 60, 61].
Neuron growth on nanoparticle monolayers is dependent on the nanometric surface topography as well as on the surface functionalization. Mostly gold nanoparticles have been used for this approach. Spatz et al. applied gold nanoparticle monolayers with defined particle spacing as carriers of single peptide guidance factors[42, 62, 63, 64, 65, 66]. Recently Kang et al. studied the growth of hippocampal neurons on silica bead monolayers prepared from different particle sizes and they show that the neurons undergo a developmental acceleration if silica beads with diameters of more than 200 nm are used[67].
In summary, the deep understanding of neuronal growth and response to nanotopographical cues will allow for the development of new devices in tissue engineering or regenerative medicine.

3.2. Neurons[68]

A neuron is a specialized cell type that processes and transports information by using electrical and chemical signals. Neurons form, together with glia cells, the nervous system, which consists of the brain, the spinal cord, and the peripheral ganglia. Depending of their function in the body, different specialized types of neurons can be found. **Sensory neurons** have neurites in the sensory surface of the body, such as the skin or the retina. These neurons are sensitive to different stimuli, like touch, sound, temperature or light and then send signals to the spinal cord and brain. **Motor neurons** have axons that form synapses with the muscles and convert signals coming from the brain into movements. Most neurons in the body are **interneurons**, which form connections with other neurons and transport the signal from one neuron to another.

A typical neuron consists of different functional parts, which will be described in more detail in the following. A pictorial view of the internal structure of a typical neuron is shown in figure 3.2.

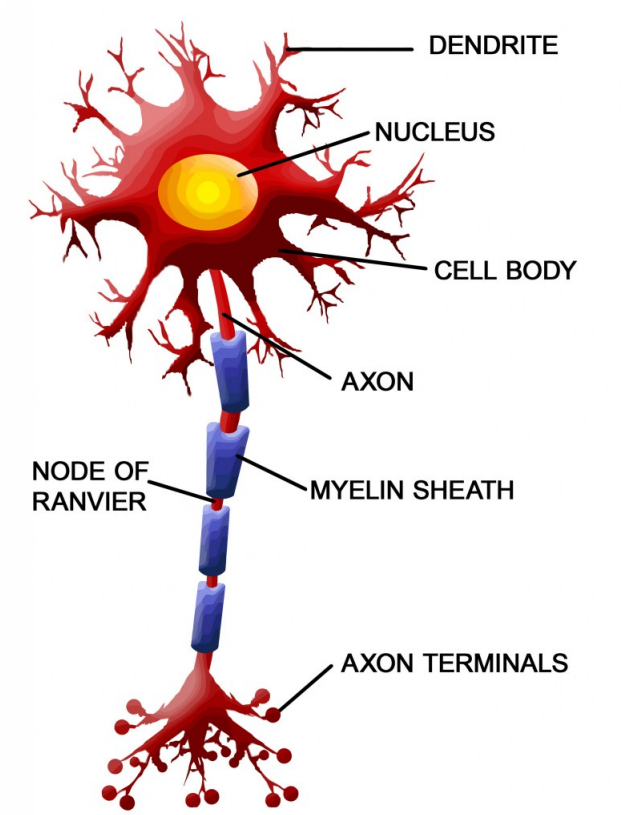

Figure 3.2. Internal structure of a typical neuron. Image taken from http://www.interactive-biology.com/3247/the-neuron-external-structure-and-classification.

The **soma**, or cell body, is roughly 20 µm in diameter, the central part of a neuron and contains the organelles. The soma is filled with a potassium rich solution, the cytosol.
The **nucleus** is centrally located in the soma and is about 5-10 µm in diameter. Like in all animal cells, the nucleus contains the DNA and it is the place where transcription takes place.
The **axon** is a part, which can specifically be found in neurons. Its function is the transfer of information over long distances in the nervous system and, depending of the function, axons with sizes from a few millimeters up to over a meter can be found. The axon emerges from the soma and begins with a region called the axon hillock. Most neurons only have one axon, but this often branches into so-called axon collaterals in order to transfer information to more than one neighbor neuron. The thickness of an axon varies from less than one micron to about 25 microns, which directly influences the speed of signal transport. The thicker axon is, the faster is the signal transport. The end of an axon (the axon terminal) is the part where the axon comes into contact with other neurons. The point of contact is called the synapse. Usually an axon is widely branched at its end, which makes several synaptic contacts between two adjacent neurons possible. The cytoplasm of the axon terminal is different from that of the axon: Microtubules do not exist in the axon terminal, Synaptic vesicles can be found in the axon terminal, the inside surface of the

axon terminal has very dense protein coverage, and it has a large number of mitochondria.

The **dendrites** are tree like branches extending from the soma. The collectiv dendrites of a neuron are called a dendtritic tree. The stucture and size of a dendritic tree is used to classify different types of neurons. The dendrites can be seen as the antenna of a neuron, which collect the signals coming from neughboring neurons. Therefore the dendrites are covered with thousands of synapses and the dendritic membrane has many specialized receptor proteins able to detect different neurotransmitters. The dendrites of some special neurons are covered with little punching bag like structures called dendritic spines.

The **synapses** connect one neuron to another and can be divided into presynaptic and postsynaptic sites. The information flows from the presynaptic site to the postsynaptic site. The presynaptic site can generally be found at an axon, while the postsynaptic site can be found on the soma or a dendrite. The space between the pre- and postsynaptic site is called the synaptic cleft and is a key parameter for signal transport. Nowadays different types of synapses are known. Electrical synapses are simple in constitution and they transport the signal directly from one cell to another. In order to form an electrical synapse the membranes of two neurons are spaced by a very small gap of just 3 nm. These specialized sites are called gap junctions and are spanned by special clustered proteins, called connexins. Six connexins then form together a channel called a connexon and two connexon form a gap junction channel. Gap junctions have a diameter of about 1-2 nm, which allows a direct transfer of ions and small molecules from the cytoplasm of one cell to another. The transport is allowed equally in both directs and therefore electrical synapses are bidirectional, unlike to chemical synapses.

Most of the synaptic communication occurs through **chemical synapses**, where communication occurs through a gap (the synaptic cleft) of about 20-50 nm. The synaptic cleft is filled with a matrix of proteins, which ensure a good adherence of pre- and postsynaptic membrane. The presynaptic side of a chemical synapse is usually an axon terminal and contains synaptic vesicles that store the neurotransmitters. Chemical synapses can be further classified according to their connections. If an axon is connected to a dendrite, the connection is called axodendritic; if an axon is connected directly to a cell body, the connection is called axosomatic; if two axons are directly connected, the connection is called axoaxonic. In some neurons two dendrites are directly connected, which is then called dendrodendritic.

Glia cells are non-neuronal cells that regulate the environment of neurons and maintain stable and constant conditions around them. At present the evidence indicated that glia cells contribute to neuron functions mostly by supporting them. The most numerous type of glia cells are astrocytes. They fill the empty space between neurons and an essential role of astrocytes is to regulate the chemical composition of the extracellular space. Astrocytes also

play an important role in synaptic communication of neurons. For example, they enclose synaptic junctions, which restricts the spreading of neurotransmitters. Above that, astrocytes show special proteins in their membrane, which are able to remove neurotransmitters from the synaptic cleft. Besides regulating neurotransmitters it has been shown that astrocytes regulate the concentration of potassium ions in the extracellular matrix.
Other types of glia cells are for example oligodendroglial and Schwann cells. They form layers of membrane around the axons to insulate them from the environment. This wrapping spirals around the axon is called myelin and is interrupted periodically (node of Ranvier).

3.3. Neuron growth on zeolite-L monolayers

This project was carried out in cooperation with the group of Professor Pape from the “Institut Für Physiologie I” of the University of Muenster. Cell culture experiments were performed by Dr. Frank Erdmann. All experiments were carried out using mouse hippocampal primary neurons doing 3 replicas for every experiment.

This project aimed to develop the optimal conditions to grow mouse hippocampal primary neurons on zeolite-L monolayers. The choice of zeolites was dictated by the fact that the channels of the crystals can be filled with small molecules and when the zeolites are assembled as a monolayer, the channels are perpendicular to the surface. This observation is of fundamental importance since the challenge of this project is to address the molecules inside the channels in order to induce either a charge transport (see chapter 4) or to release a chemical from the pores or the particle surfaces. In both conditions the neurons can be stimulated in the area where the electrical signal or the molecule release is generated. The first step is therefore the preparation and functionalization of the monolayer and the synapse formation. In order to allow for the formation of synapses, a neuron growth for more than 7 days was desired, since it has been shown that synapses do not evolve before 7 days *in vitro*[69].
Monolayers were prepared in usual conditions from disc-shaped zeolite-L crystals with a diameter of about 200 nm and a height of about 50 nm (See chapter 2.5).

As described before, integrins, which can be found also on the axons of neuros, are specific receptors for substrate adhesion molecules and are known to bind to the RGD tripeptide[56],
For this reason the first monolayer surface functionalization chosen was RGD. An amine-functionalized monolayer was prepared in usual conditions and then further functionalized with RGD via microcontact printing. The general

scheme and details on the surface printing are shown in figure 2.8 and chapter 2.6, respectively. The RGD was coupled to the zeolites by amide bond formation using its carboxylic acid groups and the monolayer amine groups. Coupling was achieved by activating the carboxylic acid with EDC/NHS.
Primary neurons were then cultured on these monolayers in the absence of glia cells, to ensure a direct growth of the neurons on top of the zeolites. This was done to favor the direct contact of the neurons on the surfaces so that an efficient electrical stimulation of the neurons, as described in chapter 1.7, can occur. The detailed cell culture conditions are reported in the experimental part at the end of this chapter.
Figure 3.3 shows a bright-field image of neurons grown on this surface after 2 days. As it can be seen, the cells don not adhere well on the RGD functionalized monolayer surface and just a very small number of cells can be found. This unexpected result can be due to various reasons. On the one hand it might be possible, that the RGD binding to the monolayer is not efficient enough so that the RGD concentration on the monolayer is too low to allow for an efficient cell growth. On the other hand, it might be possible that small amounts of the coupling agents (EDC, NHS) are still present on the monolayers after RGD functionalization, which prevents cell adhesion. Further experiments to study this unexpected behavior in detail are therefore ongoing.

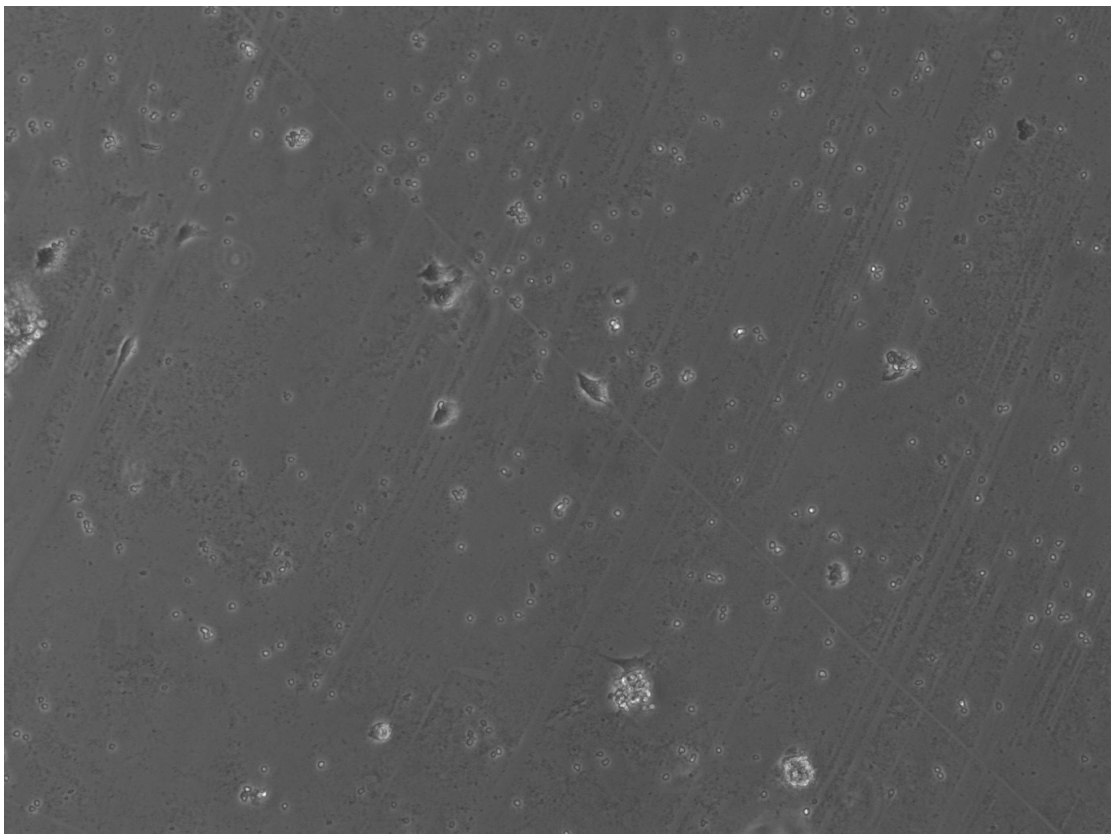

Figure 3.3. Bright field image of primary neurons grown for 2 days on a RGD functionalized zeolite-L monolayer.

In a next approach amine functionalized monolayers have been used directly as a substrate for neuron growth as it has been shown in the literature, that neurons adhere particularly well on positively charged substrates[47, 48, 49, 50, 51, 52] (See also chapter 3.1). The primary amine groups on the monolayer surface are partially protonated in physiological conditions (pH 7.4), which is therefore expected to favor cell adhesion and growth.
The neurons were cultured in the same conditions and again bright field images were taken after 2 days in vitro (See figure 3.4).
As shown in figure 3.3, a large number of cells adhere to the monolayer, which is a very promising result.
However, the situation becomes significantly different for longer incubation times. Already after 3 days the number of cells is significantly decreased and after 4 days no cells can be found on the surface.
The reason for this behavior is not known so far. A possible explanation for the lack of cell adhesion after 3 days is the use of glia-free neuron cultures. As discussed in the introduction, glia cells regulate the chemical composition of the extracellular matrix or participate directly fundamentally to the neuron growth, which makes it very difficult to maintain a long time growth of primary neurons in the absence of glia cells. Above that, glia cells are often required for an efficient intercellular synaptic communication and therefore we used a neuron/glia cell co-culture in the next step.

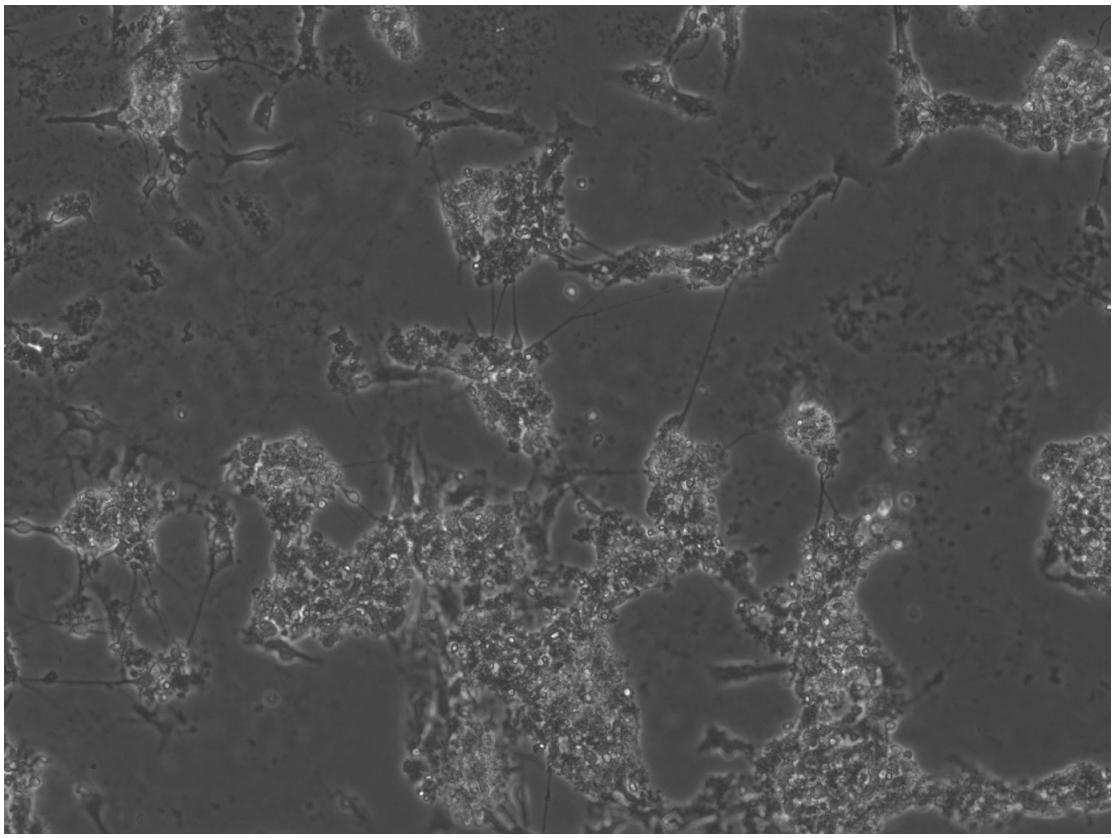

Figure 3.4. Bright field image of primary neurons grown for 2 days on an amine functionalized zeolite-L monolayer.

As last attempt we decided to use a co-culture of neurons and glia cells and cover the zeolite monolayers with a mixture of collagen and ornithine as typically used for primary neuron cultures. The monolayers were first coated with collagen overnight followed by a coating with ornithine (2 hours). Cell experiments were then done in the usual conditions, but, as mentioned, using a neuron/glia cell co-culture. Glia cell division was stopped after 72 hours by the addition of Ara-C to the culture media. Figure 3.5 shows a bright field image of neurons grown in these conditions after 9 days. It can be seen that a high number of neurons adhere and grow on the monolayer.

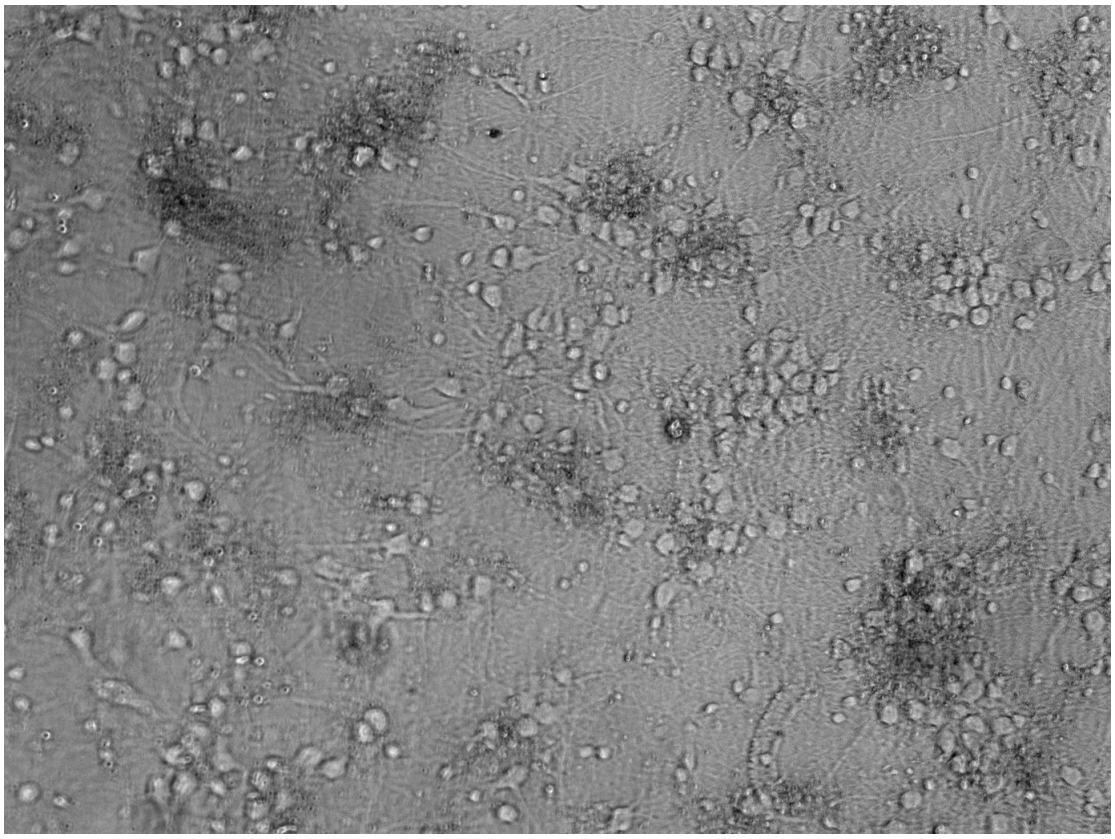

Figure 3.5. Bright field image of primary neurons grown for 9 days on zeolite-L monolayer coated with a collaged/ornithine mixture.

3.4. Conclusion

We have shown, that a long time neuron growth for 9 days on zeolite-L monolayers can be achieved by coating the monolayer with appropriate adhesive peptides and by using a neuron-glia cell co-culture. Experiments to study the neuron growth on zeolite monolayers in more detail are ongoing. In progress is also the investigation of the influence of the filler of the pores on the neuron growth. The pores could for example be filled with different cations, which will slowly be released upon cation exchange, which will then induce a cation concentration gradient in the media.

In a next step, an electrical driven device, which could address the molecules inside the pores, and therefore the neurons, is envisaged. Indeed, in the next chapter we proved that an electrical triggering might be possible since the molecules inside the pores can be addressed and allow for an electrical transport through the pores.

3.5. Experimental part

1. Zeolite synthesis, functionalization and monolayer preparation have been done in usual condition as described in chapter 2.

2. Monolayer functionalization with RGD
A PDMS stamp was inked with 50 µL of a 1.5 mM EDC solution, 50µL of a 3.0 mM NHS solution and 100 µL of a RGD solution in ethanol. The solvent was evaporated and the printing was done as described in chapter 2.

3. Mouse hippocampal primary cultures
Hippocampal cultures were prepared from embryonic 18-days-old (E18) C57BL/6 mouse brains as described elsewhere. In brief, cortical glial cells were cultured for one week and plated on collagen and ornithine coated monolayers (0.1%, Invitrogen). After another 7 days, BME-medium was exchanged to Neurobasal (Invitrogen), complemented with B27 (Invitrogen), Glutamax (Invitrogen) and penicillin/streptomycin. Cortices and hippocampi were isolated from mouse brains and treated with 0.05% Trypsin (Invitrogen) for 15 min. After trituration, hippocampal neurons were seeded onto cortical glial cells in the presence of Ara-C (25 µM, Sigma). 5 days after plating, hippocampal neurons were transfected with Lipofectamin2000 (Invitrogen) according to the manufacturer's instructions.

References

[1] Zhang, S., *Nat. Biotechnol*., **21**, 1171-1178, **2003**.
[2] Gleason, N. J., Nodes, C. J., Higham, E. M., Gucker, N., Aksay, I. A., Schwarzbauer, J. E., and Carbeck, J. D., *Langmuir*, **19**, 513—518, **2003**.
[3] Zheng, H. P., Berg, M. C., Rubner, M. F., and Hammond, P. T., *Langmuir*, **20**, 7215-7222, **2004**.
[4] Zhang, S., and Zhao, X., *J. Mater. Chem*., **14**, 2082-2086, **2004**.
[5] Kim, W., Ng, J. K., Kunitake, M. E., Conklin, B. R., and Yang P. D., *J. Am. Chem. Soc.*, **129**, 7228-7229, **2007**.
[6] Wang, S., Wang, H., Jiao, J., Chen, K. J., Owens, G. E., Kamei, K., Sun, J., Sherman, D. J., Behrenbruch, C. P., Wu, H., and Tseng, H. R., *Angew. Chem. Int. Ed.*, **48**, 8970-8973, **2009**.
[7]Wilson, C. G., Sisco, P. N., Gadala-Maria, F. A., Murphy, C. J., and Goldsmith, E. C., *Biomaterials*, **30**, 5639-5648, **2009**.
[8] Bai, H. J., Shao, M. L., Gou, H. L., Xu, J. J., and Chen, H. J., *Langmuir*, **25**, 10402-10407, **2009**.
[9]Kehr, N. S., Riehemann, K., El-Gindi, J., Schäfer, A., Fuchs, H., Galla, H. J., and De Cola, L., *Adv. Funct. Mater*., **20**, 2248-2254, **2010**.
[10] Kehr, N. S., El-Gindi, J., Galla, H. J., and De Cola, L., *Microporous Mesoporous Mater*., **144**, 9-14, **2010**.
[11] Reichert, W. M., and Saavedra, S. S., *Mater. Sci. Technol*., **14**, 303, **1992**.
[12]Langer, R., and Vacanti, J. P., *Science*, **260**, 920, **1993**.
[13] Langer, R., and Tirrel, D., *Nature*, **428**, 487, **2004**.
[14] Gates, B. D., Xu, Q., Stewart, M., Ryan, D., Wilson, C. G., and Whitesides, G. M., *Chem. Rev*., **105**, 1171, **2005**.
[15]Pattani, V. P., Li, C., Desai, T. A., and Vu, T. Q., *Biomed. Microdevices*, **10**, 367, **2008**.
[16]Khang, D. Y., Xiao, J., Kocabas, C., MacLaren, S., Banks, T., Jiang, H., Huang, Y. Y., and Rogers, J. A., *Nano Lett*., **7**, 124, **2008**.
[17]Ruiz, A. Z., Li, H., and Calzaferri, G., *Angew. Chem. Int. Ed*., **45**, 5282, **2006**.
[18] Lee, J. S., Lim, H., Ha, K., Cheong, H., and Yoon, K. B., *Angew. Chem. Int. Ed*., **45**, 5288, **2006**.
[19]El-Gindi, J., Benson, K., De Cola, L., Galla, H. J., and Kehr, N. S., *Angew. Chem., Int. Ed*., **51**, 3716-3720, **2012**.
[20]Mattila, P. K., and Lappalainen, P., *Nat. Rev. Mol. Cell Biol*., **9**, 446-454, **2008**.
[21]Polleux, F., and Snider, W., *Cold Spring Harbor Perspect. Biol*., **2**, a001925, **2010**.
[22]Fletcher, D. A., Mullins, R. D., *Nature*, **463**, 485-492, **2010**.
[23]Conde, C., and Caceres, A., *Nat. Rev., Neurosci*., **10**, 319-332, **2009**.
[24]Roach, P., Parker, T., Gadegaard, N., and Alexander, M. R., *Surf. Sci. Rep*., **65**, 145-173, **2010**.
[25]Peyrin, J. M. et al., *Lab Chip*, **11**, 3663-3673, **2011**.
[26]Riehemann, K., Schneider, S. W., Luger, T. A., Godin, B., Ferrari, M., and Fuchs, H., *Angew. Chem. Int. Ed*., **48**, 872-897, **2009**.
[27]Grill, W. M., Norman, S. E., and Bellamkonda, R. V., *Annu. Rev. Biomed. Eng*., **11**, 1-24, **2009**.

[28]Chader, G. J., Weiland, J., Humayun, M. S., in *Neurotherapy: Progress in Restorative Neuroscience and Neurology, Progress in Brain Research*, Vol. 175 (Eds: Verhaagen, J., Hol, E. M., Huitenga, I., Wijnholds, J., Bergen, A. B., Boer, G. J., Swaab, D. F.) Elsevier, Amsterdam, 317-332, **2009**.
[29]Poghossian, A., Ingebrandt, S., Offenhäusser, A., Schöning, M J., Semin. *Cell Dev. Biol*. **20**, 41-48, **2009**.
[30] Widge, A. S., et al., *Biosens. Bioelectron*., **22**, 1723-1732, **2007**.
[31] Koh, H. S. et al., *Biomaterials*, **29**, 3574-3582, **2008**.
[32] Arnold, M., Schwiedler, M., Blümmel, J., Cavacanti-Adam, E. A., Lopez-Garcia, M., Kessler, H., Geiger, B., and Spatz, J. P., *Soft Matter*, **5**, 72-77, **2009**.
[33]Vogt, A. K., Lauer, L., Knoll, W., Offenhäusser, A., *Biotechnol. Prog*., **19**, 1562-1568, **2003**.
[34] Vogt, A. K., Brewer, G. J., Decker, T., Böcker-Meffert, S., Jacobsen, V., Kreiter, M., Knoll, W., and Offenhäusser, A., *Neuroscience*, **134**, 783-790, **2005**.
[35]Staii, C., Viesselmann, C., Ballweg, J., Shi, L., Liu, G., Williams, J. C., Dent, E. W., Coppersmith, S. N., and Eriksson, M. A., *Biomaterials*, **30**, 3397-3404, **2009**.
[36] Ellis-Behnke, R. G., Liang, Y. X., You, S. W., Tay, D. K. C., Zhang, S. G., So, K. F., and Schneider, G. E., *Proc. Natl. Acad. Sci. USA*, **103**, 5054-5059, **2006**.
[37]Yavin, E., and Yavin, Z., J. Cell Biol., **62**, 540-546, **19**74.
[38]Matsuzawa, M., Potember, R. S., Stenger, D. A., Krauthammer, V., *J. Neurosci. Meth*., **50**, 253-260, **1993**.
[39]Matsuzawa, M., Ptember, R. S., Krauthammer, V., *Brain Res*., **667**, 47-53, **1994**.
[40]John, P. M. S., Kam, L., Turner, S. W., Craighead, H. G., Issacson, M., Turner, J. N., and Shain, W., *J. Neurosci. Methods*, **75**, 171-177, **1997**.
[41]Yen, S.-J., Hsu, W.-L., Chen, Y.-C., Su, H.-C., Chang, Y.-C., Chen, H., Yeh, S.-R., and Yew, T.-R., *Biosens. Bioelectron*., **26**, 4124-4132, **2011**.
[42]Gilles, S., Winter, S., Michael, K. E., Meffert, S. H., Li, P., Greben, K., S., and imon, U., Offenhäusser, and Mayer, D., *Small*, **8**, 3357-3367, **2012**.
[43] Kim, Y. H., et al., *Journal of Neuroscience Methods*, **202**, 38-44, **2011**.
[44] D'Souza, S. E., Ginsber, M. H., Plow, E. F., *Trends Biochem. Sci.*, **16**, 246-250, **1991**.
[45] Mazia, D.,Schatte, G., Sale, W., *J. Cell. Biol*. **66**, 198-200, **1975**.
[46] Fischbach, K.-F., de Couet, H. G., Hofbauer, M. in *Seyffert Lehrbuch der Genetik* (pp 735-821), **2003**.
[47] Ruoslathi, E., *Cancer Matastasis Rev.*, **3**, 43-51, **1984**.
[48] Carlsson, R., Engvall, E., Freeman, A., Ruoslathi, E. *Proc. Natl. Acad. Sci USA*, **78**, 2403-2406, **1981**.
[49] Ruoslathi, E. *Ann. Rev. Cell Dev. Biol.*, **12**, 697-715, **1996**.
[50] Dowell-Mesfin, N. M., Abdul-Karim, M A., Turner, A. M., Schanz, S., Craighead, H. G. Rysam, B., Turner, J. N., and Shain, W., *J. Neural Eng*, **1**, 78-90, **2004**.
[51] Brunetti, V., Maiorano, G., Rizzello, L., Sorce, B., Sabella, S., Cingolani, R., and Pompa, P. P., *Proc. Natl. Acad. Sci. USA*, **107**, 6264-6269, **2010**.

[52] Hällström, W., Martensson, T., Prinz, C., Gustavsson, P., Montelius, L., Samuelson, L., and Kanje, M., *Nano Lett*., **7**, 2960-2965, **2007**.
[53]Bruder, J. M., Lee, A. P., Hoffman-Kim, J. Biomater. *Sci. Polym. Ed*., **18**, 967-982, **2007**.
[54]Yao, L., Wang, S., Cui, W., Sherlock, R., O'Connell, C., Damodaran, G., Gorman, A., Windebank, A., and Pandit, A., *Acta Biomater*., **5**, 580-588, **2009**.
[55]Ferrari, A., Cecchini, M., Dhawan, A., Micera, S., Tonazzini, I., Stabile, R., Pisignano, D., and Beltram, F., *Nano Lett*., **11**, 505-511, **2011**.
[56]Johansson, P., Carlberg, P., Danielsen, N., Montelius, L., and Kanje, M., *Biomaterials*, **27**, 1251-1258, **2006**.
[57]Fozdar, D. Y., Lee, J. Y., Schmidt, C. E., and Chen, S., *Biofabrication*, **2**, 035005, **2010**.
[58]Gomez, N., Lu, Y., Chen, S., and Schmidt, C. E., *Biomaterials*, **28**, 271-284, **2007**.
[59]Kang, K., Choi, S.-E., Jang, H. S., Cho, W. K., Nam, Y., Choi, I. S., and Lee, J. S., *Angew. Chem. Int. Ed*., **51**, 2855-2858, **2012**.
[60] Prinz, C., Hällström, W., Mårtensson, T., Samuelson, L., Montelius, L., and Kanje, M., *Nanotechnology*, **19**, 345101, **2008**.
[61] Hällström, W., Prinz, C., Suyatin, D., Samuelson, L., Montelius, L., Kantlehner, M., Kessler, H., and Spatz, J. P., *ChemPhysChem*, **5**, 383-388, **2004**.
[62] Arnold, M., Cavalcanti-Adam, E. A., Glass, R., Blümmel, J., Eck, W., Kantlehner, M., Kessler, H., and Spatz, J. P., *ChemPhysChem*, **5**, 383-388, **2004**.
[63]Cavalcanti-Adam, E. A., Volberg, T., Micoulet, A., Kessler, H., Geiger, B., and Spatz, J. P., *Biophys. J*., **92**, 2964-2974, **2007**.
[64]Wolfram, T., Belz, F., Choen, T., and Spatz, J. P., Biointerphases, **2**, 44-48, **2007**.
[65]Arnold, M. et al, *Nano Lett*., **8**, 2063-2069, **2008**.
[66] Selhuber-Unkel, C., Erdmann, T., Lopez-Garcia, M., Kessler, H., Schwarz. U. S., and Spatz, J. P., *Biophys. J.*, **98**, 543-551, **2010**.
[67] Kang, K. et al., *Angew. Chem. Int. Ed.*, **51**, 2855-2858, **2012**.
[68]Bear, F. M., Connors, B. W., Paradiso, M. A., *Neuroscience. Exploring the Brain*, Lippincott Williams & Wilkins, **2007**.
[69] Dotti, C. G., Sullivan, C. A., Banker, G. A., *J. Neurosci.*, **8**, 1454-1468, **1988**.

Zeolites as key-components for electronics
-
Ultrahigh Magnetoresistance in One-Dimensional Molecular Wires

Abstract

This chapter describes the possibility of addressing neurons on a zeolite-L monolayer. First the basic principles and the desired experimental setup are illustrated. After that it will be shown that zeolites can be rendered electrically conductive by filling the pores with high amounts of organic semiconductors. The electrical behavior of those materials will be described in detail. The electrical properties will be studied in the absence and in the presence of an external magnetic field and the highest room-temperature magnetoresistance, that has ever been reported so far, will be presented.

R. N. Mahato, **H. Lülf**, M. H. Siekman, S. P. Kersten, P. A. Bobbert, M. P. de Jong, L. De Cola, W. G. van der Wiel, *Science* **341**, 257 (2013).

4.1. Introduction

This project has been carried out in cooperation with the group of Professor Wilfred van der Wiel from the University of Twente (Measurements of conductivity and Magnetoresistance) and the group of Peter Bobbert from the University of Eindhoven (Theoretical calculations).

After the optimal conditions for neuron growth on a zeolite-L monolayer have been successfully identified, as described in chapter 3, a way to address neurons on a zeolite monolayer was developed.
Stimulation (and also inhibition) of neurons can generally be done in many different ways[1]. In a very simple and straightforward approach, nerve cells can be stimulated directly by using the so-called patch-clamp technique, which was developed already in the mid-1970s[2]. However, the main drawback of this technique is its high invasive nature and other methods for stimulating and recording signals in neurons have been developed.
An interesting approach for stimulating neurons electrically is the transcranical magnetic stimulation (TMS)[3]. This method is non-invasive and uses electromagnetic induction to induce weak electrical currents in the brain, which then causes depolarization or hyperpolarization.
Another, but fundamental different way of addressing neurons is a chemical stimulation by using signal inducing chemicals (neurotransmitters). To stimulate neurons *in vitro*, the neurotransmitters can be simply added to the culture media and synaptic stimulation will occur as soon as the neurotransmitters reach the synapses. Although this method is very straightforward and simple, it often results in an uncontrolled and simultaneous stimulation of a large number of cells, which makes it very difficult to study single synaptic events, which is often desired to study fundamental neural processes, e.g. signal transport, in detail.
In order to stimulate neurons *in vitro* in spatially confined areas, neurotransmitters can be converted into a biologically inert form (caged), which can then be retransferred into the active state by exposure of light of an appropriate wavelength and intensity. This “uncaging” can be done in very confined spaces by using two-photon-excitation and a number of caged neurotransmitter with high two-photon cross sections has been developed throughout the years[4, 5].

A different way of addressing neurons relies on the direct electrical stimulation.
Although direct electrical stimulation has been done for several years, e.g. by patch-clamp, non-invasive methods are generally preferred over invasive methods.
Interfacing electronic devices with biological systems has been of great interest for several years[6, 7] and it the interface of neurons with electronics has

been reported[8]. Recent examples show the ability of those systems to deliver neurotransmitters *in vivo*[9], to control cell adhesion[10, 11] and migration[12], to measure neural activity *in vivo*[13, 14] or to assess barrier tissue layer integrity[15].
Attempts to stimulate neurons by electronic devices are usually based on the direct electrical stimulation or an exogenous drug delivery to the cells[16].
Field effect transistors (FETs) composed of inorganic semiconductors have been used in this respect to extracelluarly record neuron signals[17, 18, 19, 20, 21, 22], but however, they do not allow for cell stimulation and they show face sensitivity limitations due to low capacitivities, which can only be solved by developing complex nanoarchitectures[23, 24, 25]. Additonally, inorganic semiconductors are not suitable for an ideal interfacing with living system due to their restricted biocompatibility[26] and often show significant biofouling and low biocompatability *in vivo* for a long time exposure with neural tissue[27].
Due to their tailored surface chemistry, mechanical flexibility and high sensitivity towards electrostatic potential changes, organic materials and organic field-effect transistors (OFETs) offer significant advantages over inorganic silicon based devices[28]. Importantly, organic materials show improved long-term biocompatibility, mechanical flexibility, and low cost fabrications, which makes them particularly interesting for interfacing them with neural systems and performing extracellular recordings and stimulation of neural activity[27, 29].
In particular, organic electronics can be used for a time real monitoring of neuronal cells activity as well as for the electrical stimulation of neurons by direct exposure to electrical fields[30].
When cells adhere and grow on OFETs, it is expected that the response of the transistor can be enhanced due to the close proximity of the cells and the charge transport areas, and several examples report on interfacing neural networks with OFET devices[20, 29, 31, 32, 33].

In detail, we aim to prepare the monolayer by using well-established methods (chapter 2) and to transfer it to the OFET surface in a second step. Then we will coat the monolayer with adhesive peptides to allow for a long-term cell growth. After a growth of about 9 days, we can directly stimulate the neurons on the OFET.
To allow for a direct electrical stimulation, the monolayer must be electrically conductive to ensure an electron transport from the OFET surface to the neurons. Since the zeolites are per-se electrically insulating, the conductive nature must be introduced to the particles after their synthesis. We aimed to render the zeolites conductive by filling the pores with an electron conducting material that can transport the electrons from the OFET to the cells. The experimental setup is schematically shown in figure 4.1.

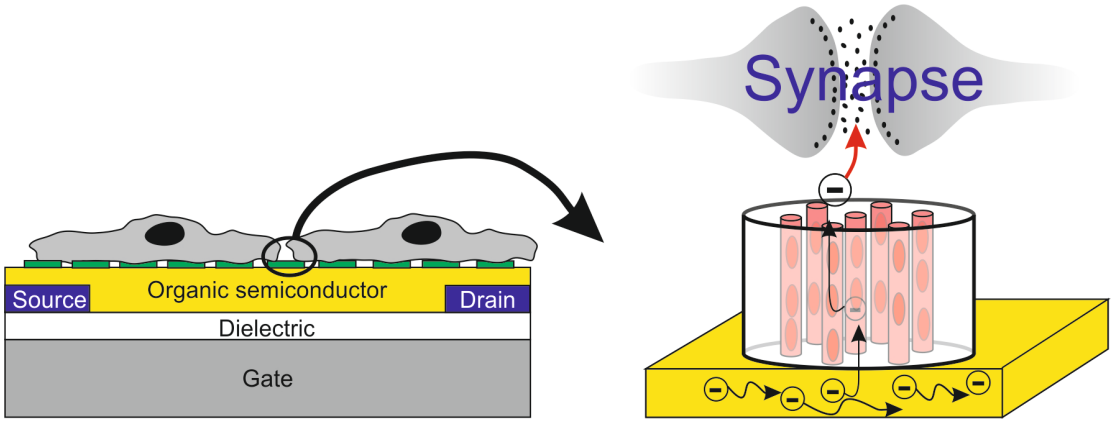

Figure 4.1. Schematic representation of addressing neuron cells by combining them with organic electronics, OFETs.

Different approaches to induce conductivity in zeolites have been reported throughout the years and are discussed in the following paragraph.

4.2. Electrical conductivity in zeolites. State of the art.

The basic principle for introducing conductivity to zeolite materials is the incorporation of conductive guests into the channel system, and a variety guests have been studied therefore. Experimentally, the conductivity of those zeolite materials has been studied by using microwave absorption techniques or impedance spectroscopy[34, 35].

Various studies have been reported to use the charge balancing cations in the pores to introduce electrical conductivity to the zeolites. Different counter cations have been studied in detail and it has been shown that those materials show a semiconductor behavior with breaking voltages strongly depending on the nature of charge-balancing cations and zeolite framework type. But the conductivity is exclusively ionic and due to movements of the cations in the framework[36, 37]. Besides using metal-ions as charge-compensating units, also the doping of zeolite hosts with metal atoms in order to create conductive materials has been investigated throughout the years and it has been documented that metal incorporation can lead to a significant increase in conductivity[8, 9, 38, 39, 40, 41].

Furthermore, zeolites have been used as host materials for the incorporation of organic conducting polymers. Although there are numerous studies dealing with the incorporation of conductive polymers in zeolites, they basically focus on the experimental conditions for incorporation and analysis of such materials. Conductivity studies about the electrical conductivity not reported so far.

Due to the fact that in our system the charge transport will occur through the zeolite-L crystal of the monolayer, it is very important to investigate the conductivity on a single crystal scale and in the direction of charge transport, in this case parallel to the channels. No conductivity measurements through sin-

gle oriented particles have been reported so far. The only single-zeolite study that has been reported is on carbon nanotubes embedded in an $AlPO_4$-5 (AFI) crystal[42].

4.3. Electrical conductivity in dye loaded single zeolite crystals.

Perylene diimides are frequently used as fluorescent labels inside of zeolite-L pores[20] and interestingly, these molecules are organic semiconductors with good electron conducting properties[43]. Additionally, it has be shown that the perylene diimide *N,N'*-Bis(2,6-dimethylphenyl)perylene-3,4,9,10-tetracarboxylic diimide (DXP) shows orbital overlap when introduced in the pores of zeolite-L in high concentrations[44], which should lead to an efficient electron hopping from one molecule to another and therefore to good conductivities along the pores. On the other hand it has been shown that perylene derivatives are potential candidates for integration in bioorganic devices and that they show a good biocompatibility even when used in combination with hippocampal neurons[45], [46].

For these reasons we decided to use DXP to render the crystals conductive. The molecular structure of DXP is depicted in figure 4.2.

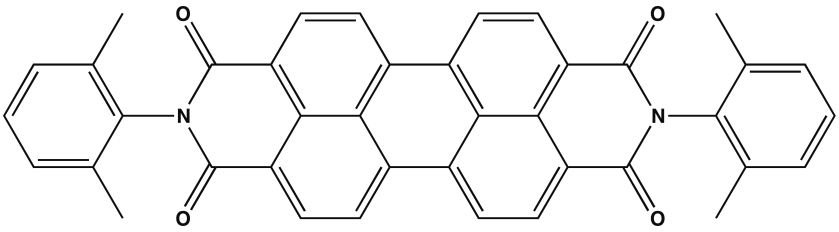

Figure 4.2. Structure of DXP

Disc shaped zeolite-L crystals with a diameter of about 200 nm and heights between 30 and 100 nm have been used. The potassium-exchanged form has been prepared and filled with high amounts of DXP in a standard procedure (See chapter 2). The loading was determined by thermogravimetric analysis (TGA) to be 5.95 wt.% or a loading ratio of 86% (see equation 2.2). The TGA data are shown in figure 4.3.

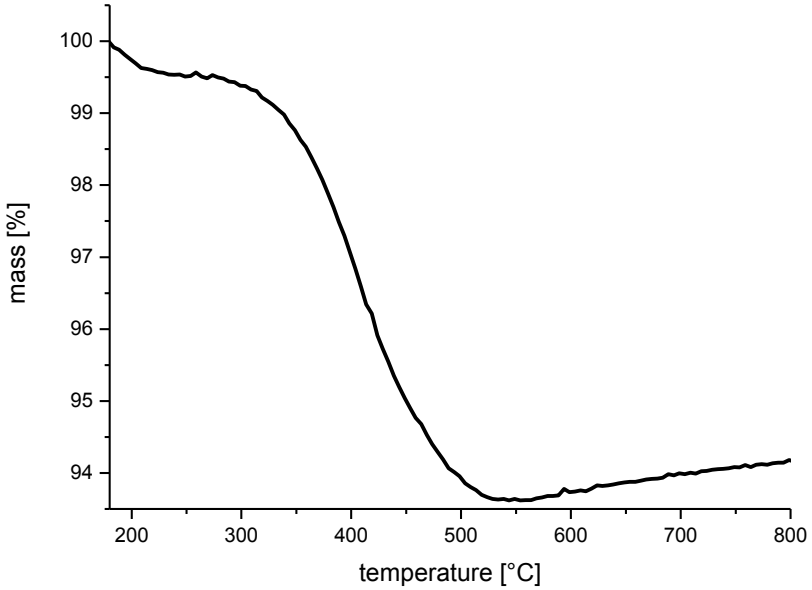

Figure 4.3. TGA analysis of DXP loaded zeolites. The weight loss can be calculated to a loading of 86%.

To measure the conductivity we first self-assembled these DXP loaded zeolites into monolayers on a glass substrate and then transferred them to a conductive ITO|PEDOT:PSS substrate as described in chapter 2 of this thesis. The conductivity of single zeolite crystals was then measured by using conducting probe atomic force microscopy (CP-AFM). All data have been recorded at room temperature. The experimental setup is depicted in figure 4.4.

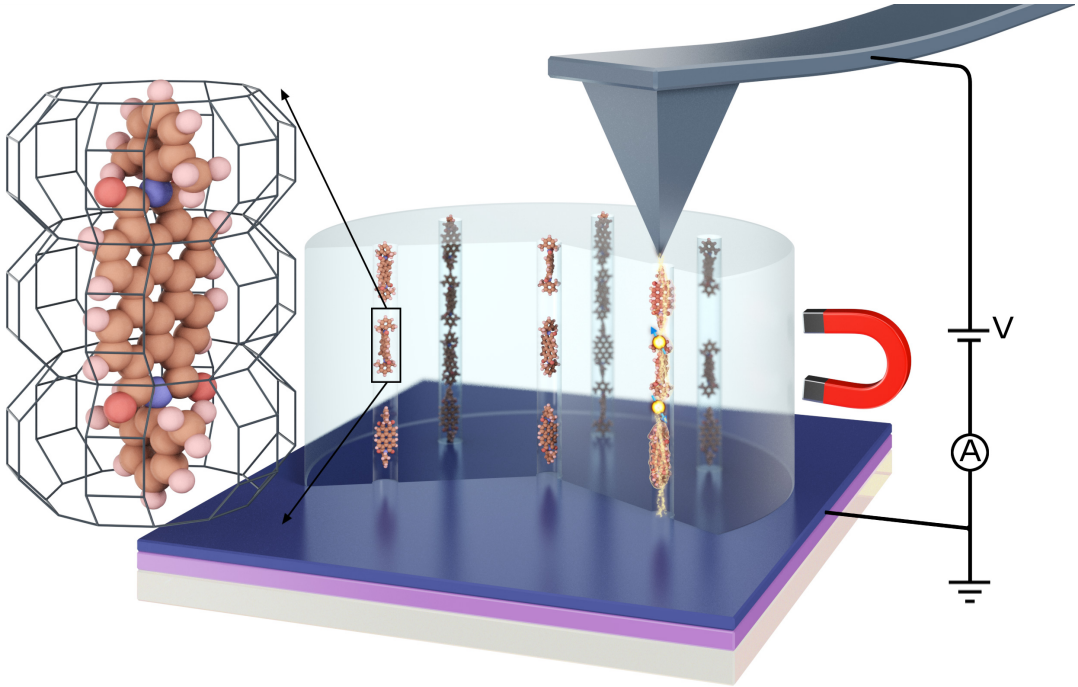

Figure 4.4. Schematic representation of the experimental setup to record the conductivity of DXP loaded zeolites. To investigate the magnetic field dependence of electrical conductivity through one-dimensional DXP wires in a zeolite host an external magnetic field can be applied.

Due to geometrical constraints, the DXP molecules are oriented with their long molecular axis parallel to the channels and form one-dimensional organic wires inside the zeolite host. The high orientation of DXP molecules in zeolite-L channels has previously been confirmed by means of fluorescence polarization microscopy, which shows that the emission of the DXP zeolites is polarized along the axis of the crystal. This indicates that the electronic transition dipole moments are aligned parallel to the channels and proves that the molecules are incorporated into the channel system and not just adsorbed on the zeolite surface[47, 41].
The number of channels, which is addressed during a measurement, can be calculated as shown below.
The number of parallel channels n_{ch} in a zeolite L crystal with a diameter d is given by

$$n_{\mathrm{ch}} = \frac{\pi\left(\frac{d_z}{2}\right)^2}{|a|^2 \sin(60^\circ)} = \frac{\pi}{2\sqrt{3}}\left(\frac{d_z}{|a|}\right)^2 \qquad \text{Eq.4.1.}$$

This equation can be approximated to

$$n_{\mathrm{ch}} \cong 0.268(d_z)^2 \qquad \text{Eq. 4.2.}$$

Thus, a zeolite-L crystal with a diamter of 200 nm exhibits about 10720 channels. With consideration of a PtSi CP-AFM tip radius of 10 nm, the number of zeolite-L channels contributing to a measurement is about 100.

The intactness of the DXP molecules after insertion and the presence of aggregates inside the channels, due to the very high loading of 86%, was confirmed by fluorescence spectroscopy. The absorption and emission spectra of DXP in DCM solution and inside zeolites are shown in figure 4.5. The absorption and emission spectra of the zeolite samples have been measured directly in solid state.
The absorption spectrum of DXP loaded zeolites resembles the typical shape of monomeric DXP with vibronic bands at 458, 488 (0,1 transition), and 525 nm (0,0 transition)[48], which confirmes that the DXP molecules are still intact inside the zeolites. The aggregation of DXP inside the zeolites can be deduced from the red-shift of the emission compared to monomeric DXP in DCM solution (See red line in figure 4.5.), which is accordance to the literature[49]. The DXP loaded zeolites show a very broad emission ranging from 525 to about 850 nm, with peaks located at 600 and 650 nm.

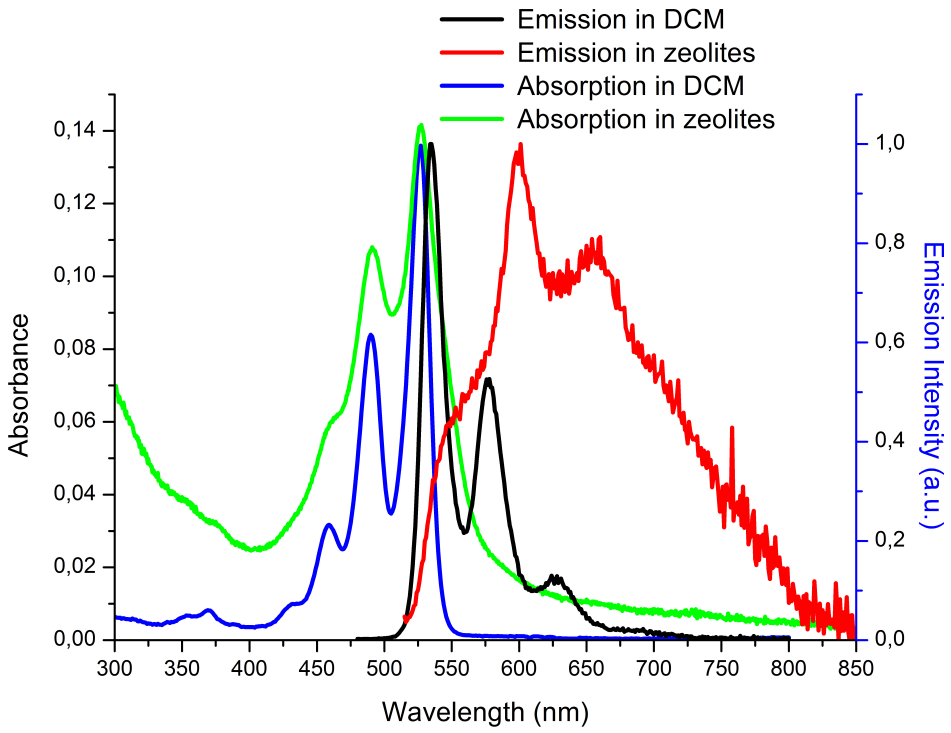

Figure 4.5. Photophysics of DXP loaded zeolites and DXP in DCM solution. Emission spectra have been recorded with λ_{exc} = 460 nm.

After the loading has been determined and the intactness of the DXP inside the zeolites has been confirmed, the conductivity through these organic wires formed by the very closely packed DXP inside the channels has been measured according to figure 4.4.A.

In order to investigate the influence of the wire length on the electrical conductivity, zeolite crystals with heights (and therefore wire lengths) from 30 to 90 nm have been studied. For every height the results have been reproduced at least for 2 different crystals.

The corresponding current (I) – voltage (V) characteristics from these measurements are shown in figure 4.6.

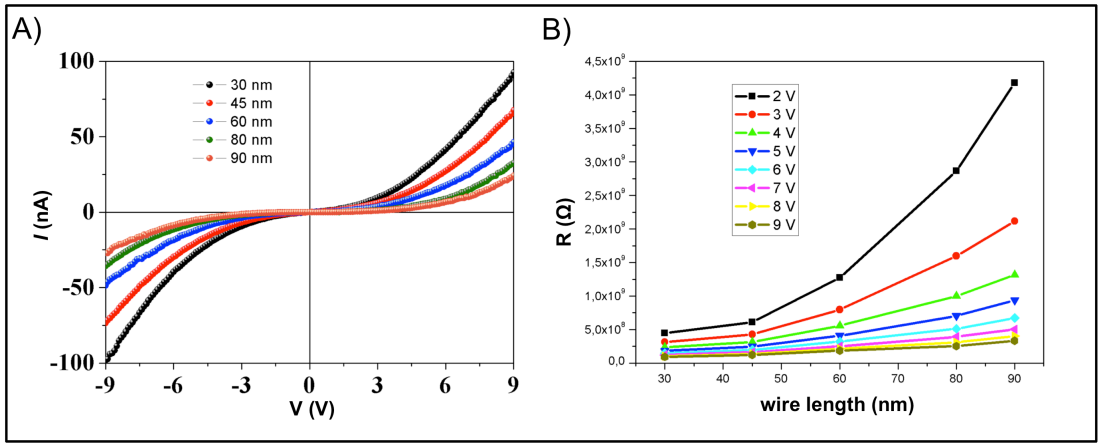

Figure 4.6. A) I|V curves of one-dimensional DXP wires in a zeolite-L host showing the influece of the wire length on the current. B) Resistance in one-dimensional DXP wires in a zeolite host in dependence of wire length and voltage.

The curves are strongly nonlinear, which is a characteristic for (sequential) tunneling behavior (Figure 4.6.A). Furthermore the curves are symmetric in voltage, which is in accordance with the similar work functions of both contacs. It can be seen that the current decreases with increasing channel length. This fact can be described better when plotting the resistance, R=V/I, for different currents against the channel lengths varying from 30 to 90 nm (Figure 4.6.B). The resistance increases exponentially for low voltages and linear for higher voltages with increasing channel lengths. This behavior of the resistance being clearly dependent on the chanel lengths is further proof that the conductivity is limited by the transport through the molecular wires rather than by the contacts.

The symmetry of the *I-V* curves and the absence of a large injection barrier point in the direction of unipolar transport. Both PEDOT:PSS and PtSi have work functions of around -5 eV[50, 51], which is roughly in the middle between the energies of the highest occupied and lowest unoccupied molecular orbital (HOMO and LUMO) of DXP, as determined from cyclic voltammetry measurements in solution (-6.0 eV and -3.9 eV, respectively)[52]. However, because of the presence of the potassium ions, the HOMO and LUMO energies are considerably to be more negative inside the zeolite channels. This should lead to efficient electron injection and charge transport is expected to occur by electrons.

To prove that the conductivity is indeed due to the inserted DXP, the conductivity was also measured in a control sample. The control was treated in the same way as the DXP samples, with the only difference, that no DXP was inserted in the zeolites. The *I-V* characteristics of the empty zeolites and the substrate were measured both by CP-AFM. The *I-V* measurements show insulating behavior for empty zeolites. Even at 9 V bias voltage, the current through the empty zeolite-L crystals was below the detection limit of the system. When placing the CP-AFM tip on the ITO|PEDOT:PSS substrate, ohmic behavior was observed with a typical resistance of 10 Ohms, i.e. orders of

magnitude smaller than the resistance of zeolite-L crystals filled (to 86%) with DXP molecules.
In summary these experiments show, that zeolites can be rendered electrically conductive by inserting DXP in their channels.

In addition, the magnetic field dependence of the conductivity (magnetoresistance) has been investigated.
Before continuing with the experimentally results obtained from our studies, the terms magnetoresistance (MR) and in particular organic magnetoresistance (OMAR) are introduced.

4.4. Magnetoresistance

Magnetoresistance is referred to a materials property to change its resistance in dependence of an externally applied magnetic field. Magnetoresistance was discovered already in 1857 by William Thompson, and was referred to as a type of anisotropic mangetoresistance (AMR). He found that the resistance in a piece of iron decreases when the electron-flow is directed in the same direction as the magnetisation, compared to an electron-flow directed 90 degrees to the direction of magnetisiation. The physical origin of magnetoresistance is based on the scattering of electrons in dependence of magnetization. Nowadays there are many types of magnetoresistance known, like giant magnetresistance (GMR), colossal magnetoresistance (CMR), tunnelmagnetoresistance (TMR) and organic magnetoresistance (OMAR).
GMR was discovered independently from Albert Fert and Peter Grünberg in 1988 and was honored with the Nobel Prize in physics for both Fert and Grünberg in 2007. GMR is based on spin-depending scattering in alternating magnetic and non-magnetic layers, such as Fe/Cr or Co/Cu[53, 54]. An electron passes easily through a material, which electron spins are aligned in the same direction as the passing electron. On the other hand, the electron will encounter a significant resistance, when ist spin is aligned antiparallel to the spins of the material. Without any applied magnetic field the spins of the two ferromagnetic layers are aligned antiparallel (up and down) and either electrons with spin up or down will be scattering in one of the layers.
If an external magnetic field is applied, the spins in the magnetic layers are oriented parallel to each other (both up or both down). Now, an electron with its psin aligned parallel to the spin of the magnetic layers can pass the material without showing a significant resistance. This phenomena can reach values of more than 100% and is therefore described as GIANT magnetoresistance (GMR).
TMR is a pure quantummechanical effect, that is observed when two magnetic layers are separated by a very thin tunnel barrier. According to classical physics electrons can not pass the insulating layer between the

magnetic layers, but, if the layer is thin enough, there is a given possibility for tunneling through the insultaing layer[55, 56]. Nowadays TMR is widely used in magnetic random-access memory (MRAM) devices, that allows for „instant-on“ computing.

CMR can be found mostly in perovskite materials based on manganese. In 1950 it was found that LaMnO3 shows metallic properties upon exchanging small amounts (around 30%) of La with Sr and cooling. At the insulator-metal transition, the system becomes ferromagnetic, which is called Zener Double Exchange, but will not be discussed in this thesis.

4.5. Organic Magnetoresistance

All of these discussed mangetoresistive effects (AMR, GMR, TMR, CMR) have in common, that they are based on magnetic materials.

Another, particularly different class of materials showing magnetoresistance, are organic semiconductors, small organic molecules or organic polymers. This very special kind of magnetoresistance is therefore called **Organic Magnetoresistance (OMAR)**[57]. Due to long spin coherence times in organic molecules, which consist of low molecular weight elements, these materials show interesting properties for exploring their magnetoresistance properties in detail. It has been shown that replacing either the non-magnetic spacing layer (GMR) or the tunnel barrier (TMR) by thick (about 100 nm) or very thin films can lead to interesting properties[58, 59, 60, 61]. Additionally to these efforts, organic materials themselves are known to show remarkably magnetoresistance, which occurs at room temperature, small magnetic fields (a few mT) and without any ferromagnetic materials present[62, 63, 64, 65, 66, 67, 68, 69, 70], which makes these materials very interesting for real-world applications. In addition, the ease of fabrication, low cost and easy tunability of the materials themselves make organic materials especially interesting for applications in electronic devices.

Even though small magnetic fields are known for several years to effect various properties like photoluminescence or chemical reactions[71], the first example of organic materials showing a dramatic change in current (20%) upon applying a small magnetic fiels is reported only in 2004[72]. This discovery can be seen as the starting point for intense research on OMAR and models to explain the physics behind it. It should be emphasized once again that OMAR is not an exotic phenomenon, but quite common in organic semiconductors, small molecules and polymers. Furthermore OMAR is not an organic analogue of GMR, but a totally new effect with entirely different physics behind it.

However, the physics behind OMAR is not fully understood yet and there are still different models to explain OMAR, spin dephasing due to hyperfine fields plays an essential role. The general idea is, that charge carriers diffusing

along the organic molecules experience small hyperfine fields coming from the hydrogen nuclei of the organic compounds, which is an efficient source for spin decoherence and leads to a fast and efficient change in singlet and triplet character. In presence of an external magnetic field, the spin precision on different sites becomes more coherent and the spin-character (singlet or triplet) is preserved for much longer times. That hyperfine fields play a key role in OMAR has been confirmed by comparing polymers with their deuterated analogues[41].
It has been shown that the (organic) magnetoconductance MC, given as [I(B) – I(0)/I(0)], can either be positive or negative. Furthermore, OMAR is known to appear in two characteristic line shapes, which can be fitted by a Lorentian or a non-Lorentian fit[33], when plotting MC against the magnetic field B. The different fittings are described by

$$MC(B) \propto \frac{B^2}{B_0^2+B^2} \qquad \text{Eq. 4.3.}$$

for a Lorentian fit, and by

$$MC(B) \propto \frac{B^2}{(B_0+|B|)^2} \qquad \text{Eq. 4.4.}$$

for a non-Lorentian fit.

The width of both curves, characterized by the paramter B_0, is very similar and reflects the value of the hyperfine fields, typically between 3 and 6 mT.
Depending on the model that is applied to describe OMAR, different pairs of charge carriers (plarons, excitons) are considered to interact and to cause magnetic field dependend currents. Both the electron-hole pair model (e-h) and the exciton model rely on the interaction of oppositely charged carriers. The e-h model is based on the interaction of electrons and holes, and the exciton model takes into account the interaction between excitons and charges. In contrast to these models the bipolaron model is based on the spin dependend formation of molecular sites occupied by two polarons of the same type, causing electron-electron or hole-hole bipolarons. In the following chapter the bipolaron model will be described in more detail, since it will be used to explain the results shown in chapter 4.7.

4.6. The bipolaron model[36]

In usual organic semiconductors, the different energy levels are not perfectly isoenergetic, but displaced by about 0.1 – 0.2 eV from each other in a Gaussian way. This notion is the basis of the bipolaron model, which has been proposed by Bobbert et al.
Furthermore, charge transport through organic semiconductors occurs via specific quasi-one dimensional pathways. The bipolaron model considers

charge transport due to polarons. The energy cost to form a doubly occupied site is relatively low and about the same magnitude as the Gaussian displacement of energy levels (0.1 – 0.2 eV). Therefore the formation of bipolarons is possible and allowed (at least for short time scales).
But the possibility for bipolaron formation is strongly spin-dependent and very likely to occur for spin singlets, but not for spin triplets. Taking into account charge transport along a one-dimensional pathway, the following scenario can occur and explains the magnetic field dependence of the current in organic semiconductors (See figure 4.7): A charge carrier, which diffuses along the organic semiconductor comes to a site that is already occupied by another charge carrier. In order to diffuse along its way through the semiconductor, occupation of the same molecular site by both charge carriers and therefore bipolaron formation is necessary. But this is just possible for spins meeting in a singlet formation. For two polarons meeting in a triplet formation, bipolaron formation is efficiently blocked. At low magnetic fields this blockade is efficiently lifted due to fast spin mixing due to the small random hyperfine fields B_{hf}.
On the contrary at large magnetic fields, $B_0 >> B_{hf}$, the spins are aligned in the same direction and the spin character is well conserved. Therefore the formation of bipolarons is efficiently blocked when an external magnetic field applied.

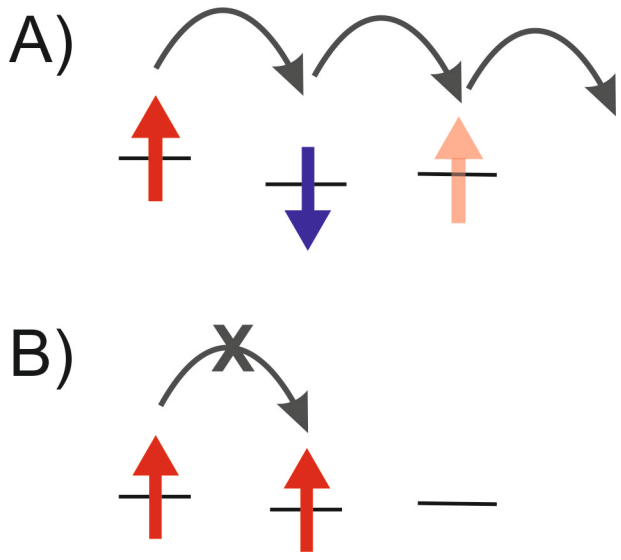

Figure 4.7. Schematic representation of the bipolaron model. A) No external magnetic field. The molecular site is already occupied by the purple polaron (here spin down). In order to pass through the material, the red polaron (here spin up) must occupy the same molecular site for a short time. This is possible, since the two polarons are combining in a singlet formation. B) External magnetic field applied. The molecular site is already occupied by the red polaron (here spin up). In order to pass through the material, the other red polaron (here spin up) must occupy the same molecular site for a short time. This is forbidden, since the two polarons are combining in a triplet formation.

4.7. Ultrahigh Magnetoresistance in one-dimensional molecular wires

To investigate whether the one-dimensional molecular wires also show OMAR, as observed in various bulk systems of organic semiconductors, we have studied the magnetic field dependence of the current through the molecular wires for different lengths. Therefore the CP-AFM has been equipped with an electromagnet providing a magnetic field up to 14 mT, which is directed perpendicular to the channels. Again crystals with heights of 30, 45, 60, 80 and 90 nm have been measured and the results have been reproduced for at least 2 different crystals. In accordance to other reports in the literature[73], the magnetoconductance is described as

$$MC = \frac{I(B)-I(0)}{I(0)} \qquad \text{Eq. 4.5.}$$

where I(B) is the current at magnetic field B, which is applied perpendicular to the wires, and I(0) the current at zero magnetic field. The maximum possible magnetoconductance is therefore +/- 100%.

The results are shown in figure 4.8 and 4.9. Figure 4.8 shows the magnetoconductance for different wire lengths with a non-Lorentian fit and figure 4.8. shows the same but fitted with a Lorentian function. Exceptionally high magnetoresistance values of values approaching -100% were observed. The overall trend shows negative magnetoconductances increasing with decreasing voltages. The different fits show that our data can be fitted the best with a non-Lorentian function. The B_0 values vary between 2 and 6 mT, which is comparable to values obtained for bulk OMAR[43]. Furthermore, the B_0 values do not show a clear voltage or length dependence. As it can be seen in figure 4.8, the largest magnetoconductance value of almost -100% is obtained for a wire length of 60 nm and 2 V.

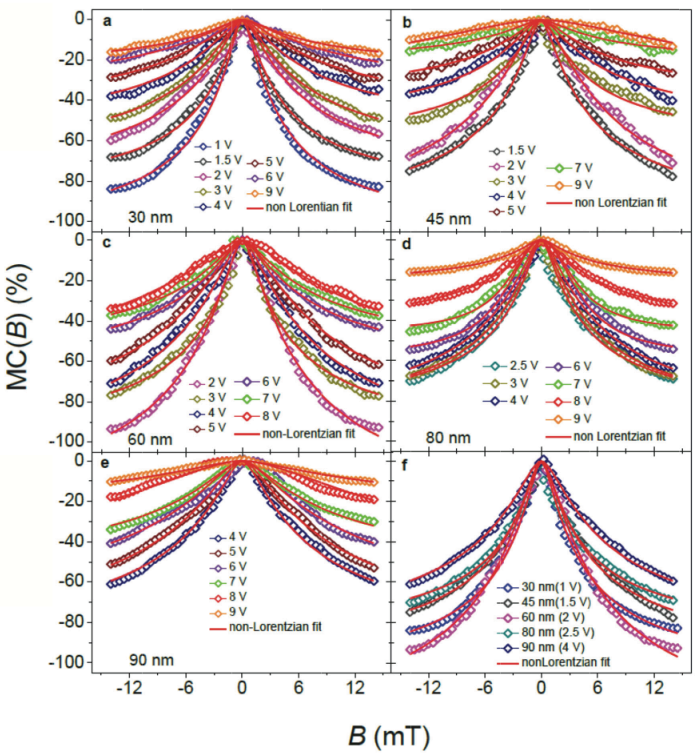

Figure 4.8. Magnetoconductance in dependence of magnetic field B for different wire lengths. f shows the maximum values for each wire length plotted together. The data were fitted with a non-Lorentian fit.

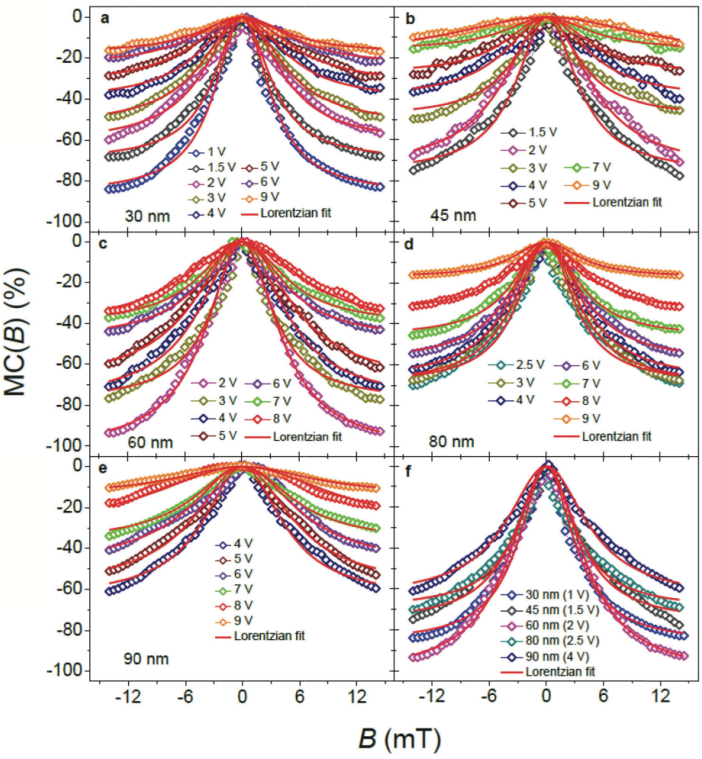

Figure 4.9. a – e: Magnetoconductance in dependence of magnetic field B for different wire lengths. **f** shows the maximum values for each wire length plotted together. The data were fitted with a Lorentian fit.

The voltage dependence is more clearly represented if the magnetoconductance MC is converted into magnetoresistance MR, which is defined as

$$\mathrm{MR}(B) \equiv \frac{R(B)-R(0)}{R(0)} = \frac{I(0)-I(B)}{I(B)} \qquad \text{Eq. 4.6.}$$

With R(B) being the resistance at field B and R(0) the resistance at zero magnetic field. As it can be seen in figure 4.10, the magnetoresistance increases with decreasing voltage and reaches a maximum value of more than 2000% for a wire length of 60 nm. The magnetoresistance for 0 V could not be determined as the current level was below the noise level of the system.

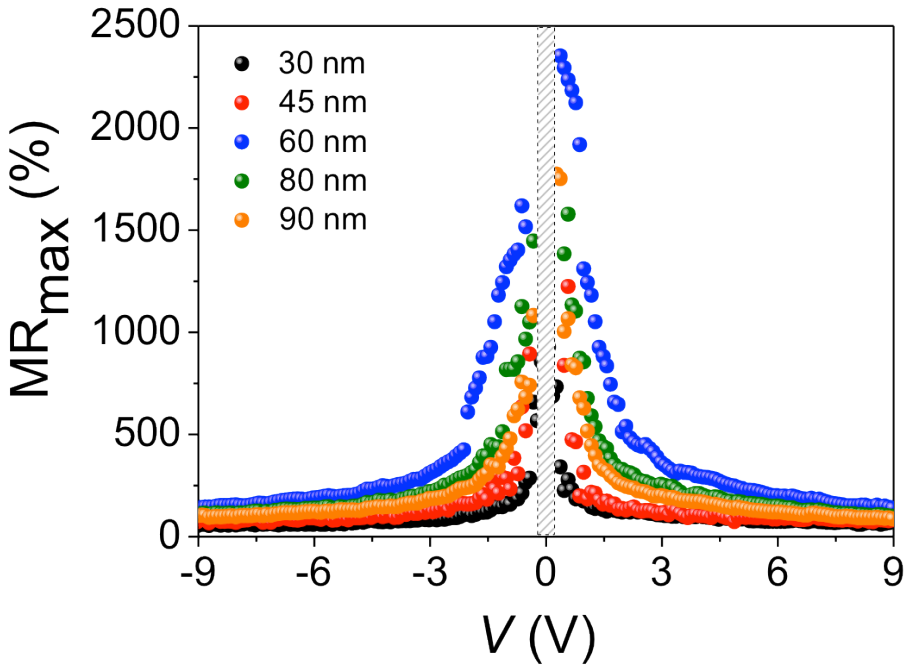

Figure 4.10. MR in dependence of the voltage in wires of different lengths.

The obtained magnetoresistance values in our system are not only the highest magnetoresistance values that have ever been measured for OMAR, but also the highest MR values that have ever been measured at room temperature. The highest room temperature magnetoresistance (TMR) to date is reported for an epitaxial CoFeB/MgOCoFeB magneto tunnel junction[74]. Collosal magnetoresistance manganites are known to show very large magnetoresistances, but only at low temperatures and strong magnetic fields[75]. At room temperature and small magnetic fields these systems just show magnetoresistances of a few percent[76, 77]. Similar magnetoresistance values have been reported for nanocomposites containing magnetic nanoparticles[78]. A large room temperature magnetoresistance has also been reported for a graphene nanoribbon field-effect transistor[79].

We ascribe the obtained very high magnetoresistance to the unique properties of one-dimensional wired embedded in a zeolite-L host. As it is shown in

figure 4.11, bulk DXP with a comparable height of about 40 nm just shows a magnetoresistance of about -20% when the same PtSi-CP-AFM tip is used. When the tip is replaced by a platinum wire (diameter 250 µm), the magnetoresistance further drops to about -5%. This results points strongly in the direction, that the confinement and the formation of the one-dimensional DXP wires is the reason for these very high values.

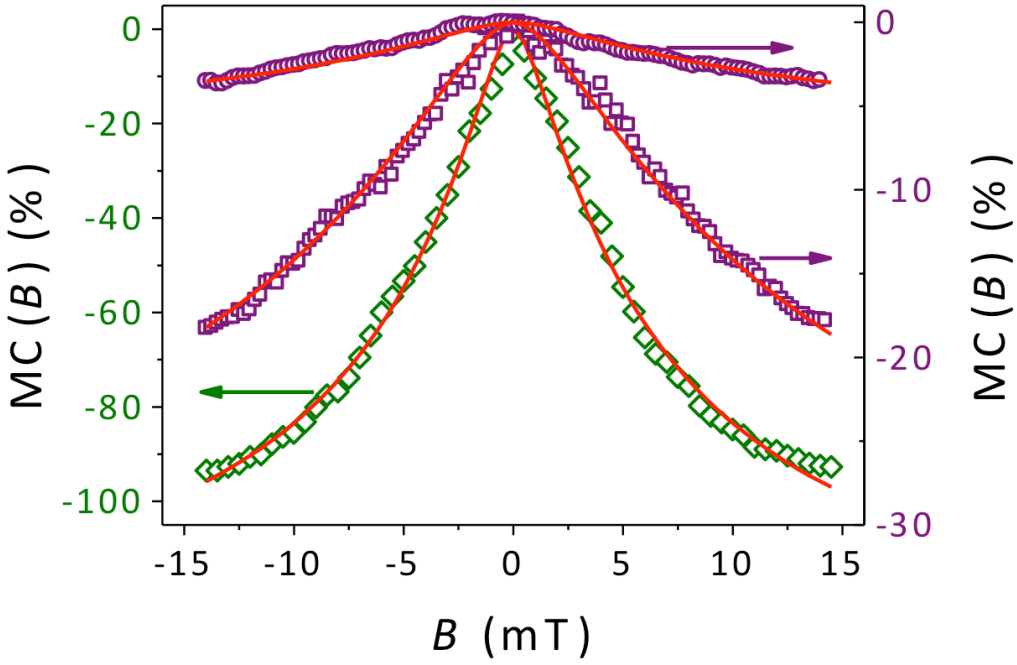

Figure 4.11. MC in different DXP morphologies. Violet circles: MC in a 40 nm DXP film contacted with a platinum wire (d=250 µm); violet squares: MC in a 40 nm DXP film contacted with CP-AFM tip; green squares: MC in a 60 nm one-dimensional wire of DXP entrapped in zeolite-L.

In the following, the origin of the very large MCs will be explained on the basis of the bipolaron model[36]. The bipolaron model is taken as the model of choice for different reasons.
Very importantly, the energy to form a doubly reduced DXP is remarkably low (about 0.2 eV), as it is reported in the literature[80]. This value is also taken as the energy cost for bipolaron formation on the DXP. The energy cost to form doubly oxidized DXP species is much higher, which confirms the assumption of electron transport through our wires.
In addition, OMAR is also observed below the DXP HOMO-LUMO gap (about 2 eV) and mechanisms based on excited states can be ruled out.

Simulations show, that MC values close to -100% can be obtained with MC curves having the line shape of equation 4.4.

Figure 4.11.A shows simulated room temperature MCs at an electric field F = 0.1 V/hop, a bipolaron formation energy U = 0.2 eV[51], and an electron concentration c = 0.3.
Figure 4.12 B shows the MCs in a range of electric field F corresponding to the voltages in the experiment and for a hop distance around 0.2 nm.

It can be seen, that a noticeable MC is obtained for an electron concentration of 0.3, but however, not as large as obtained from the experiments and the voltage dependence is the opposite. The difference was attributed to a Coulomb-trapping of electrons by the potassium counter-cations while the electrons travel through the one-dimensional wires. This was modeled by introducing randomly distributed trap sites with a concentration c_{trap} and trap energy U_{trap}. Bipolaron formation now occurs exclusively at the trap sites. For U_{trap} = 0.2 eV[51], the size of the MC is about the same as the experimental values obtained for a wire length of 60 nm and a voltage of 2 V (red dots in figure 4.12 A). As the experimental results, the simulated MCs can be fitted with a non-Lorentian fit (Equation 4.4.).

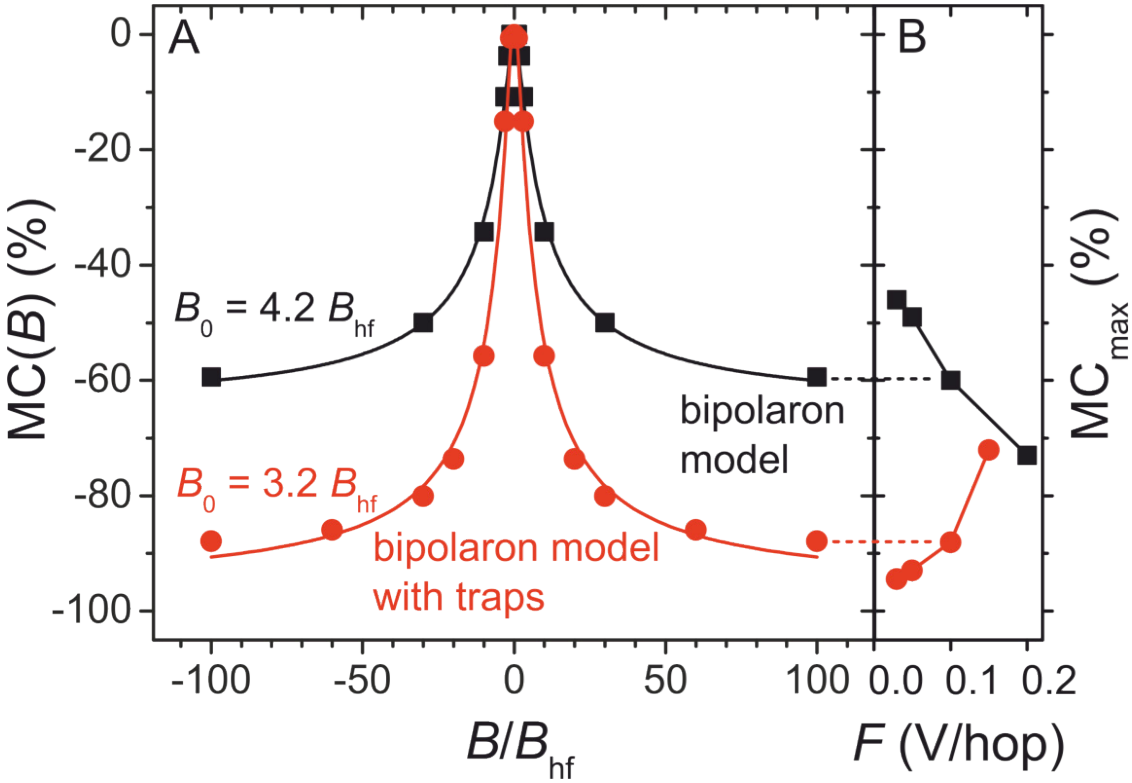

Figure 4.12. (A) Simulated room-temperature magnetoconductance MC(B) at an electric field F = 0.1 V/hop, bipolaron formation energy U = 0.2 eV, and electron concentration c = 0.3. Black squares: Gaussian energy disorder with standard deviation σ = 0.1 eV. Red dots: trap sites with concentration c_{trap} = 0.15 and trap energy Utrap = -0.2 eV (no energy disorder). Lines: fits to the empirical line shape of Eq. 2. (B) Voltage dependence of MCmax = MC(100 Bhf). All error bars are of the order of or smaller than the symbols.

In summary, we obtained by far the highest room temperature magnetoresistance ever reported.
The very high values are ascribed to the unique combination of one-dimensional DXP wires being entrapped in a potassium exchanged zeolite host, as confirmed by simulations.
As confirmed by CV measurements, doubly reduced DXP species can easily be formed and the difference between the first and second reduction potential is remarkably small. This ease of double reduction leads to the very likely situation of finding 2 electrons (or polarons) at the same site, which then leads to a current strongly depending on an external magnetic field, as described above.

According to this argumentation, preventing a second reduction of the organic semiconductor should lead to a prevention of bipolaron formation and the MCs should dramatically change.
For DXP, and perylene bisimides in general, the very small energy difference between the first and second reduction is due to the presence of two perylene monoimide groups, each of them can accommodate one electron.
This second reduction is efficiently blocked for perylene imides, where just one of the imide groups is present. In particular this has been shown for the following molecule, which will be called PMI-1, by cyclic voltammetry[52]. For this reason we chosed to fill zeolites with this compound and to measure the MC of these crystals.

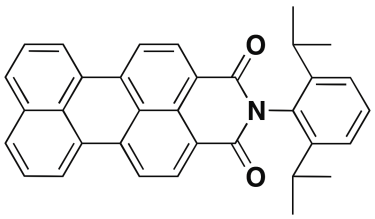

Figure 4.13. Structure of PMI-1.

PMI has been synthesized and incorporated in a potassium exchanged zeolite-L host in high loading levels.
The synthesis scheme is shown in figure 4.14. The experimental details can be found in the experimental section.

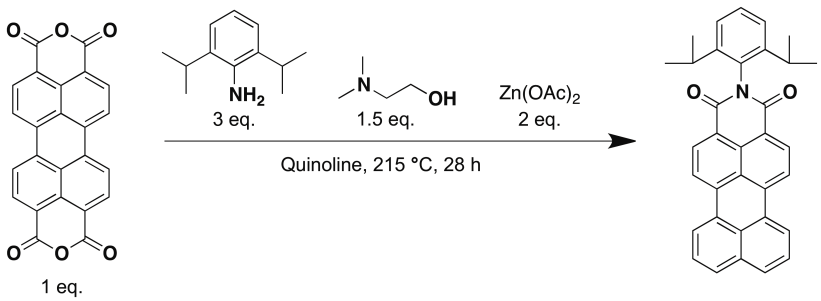

Figure 4.14. Synthesis of PMI-1.

In order to incorporate PMI-1 into the channels of zeolite-L by sublimation, the sublimation temperature at 1E-5 mbar has been determined to be about 250 °C by TGA/DSC analysis.
The incorporation into zeolite-L has been done from the gas phase as described in chapter 2. The intactness of the PMI inside the zeolites has again been confirmed by means of fluorescence spectroscopy. Figure 4.15 shows the absorption and emission spectra of PMI in zeolites and in DCM solution.
The absorption spectrum of PMI loaded zeolites resembles the same shape of monomeric PMI in DCM solution with bands at 485 and 505 nm, which proves that the DXP molecules are still intact inside the zeolites. In DCM solution PMI shows an emission ranging from about 500 to 700 nm with strong bands at 545 and 580 nm. As for the DXP sample, the emission of PMI inside zeolites is redshifted. The emission maximum is shifted by 110 nm to 655 nm, which indicates an efficient aggregation of PMI inside the zeolites.

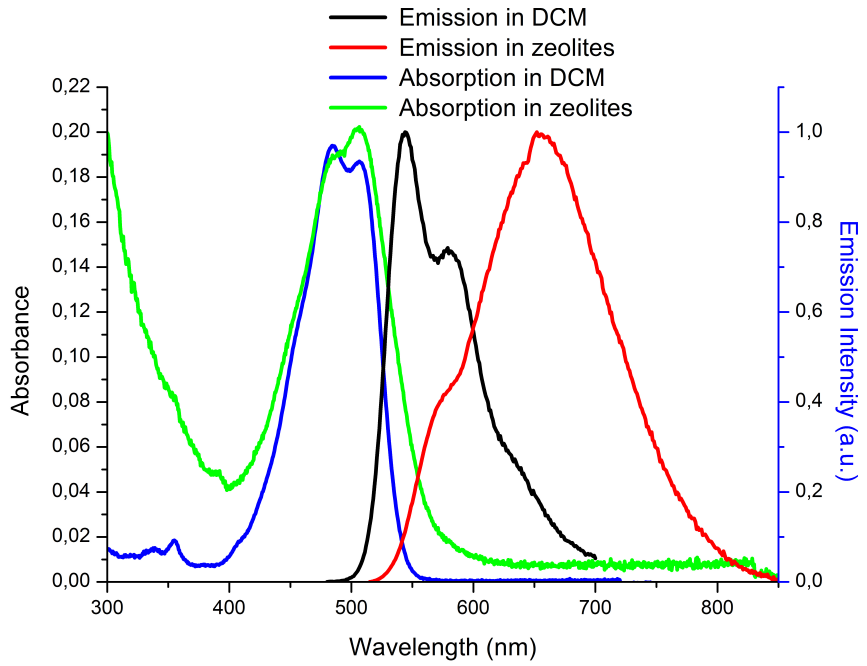

Figure 4.15. Photophysics of PMI loaded zeolites and PMI in DCM solution. Emission spectra have been recorded with λ_{exc} = 460 nm.

Again, these zeolites have been assembled into monolayers, which then have been transferred to a ITO|PEDOT:PSS substrate.
The conductivity and the MC will be measured in the same way as done for DXP loaded zeolites presented above. The experiments are ongoing.

4.8. Conclusion

This chapter presents first important import experiments to allow for a direct electrical stimulation of neurons by combining them with an organic electronic device (OFET). It has been shown, that zeolite crystals can be rendered elec-

trically conductive by filling the pores with organic semiconductor molecules. Above that, the presented material shows extraordinary magnetoresistive properties. The results belong to the largest room-temperature magnetoresistance effects ever observed at a magnetic field scale of a few mT, which in combination with the facile and cheap low-temperature, bottom-up fabrication procedure, offers very good perspectives for technological application. Moreover, we expect that the generic nature of our results will make it possible to exploit this ultra-high magnetoresistance in a wide range of low-dimensional systems.

4.9. Experimental part

Chemicals

Potassium hydroxide (90%), sodium hydroxide (≥98%), Ludox HS-40, 3-chloropropyltrimethoxysilane (CPTMS, 97%), 3-aminopropyltriethoxysilane (APTES, ≥98%) and N,N´-bis(2,6-dimethylphenyl)perylene-3,4,9,10-tetracarboxylicdiimide (DXP) (≥90%) were purchased from Sigma Aldrich. Aluminium hydroxide (extra pure) was purchased from Acros Organics. Toluene (dry), ethanol, chloroform and n-butanol (used as received) were purchased from VWR. PDMS (184 silicon elastomer base, SYLGARD) was purchased from Dow Corning Corporation. Glass slides (round shape, diameter: 12 mm, thickness: 0.13 – 0.17 mm) were purchased from R. Langenbrinck Labor- und Medizintechnik.
PEDOT:PSS was purchased from H. C. Starck.

Zeolite Synthesis

Disc-shaped zeolite-L crystals (length = 30-100 nm, diameter = 200-500 nm) were synthesized as described in chapter 2.

Cation exchange

In order to exchange the cations in the zeolite channels with potassium ions, 50 mg zeolites were added to 100 mL of a 0.1 M aqueous solution of KNO_3 and refluxed for 3 hours. After cooling to room temperature the zeolites were washed with bidistilled water (5 x 20 mL). The zeolites were dried in vacuum and the shape and size was controlled by means of scanning electron microscopy.

Dye insertion

DXP was inserted from the gas phase at 300 °C as described in chapter 2. In order to obtain the maximum loading a calculated amount of 150% DXP was used for insertion (The calculation was done by considering that DXP occupies 3 unit cells and a loading of 100% corresponds to the highest loading possible). Therefore 100 mg of zeolite-L crystals were mixed with 10.4 mg DXP in a glass ampoule. The loading was determined by means of thermogravimetric analysis.

Monolayer preparation

The zeolite monolayers were prepared by sonication method as described in chapter 2.

Zeolite transfer

The zeolite monolayer has been transferred to a conductive ITO|PEDOT:PSS substrate as described in chapter 2.

Preparation of reference sample for measuring electrical properties of bulk DXP

First a thin layer of PEDOT:PSS was spin coated on a ITO substrate following the above mentioned protocol. After that a thin layer (about 40 nm) of DXP was spin coated on top of ITO-PEDOT:PSS substrate. Spin coating was done from a chloroform solution (5.2 mg / mL) at 2000 rpm for 15 seconds with following drying on a heating plate at 50 °C.

Monte Carlo simulations of the bipolaron model

The simulations of the bipolaron model were performed for a one-dimensional chain of sites with periodic boundary conditions. Random hyperfine fields at these sites were drawn from a three-dimensional Gaussian distribution with standard deviation B_{hf}. Miller-Abrahams electron hopping rates were assumed between neighbouring sites[81], with the bipolaron formation energy U added in case of hopping to an already occupied site. Since the effect of hyperfine interactions is quenched when such a hopping event is fast (hopping frequency higher than the hyperfine precession frequency) we took the opposite limit of "slow hopping", where the Miller-Abrahams hopping rates can simply be multiplied with factors including projections of polaron-pair spin configurations onto the spin-singlet space in the case of bipolaron formation[36]. Is that was checked that the experimentally measured currents are compatible with the slow-hopping limit

Synthesis of PMI

The perylene monoimide PMI was synthesized and purified following a literature protocol[82].

Analysis was done by ^{1}H-NMR spectroscopy and mass spectrometry.

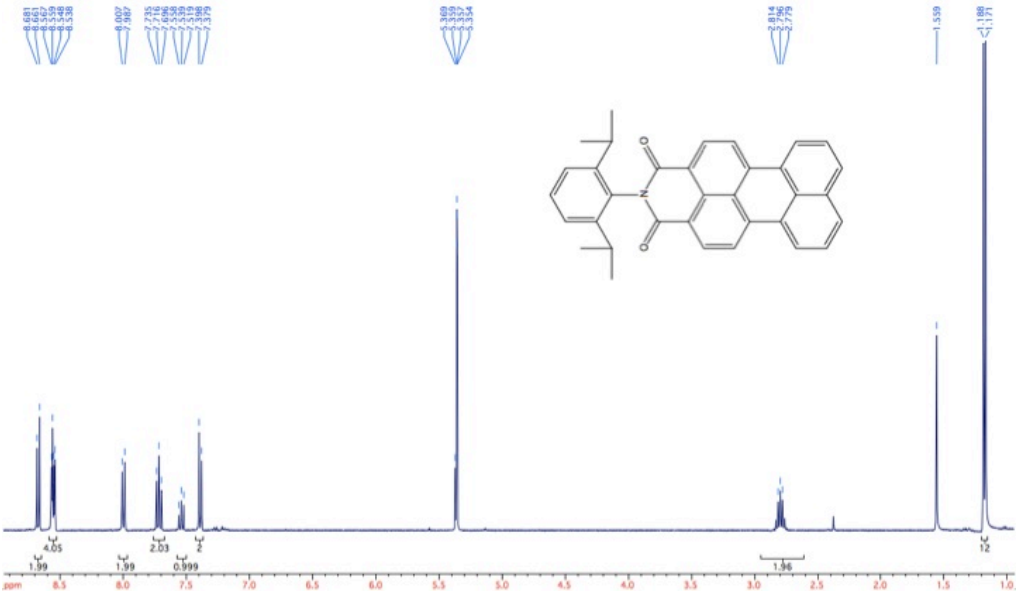

Figure 4.16. ^{1}H NMR spectrum of PMI in CD_2Cl_2.

^{1}H NMR (400 MHz, CD_2Cl_2): δ 8.67 (d, J = 8.1 Hz, 2H), 8.56 (d, J = 7.6 Hz, 2H), 8.54 (d J = 7.6 Hz, 2H), 7.99 (d, J = 8.1 Hz, 2H), 7.71 (t, J = 7.8 Hz, 2H), 7.54 (t, J = 7.8 Hz, 1H), 7.39 (d, J = 7.8 Hz, 2H), 2.80 (hept, J = 6.9 Hz, 2H), 1.18 (d, J = 6.9 Hz, 12H).
HRMS (ESI): m/z calc. for $C_{34}H_{27}NO_2$ [M+H]+ 482.2115; found 482.2121.

Instrumentation
All SEM measurements were carried out using a Zeiss 1540 EsB focused-ion-beam/field-emission microscope.
TGA: Netzsch STA 409 C/CD.
Spin coater: Specialty coating Systems Inc. Model P6700 Series.
UVO cleaner: Jelight Company Inc. Model No. 144AX.
UV/vis Spectrometer: Cary Varian 5000.

References

[1] Pilowski, P.M., Farnham, M.M.J., Fong, Angelina, Y. (Eds.), *Stimulation and Inhibition of Neurons*, Springer, **2013**.
[2] Bear, M.F., Connors, B.W., and Paradiso, M.A., *Neuroscience – Exploring the Brain*, Lippincott Williams & Wilkins, **2007**.
[3] Barker, A.T., Jalinous, R., and Freeston, I.L., *The Lancet*, **325**, 1106-1107, **1985**.
[4] Chambers, J. J., Kramer, R. H., in *Photosensitive Molecules for Controlling Biological Function Neuromethods*, *Springer Science + Business Media*, **2011**.
[5] Mayer, G., and Heckel, A., *Angew. Chem. Int. Ed*., **45**, 4900-4921, **2006**.
[6] Simon, D.T., Larsson, K.C., Berggren, M., and Richter-Dahlfors, A., *J. Biomedical Science and Engineering*, **3**, 208-217, **2010**.
[7] Bink, H., Lai, Y., Saudari, S.R., Helfer, B., Viventi, J., Van der Speigel, J., Litt, B., and Kagan, C., *Conf. Proc. IEEE Eng. Med. Biol. Soc*., 5400-5403, **2011**.
[8] Kawano, T., Harimoto, T., Ishihara, A., Takei, K., Kawashima, T., Usui, S., Ishida, M., *Biosens. Bioelectron*. **15**, 1809-1815, **2010**.
[9] Simon, D. T. et al., *Nat. Mater*., **8**, 742, **2009**.
[10] Bolin, M. H. et al., *Adv. Mater*., **21**, 4379, **2009**.
[11] Wan, A. M. D., Brooks, D. J., Gumus, A., Fischbach, C. Malliaras, G. G., *Chem. Commun*., 5278, **2009**.
[12] Gumus, A., Califano, J. P., Wan, A. M. D., Huynh, J, Reinhart-King, C. A., Malliaras, G. G., *Soft Matter*, **6**, 5138, **2010**.
[13] Abidian, M. R. et al., *Adv. Mater*., **21**, 3764, **2009**.
[14] Khodagholy, D. et al., *Adv. Mater*., **23**, 268, **2011**.
[15] Jimison, L. H. et al., *Adv. Mater*., **24**, 5919-5923, **2012**.
[16] Simon, D. et al., *J. Biomech. Sci. Eng*., **3**, 208-217, **2010**.
[17] Poghossian, A. et al., *Semin. Cell. Dev. Biol*., **20**, 41-48, **2009**.
[18] Offenhäusser, A., *Biosens. Bioelectron*., **12**, 819-826, **1997**.
[19] Fromherz, P., Offenhäusser, A., Vetter, T., Weis, J., *Science* **252**, 1290–1293, **1991**.
[20] Besl, B., Fromherz, P., *Eur. J. Neurosci*. **15**, 999–1005, **2002**.
[21] Voelker, M., Fromherz, P., *Small* **1**, 206–210, **2005**.
[22] Eickenscheidt, M., Jenkner, M., Thewes, R., Fromherz, P., Zeck, G., *J. Neurophysiol.* **107**, 2742–55, **2012**.
[23] Cohen-Karni, T., Timko, B. P., Weiss, L. E., Lieber, C. M., *Proc. Natl Acad. Sci. USA* **106**, 7309–7313, **2009**.
[24] Patolsky, F. et al., *Science* **313**, 1100–1104, **2006**.
[25] Duan, X. et al., *Nature Nanotech*. **7**, 174–179, **2012**.
[26] Voskerician, G. et al., *Biomaterials* **24**, 1959–1967, **2003**.
[27] Benfenati, V. et al. *Nature Mat*., **12**, 672-680, **2013**.
[28] Horowitz, G., *Adv. Mater*., **10**, 365-377, **1998**.
[29] Cramer, T. et al., *Phys. Chem. Chem. Phys*., **15**, 3897, **2013**.
[30] Benenfanti, V. *WO 2012089608 A1*, **2011**.
[31] Bystrenova, E. et al., *Adv. Funct. Mater*., **18**, 1751-1756, 2008.
[32] Toffanin, S. et al., *J. Mater. Chem. B*, **1**, 3850-3859, **2013**.

[33] Cramer, T. et al., *J. Mater. Chem. B*, **1**, 3728-3741, **2013**
[34] Bein, T., *Studies in Surface Science and Catalysis*, **102**, 295-322, **1996**.
[35] Cardin, D.J., *Adv. Mater.*, **14**, 553-563, **2002**.
[36] Simon, U., Franke, M.E., in *Host-Guest-Systems Based on Nanoporous Crystals*, Laeri, F., Schüth, F., Simon, U., Wark, M. (Eds.), (*Wiley*, **2003**), pp. 364-378.
[37] Alvaro, M., Cabeza, J.F., Fabuel, D., Garcia, H., Guijaro, E., and Martinez de Juan, J.M., *Chem. Mater.*, **18**, 26-33, **2006**.
[38] Anderson, P.A., Armstrong, A.R., Barker, P.D., Edmonson, M.J., Edwards, P.P., and Porch, A., *Dalton Trans.*, 3122-3128, **2004**.
[39] Anderson, P.A., Armstrong, A.R., Porch, A., Edwards, P.P., and Woodall, L.J., *J. Phys. Chem. B*, **101**, 9892-9900, **1997**.
[40] Wu, C.G., and Bein, T., *Science*, **266**, 1013-1015, **1994**.
[41] Wu, C.G., and Bein, T., *Science*, **264**, 1757-1759, **1994**.
[42] Thang, Z.K. et al., *Science*, **292**, 2462, **2001**.
[43] Lehmann, D., Zahn, D. R. T., *Appl. Phys. A*, **95**, 203-207, **2009**.
[44] Busby, M., Devaux, A., Blum, C., Subramaniam, V., Calzaferri, G., and De Cola, L., *J. Phys. Chem. C*, **115**, 5974-5988, **2011**.
[45] Margineanu, A. et al., *Biophys. J*. **93**, 2877–2891, **2007**.
[46] Zhao, Y. et al., *Luminescence* **24**, 140–143, **2009**.
[47] Megelski, S., Lieb, A., Pauchard, M., Drechsler, A., Glaus, S., Christina, D., Meixner, A.J., Calzaferri, G., *J. Phys. Chem. B*, **105**, 25-35, **2001**.
[48] El-Daly, S. A., *Spectrochimica Acta*, **55**, 143-152, **1999**.
[49] Busby, M., Devaux, A., Blum, C., Subramaniam, V., Calzaferri, G., and De Cola, L., *J. Phys. Chem. C*, **115**, 5974-5988, **2011**.
[50] A. M. Nardes et al., *Org. Electr*. **9**, 727, **2008**.
[51] H. Bentmann, A. A. Demkov, R. Gregory, S. Zollner, *Phys. Rev. B* **78**, 205302, **2008**.
[52] S. K. Lee et al., *J. Am Chem. Soc*. **121**, 3513, **1999**.
[53] M. N. Baibich et al., *Phys. Rev. Lett*. **61**, 2472, **1988**.
[54] G. Binasch, P. Grünberg, F. Saurenbach, W. Zinn, *Phys. Rev. B* **39**, 4828, **1989**.
[55] M. Jullière, *Phys. Lett*. **54**, 225, **1975**.
[56] J. S. Moodera, L. R. Kinder, T. M. Wong, R. Meservey, *Phys. Rev. Lett*. **74**, 3273, **1995**.
[57] W. Wagemans et al., *Spin* **1**, 93, **2011**.
[58] Xiong, Z.H., Wu, D., Vardeny, Z.V., and Shi, J., *Nature*, **427**, 821, **2004**.
[59] Dediu, V. et al., *Phys. Rev. B*, **78**, 115203, **2008**.
[60] Dediu, V.A., Hueso, L.E., Bergenti, I., and Taliani, C., *Nat. Mater.*, **8**, 707, **2009**.
[61] Yoo, J.W., Jang, H., Prigodin, V., Kao, C., Eom, C., and Epstein, A., *Synth. Met.*, **160**, 216, **2010**.

[62] Mermer, O., Veeraraghavan, G., Francis, T., Sheng, Y., Nguyen, D., Wohlgenannt, M., Kohler, A., Al-Suiti, M., and Khan, M., *Phys Rev. B*, **72**, 205202, **2005**.
[63] Prigodin, V., Bergeson, J., Lincoln, D., and Epstein, A., *Synth. Met*., **156**, 757, **2006**.
[64] Bloom, F.L., Wagemans, W., Kemerink, M., and Koopmans, B., *Phys. Rev. Lett*. **99**, 257201, **2007**.
[65] Bobbert, P.A., Nguyen, T.D., van Oost, F.W.A., Koopmans, B., and Wohlgenannt, M., *Phys. Rev. Lett*., **99**, 216801, **2007**.
[66] Desai, P., Shakya, P., Kreouzis, T., and Gillin, W.P., *J. Appl. Phys*. **102**, 073710, **2007**.
[67] Hu, B., and Wu, Y., *Nat. Mater*., **6**, 985, **2007**.
[68] Niedermeier, U., Vieth, M., Patzold, R., Sarfert, W., and von Seggern, H., *Appl. Phys. Lett*., **92**, 193309, **2008**.
[69] Wang, F.J., Baessler, H., and Vardeny, Z.V., *Phys. Rev. Lett*., **101**, 236805, **2008**.
[70] Nguyen, T.D., Hukic-Markosian, G., Wang, F., Wojcik, L., Li, X.-G., Ehrenfreund, E., and Vardeny, Z., *Nat. Mater*., **9**, 345, **2010**.
[71] Schulten, K., and Wolynes, P. G., *J. Chem. Phys*., **68**, 3292, **1978**.
[72] Francis, T., Mermer, O., Veerarghavan, G., and Wohlgenannt, M., *New. J. Phys*., **6**, 185, **2004**.
[73] Koopmans et al., *Phil. Trans. R. Soc*. A **369**, 3602-3616, **2011**.
[74] Ikeda, S. et al., *Appl. Phys. Lett*. **93**, 082508, **2008**.
[75] Gong, G. Q. et al., *Appl. Phys*. Lett. **6**7, 1783, **1995**.
[76] Siwach, P. K., Singh, H. K. & Srivastava, O. N., *J. Phys.: Condens. Matter* **20**, 273201, **2008**.
[77] Zhang, Y. T., Chen, Z. Y., Wang, C. C., Qiu, J. & Lu, H. B., *J. Magn. Magn. Mater*. **321**, 1199, **2009**.
[78] Yue, F. J., *J. Phys. D: Appl. Phys*. **44**, 025001, **2011**.
[79] Bai, J. et al., *Nature Nanotech*. **5**, 655-659, **2010**.
[80] Lee, S. K. et al., *J. Am Chem. Soc*. **121**, 3513-3520, **1999**.
[81] A. Miller, E. Abrahams, *Phys. Rev*. **120**, 745, **1960**.
[82] Koenemann, M., Blaschka, P., Reichelt, H., Verfahren zur Herstellung von Perylen-3,4-dicarbonsäureimiden, *DE102004054303*, *US2008114170 (A1)*.

Self-assembly from the gas phase – A new facile way towards highly ordered structures

Abstract

This chapter describes a rather unexplored way of self-assembling functional organic molecules, perylene monoimide derivatives – by a direct self-assembly from the gas phase. A series of perylene monoimides has been synthesized and their self-assembly from solution and gas phase was studied. The assembled systems present a morphology that is dependent on the nature of the functionalization introduced on the nitrogen and on the conditions the self–assembly has been performed (drop cast vs sublimation).

5.1. Introduction

The assembly of perylene diimides and perylene monoimides into one-dimensional wires in the pores of zeolite-L has been discussed in the previous chapter. Indeed, during the sublimation of the perylene derivative for the insertion in the channels of the zeolites, we noticed an interesting morphology for the different compounds. Therefore we decided to investigate in more details how the formation of organized and well-oriented one-dimensional structures from perylene monoimides occurs.

This project has been carried out in collaboration with my colleague Dr. Eko Adi Prasetyanto from the University of Strasbourg.

"*Beyond molecular chemistry based on the covalent bond there lies the field of supramolecular chemistry, whose goal it is to gain control over the intermolecular bond*"
Jean-Marie Lehn, Nobel laureate 1987

Supramolecular chemistry is an interdisciplinary field, which combines elements of organic-, inorganic-, coordination-, physical- and biochemistry with the goal to understand and control intermolecular weak interactions[1, 2, 3, 4].
Supramolecular chemistry uses weak and reversible interactions between molecules, like hydrogen bonds, hydrophobic interactions, van der Waals forces, pi-pi interactions or electrostatic interactions, to form large molecular systems or materials from a bottom-up approach, often inspired from biological systems and processes in nature.
However the term supramolecular chemistry was coined in the 1970's, the origin of supramolecular chemistry dates back to the postulation of intermolecular forces by Johannes Diderik van der Waals in 1873 or the introduction of the "lock and key" principle by Herman Emil Fischer in 1894[5].
The great importance of supramolecular chemistry was finally awarded with the Nobel Prize for Chemistry to Jean-Marie Lehn, Donald J. Cram and Charles J. Pedersen in 1987.

One of the key-concepts of supramolecular chemistry is **molecular self-assembly**, a process by which molecules assemble themselves into larger structures by building non-covalent weak interactions between them. Molecular self-assembly is not just a laboratory tool - you are actually reading this sentence by using millions of self-assembled structures: The lipid bilayer membranes that encapsulate your cells in your eyes and your brain, the cytoskeletal lattice that supports them or the formation of your DNA double helix, all formed by molecular self-assembly. Other very prominent examples are the assembly of small surfactant molecules into micelles[6], vesicles[7, 8], liposomes[7, 8] or lipid bilayers[7, 8].

Self-assembly is nowadays used as a key-aspect in modern nanotechnology, where it is applied to form large nanostructures from single molecules and their functions is not the sum of each component[9, 10]. Indeed, the emerging properties of the assemblies are often very different from those of the units and can show cooperative effects as well processes (conductivity, charge transport, energy transfer…) not present when the components are isolated.

A variety of different approaches to self-assemble small molecules into larger structures has been developed over the last decades and the majority of them use solution-based methods, where all the components are dissolved in an appropriate solvent and assembly takes place directly in solution[10, 11, 12].

A slightly younger field of research is the molecular self-assembly of molecules at solid surfaces, where also mostly solution-based approaches are used[9, 13].

One research field, where self-assembly at surfaces is thought to have a great impact, is the field of organic electronics with the final goal to adapt nature's methods to build circuits or other electronic devices directly from small molecules from solution[14]. Devices built in this way should be more robust, cheaper, easier to produce, and more reproducible than devices fabricated from a top-down approach.

Famous areas in which organic electronic devices are strongly sought-after are photovoltaics, optoelectronics or fuel cells, which mostly require highly organized one-dimensional structures built up from organic semiconductors[15, 16].

Organic solar cells operate following a cascade process. First, photon absorption in the active layer results in the formation of excitons, which then migrate to a donor/acceptor interface. Charge separation then occurs and the holes and electrons are transported by the matrix to the electrodes. Considering all these processes, the donor/acceptor morphology is of crucial importance. First, for exciton diffusion (5-20 nm) and second, for efficient transport of charge carriers, where well-interconnected domains of donors and acceptors creating percolating networks need to be formed.

The morphology of the assembled organic semiconductors has been shown to be especially important for organic photovoltaics and bulk-heterounction solar cells in detail[17], where controlling the morphology at the nanoscale donor and acceptor blend has been one of the dominate research areas during the last years[18, 19].

However, the ideal morphology of a bulk-hetrojunction solar cell has not been achieved so far by reported methods. A very fine dispersion of the donor in the acceptor will cause a very efficient charge generation but poor charge transport (See figure 5.1A). On the other hand arranging the donor and acceptor in a bilayer stack will lead to a very efficient charge transport, but to a very poor charge generation (See figure 5.1B). Calculations and simulations suggest an ideal morphology as shown in figure 5.1C. The highly ordered do-

nor and acceptor domains will lead to efficient generation and charge transport[20].
However, this structure is very difficult to achieve in practice, finding “real” bulk hetrojunctions with cross sections like the one shown in figure 5.1D. A detailed review about nano-morphologies in organic photovoltaics can be found elsewhere[21].

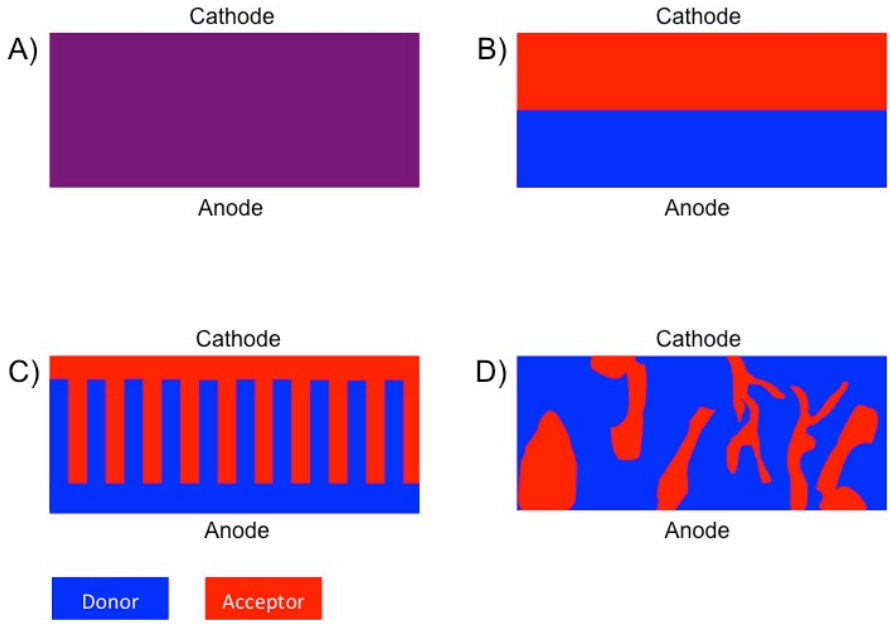

Figure 5.1. Schematic cross section of different nanomorphologies of bulk heterojunctions. A) Fine mixture of donors and acceptors; B) Bilayer arrangement; C) Calculated ideal morphology; D) Typical morphology of a solution processed device.

Due to their excellent optical properties, including large absorption coefficients and high luminescence quantum yields, and semiconducting nature, perylene imides are a widely studied class of organic semiconductors for applications in organic photovoltaics and in particular for bulk heterojunction solar cells or dye-sensitized solar cells[22, 23, 24, 25,] . Additionally they are among the most stable class of organic molecules, which makes them very suitable for practical applications[26, 27].
Perylene Imides can be further divided into perylene monoimides (PMIs) and perylene diimides (PDIs), which general structures are shown in figure 5.2.

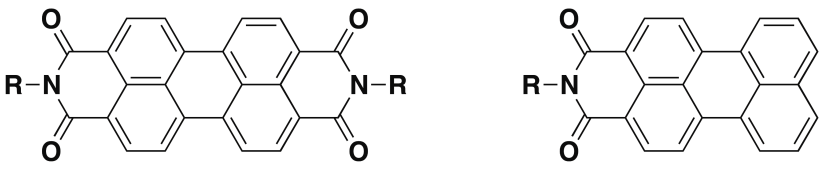

Figure 5.2. Basic structures of perylene diimides (left) and perylene monoimides (right).
Due to the large flat π-system leading to strong π-π interactions, they both show great affinity to self-assemble in solution or solid state. Compared to perylene diimides, perylene monoimides are less symmetrical, but show simi-

lar π-stacking behavior[28], [29]. However, whilst perylene diimides are widely studied in this respect[30, 31, 32, 33, 34, 35, 36, 37, 38, 39, 40, 41, 42, 43, 44, 45, 46, 47, 48, 49, 50, 51, 52], the self-assembly of perylene monoimides is rarely studied[53, 54, 55].
Other reasons why perylene diimides are much more studied than perylene monoimed are their higher tendency to self-assemble due to their high symmetry and their much higher absorption coefficients[20].
Nevertheless, the challenge of using perylene monoimides for organic photovoltaics was faced and a few examples can be found in the literature[20, 56, 57, 58, 59, 60, 61, 62, 63].
Interestingly, it has been found that the substituents in the imide structure of perylene diimides have a great influence on the self-assembly and film morphology[64]. Analogously differently substituted perylene monoimides, could lead to assemblies of different morphologies and properties.

This study is the first report of the self-assembly of perylene monoimides into large and oriented structures.
Three slightly different perylene monoimides have been synthesized, characterized and self-assembled via 2 different approaches: 1) from solution by using the drop-casting method (See figure 5.5A); 2) directly from the gas phase without using any solvents (See figure 5.5B).

5.2. Synthesis and characterization of the perylene monoimides

The perylene monoimides (PMI-1, PMI-2 and PMI-3), which have been used for this project are shown in figure 5.3.

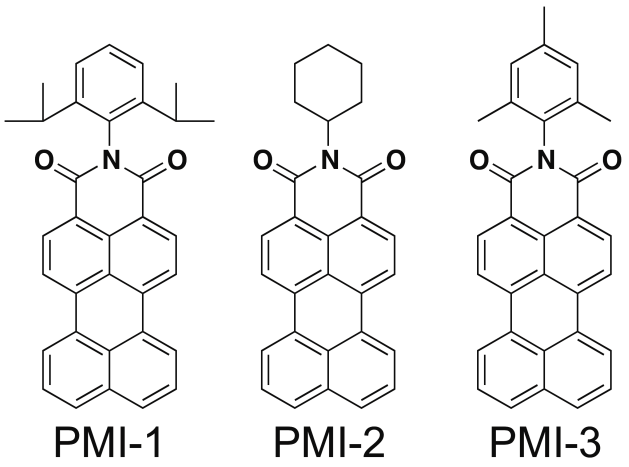

Figure 5.3. Molecular structures of the three perylene monoimides used in this study

Perylene monoimides PMI-1, PMI-2 and PMI-3 were designed so the only modification was at the head group. All head groups consist of six-membered rings, two of which are aromatic and one is a cyclohexane ring. The aromatic head groups are further functionalized with methyl- or with bulkier diisopropyl

substituents. In detail, PMI-1 was functionalized with a 2,6 diisopropylphenyl group, PMI-2 was functionalized with a cyclohexyl group and PMI-3 was functionalized with a 2,4,6-trimethylphenyl headgroup. This allowed us to study how these steric and electronic differences influence the self-assembly.
The synthesis of PMI-1 is shown in chapter 4. PMI-2 was commercially received from ChemPoint.
PMI-3 was synthesized and purified following a standard literature protocol[65]. The reaction conditions are illustrated in scheme 5.1.

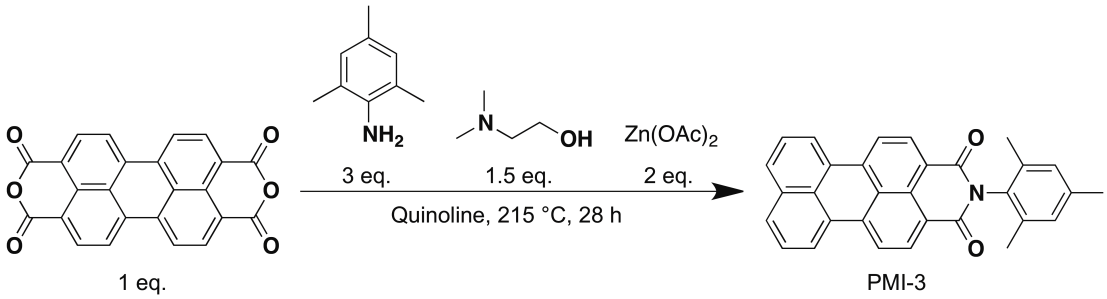

Scheme 5.1. Synthesis scheme for the preparation of PMI-3

The compounds have been characterized by ^{1}H NMR spectroscopy and mass spectrometry. The results are shown in the experimental part of chapter 4 (for PMI-1) and in the experimental part at the end of this chapter (PMI-2 and PMI-3). They have been crystallized from dichloromethane/hexane (PMI-1 and PMI-3) or from dichloromethane/chloroform/hexane (PMI-2). Their structures are shown and discussed below.

5.3 Solution vs. gas phase self-assembly.

The self-assembly of PMI-1, PMI-2, and PMI-3 was studied from solution and directly from gas phase using a custom made experimental setup. The different approaches are depicted in figure 5.4.

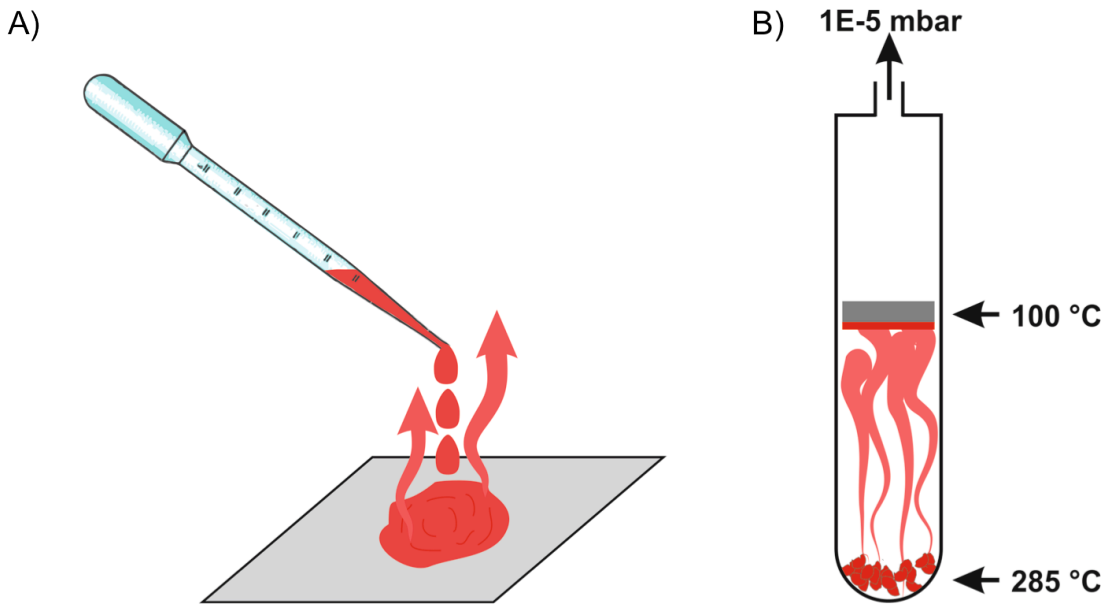

Figure 5.4. Schematic representation of 2 different approaches to self-assemble PMI-1, PMI-2 and PMI-3. A) Self-assembly from solution. B) Self-assembly from the gas phase.

5.3.1. Morphology of the self-assemblies from solution

Self-assembly from solution is done by drop-casting and evaporating the solvent at room temperature (Figure 5.5A). The PMIs were therefore dissolved in dichloromethane (0.1 mg / mL) and the solution was dropped on a glass slide or gold substrate. After solvent evaporation, the self-assembled structures were characterized by using scanning electron microscopy (SEM).

Depending on the head group, different self-assembled structures were obtained. The driving force for the assembly is believed to be a very efficient π-π interaction caused by the large and planar π system of the molecules, which is also supported by the crystal packing as shown in chapter 5.5.

In the following paragraph, the self-assembled structures obtained from drop casting will be described.

PMI-1 assembles into plate-like structures, which are mostly oriented parallel to each other. The plates are 11.5 x 7 µm in size with a thickness of 0.2 to 0.5 µm. The plates show a random orientation versus the glass or gold surface without long-range order (See figure 5.6, top row).

PMI-2 forms rose-blossom-like structures built up from plates. The structures have a size of 6 to 7 µm.

PMI-3 self-assembles into very long fibers with a wide size distribution and lengths from just a few µm up to 150 µm (See figure 5.5 bottom). The fibers do not show any long-range orientation and a representative description is very difficult due to the very broad size distribution.

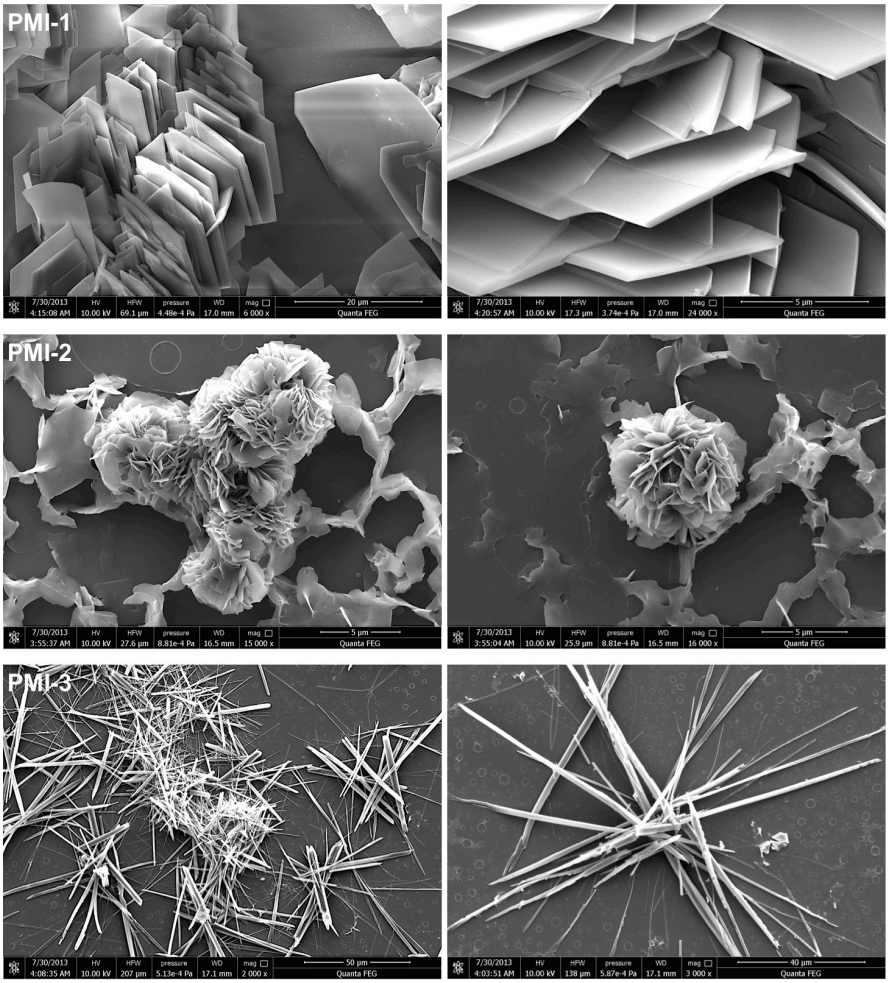

Figure 5.5. Self-assembly from solution. Top: self-assembled structures of PMI-1. Middle: self-assembled structures of PMI-2. Bottom: self-assembled structures of PMI-3.

5.3.2. Morphology of the self-assemblies from the gas phase

The sublimation temperature of each compound was determined by thermogravimetry (figure 5.6) to be approximately 250 °C at 1E-05 mbar. Therefore we have decided to perform the sublimation to obtain the assembled structures on a substrate at 285 °C.

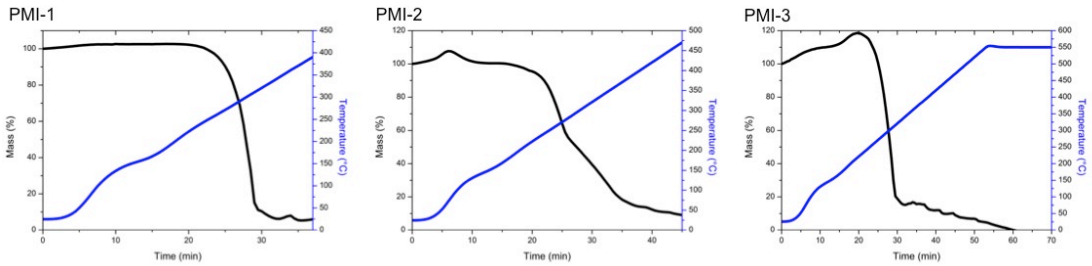

Figure 5.6. Thermogravimetric analysis to determine the sublimation temperature of each compound at 1E-5 mbar.

The experimental setup for the self-assembly from the gas phase onto a substrate is shown in figure 5.4B.

The compounds (about 7 mg) were filled into a glass tube and a substrate (gold or glass) was placed upside down about 5 cm above the bottom of the glass tube. The tube was then evacuated to about 1E-05 mbar and the bottom of the tube was heated to 285 °C, resulting in the sublimation of the compound. The substrate was not cooled externally during the sublimation process. The natural temperature gradient leads to a substrate temperature of 100 °C, which was determined by placing a thermometer at the same position of the substrate (5 cm above the bottom) and recording the temperature after stabilization. The compounds finally condense at the tube walls and the substrate, which leads to a very homogeneous coating of the surface. Assembly was done for 2 hours (PMI-1) or over night (PMI-2 and PMI-3).
After sublimation, the tube was slowly cooled to room temperature and the substrate was carefully removed.

The sublimation onto the substrate (gold or glass) leads to a homogeneous coating, as can be seen by the naked eye (figure 5.7).

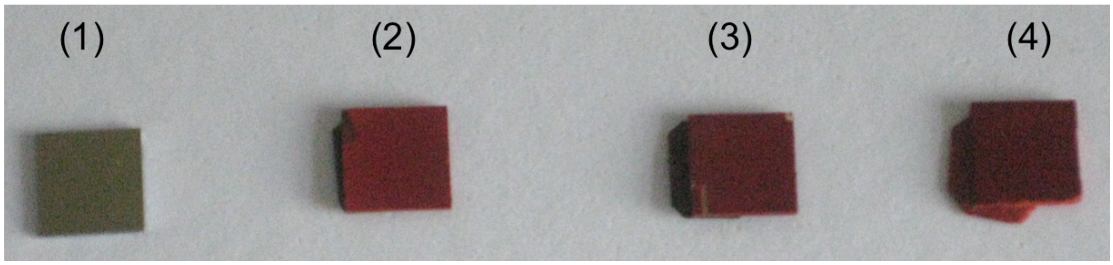

Figure 5.7. Photograph of gold surfaces coated with different perylene monoimides from the gas phase. (1): Blank gold substrate; (2) PMI-1; (3) PMI-2; (4) PMI-3

The morphology of the self-assembled structures was analyzed by using SEM after either removing the organic layer from the substrate, for compound PMI-1 or analyzing the morphology in the presence of the surface (PMI-2 and PMI-3). Figure 5.8 shows the results for PMI-1. The compound assembles into one-dimensional structures oriented with their long axis perpendicular to the substrate. The layer which was anchored to the substrate show is flat and compact for few nm and then some pillars can be observed having a diameter of about 1 µm and a height of roughly 9 µm. From these fibers can be noted a bigger plate (2.7 x 2.7 µm) located at the top. The assemblies are distributed homogenously over the whole substrate and show a parallel orientation with respect to each other.
Figure 5.9 shows the structures forming from PMI-2.
One-dimensional structures oriented with their long axis perpendicular to the substrates are obtained. PMI-2 forms cylindrical highly and monodisperse rod-like assemblies with a length of approximately 10 µm and a diameter of 1 µm. Different magnification confirms (Fig. 5.9 top right) that the fibers are not interconnected. The images of a single fiber removed from the substrate reveal,

dispersed in water and drop casted onto a glass substrate, (bottom left and bottom right of figure 5.9) reveal an interesting substructure.
Figure 5.10 shows the self-assembled structures obtained from PMI-3.
The structures are similar to the ones observed from PMI1. The molecules assemble into long blade-like structures growing perpendicular to the substrate. Each blade has a size of 20 x 1,5 µm and they are growing in high density over the whole surface of the substrates.

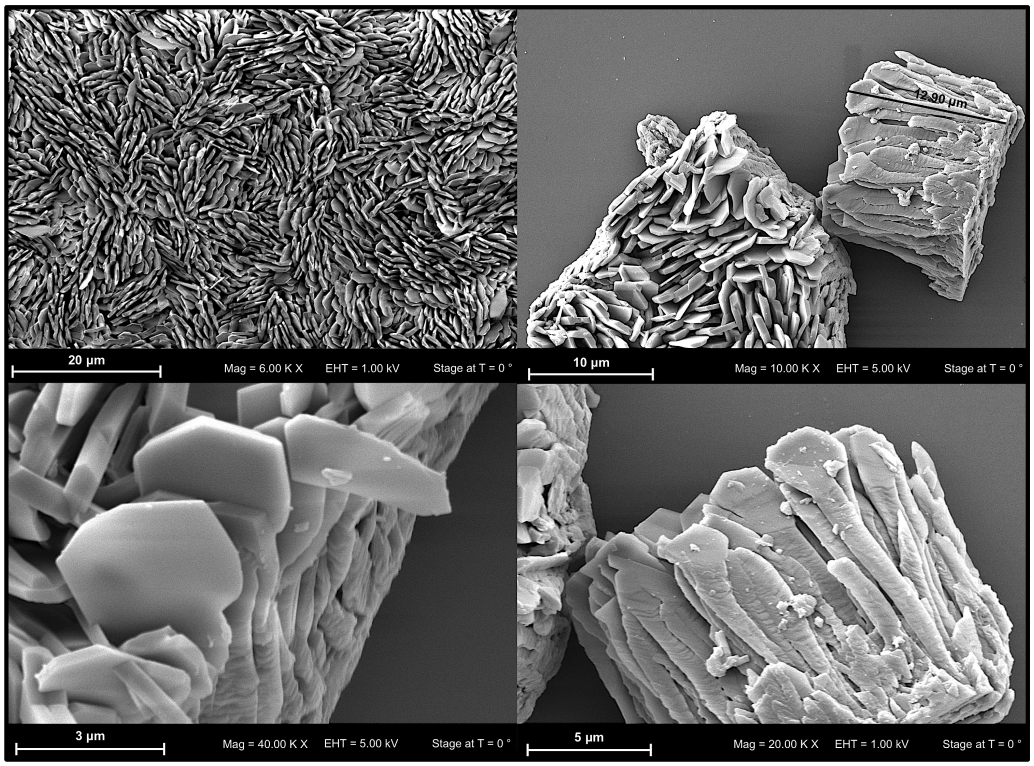

Figure 5.8. Self-assembled structures obtained by sublimation of PMI-1.

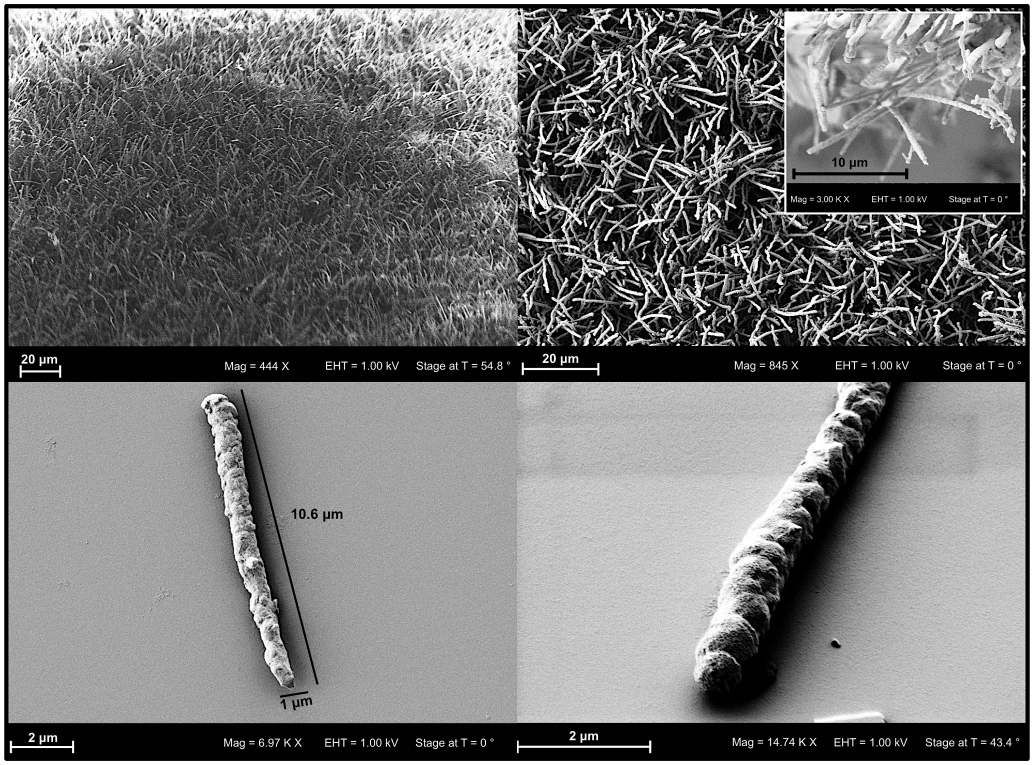

Figure 5.9. Self-assembled structures obtained by sublimation of PMI-2.

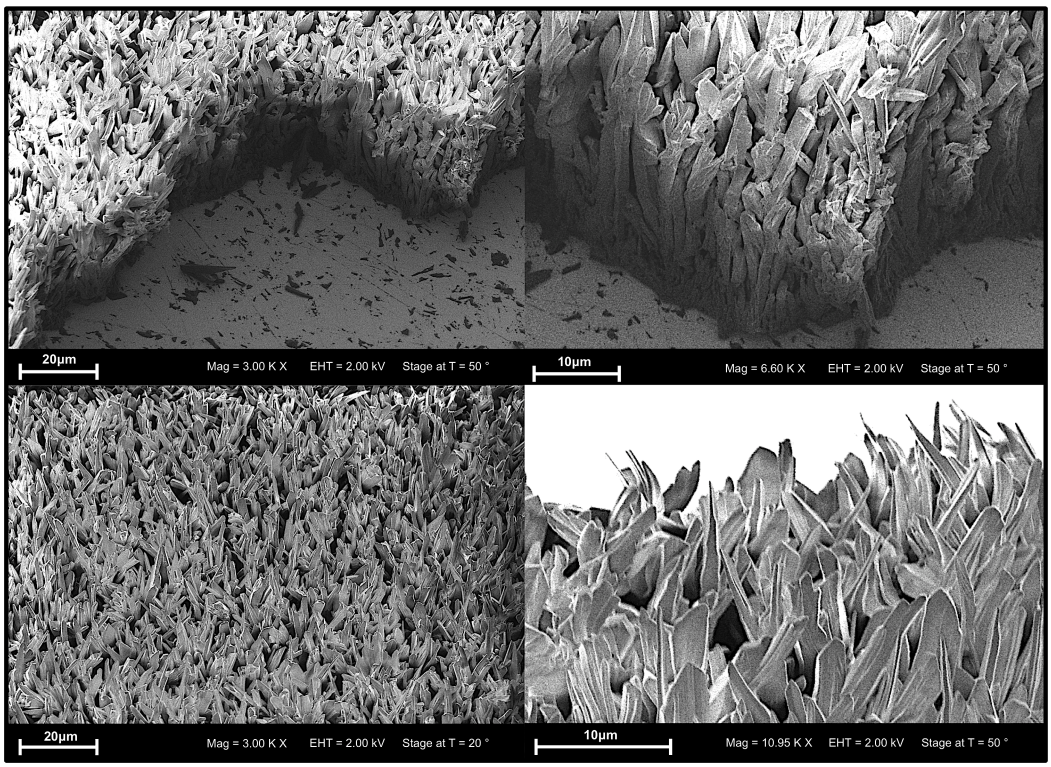

Figure 5.10. Self-assembled structures obtained by sublimation of PMI-3.

In a next step the influence of self-assembly on the photophysical properties of the PMIs was investigated.

5.4. Photophysics in solution and in different solid-state morphologies

The absorption spectra of PMI-1, PMI-2, and PMI-3 in dichloromethane (DCM) and solid state are shown in figure 5.11 – 5.13.

In DCM solution, all compounds absorb between 400 nm and 550 nm consisting of two vibronic transitions, which is in accordance to previously reported results for PMIs[66, 67, 68]. They show intense bands with extinction coefficients ranging from 23,000 M^{-1} cm^{-1} (PMI3) to 35,000 M^{-1} cm^{-1} (PMI1 and PMI2) at 485 nm ((1,0) transition). A second intense transition is present at 507 nm and can be ascribed to a (0,0) transition. A small shoulder is present at 455 nm, which is due to a strong π-π stacking and the formation of H-aggregates even in diluted solution.

All compounds show broadened absorption spectra ranging from 400 nm to 650 nm in the solid state, independent of the substrate used, the assemble technique (from solution or gas phase) or the morphology of the solid.

The vibronic structure of the bands is not resolved in solid state. The absorption maximum in solid state matches with the maximum in solution (PMI-1 and PMI-2) or is slightly blue shifted (PMI-3). Interestingly the solid state spectra show very broad and also red shifted bands which is typically a sign of the effective π-π-interaction in co-facial configuration of molecular stacking[69, 70, 71, 72] and the formation of J-aggregates[73, 74].

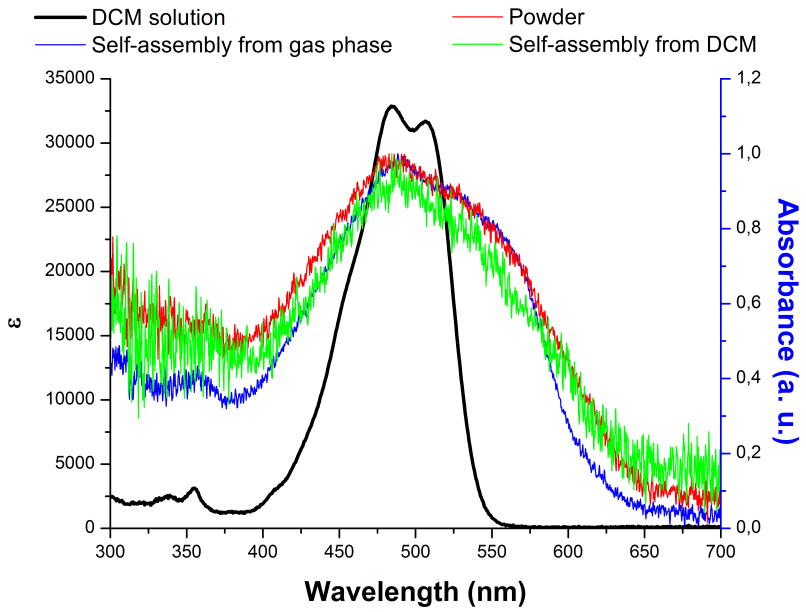

Figure 5.11. Absorption of PMI-1 in DCM solution [6.0E-6 M] (black) and in different solid-state morphologies (red, green and blue)

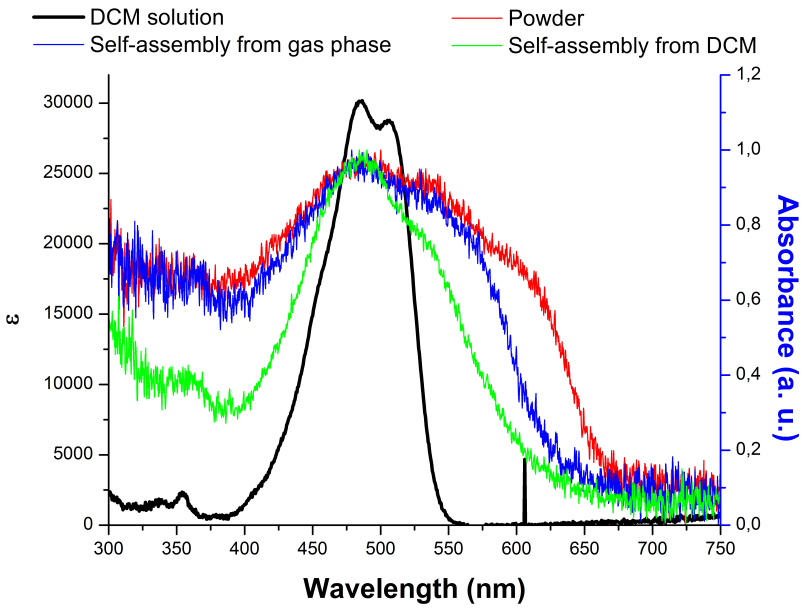

Figure 5.12. Absorption of PMI-2 in DCM solution [3.1E-6 M] (black) and in different solid-state morphologies (red, green and blue)

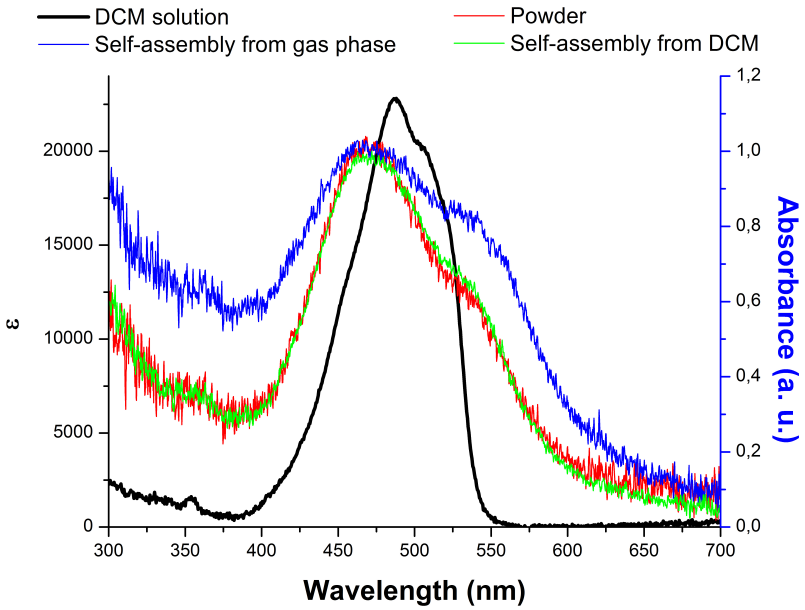

Figure 5.13. Absorption of PMI-3 in DCM solution [2.7E-6 M] (black) and in different solid-state morphologies (red, green and blue)

The fluorescence spectra of the compounds in DCM solution and in different solid-state morphologies are depicted in figures 5.15 – 5.17.
In DCM solution, all compounds show green emission with broad bands ranging from 500 to 700 nm, and λ_{max} at 544 nm, for PMI-1 and PMI-2, and at 534 nm for PMI-3. The maximum can be assigned to a (0,0) transition. A second band ((0,1) transition) can be monitored at 584 nm, for PMI1 and PMI2, and at 574 nm for PMI3. The emission spectra show a weak shoulder at 630 nm, for PMI1 and PMI2, and at 622 nm, for PMI3, which is due to a (0,2) transition.[61, 62, 63]

All compounds show red-shifted emission in solid state due to a strong π-π stacking and the formation of aggregates[63], which will be further discussed in the next paragraph. In the case of PMI-2 and PMI-3, the emission maxima of the different solid-state morphologies (powder, solution and gas phase assemblies) are all located around 700 nm and are shifted by just a few nanometers compared to each other. These compounds do not show any monomer emission in solid state.

The situation in solid state is slightly different for the self-assembled structures formed by sublimation of PMI-1 (blue line in figure 5.15). Additionally to the intense aggregate emission, weak bands at 524 and 562 nm are observed, which is most likely due to monomer emission.

Different to PMI-2 and PMI-3, the self-assembled structures from DCM solution of compound PMI-1 show a blue-shifted emission (630 nm) compared to its other solid-state morphologies.

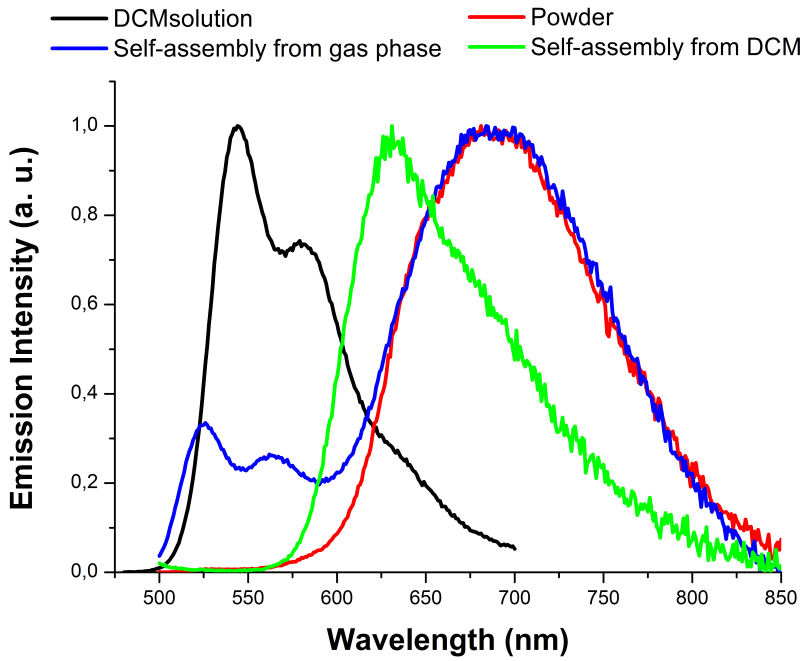

Figure 5.15. Emission spectra of PMI-1 in DCM solution (black) and in different solid-state morphologies (red, green and blue). λ_{exc} (DCM solution) = 470nm. λ_{exc} (solid state) = 460 nm.

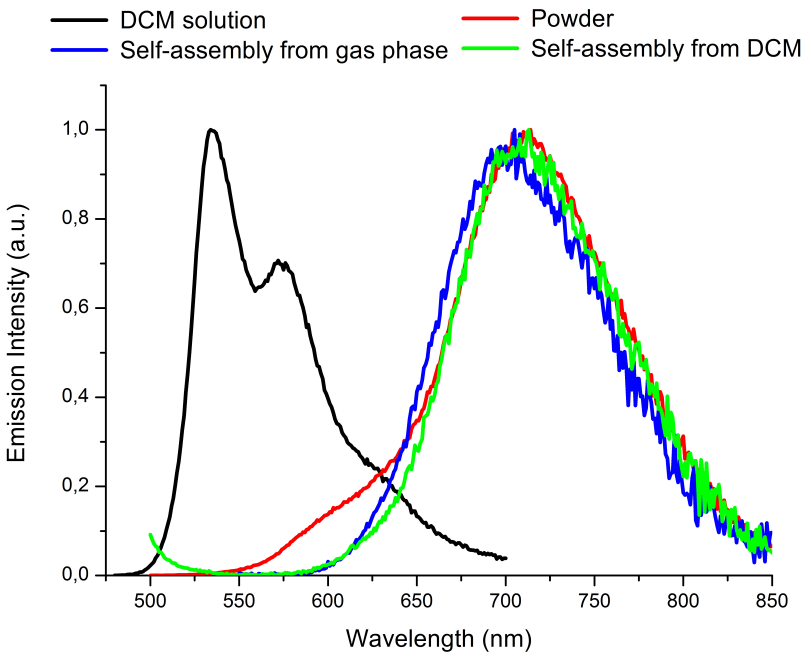

Figure 5.16. Emission spectra of PMI-2 in DCM solution (black) and in different solid-state morphologies (red, green and blue). λ_{exc} (DCM solution) = 470nm. λ_{exc} (solid state) = 460 nm.

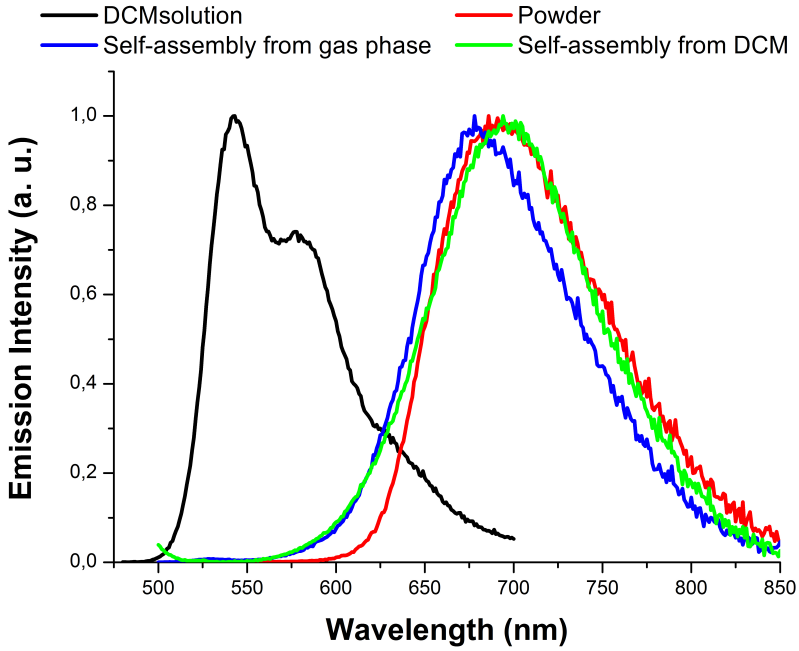

Figure 5.17. Emission spectra of PMI-3 in DCM solution (black) and in different solid-state morphologies (red, green and blue). λ_{exc} (DCM solution) = 470nm. λ_{exc} (solid state) = 460 nm.

5.5. Packing of PMI-1, PMI-2 an PMI-3

The packing of the perylene monoimides in the different morphologies was determined by using single-crystal x-ray diffractometry, small-angle x-ray scattering (SAXS) and wide-angle x-ray scattering (WAXS).

Single-crystal x-ray diffractrometry was used to obtain a benchmark structure of the packing of all compounds. As described above, the compounds were

crystallized from dichloromethane/hexane (PMI-1 and PMI-3) or dichloromethane/chloroform/hexane by diffusion method.
Strong π-π-interactions are obtained for all compounds as illustrated by the short intermolecular distance around 3.5 Å (See figures 5.18, 5.20 and 5.22). They tend to form dimers that are oriented head-to-tail to each other (figures 5.18, 5.20 and 5.22), to avoid steric interactions between the bulky head-groups.
In detail, PMI-1 forms aggregates with a π-π-distance 3.514 Å. The dimers are then stacked into columns with a distance of 3.415 Å between the dimers (figure 5.18) and the columns are oriented parallel to each other, as shown in figure 5.19.

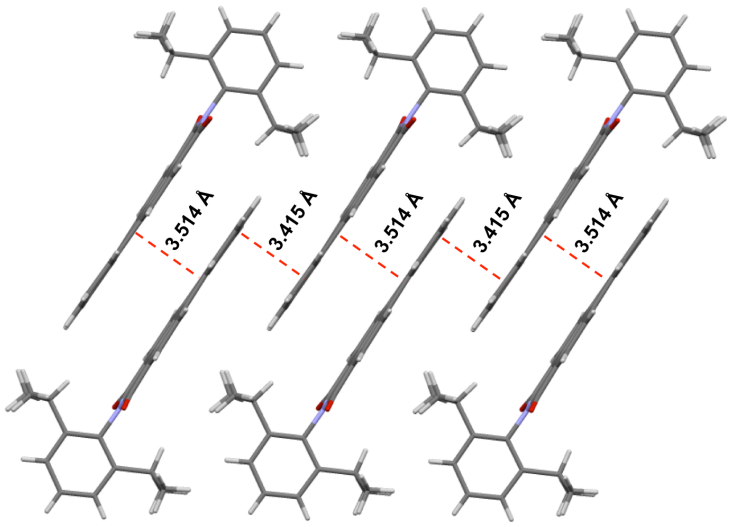

Figure 5.18. Columnar packing of PMI-1. Two molecules are forming π-stacked pair, which orient themselves into columns of parallel molecule pairs. Solvent molecules are removed for clarity.

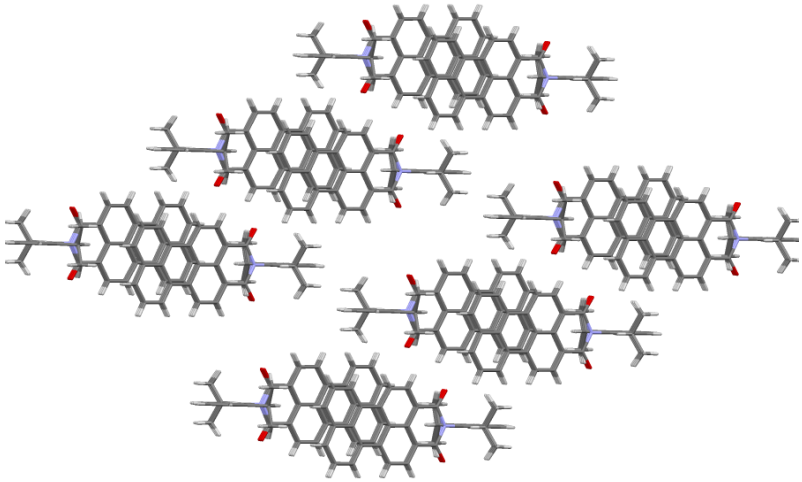

Figure 5.19. PMI-1 parallel packing of the columns (Top view). Solvent molecules are removed for clarity.

Also PMI-2 assembles into π-stacked dimers with a shorter π-π distance of 3.390 Å, compared with the previous case, as shown in figure 5.20. The dimers are then oriented orthogonally to the next pair so that every second dimer is oriented parallel to each other, as shown in figure 5.21.

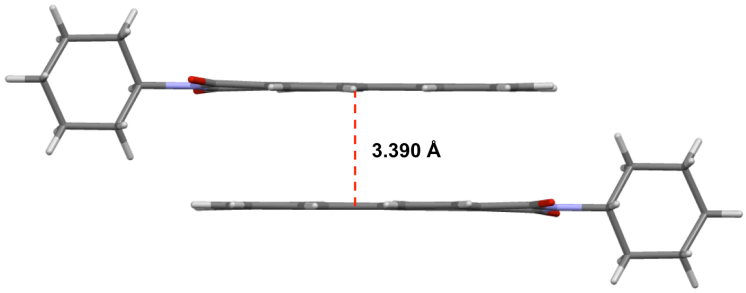

Figure 5.20. Two PMI-2 molecules forming a π-stacked molecule pair with a π-π distance of 3.390 Å. Solvent molecules are removed for clarity.

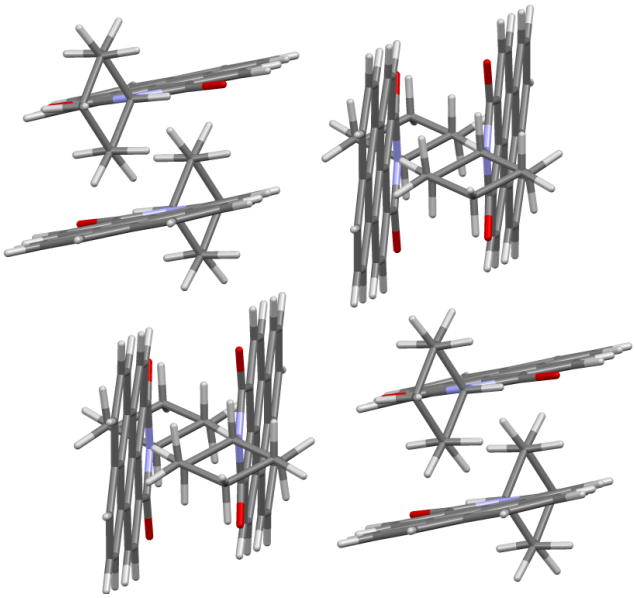

Figure 5.21. Adjacent pairs are oriented perpendicular to each other. Solvent molecules are removed for clarity.

In analogy to PMI-1 and PMI-2, also PMI-3 assembles into π-stacked dimers. The intermolecular π-π distance is 3.473 Å within the dimer and 3.394 Å between adjacent dimers as shown in figure 5.22. Similar to PMI-1, the pairs assemble into columnar structures as shown in figure 5.23.

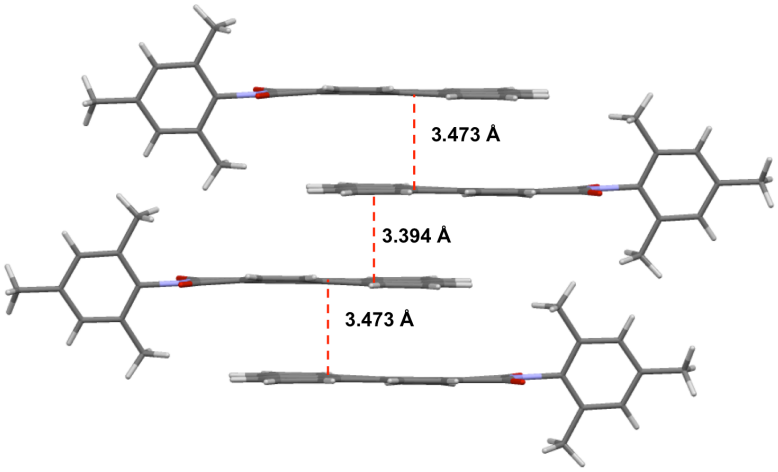

Figure 5.22. Assembly of PMI-3 into π-stacked pairs assembling into columnar structures. Solvent molecules are removed for clarity.

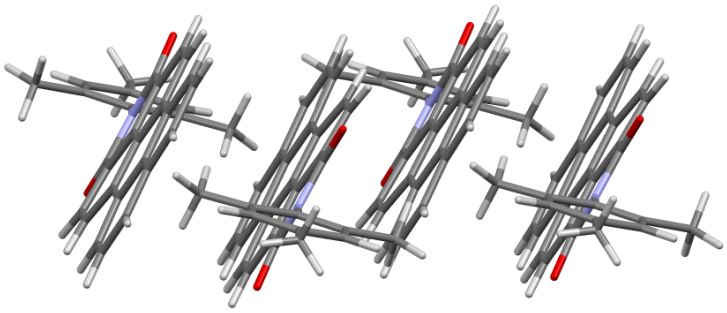

Figure 5.23. Different view on the columnar structures. Solvent molecules are removed for clarity.

The packing in the self-assembled structured from DCM and from the gas phase was then obtained by using SAXS and WAXS.
For clarity, the self-assembled structures from the gas phase will be denoted by “g” and the ones obtained from DCM solution will be denoted by an “s” (e.g. gas phase assembly from PMI-1 = PMI-1g).

PMI-1s shows the same intermolecular distances of 3.415 and 3.514 Å as obtained from single-crystal x-ray and we therefore conclude the same or very similar packing compared to that obtained in single crystals (see figure 5.24 green line).
The WAXS pattern of PMI-1g shows just one peak at 3.53 Å, which indicates slightly larger π-π distances compared to the single crystals or PMI-1s. This loosened packing is also believed to be the reason for the presence of the weak monomer emission for PMI-1g (figure 5.24 red line).

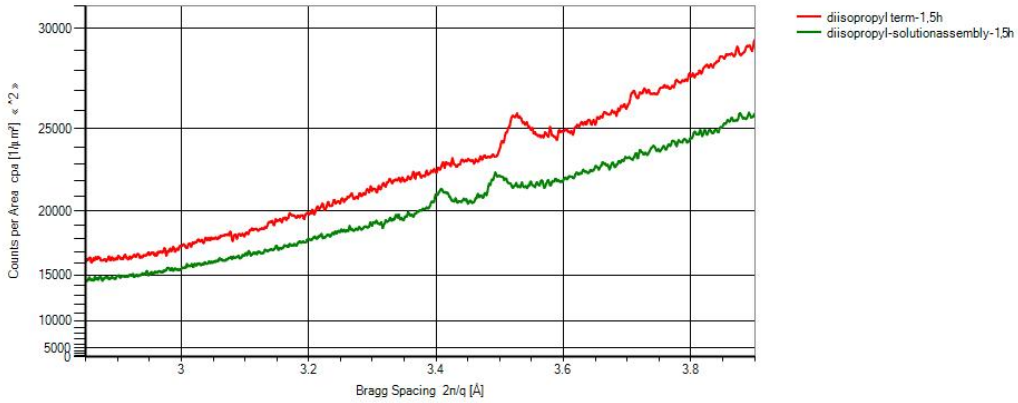

Figure 5.26. WAXS patterns of PMI-1. Red line: PMI-1g. Green line: PMI-1s.

The WAXS pattern of PMI-2s shows a single peak at 3.48 Å, which points in the direction of just one π-π-stacking motif being present. This is in accordance with the single-crystal packing, where just one π-π-stacking motif can be found. As described before, adjacent dimers are oriented perpendicular to each other preventing π-π-stacking between them (figure 5.21). The π-π distance is slightly larger, which could be due to the shorter time available for the molecules to self-assemble compared to the very slow crystallization process. Additionally, compared to PMI-1 and PMI-3, PMI-2 is substituted with the relatively floppy cyclohexyl head group, which can easily rearrange at elevated temperatures as used for the gas phase assembly.
The WAXS pattern of PMI-2g shows two intense peaks at 3.33 and 3.52 Å. We conclude that this is due to a second π-π-stacking motif present in the assemblies of PMI-2g, but detailed investigations to understand the packing are ongoing.

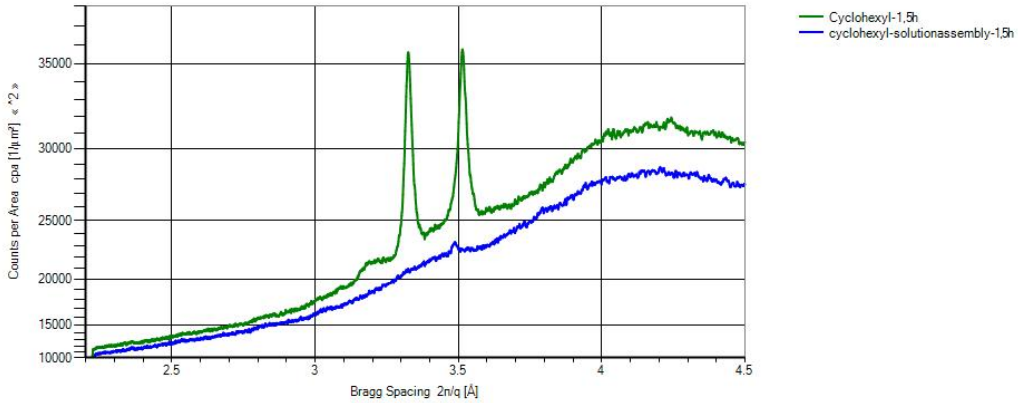

Figure 5.27. WAXS patterns of PMI-2. Green line: PMI-2g, blue line: PMI-2s.

The WAXS patterns of PMI-3s and PMI-3g are very similar to each other. We conclude, that this compound shows very similar packing when assembled from DCM solution or from the gas phase. Further investigations to reveal the packing are ongoing.

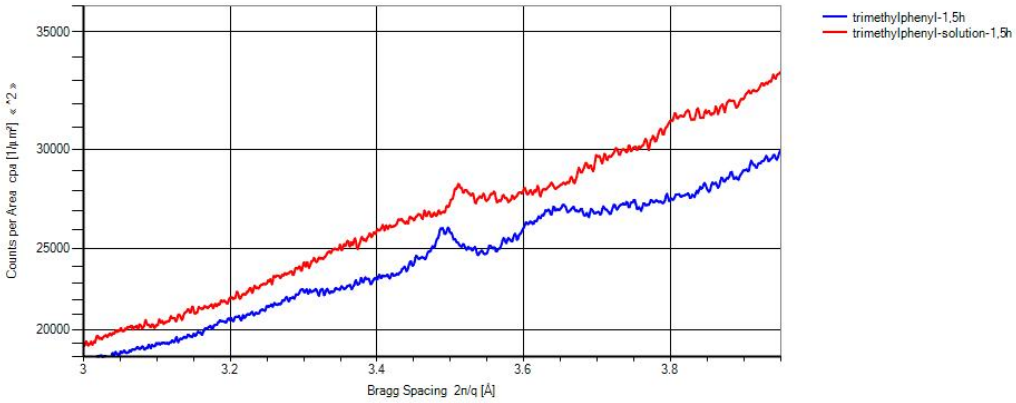

Figure 5.27. WAXS patterns of PMI-3. Red line: PMI-3s. Blue line: PMI-3g

Unfortunately the SAXS patterns of the compounds do not give significant information about the packing due to the fact that all compounds form assemblies in the micrometer range, which is not applicable for SAXS analysis. The SAXS pattern is shown in the experimental part at the end of this chapter.

5.6. Conclusion

In summary we presented a rather new way to easily self-assemble molecules into highly ordered structures. The presented compounds form one-dimensional structures oriented perpendicular to the substrate that are aspired for applications in organic photovoltaics and bulk heterojunction solar cells in detail. Interestingly, the size and shape of the assemblies can be fine-tuned by just modifying the head group, which does not alter the electronic structure of the perylene monoimides.

In a next step, further experiments to understand and eventually predict the structures of the forming assemblies will be performed.

In order to apply these structures in bulk hetrojunction solar cells, the diameter of the assemblies can be reduced to just a few tenths of nanometers, so that very efficient exciton diffusion to the donor-acceptor interface assured.

5.7. Experimental part

^{1}H NMR spectroscopy and mass spectrometry data of PMI-2.

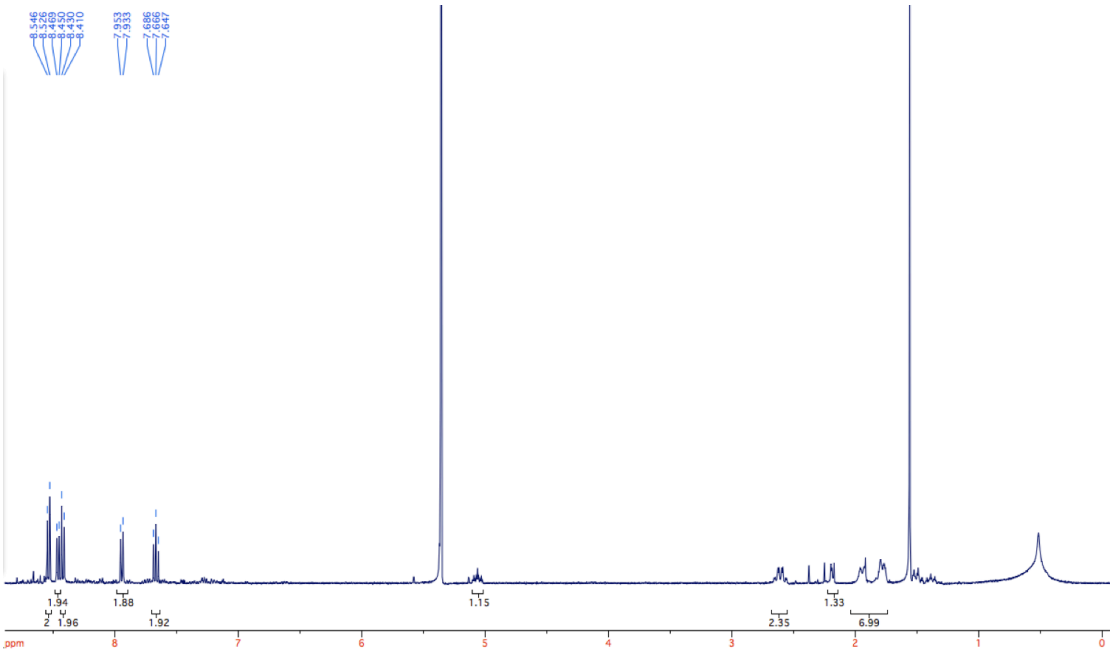

Figure 5.25. ^{1}H NMR spectrum of PMI-2 in CD_2Cl_2

^{1}H NMR (400 MHz, CD_2Cl_2): δ 8.53 (d, 2H), 8.46 (d, 2H), 8.42 (d, 2H), 7.94 (d, 2H), 7.66 (t, 2H), 5.06 (m, 1H), 2.60 (m, 2H), 2.19 (m, 1H), 1.87 (m, 7H)
HRMS (ESI): m/z calc. for $C_{28}H_{21}NO_2$ [M+H]+ 403.16; found 403.17. [M+Na]+ 426.15; found 426.15.

^{1}H NMR spectroscopy and mass spectrometry data of PMI-3

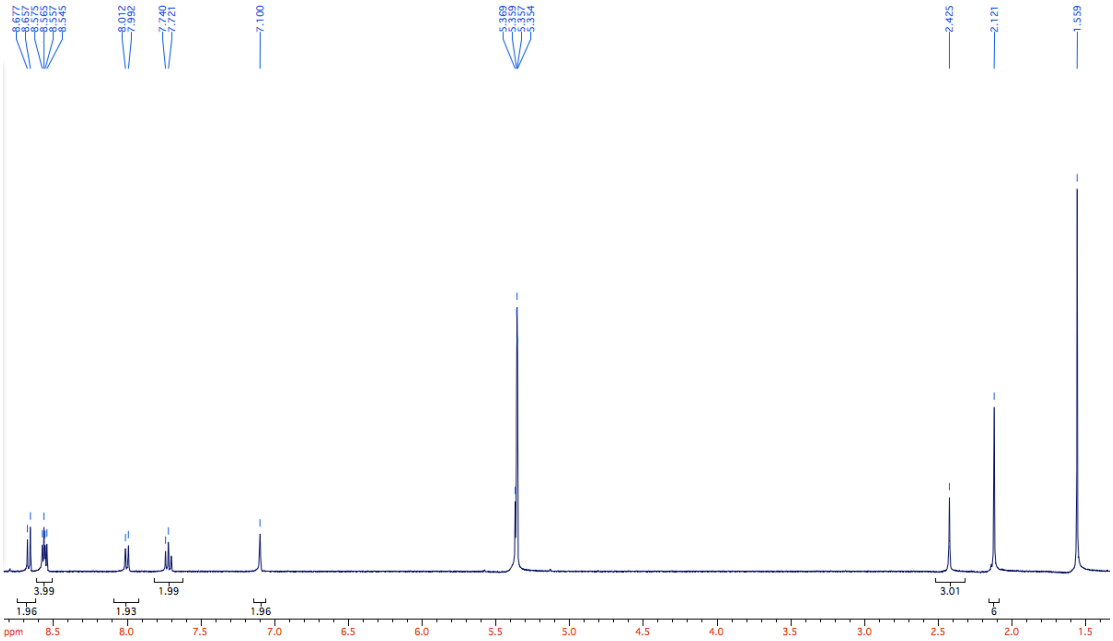

Figure 5.25. ^{1}H NMR spectrum of PM3 in CD_2Cl_2

^{1}H NMR (400 MHz, CD_2Cl_2): δ 8.67 (d, 2H), 8.56 (m, 2H), 8.00 (d, 2H), 7.74 (t, 2H), 7.10 (s, 2H), 7.54 (t, J = 7.8 Hz, 1H), 2.42 (s, 3H), 2.12 (s, 6H).
HRMS (ESI): m/z calc. for $C_{31}H_{21}NO_2$ [M+H]+ 440.1651; found 440.1655.

Preparation of single crystals

PMI-1 and PMI-3: PMI-1was dissolved (saturated solution) in DCM and crystallization was done by using the diffusion method with using hexane as a non-solvent. Crystallization was done for 7 days.

PMI-2: PMI-1was dissolved (saturated solution) in a 1:1 mixture of DCM and chloroform. Crystallization was done by using the diffusion method with using hexane as a non-solvent. Crystallization was done for 28 days.

SAXS and WAXS

The SAXS/WAXS measurements of the samples were performed with SAXSess Small-Angle X-Ray Scattering Instrument by Anton Paar. This Kratky type of camera is attached to a laboratory X-ray generator (PW3830, PANalytical), and was operated with a fine focus glass sealed X-ray tube at 40 kV and 50 mA (CuKα, λ=0.1542 nm). Detection was performed with the 2D imaging-plate reader Cyclone® by Perkin Elmer.
Measurements were performed in standard solid sample holder for 90 minutes. The data were collected up to a q value of 28 nm^{-1}, where q = (4 π/λ) sin(θ/2) is the length of the scattering vector and θ is the scattering angle, i.e. the angle of observation. The temperature was controlled with a TCS 120 sample holder (Anton Paar) with an accuracy of ±0.2°C. A reusable sample holder was used for all measurements to attain the same scattering volume and background contribution.
The two-dimensional intensity data was converted to one- dimensional data with SAXSQuant software (Anton Paar). The scattering intensities were corrected for background noise, detector efficiency, empty cell scattering, and sample transmission and were placed on an absolute scale using beam flux measurements.

SAXS patterns

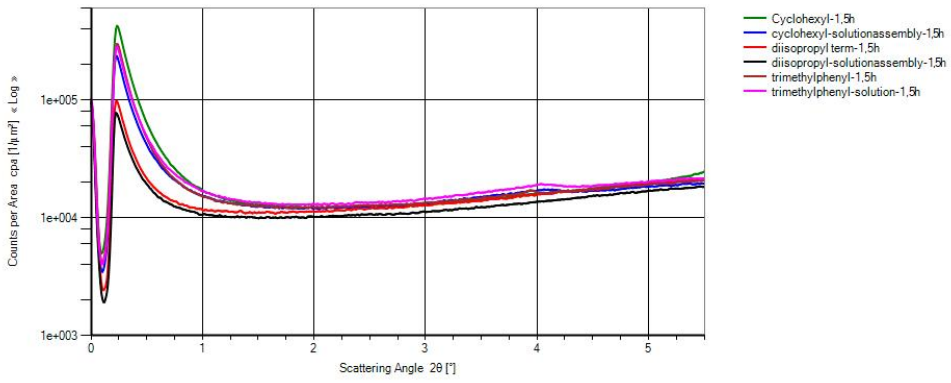

Figure 5.25. SAXS patterns of PMI-1, PMI-2 and PMI-3.

References

[1] Lehn, J. M., Science, 260, 1762, 1993.
[2] Steed, J. W., Gale, P. A., Supramolecular Chemistry: From Molecules to Nanomaterials, 8 Volume Set, WILEY, 2012.
[3] Lehn, J. M., Proc. Natl. Acad. Sci. USA 99, 4763-4768, 2002.
[4] Lehn, J. M., Chem. Soc. Rev. 36, 151-160, 2007.
[5] Fischer, H. E., Chem. Ber. 27, 2985-2993, 1894.
[6] Hartley, G.S., Aqueous Solutions of Paraffin Chain Salts, A Study in Micelle Formation, Hermann et Cie, Paris, 1936.
[7] Israelachvili, J. N., Mitchell, D. J., Ninham, B. W., BBA – Biomembranes 470, 185-201, 1977.
[8] Antonietti, M., and Förster, S., Adv. Mater. 15, 1323-1333, 2003.
[9] Lee, I., Langmuir 29, 2476-2489, 2013.
[10] Whitesides, G. M., and Grzybowski, B., Science 295, 2418-2421, 2002.
[11] Whitesides, G. M., Mathias, J. P., Seto, C. T., Science 254, 1312-1319, 1991.
[12] Deguan, A. L. (Ed.), Molecular Self-Assembly: Advances and Applications, Pan Stanford Publishing, 2012.
[13] Otero, R. et al., Adv. Mater. 23, 5148-5176, 2011.
[14] Smith, W. F., Nat. Nanotechnol. 2, 77-78, 2007.
[15] Ruiz-Carretero, A. et al., J. Mater. Chem. A, 1, 11674-11681, 2013.
[16] Ruiz-Carretero, A. et al., Chem. Commun., 47, 884-886, 2011.
[17] Scharber, M. C., and Sariciftci, M. C., efficiency of bulk-heterojunction organic solar cells. Prog. Polym. Sci., Article in press, 2013.
[18] Hoppe H., Sariciftci N. S., J Mater Chem 16, 16-45, 2006.
[19] Yang X., Loos J. Macromolecules 40, 1353-1362, 2007.
[20] Watkins P. K., Walker A. B., Verschoor G. B., Nano Lett 5, 1814-1818, 2005.
[21] Hoppe H., Sariciftci N. S., J Mater Res 19, 1924-1945, 2004.
[22] Li, C., and Wonneberger, H., Adv. Mater. 24, 613-636, 2012.
[23] Kamm, V., Battagliarin, G., Howard, I. A., Pisula, W., Mavriskiy, A., Li, C., Müllen, K., Laquai, F., *Adv. Energy Mater*. **1**, 297-302, **2011**.
[24] Schmidt-Mende, L., Fechtenkötter, A., Müllen, K., Moons, E., Friend, R. H., MacKenzie, J. D., *Science* **10**, 1119-1122, **2001**.
[25] Morteani, A. C., Friend, R. H., Silva, C. in *Organic Light-Emitting Devices* (Eds. Müllen, K., Scherf, U.), pp. 35-95, **2005**.
[26] Avlasevic, Y., Li, C., Müllen, K., J. Mater. Chem. 20, 3814-3826, 2010.
[27] Herrmann, A., Müllen, K., Chem. Lett. 35, 978-985, 2006.
[28] Nolde, F., Pisula, W., Müller, S., Kohl, C., and Müllen, K., Chem. Mater. 18, 3715-3725, 2006.
[29] Tasios, N. et al., J. Am. Chem. Soc. 132, 7478-7487, 2010.
[30] Boobalan, G., Imran, P. K., Manoharan, C., and Nagarajan, S., J. Colloid Infterface Sci. 393, 377-383, 2013.
[31] Ghosh, S., et al., Chem. Eur. J. 14, 11343-11357.
[32] Dehm, V. et al., Org. Lett. 9, 1085-1088, 2007.
[33] Ahrens, M. J. et al., J. Am. Chem. Soc. 126, 8284-8294, 2004.
[34] Würthner, F., Chem. Commun. 1564-1579, 2004.
[35] Würthner, F. et al., J. Am. Chem. Soc. 126, 10611-10618, 2004.
[36] Würthner, F. et al., Chem. Commun. 1188-1190, 2006.

[37] Chen, Z. et al., Chem. Eur. J. 13, 450-465, 2007.
[38] Chen, Z. et al., Chem. Eur. J. 13, 436-449, 2007.
[39] Kaiser, T. E. et al., Angew. Chem. Int. Ed. 46, 5541-5544, 2007.
[40] Wang, H., et al., Chem. Commun. 1181-1183, 2008.
[41] Görl, D., Xin, Z., Würthner, F., Angew. Chem. Int. Ed. 51, 6328-6348,2012.
[42] Changzhun, S. et al., Chem. Eur. J. 18, 13665-13677, 2012.
[43] Würthner, F., Thalacker, C., and Sautter, A., Adv. Mater. 11, 754-758, 1999.
[44] Thalacker, C., and Würthner F., Adv. Funct. Mater. 12, 209-218, 2002.
[45] Würthner, F., Chem. Eur. J. 7, 2245-2253, 2001.
[46] Kaiser, E. T., J. Am. Chem. Soc. 131, 6719-6732, 2009.
[47] Tolkki, A. et al., Langmuir 26, 6630-6637, 2010.
[48] Lu., J. et al., Mater. Sci. Eng. C 32, 1948-1954, 2012.
[49] Wang, S. et al., Small 7, 2841-2846, 2011.
[50] Hu, J. et al., Adv. Funct. Mater. 22, 4149-4158, 2012.
[51] Balakrishnan, K. et al., J. Am. Chem. Soc. 128, 7390-7398, 2006.
[52] Yan. P. et al., J. Phys. Chem. B 109, 724-730, 2005.
[53] Mativetsky, J. M. et al., Adv. Funct. Mater. 19, 2486-2494, 2009.
[54] Samori, P. et al., Adv. Mater. 18, 1317-1321, 2006.
[55] Wang, J. et al., J. Phys. Chem. B 117, 9288-9304 2013.
[56] Cremer, J., and Bauerle, J., J. Mater. Chem. 16, 874-884, 2006
[57] Cremer, J. et al., Org. Biomol. Chem. 3, 985-995, 2005.
[58] Cremer, J., and Bauerle, P., Eur. J. Org. Chem. 3715-3723, 2005.
[59] Wonneberger, H., et al., J. Phys. Chem. B 114, 14343-14347, 2010.
[60] Palermo, V. et al., J. Am. Chem. Soc. 130, 14605-14614, 2008.
[61] Hagfeldt, A. et al., Chem. Rev. 110, 6595-6663, 2010.
[62] Ferrere, S., and Gregg, B. A., J. Phys. Chem. B 105, 7602-7605, 2001.
[63] Ferrere, S. G., and Brian, A., Proc. Electrochem. Soc. 10, 161-172, 2001.
[64] Würthner, K., Chem. Commun. 1564-1579, 2004.
[65] Böhm, A., Arms, H., Henning, G., Verfahren zur Herstellung von Perylen-3,4-dicarbonsäureimiden, DE 196 22 673 A1, 1997.
[66] Tomizaki, K. et al., J. Org. Chem. 67, 6519-6534, 2002.
[67] Cheriya, R. T., Nagarajan, K., and Hariharan, M., J. Phys. Chem. C 117, 3240-3248, 2013.
[68] Margineanu, A. et al., Biophys. J. 93, 2877-2891, 2007.
[69] Balakrishnan, K., Datar, A., Oitker, R., Chen, H., Zuo, J., Zhang, L., J. Am. Chem. Soc. 127, 10496, 2005.
[70] Balakrishnan, K., Datar, A., Naddo, T., Huang, J., Oitker, R., Yen, M., Zhao, J., Zhang, L., J. Am. Chem. Soc. 128, 7390, 2006.
[71] Vajiravelu, S., Ramunas, L., Vidas, G. J., Valentas, G., Vygintas, J., Valiyaveettil, S., *J. Mater. Chem*. **19**, 4268, **2009**.
[72] Chen, Y., Feng, Y., Gao, J., Bouvet, M., Journal of Colloid and Interface Science **368**, *387-394*, **2012**.
[73] Wang, H., Kaiser, T. E., Uemera, S., Würthner, F., *Chem. Commun*. 1181-1183, **2008**.
[74] Kaiser, T., Stepanenko, V., Würthner, F., *J. Am. Chem. Soc*. **131**, 6719-6732, **2009**.

Zeolites as key-components for bio-medicine - Zeolite-L as a multifunctional DNA and drug delivery system

Abstract

This chapter describes the use of zeolites as a multifunctional DNA and drug release systems. First, the DNA binding to zeolite-L micro- and nanoparticles is investigated qualitatively and quantitatively. After that it will be shown that DNA functionalized zeolites can be used as a multifunctional DNA and drug release system in living cells. The release of DNA and a model drug (DAPI) in HeLa cells will be shown and the particle uptake and kinetics of the DNA and DAPI release will be investigated in detail. Finally, it will be shown, that the particles and also the detached DNA are localized in certain organelles.

Henning Lülf, Alessandro Bertucci, Dedy Septiadi, Roberto Corradini, Luisa De Cola*, *Angew. Chem. Int. Ed.*, 2013, submitted.

6.1. Introduction

After using zeolite-L crystals extracellularly as a substrate for neuron growth (chapter 3) or for applications in the field of organic electronics (chapter 4), the next chapters describe the possibility of using zeolites-L intracellularly as multifunctional oligonucleotide and drug delivery systems.
This chapter describes the first example of using zeolite-L particles as a multifunctional drug and DNA delivery system.

This project was carried out in cooperation with Professor Corradini from the University of Parma and in particular with Mr. Alessandro Bertucci and Mr. Dedy Septiadi from the group of Professor De Cola (cell culture and confocal microscopy).

6.1.1. Transfection

The transfer of foreign DNA into living cells (transfection) is a fundamental goal in biotechnology and a very intense research field since more than 40 years. Searching for the keyword “transfection” using SciFinder® (13.10.2013) yields to more than 225,092 direct hits, the earliest dated to 1966[1]. The development of publications dealing with transfection (as a direct hit in SciFinder®) as a function of time is illustrated in figure 6.1. A very strong increase of publication after 1985 can be seen until 2005, where a plateau seems to be reached.

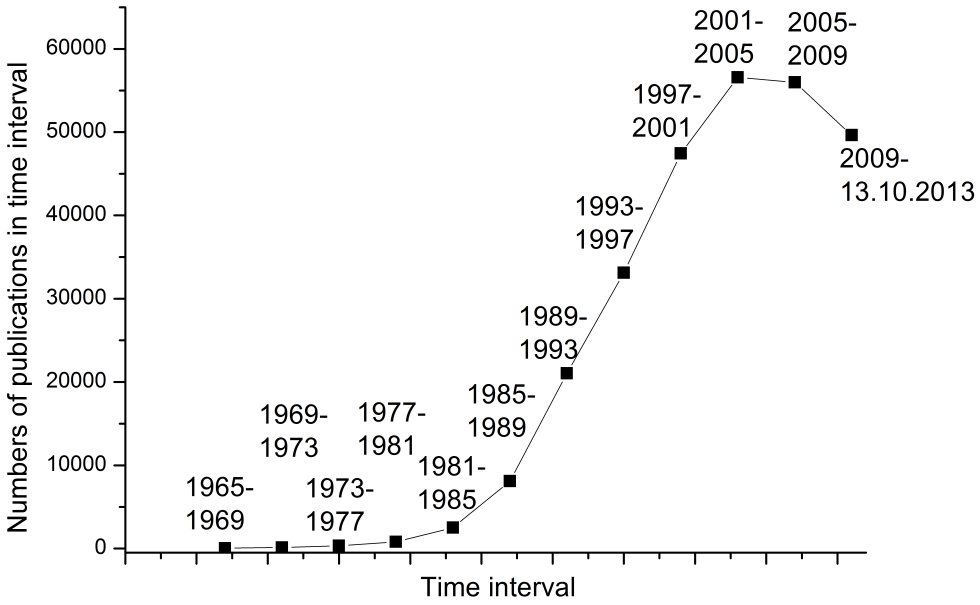

Figure 6.1. Number of publications dealing with transfection (as a direct hit in SciFinder® in time intervals of 4 years.

The ultimate goal of transfection is to use DNA as a pharmacological agent, which is called gene therapy. Already in 1972 Friedmann and Roblin discussed the possibility of treating human diseases in this way[2].

However, before first real applications are realistic, problems like the inefficiency and cytotoxicity of modern DNA delivery systems must be addressed and solved. Even after many years of intense research, the transfection efficiency is still one of the main problems and is dependent on both the delivery efficiency (the number of foreign DNA delivered into the nucleus) and the DNA expression efficiency (the number of foreign DNA that undergoes transcription)[3]. In addition, *in vitro* results obtained in laboratory conditions are not always transferrable to *in vivo* systems, which makes applications in gene therapy generally very striking and time consuming[4, 5].
Throughout billion of years nature developed a large number of different viruses that are specialized to transfer their own oligonucleotides into all kinds of different cells. Researchers have been trying to adapt this concept for a long time and to date viral systems are still the most efficient species for transfection. On the other hand these systems show disadvantages due to limited DNA carrying capacity, toxicity, unspecific targeting, production and packaging problems as well as high cost[3, 6, 7]. Above that, the handling of viruses is not trivial due to possibly very high toxicities and immunogenicity, which further restricts their use. Due to these disadvantages the development of cheap and non-toxic DNA delivery systems has become a huge research field.

6.1.2. Artificial transfection systems

Many different approaches to deliver foreign DNA into cells have been developed throughout the years. A very straightforward way is the mechanical injection of DNA directly into the nucleus, but only a very small number of cells can be addressed at the same time, which makes this approach very slow. It is applicable neither for laboratory research or for *in vivo* applications.
Beyond that, different mechanical or electrical methods have been developed. For example, Mann et al. reported a pressure-mediated method, which can lead to delivery efficiencies of more than 50%[8]. For a detailed overview about this research field, the reader is referred to a very recent review by Yao *et al*.[9]
Above that, it has been shown that DNA can also be delivered by using hydrodynamic forces[10, 11, 12], ultrasonic nebulization[13, 14, 15, 16] or particle bombardment[17, 18, 19, 20, 21, 22].
Another well-known approach is the so-called electroporation method, which was developed in 1982[23, 24, 25, 26, 27, 28, 29, 30].

In addition, chemical methods have gained much attraction in the last 30 years. The use of uptake-enhancing chemicals has been shown to be a very straightforward and a widely applicable way to bring DNA into cells. The general idea is to link the DNA electrostatically to positively charged uptake-enhancing molecules, usually polymers. The first example was reported in the

late 1950s and employs high salt concentrations and cationic proteins to enhance cellular uptake[31]. After that, a variety of other uptake enhancing chemicals were reported[28, 32, 33, 34, 35, 36, 37, 38, 39]. Notably is the development of the cationic lipid Lipofectin in 1987, which is one of the first systems used *in vivo* and a widely applied system for laboratory research[40].
Other approaches use different peptides and proteins as DNA delivery platforms. Widely studied peptides for DNA delivery are poly-L-lysine (PLL)[41, 42, 43, 44, 45, 46, 47, 48], protamine sulfate[49] or other proteins[50, 51, 52, 53, 54]. The structure of PLL is shown in figure 6.2.
Furthermore, dendrimers like polyamidoamine (PAMAM) have been studied for DNA delivery, since they show well-defined structures and architectures[55, 56, 57, 58, 59, 60, 61, 62]. Very popular is also the application of synthetic polymers, since they can be synthesized and tuned for every different application[63, 64, 65, 66, 67, 68, 69, 70].
These systems are usually uptaken by endocytosis, which causes a few general problems in transfection research.
Endocytosis is a multistep mechanism including binding, internalization, formation of endosomes, fusion with lysosomes and lysis[59]. Due to a very low pH and the presence of enzymes within the endosomes, the DNA is exposed to very harsh conditions and a certain amount of DNA will degrade before even being close to the nucleus. Finally, the DNA that arrives at the nucleus must be able to dissociate from the carrier before or after entering the nucleus. The overall transfection efficiency is a sum of all steps and certain amounts of DNA will be lost in each step.
In summary there are 3 major bottlenecks for a DNA delivery to the nucleus – low cellular uptake, low release with limited stability of DNA and inadequate nuclear targeting.
In addition, the above-mentioned chemical systems deliver the DNA in a single step and the DNA is just available for a very short time, which again decreases the efficiency notably.
To overcome these problems, controlled delivery systems have gained much attention in the past and mostly polymer-based systems have been used to achieve a slow release of DNA from its carrier[63, 64, 65, 66, 67, 68, 69, 70, 71, 72, 73, 74, 75, 76].

6.1.3. Nanoparticles for transfection

Recently, also the use of different nanoparticles as DNA carriers has become very popular. Most reports deal with soft, cationic, polymeric nanoparticles where the general concept of electrostatically binding the negatively charged DNA to a positively charged carrier has been kept[77, 78, 79, 80].
When going from soft particles to “hard” nanoparticles, gold nanoparticles are the most popular ones, where the DNA can be released photothermally from

the surface, but *in vitro* or *in vivo* experiments are rare[81, 82, 83, 84, 85, 86, 87, 88, 89, 90].

Superparamagnetic iron oxide nanoparticles have also been reported as DNA carrier systems, but again *in vitro* or *in vivo* experiments are not reported so far[91, 92], [93]. Above that, also nanorods[94, 95, 96, 97, 98, 99, 100, 101] and nanotubes[102], [103] have been investigated as DNA carriers.

However, in all of these examples the particle itself is simply used as the carrier and has no further function when the DNA is desorbed from its surface. The use of porous materials would therefore allow introducing a further function to the particle itself - a drug could for example be released from the pores after DNA desorption.

Indeed, recent publications report the use of mesoporous silica nanoparticles (MSNP) as DNA carriers and it has been shown that they can be used to transfer high amounts of plasmid DNA into HeLa[104], [105] and A549-cells[104] or plant cells[106].

However, the number of reports dealing with the use of porous materials as a DNA carrier is small and they mostly report proof of principle experiments, where the possible multivalency has not been exploited *in vitro* or *in vivo*[107] [108]. Above that, the fate of the nanoparticles in the cells or the kinetics of the DNA release has not been studied and nothing is reported about a simultaneous DNA and drug delivery from the same system.

Furthermore, the application of zeolite crystals as a DNA carrier system is not reported so far. This work will be the first report on using zeolites as a DNA carrier for transfection experiments. The DNA is attached to the zeolite surface, allowing the filling of the pores possibly with drug molecules before the coating with the oligonucleotide. Above that, this work investigates the kinetics of the DNA and drug delivery by selectively labeling the DNA with a fluorescent dye and using a luminescent model drug to follow its delivery in the nucleus. The confocal microscopy analysis has therefore allowed us to monitor in real time the detachment of the DNA and the migration of the drug from the interior of the crystals to the nucleus. We have shown that detached DNA is located in certain organelles of the cells.

6.2. Particle preparation and analysis

The synthetic pathway is shown in figure 6.2. Zeolite crystals in two different sizes, 50 nm (nanozeolite-L) and about 1000 nm (microzeolite-L), were synthesized as described in chapter 2 and characterized by SEM, TEM, DLS and zeta potential measurements. In a next step the zeolite pores were filled with the guest molecules[109], like the neutral fluorescent dye DXP (for the molecular structure see chapter 4) or the nucleus stain 4',6-diamidino-2-phenylindole (DAPI), which is present in its protonated form when intercalated in the acidic

environment inside zeolite pores (pH = 3.38)[110]. The structures of DAPI and PLL are shown in figure 6.2.

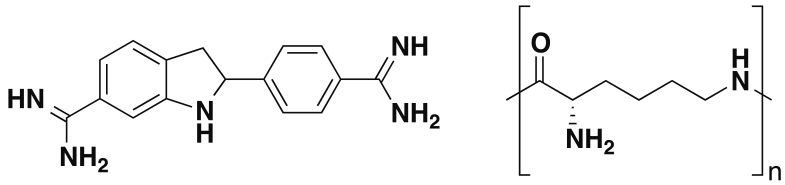

DAPI PLL

Figure 6.2. Structures of DAPI and PLL

The DAPI loading was then determined by thermogravimetric analysis (TGA) and resulted to be 1.55 wt% for nanozeolite-L and 0.9 wt% for microzeolite-L particles.

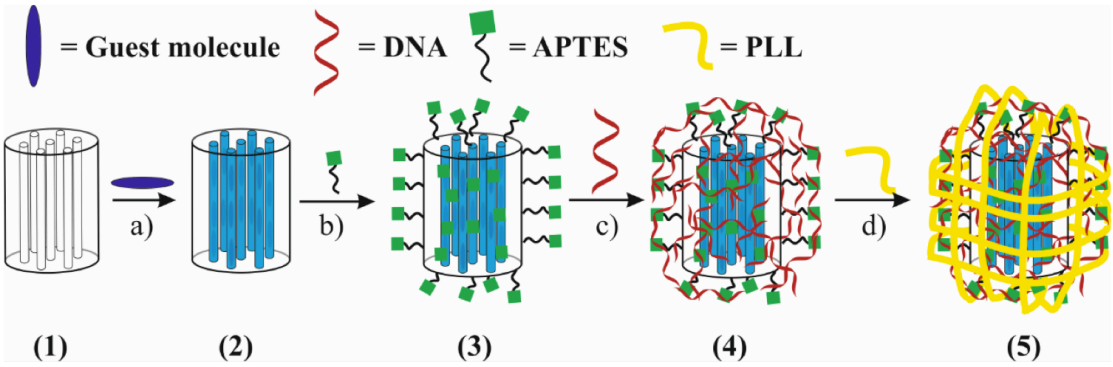

Figure 6.3. Preparation of the designed particles. (1) = empty zeolites, (2) = pores filled with guests, (3) = NH_2 functionalization of the filled zeolites, (4) DNA electrostatic binding, (5) wrapping of PLL on the DNA.

A general procedure for the loading with the model-drug molecules and the coating of DNA and PLL is depicted in Figure 6.3. The scheme shows that after filling the zeolites L we can electrostatically bind the DNA to the zeolites, after functionalizing them with (3-Aminopropyl)triethoxysilane (APTES) as described in chapter 2. Indeed, the NH_2 groups are partially protonated in physiological conditions leading to a positively charged particle surface, which allows the electrostatic binding of the DNA oligonucleotide strands (5'-GCAACAGTGAAGGAAAGCC-3') to the particles. Functionalization was confirmed by a zeta potential shift from negative to positive potentials for both zeolite sizes (see below for details). The NH_2 groups were further revealed by a positive ninhydrin test.

DNA binding was achieved by dispersing the zeolites (1 mg) in a solution of DNA in PBS buffer. Incubation was done at 37 °C for 30 minutes and the particles were washed with deionized water (2 x 1 mL) before cell experiments. Upon DNA binding the zeta potential decreases to negative values and the particle size increases, which is a first proof of a successful DNA binding.

The electrostatic DNA binding was further confirmed by confocal microscopy. We therefore filled the pores of nanozeolites-L with the green fluorescent dye

DXP (see chapter 2 for the procedure) and electrostatically bound a Cy5 labeled DNA to its surface. Both dyes were then localized independently from each other and a perfect overlap of both signals was obtained, as shown in figure 6.4.

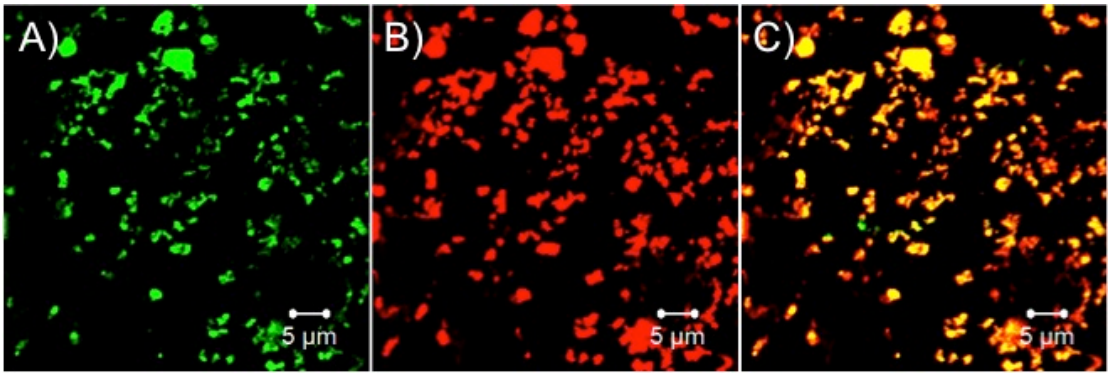

Figure 6.4. Confirmation of DNA binding by a signal overlap of DXP and Cy5. A) DXP signal; B) Cy5 signal; C) Overlap. The dyes were excited at 514 (DXP) and 633 nm (Cy5).

6.3. Microzeolite preparation and functionalization.

We have prepared the 900/1000 nm microzeolites according to a literature procedure (See also chapter 2 for details). The particles have been characterized by SEM and DLS and the data are depicted in figure 6.5.

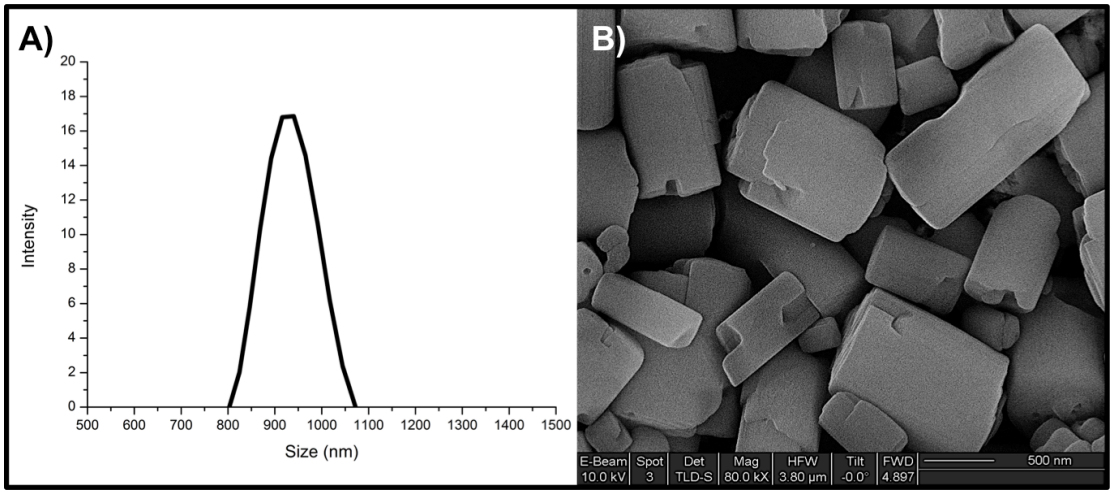

Figure 6.5. Characterization of microzeolite-L. A) Size distribution by DLS; B) Scanning electron micrograph.

The crystals were filled with DAPI by cation exchange in water solution. Then functionalization with the amino derivative and coating with the DNA was done accordingly to the scheme in figure 6.2. In order to quantify the DNA bound to the zeolites, a method described in the literature[108] was followed. Seven solutions containing each 1 mg of NH_2 functionalized zeolites were incubated with different concentrated solutions of dye labeled DNA (0.5 mL PBS buffer, 37 °C, 30 min). The particles were removed by centrifugation and the amount

of DNA binding to the particles was calculated using the characteristic UV/Vis absorption of the dye, by subtracting the DNA concentration in the supernatant from the initial DNA concentration.
A linear increase of DNA binding to the microzeolite-L particles with increasing DNA concentrations is observed until a plateau is reached at a concentration of 15 nmol DNA per 0.5 mL PBS. At this point about 7.8 nmol DNA are binding to 1 mg of microzeolites and a further increase in DNA concentration does not lead to an increased binding as shown in Figure 6.6.

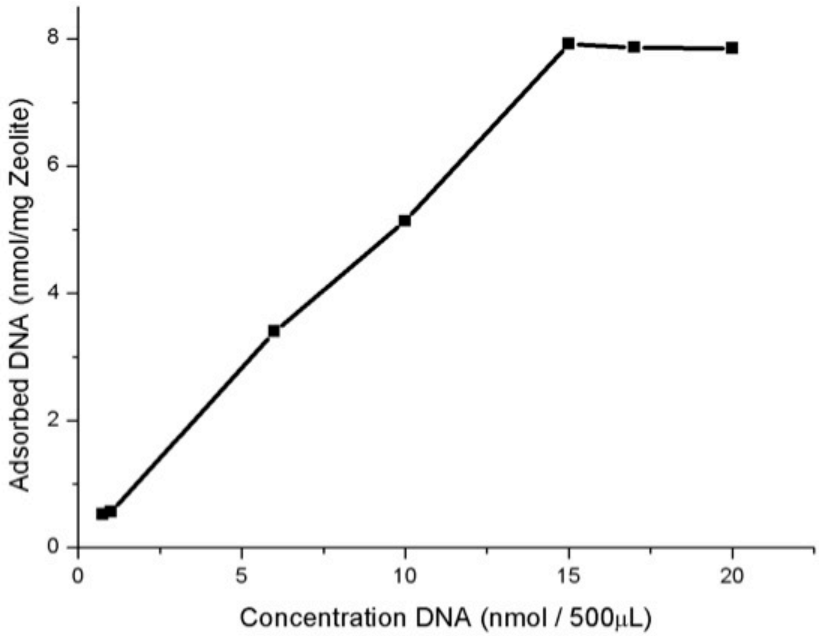

Figure 6.6. Amount of DNA binding to 1 mg of microzeolite-L in dependence of the DNA concentration in solution.

These results are also in accordance to previously reported results for mesoporous silica nanoparticles[108]. The binding can further be expressed as the number of DNA molecules attached to a single zeolite crystals and we determined an amount of about 8,300,000 DNA molecules per microzeolite-L particle. Fur further details and calculation see the experimental part at the end of this chapter.

6.4. DAPI release from DNA functionalized microzeolite-L.

The electrostatic anchoring of DNA to the surface of the crystals leads to a nearly complete closing of the pores resulting in an inhibition of DAPI release, which has been recently shown for mesoporous silica nanoparticles, where the DNA acts as a stimuli responsive pore-closing/pore-opening moiety[108]. Indeed this concept also works for zeolites as demonstrated in the following where a DNA/DNA duplex formation was used to detach the DNA from the particles. This was done by filling the channels with DAPI and covering the zeolites with DNA. The DNA functionalized zeolites in PBS were then incu-

bated and a full complementary DNA oligonucleotide was added to this dispersion. Upon recognition of the complementary strand the DNA anchored to the surface is removed and the DAPI can be released in the solution. Centrifugation of the dispersion, and quantification of the fluorescence obtained from the supernatant, allowed the evaluation of the DAPI concentration. The results are summarized in figure 6.7 and correspond to the DAPI concentration in the supernatant after its release. In order to have a clear comparison with the reference (amine functionalized zeolites), the DNA in the presence and absence in solution of the complementary sequence, different experiments that were performed as follows:

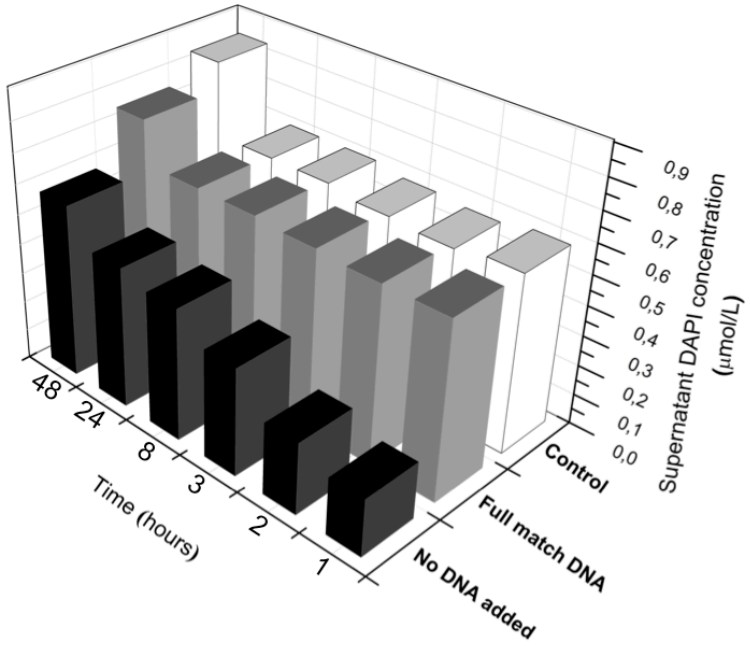

Figure 6.7. Summary of the leaking experiments to confirm the stimuli responsive release of DAPI from DNA functionalized zeolite-L.

Exp-1: Control Experiment. NH_2 functionalized zeolites (1 mg) were dispersed in PBS (2 mL). Aliquots of the supernatant were collected after 1h, 2h, 3h, 8h, 24h, and 48h. This experiment was performed to define the fastest release (see white bars in figure 6.7).
Exp-2: DNA functionalized zeolites (1 mg) were dispersed in PBS (2 mL). Aliquots of the supernatant were collected after the same times. A very slow DAPI release is observed (green black, figure 6.7).
Exp-3: DNA functionalized zeolites (1 mg) were dispersed in PBS (2 mL). A full match DNA (GCTTTCCTTCACTGTTGC) was added and aliquots of the supernatant were collected after the above mentioned times. The addition of the full match DNA leads to a fast DNA/DNA duplex formation, which triggers the detachment of the DNA from the particles. A relatively fast DAPI release is observed.
Quantification was done by using a calibration curve, which is shown in figure 6.8.

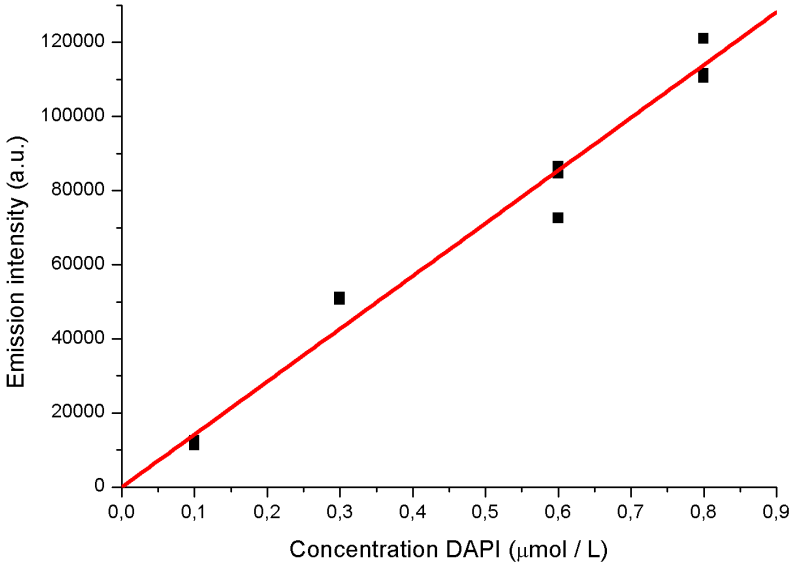

Figure 6.8. Calibration curve for the quantification of DAPI release. Fluorescence intensity was monitored at 440 nm.

In summary, these experiments prove the possibility of functionalizing zeolite particles with DNA oligonucleotides, which then works as a stimuli responsive pore-closing/pore-opening moiety. The principle is illustrated in figure 6.9.

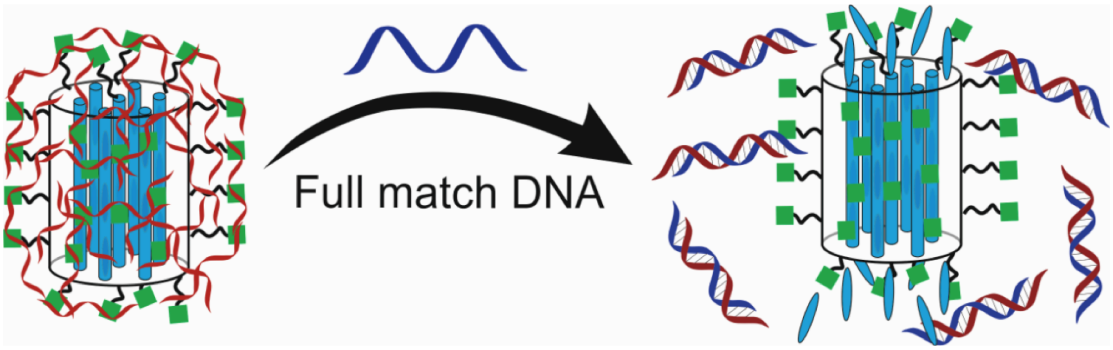

Figure 6.9. Illustration of the paradigm of using DNA as a stimuli responsive pore-closing/pore-opening moiety for zeolite particles. DNA binding to the zeolite surface leads to a closing of the pores and addition of a full-match oligonucleotide can be used to detach the DNA probes from the surface upon DNA/DNA duplex formation and release the drug.

The fact that we observe some DAPI release also in the absence of the complementary DNA, is attributed to slow detachment of DNA from the particles due to an exchange with anions from the media, which is further confirmed by the cell experiments.
These particles were then applied *in vitro* to investigate the DNA and DAPI release in living cells.

6.5. Intracellular DNA and DAPI release from microzeolite-L

The uptake of DNA functionalized microzeolites and the DNA and DAPI release from those particles were studied by confocal microscopy.

Due to the very large size of the particles and their negative charge, the particles were coated with the positive PLL, a commonly used polymer to enhance nanoparticle uptake[111, 112, 113]. Additionally, this coating prevents interactions of the DNA with other molecules and assures the integrity of the system until it is taken inside the cell. Due to its biodegradability, the PLL coating will be destroyed in the cell, which uncovers the DNA layers[114]. Cell experiments were done by using HeLa cells (approximately 50,000 cells per well) and incubation was done for 1, 4 and 24 hours using a particle concentration of 0.01 mg zeolites per mL culture media. After incubation, the cells were fixed, washed with PBS and the actin filaments were stained with Alexa Fluor® 568 Phalloidin. A Cy5 labeled DNA was used, so that the red emission does not overlap with the yellow fluorescent actin stain or the blue DAPI fluorescence. The results are shown in figure 6.10.

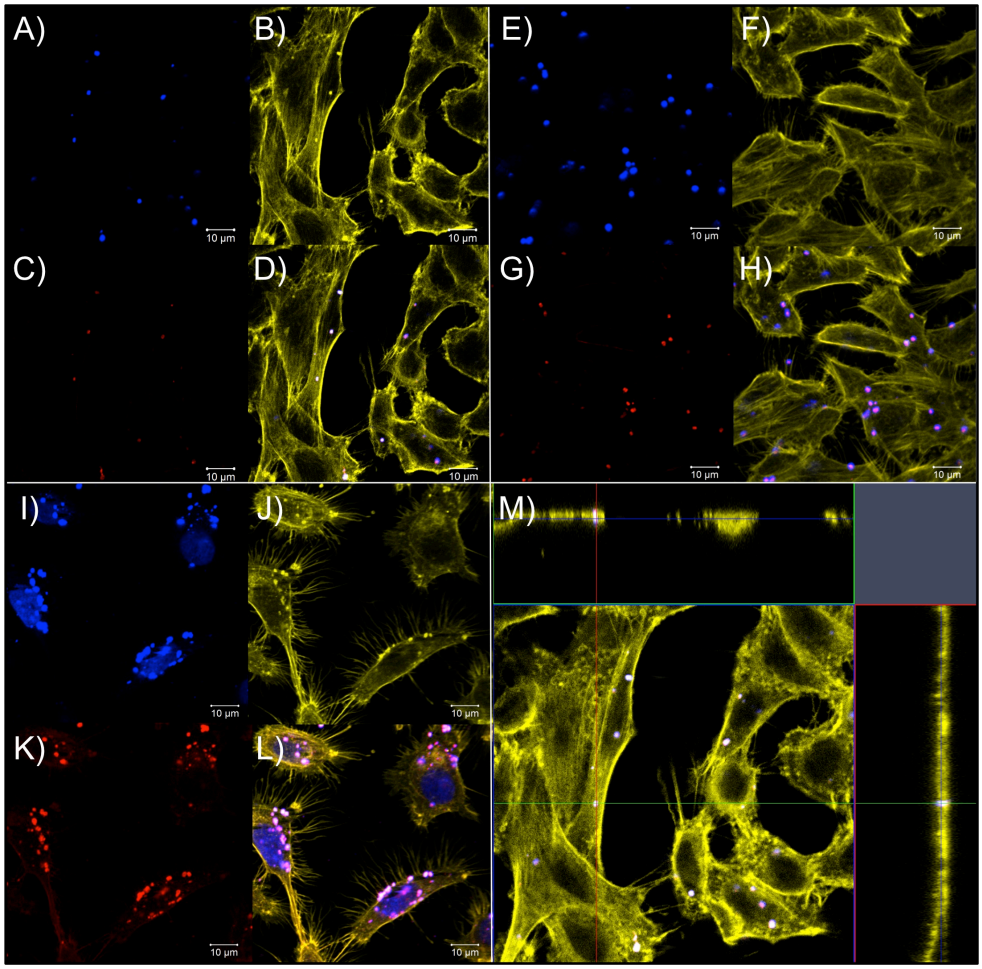

Figure 6.10. Confocal micrographs showing the uptake of DAPI loaded microzeolite-L. A to D: 1 hour incubation; E to H: 4 hours incubation; I to L: 24 hours incubation. M: z-stack after 1 hour incubation. A, E, I: DAPI emission; B, F, J: Alexa Fluor® 568 Phalloidin fluorescence; C, G, K: Cy5 emission; D, H, L: overlay. Excitation: 405, 514 and 633 nm.

After 1 hour only very few particles are uptaken by the cells and their uptake was confirmed by recording z-stacks (figure 6.10 M). From the overlap of the DAPI and Cy5 signals, it can be concluded that the DNA is indeed bound to the particles even after cell uptake.
After 4 hours a slightly higher amount of particles is internalized but the total number is still very small. The Cy5 signal is still present only on the particles (colocalization of the DAPI and Cy5 signal), and no DAPI fluorescence is recorded in the nucleus.
The number of particles uptaken by the cells is further increased after 24 hours and a very pale red staining of the cytoplasm is observed, which is ascribed to the detachment of very small amounts of DNA from the zeolites. Since no full-match DNA is present in the cytoplasm, the slow DNA detachment from the surface is believed to be due to a slow exchange with proteins and ions from the media. Sufficient amount of DAPI is now released from the pores staining the nucleus. However, the majority of DAPI is still present inside the zeolites and the majority of DNA is bound to the crystals as it can be seen from the very bright co-localized blue and red spots in figure 6.10 I and K.
In view of the obtained results we decided to decrease the particle sizes to achieve a higher cell uptake and to study more in detail the kinetics of the DNA and DAPI release.

6.6. Nanozeolite preparation and functionalization.

Nanozeolites have been prepared as described in chapter 2 and characterized by TEM, and DLS as shown in figure 6.11.

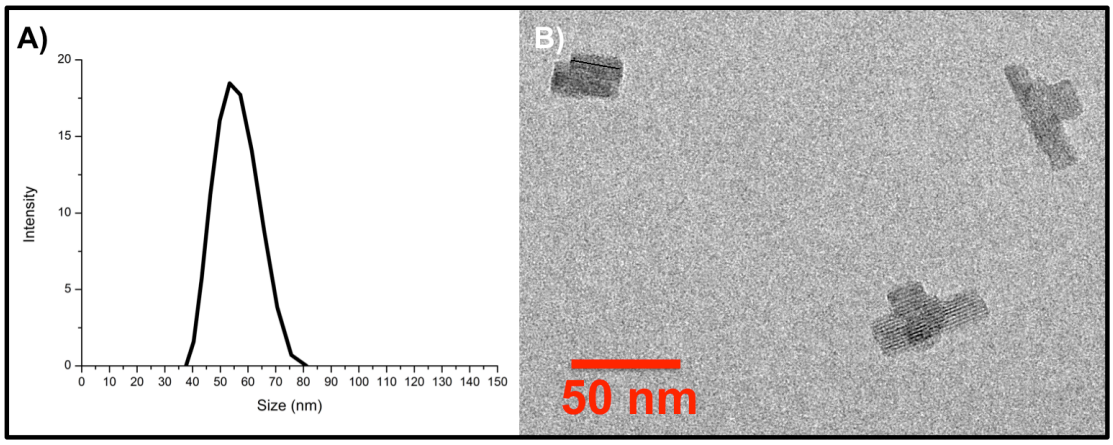

Figure 6.11. Characterization of nanozeolite-L. A) Size distribution by DLS. B) Transmission electron micrograph.

DNA functionalized nanozeolites have been prepared according to the preparation scheme shown in figure 6.3.

In a first step the pores were filled with DXP (from the gas phase) or with DAPI (by cation exchange), as it is described in chapter 2. The DNA binding was then done according to figure 6.3 and as already described for the microzeolites. Upon functionalization with APTES we observe a zeta potential shift from -33.50 mV to +2.58 mV, which confirms the functionalization with amine groups. We also confirmed the functionalization by a positive ninhydrin test. In a next step the DNA was electrostatically attached to the zeolites by incubating 1 mg of amine-functionalized nanozeolites in a solution of DNA in PBS buffer (15 nmol / 0.5 mL) at 37 °C for 30 minutes. Upon DNA binding the zeta potential shifts from +2.58 mV to a value of -17.04 mV and the size increased from about 55 to 119 nm, which is a first proof of a successful binding. Additionally, we confirmed the binding by confocal microscopy as shown in figure 6.4.
The electrostatically bound DNA was quantified according to a literature protocol and as already described for the microzeolite particles. We calculated a binding of 8.6 nmol DNA per mg of nanozeolites, which corresponds to a number of about 1400 DNA molecules per nanozeolite-L particle.
In a last step the DNA functionalized zeolites can be coated with PLL by dispersing them for 1 hour in an aqueous solution of PLL (1% wt/wt) at 37 °C.
Upon PLL binding the zeta potential become positive and the size further increases to about 157 nm, which is a good size regime for further cell experiments[115, 116, 117].
The data for each functionalization step are summarized in figure 6.12.

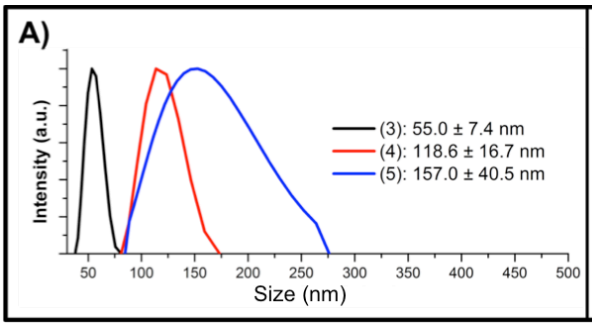

B)

Sample	Zeta potential (mV) in PBS
(1) and (2)	- 33.59
(3)	+ 2. 58
(4)	- 17.04
(5)	+ 28.28

Figure 6.12. Analysis of every functionalization step of the nanozeolites-L. A) size distribution by DLS of amine functionalized nanozeolites (black curve), DNA functionalized nanozeolites (red curve) and DNA and PLL coated nanozeolites (blue curve). C) Zeta potentials of every preparation step.

6.7. Intracellular DNA and DAPI release from nanozeolite-L

Due to the very poor uptake of the microzeolite-L the uptake was increased by using nanozeolite-L particles with a size of just a few tenth of nanometers. The same cell experiments were then performed with these particles.
DXP was first used as label since it is a fluorescent dye, which, due to its insolubility in water, is not able to leak from the zeolites. Therefore it will give us

information on the localization of the zeolites even after the complete detachment of the DNA. That allows for an independent kinetic study of the DNA release whilst monitoring the particle uptake and localization by using the DXP signal. Due to a very high particle uptake after 4 and 24 hours, the particles were not coated with PLL. No actin stain was used due to the emission overlap with DXP. DAPI staining for visualization of the cell nucleus was done after cell fixation. Additionally the uptake of these particles was proved by taking z-stacks after 24 hours. The results are shown in figure 6.13 and 6.14.

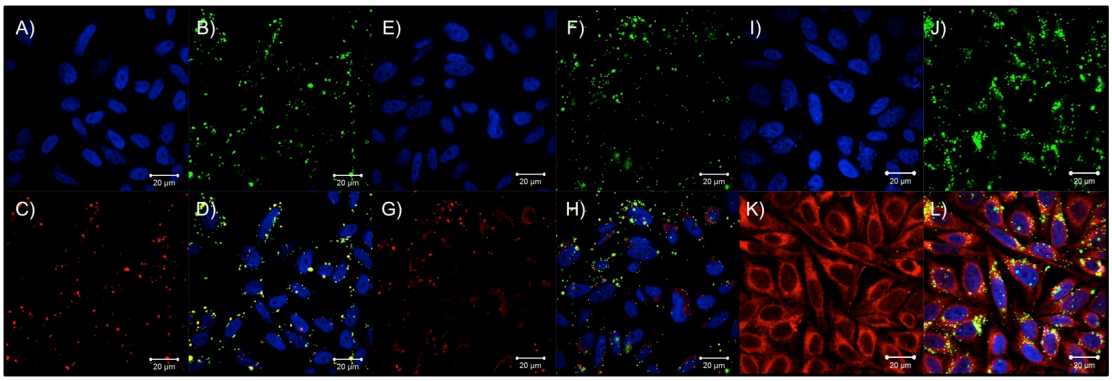

Figure 6.13. Confocal micrographs showing the uptake of DXP loaded nanozeolite-L. A to D: 1 hour incubation; E to H: 4 hours incubation; I to L: 24 hours incubation. A, E, I: DAPI emission; B, F, J: DXP fluorescence; C, G, K: Cy5 emission; D, H, L: overlay

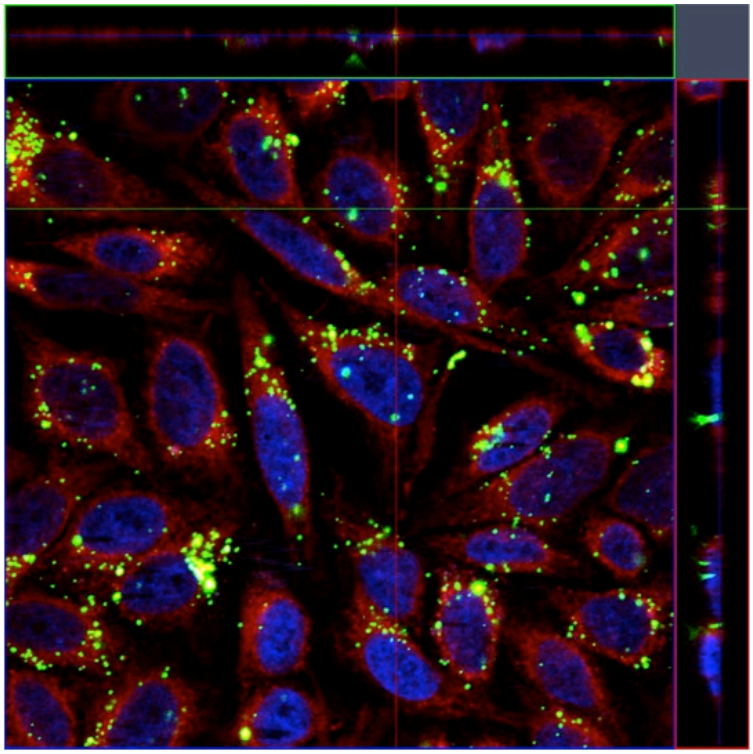

Figure 6.14 Confirmation of particle uptake by collecting z-stacks after 24 hours incubation.

Already after 1 hour, a significant amount of particles is uptaken by the cells. As it can be seen from the overlap of the DXP and Cy5 emission, the DNA is bound to the particles (See figure 6.13B and C). After 4 hours the intracellular

particle concentration is further increased. At this time we observe a very pale red staining of the cytoplasm, which we ascribe to small amounts of DNA detaching from the high number of particles inside the cells. However, the main part of the DNA is still located at the particle surface, which is confirmed by the overlap of the DXP and Cy5 signal. These effects are further enhanced for an incubation of 24 hours. The particle concentration in the cells is further increased which leads to a higher amount of detached DNA in the cytoplasm, see figure 6.13K.

In a next step the simultaneous intracellular DNA and DAPI release from those particles was studied in detail. DAPI loaded and DNA (Cy5 labeled) functionalized nanozeolite-L particles have been used and cell culture experiments have been performed as described for the microzeolite-L particles. The results are shown in figure 6.15.

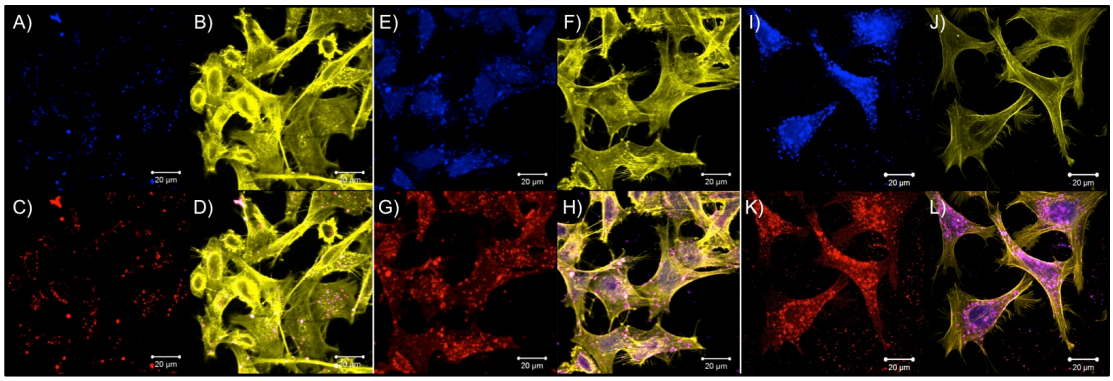

Figure 6.15. Confocal micrographs showing the uptake of DAPI loaded nanozeolite-L. A to D: 1 hour incubation; E to H: 4 hours incubation. I to L: 24 hours incubation. A, E, I: DAPI signal; B, F, J: Alexa Fluor® 568 Phalloidin signal; C, G, K: Cy5 signal; D, H, L: overlay.

After 1 hour, a small amount of particles is uptaken and the DNA is located at the particle surface, as proved by the overlap of the DAPI and Cy5 signals. The particle uptake is further increased after 4 hours and a pale staining of the nucleus, due to small amounts of DAPI leaking from the pores, can be seen. This effect is further increased after 24 hours of incubation. That the particles are indeed uptaken and not just being adsorbed on the cell membrane was further proven by recording z-stacks as shown in figure 6.16.

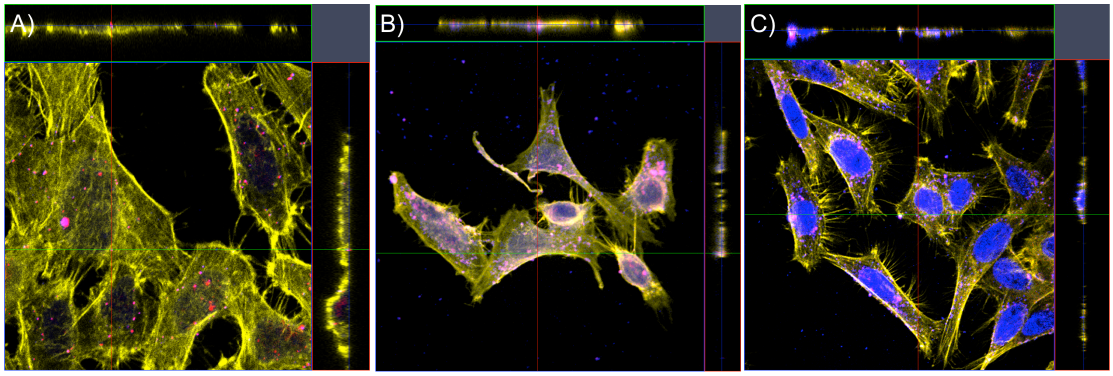

Figure 6.16. Z-stack to confirm particle uptake after 1 (A), 4 (B) and 24 hours (C) incubation.

Additionally, a cell viability study after 24 hours incubation shows negligible toxicity of our system, which is shown in figure 6.17. For experimental details of the viability study, see the experimental part at the end of this chapter.

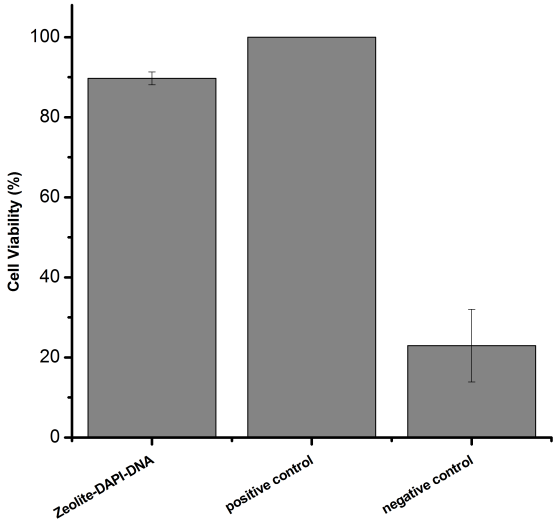

Figure 6.17. Cell viability studies of zeolite-DAPI-DNA towards HeLa cells for 24 hours.

These experiments already clearly prove the possibility of using zeolite-L nanoparticles as an efficient multifunctional drug and DNA delivery system to living cells. It has been shown that both the DAPI and DNA are slowly being released from the zeolites and accumulate in different cell compartments. Whereas the DAPI is localized in the nucleus, the DNA is localized around the cytoplasm, which will be further investigated in chapter 6.8.
However, one should be aware that the increasing concentrations of DAPI in the nucleus and DNA in the cytoplasm are affected by two independent mechanisms. On the one hand the DAPI and DNA are continuously released from the zeolites, which leads to increasing concentration of those in the nucleus and cytoplasm. But on the other hand the intracellular particle concentration increases over time, most probably linearly[118], which also leads to increasing concentrations of DNA and DAPI in the cells.

In a next step the kinetics of the DNA and DAPI release from the particles were studied in detail while keeping the intracellular particle concentration constant.

To determine the kinetics of DNA and DAPI release from the nanozeolite-L particles, the experimental conditions for cell incubation were slightly modified. To protect the DNA and the DAPI from a fast release and to increase the cell uptake by changing the total charge of the DNA modified zeolite from negative to positive, we have wrapped PLL on top of the oligonucleotide. The incubation time was reduced to 1 hour and a concentration of 0.01 mg/mL of zeolites was employed. After incubation the cells were extensively washed with PBS buffer to remove loosely bound zeolites from the cell surfaces. Then the cells were cultured and imaging was done directly after incubation, after 1 hour, 2 hours, 4 hours, 6 hours, 24 hours, 48 hours and 72 hours to follow the DAPI and DNA signals. The results are shown in figure 6.18.

To determine the effect of the PLL coating on the DAPI release kinetics, the cells were also incubated with DNA-functionalized particles, in the absence of PLL, and a concentration ten times higher, of 0.1 mg/mL, was used to achieve a sufficient uptake already after 1 hour. The results are summarized in figure 6.19.

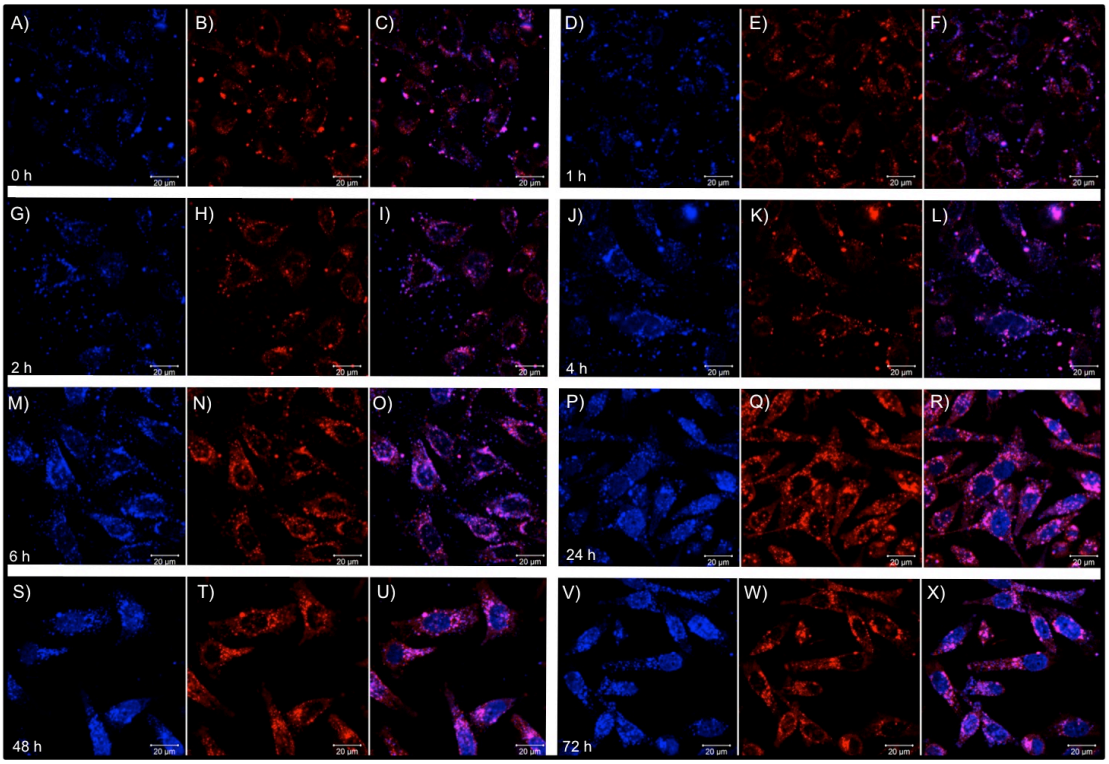

Figure 6.18. Confocal micrographs showing the kinetics of DAPI and DNA release from PLL covered nanozeolite-L. Incubation was done for 1 hour followed by an extensive washing with PBS buffer to remove surface adsorbed particles. The cells were incubated and the images recorded directly after incubation (A, B, C); after 1 hour (D, E, F); after 2 hours (G, H, I); after 4 hours (J, K, L); after 6 hours (M, N, O); after 24 hours (P, Q, R); after 48 hours (S, T, U) and after 72 hours (V, W, X). Left image: DAPI fluorescence; middle image Cy5 emission; right image overlay. Excitation = 405 and 633 nm for DAPI and Cy5 respectively. Emissions were recorded with a DAPI emission filter and a Cy5 emission filter.

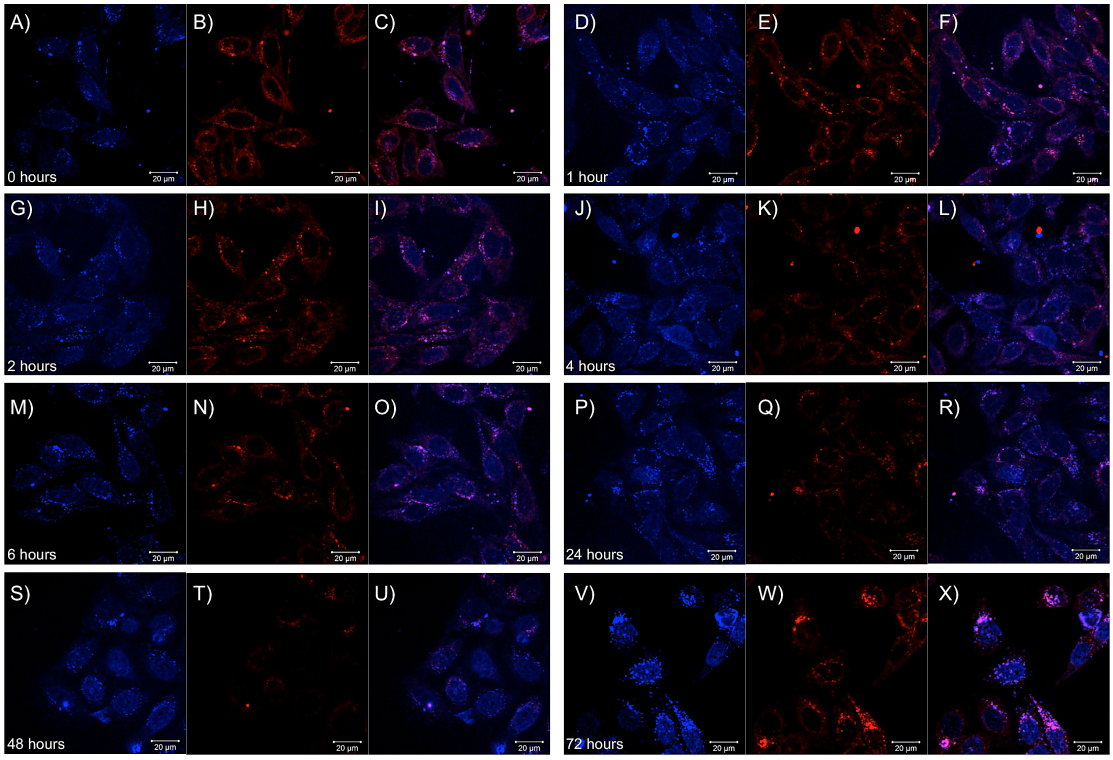

Figure 6.19. Confocal micrographs showing the kinetics of DAPI and DNA release from nanozeolite-L without PLL coating. Incubation was done for 1 hour followed by an extensive washing with PBS buffer to remove surface adsorbed particles. The cells were incubated and imaging was done directly after incubation (A, B, C); after 1 hour (D, E, F); after 2 hours (G, H, I); after 4 hours (J, K, L); after 6 hours (M, N, O); after 24 hours (P, Q, R); after 48 hours (S, T, U) and after 72 hours (V, W, X). Left image: DAPI signal; middle image: Cy5 signal; right image: Overlay. Excitation = 405 and 633 nm. Emission was recorded with a DAPI emission filter and a Cy5 emission filter.

As it can be seen, both particles were uptaken in sufficient amounts to study the kinetics. Although using a tenfold lower particle concentration, the uptake of the PLL coated particles was similar or even slightly higher compared to the uncoated particles.

Both samples show a slow release of DAPI and DNA from the zeolites and in both cases high intensities of DAPI (in the nucleus) and DNA (in the cytoplasm) can be recorded after 24, 48 and 72 hours. Keeping in mind that cell division occurs first after 24 hours, a decrease of the number of zeolites to about half is expected for each division. The main differences in the two experiments are the number of the particles that internalize in the living cells and the fact that for the PLL coated particles the release of the DAPI takes at least 4 hours. For the uncoated particles we observe a pale nucleus staining already after 1 hour of incubation. This time delay is indeed due to the time required by the PLL to degrade allowing the DAPI and DNA to leak into the cell.

6.8. Fate of the particles and the DNA after uptake

As reported for a variety of particle compositions and sizes, the particles are expected to accumulate in the lysosomes of the cells[115, 119, 120]. To prove this hypothesis, the lysosome was stained after 72 hours with the green fluorescent dye Lysotracker Green DND-26 and we checked the overlap of this emission with the fluorescence from the particles. As shown in figure 6.20 A-D, the emissions are very well overlapping (colocalization coefficient = 0.86), which proves the accumulation of the particles in the lysosomes.

Additionally, the intracellular localization of the desorbed DNA was studied. As reported in *in vitro* experiments, the DNA tends to migrate to the mitochondria and therefore we have checked if also for our system we can observe the same behavior. We have labeled the mitochondria with the yellow-orange emissive dye MitoTracker Orange CMTMRos, as shown in figure 6.20 E-H. A very good overlap (colocalization coefficient = 0.91) of the DNA signal with the mitochondria stain can be seen, which proves this hypothesis.

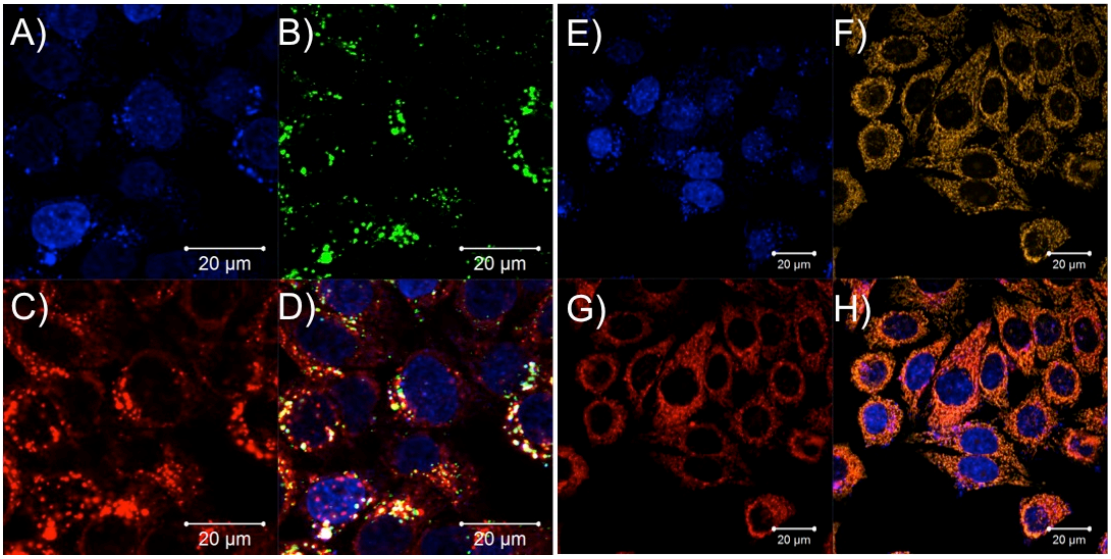

Figure 6.20. Confocal micrographs showing the localization of the particles in the lysosome (A – D) and the localization of the DNA in the mitochondria (E – H). A, E: DAPI emission; B: Lysosome stain; F: Mitochondria stain; C, G: Cy5 fluorescence; D, H: Overlay.

6.9. Conclusion

For the first time, the design and preparation of a multi-functional DNA and model drug (DAPI) release system based on zeolite-L particles has been demonstrated into living cells. We show, that the uptake can be significantly increased by using nanozeolite-L particles vs larger micrometer particles and that the presence of a polycation such as PLL can also play an important role for the internalization.

Upon degradation of the PLL both DAPI and DNA are released and using confocal microscopy we have investigated the kinetics and localization of the components. In living cells the particles are localized in the lysosome while

the desorbed DNA is localized in the mitochondria and the released DAPI migrates into the nucleus.

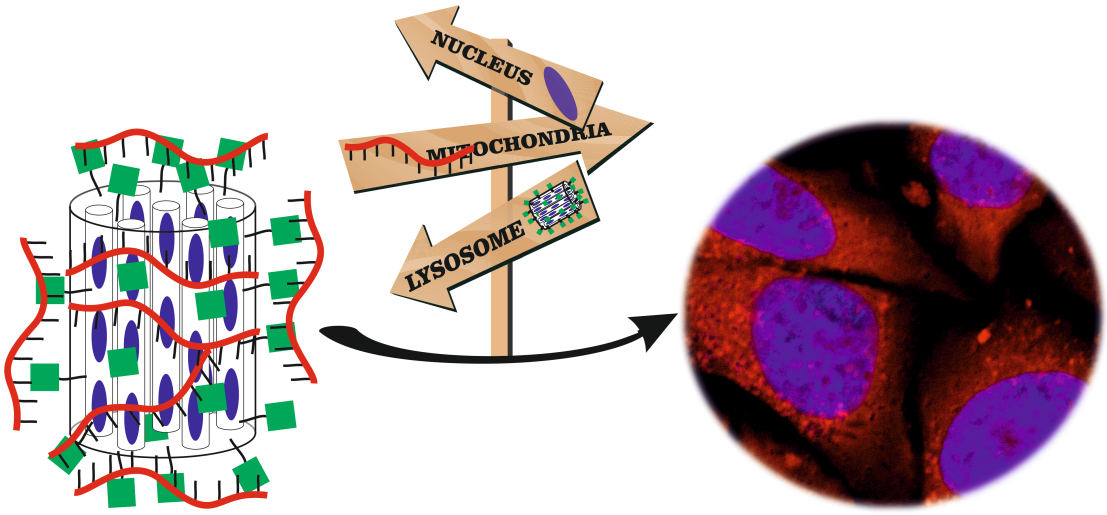

Figure 6.22. The zeolites are transported to the lysosomes, the DNA to the mitochondria and the DAPI into the cell nucleus.

The presented multifunctional system may be a prototype for the development of a new class of particles for a simultaneous oligonucleotides and drug delivery. In a next step a plasmid oligonucleotide can be used as well as Si-RNA for gene therapy. The combination of Si-RNA with drugs is of a particular interest for cancer therapy.

6.10. Experimental part

Synthesis of micro- and nanozeolite-L

For the synthesis procedure see chapter 2.

DXP loading of nanozeolite-L

DXP loading was done as described in chapter 2. In this case a loading of 7% was chosen.

Amino-functionalization using APTES

See chapter 2.

PLL coating

The zeolites were dispersed in a 1% (wt/wt) aqueous PLL solution and incubated for 1 hour. The zeolites were rrcovered by centrifugation and washed 2 times with deionized water.

Quantification of the DNA binding to microzeolite-L

Microzeolite-L (1mg) were incubated in different concentrated dye labeled DNA solutions in PBS buffer. The particled were incubated for 30 min at 37 °C and then removed by centrifugation. Quantification was then done by subtracting the DNA concentration in the supernantant and from the initial DNA concentration. A calibration curve was used for quantification. The final curve (5 levels, n = 3 for each level) is shown in figure 6.17. Its equation is y = 0.1923x and the significance of the linear model was confirmed by Mandel test.

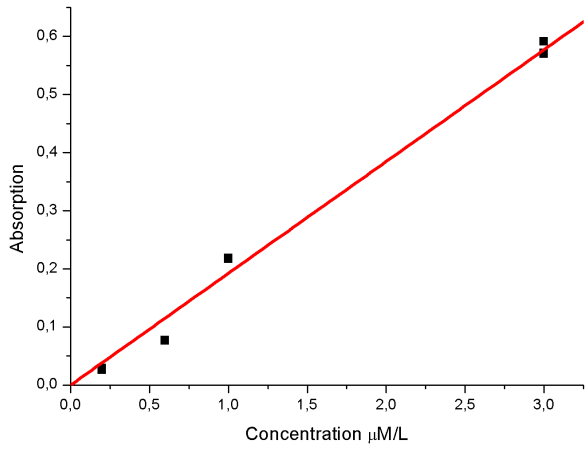

Figure 6.22. Calibration curve.

Calculation of the number of DNA molecules binding to one single microzeolite-L particle

Zeolite-L dimensions: diameter = 1000 nm
radius = 500 nm
length = 1000 nm
mass = 0.001 g

Number of parallel channels:

$n_{ch} = \frac{(r)(r)^2\pi}{|a|^2\, sin\, 60} = \frac{\pi}{2\sqrt{3}}\left(\frac{2r}{|a|}\right)^2$ with (1)

a: primitive vector perpendicular to the c-axis
r: zeolite-L diameter radius in nm

Equation (1) can be approximated as

$\mathrm{n_{ch}} = 1.104\ \mathrm{r}^2$ (2)

Thus a zeolite-L with a radius of 500 nm obtains about 276000 parallel channels.

Number (mol) of unit cells in one crystal:

$\mathrm{N_{ch}} = \mathrm{n_{ch}}\left(\frac{\mathrm{l}}{\mathrm{N_A}\,|\mathrm{c}|}\right)$ with (3)

l: length of zeolite crystal
|c|: primitive c-vector (0.75 nm)

Thus a zeolite L crystal with a length of 1000 nm has 6.011E-16 mol unit cells.

Weight of one crystal:

$\mathrm{m_{Zeo}} = \mathrm{N_{ch}}\ \mathrm{M_{u.c.}}$ with (4)

$M_{u.c.}$ being the molecular weight of one unit cell (2880 g/mol)
Thus the weight of one zeolite-L crystal is about 1.76E-12 g.

Number of crystals in 1 mg:

$\mathrm{N_{Zeo}} = \frac{\mathrm{Sample\ mass}}{\mathrm{m_{Zeo}}}$ (5)

Thus in 1 mg of zeolites there are 5.68E8 single crystals.

DNA absorbed on 5.68E8 zeolite-L particles (1 mg): 8 nmol

DNA molecules on one zeolite crystal:

$\frac{8\mathrm{E}-9*6.022\mathrm{E}23}{5.68\mathrm{E}8}$ = **8.5E6** (6)

Quantification of the DNA binding to nanozeolite-L

Nanozeolite-L (1mg) were incubated in DNA (Cy5 labeled) solutions of different concentrations of in PBS buffer. The particled were incubated for 30 min at 37 °C and then removed by centrifugation. Quantification was then done by subtracting the DNA concentration in the supernantant and from the initial DNA concentration.Quantification was done by usinf the literature molar extinction coefficient of 250000 M^{-1} cm^{-1}. An absorption of the supernatant of 0.2 was obtained, which corresponds to a concentration of 6.4 nmol / 0.5 mL.

Calculation of the number of DNA molecules binding to one single nanozeolite-L particle

This was done as described for the microzeolite-L particles.

Cell viability study

Cell viability was measured by an automatic cell counter CASY (Roche Innovatis AG, Bielefeld, Germany). 50,000 cells were grown in 2 ml of culture media inside 6 well plates at 37oC, 5 % CO2 environment for 24 hours. Culture media was removed and replaced by solution containing 0.01 mg/ml of zeolites-DAPI-DNA, followed by cell incubation. After 24 hours of incubation, the culture media were removed to 2 ml of eppendorf tube and 0.5 ml of trypsin were added. In order to detach the cell from the surface of the plate, cells were incubated for the next 10 minutes. Subsequently, 1.5 ml of new culture media were added to neutralize trypsin. Cell suspension together with first solution collected were removed into 10 ml eppendorf tube and centrifuged at 1000rpm for 5 minutes. Supernatant were removed and cell palates were suspended into 1 ml of new culture media. 200 µl of the cell suspension was dissolved in 10 ml of CASY solution and measurement was performed. To add negative control experiment, the exact same procedure was performed by incubating cells in 50% of ethanol in culture media while for positive control, cells were incubated only with culture media.

References

[1] Spizizen, J., Reilly, B. E., and Evans, A. H., *Ann. Rev. Microbiol.*, 20, 371-400, **1966**

[2] Friedmann, T., and Roblin, R., *Science*, **175**, 949-955, **1972**.

[3] Luo, D., and Saltzman, W. M., *Nat. Biotech*., **18**, 33-37, **2000**.

[4] Fasbender, A., Zabner, J., Zeiher, B.G.& Welsh, M.J. *Gene Ther.* **4**, 1173–1180, **1997**.

[5] Matsui, H., Johnson, L.G., Randell, S.H. & Boucher, R.C. *J. Biol. Chem*. **272**, 1117–1126, **1997**.

[6] Crystal, R.G. *Science* **270**, 404–410, **1995**.

[7] Tripathy, S.K., Black, H.B., Goldwasser, E. & Leiden, J.M. *Nat. Med.* **2**, 545–550, **1996**.

[8] Mann, M.J. et al. *Proc. Natl. Acad. Sci. USA* **96**, 6411–6416, **1999**.

[9] Yao, C., Guo, F., Li, C., and Sun, C., *Curr. Drug. Metab.* **14**, 319-3123, **2013**.

[10] Liu, F., Song, Y. & Liu, D. *Gene Ther*. **6**, 1258– 1266, **1999**.

[11] Zhang, G., Budker, V. & Wolff, J.A. *Hum. Gene Ther.* **10**, 1735–1737, **1999**.

[12] Shi, Q. et al., *J. Biomed. Biotechnol.*, doi: 10.1155/2011/148763, **2011**.

[13] Pillai, R et al. *Pharm. Res.* **15**, 1743– 1747, **1998**.

[14] Endo-Takahashi, Y. *et al*., *Biomaterials* **34**, 2807-2813, **2013**.

[15] Anderson, C. D. *et al.*, *Ultrasound Med. Biol.* **13**, 872-877, **2013**.

[16] Sirsi, S. R., and Borde, M. A., *Theranostics* **2**, 1208-1222, **2013**.

[17] Yang, N.S., Burkholder, J., Roberts, B., Martinell, B. & McCabe, D. *Proc. Natl. Acad. Sci. USA,* **87**, 9568–9572, **1990**.

[18] Yang, N.S. & Sun, W.H. *Nat. Med.* **1**, 481 –483, **1995**.

[19] Ye, G.N., Daniell, H. & Sanford, J.C. *Plant Mol. Biol.* **15**, 809– 819, **1990**.

[20] Yen, M.-C., Lai, M.-D., *Methods Mol. Biol.* **940**, 169-174, **2013**.

[21] Wang, H., Jiang, L., *Nature Prot.* **6**, 419-426, **2011**.

[22] Chang, M. et al., *Human Gene Therap.* **19**, 391-395, **2008**.

[23] Wong, T.K. & Neumann, E. *Biochem. Biophys. Res. Commun.* **107**, 584 – 587, **1982**.

[24] Neumann, E., Schaefer-Ridder, M., Wang, Y. & Hofschneider, P.H. *EMBO J.* **1**, 841–845, **1982**.

[25] Banga, A.K. & Prausnitz, M.R. *Trends Biotechnol.* **16**, 408–412, **1998**.

[26] Oshima, Y. et al. *Gene Ther.* **5**, 1347–1354, **1998**.

[27] Aihara, H. & Miyazaki, J. *Nat. Biotechnol.* **16**, 867– 870, **1998**.

[28] Rizzuto, G. etal. *Proc. Natl. Acad. Sci. USA* **96**, 6417–6422, **1999**.

[29] Heller, R., *Preclinica* **1**, 198-208, **2003**.

[30] Zhou, R., Norton, E., David, A., *Meth. Molec. Biol*., 233-247, **2008**.

[31] Felgner, P.L. *Adv. Drug Deliv. Rev.* **5**, 163– 187, **1990**.

[32] Vaheri, A. & Pagano, J.S. *Virology* **27**, 434– 436, **1965**.

[33] Graham, F.L. & Eb, A.J.V.D. *Virology* **52**, 456–467, **1973**.

[34] Chen, L. et al., *PLoS One*, **8**, 71053, **2013**.

[35] Chen, S. et al., *Pharma. Res*. **30**, 1968-1978, **2013**.

[36] Trabulo, S. et al., *Pharmaceut. Des*. **19**, 2895-2923, **2013**.

[37] Cardoso, A. M. et al., *Molec. Pharmaceut*. **10**, 2653-2666, **2013**.
[38] Alhakamy, N. et al., *Therapeut Deliv*. **4**, 741-757, **2013**.
[39] Lee, C.-Y. et al., *Biomaterials* **32**, 6264-6276, **2011**.
[40] Felgner, P.L. et al. *Proc. Natl. Acad. Sci. USA* **84**, 7413–7417, **1987**.
[41] Zauner, W., Ogris, M. & Wagner, E. *Adv. Drug Del. Rev.* **30**, 97–113, **1998**.
[42] Kim, J.S., Kim, B.I., Maruyama, A., Akaike, T. & Kim, S.W., *J. Contr. Release* **53**, 175– 182 , **1998**.
[43] Wu, C.H., Wilson, J.M. & Wu, G.Y., *J. Biol. Chem.* **264**, 16985–16987, **1989**.
[44] Schaffer, D.V.& Lauffenburger, D.A., *J. Biol. Chem.* **273**, 28004 –28009, **1998**.
[45] Sanjoh, M. et al., *Macromol. Rapid Commun*. **31**, 1181-1186, **2010**.
[46] Ma, D. et al., *J. Colloid Interface Sci*. **405**, 305-3011, **2013**.
[47] Sanjoh. M. et al., *Biomacromolecules* **13**, 3641-3649, **2012**.
[48] Wang, et al., *Colloids and Surfaces* **326**, 29-36, **2008**.
[49] Sorgi, F.L., Bhattacharya, S. & Huang, L. *Gene Ther.* **4**, 961–968, **1997**.
[50] Paul, R.W. et al., *Hum Gene Ther.* **8**, 1253–1262, **1997**.
[51] Smith, L.C. et al., *Adv. Drug Del. Rev.* **30**, 115– 131, **1998**.
[52] Huang, Y., *Adv. Drug Deliv. Rev.* **65**, 1299-1315, **2013**.
[53] Simeon, R. et al., *ACS Chem. Biol*. DOI: 10.1021/cb4004089, **2013** (ASAP)
[54] Tao, P. et al., *Proc. Natl. Acad. Sci. USA* **110**, 5846-5851, **2013**.
[55] Karak, N. & Maiti, S., *J. Polymer Mater.* **14**, 105, **1997**.
[56] Haensler, J. & Szoka, F.C., Jr., *Bioconjug. Chem.* **4**, 372–379, **1993**.
[57] Kukowska-Latallo, J.F. et al., *Proc. Natl. Acad. Sci. USA* **93**, 4897–4902, **1996**.
[58] Tang, M.X., Redemann, C.T. & Szoka, F.C. Jr., *Bioconjug. Chem.* **7**, 703–714, **1996**.
[59] Luo, D., and Saltzman, *Nature Biotechnol.* **18**, 33-37, **2000**.
[60] Navarro, G. et al., *Gene Med*. **3**, 135-144, **2001**.
[61] Arima, H., Motoyama, K, and Higashi, T., *Pharmaceutics* **4**, 130-148, **2012**.
[62] Turrin, C.-O., and Caminade, A.-M., in *Dendrimers* (Eds. Caminade, A.-M., Turrin, C.-O., Laurent, R., Ouali, A., and Delavaux-Nicot, B.) WILEY-VCH, Chichester, 413-435, **2011**.
[63] Truong-Le, V.L., August, J.T. & Leong, K.W., *Hum. Gene Ther.* **9**, 1709–1717, **1998**.
[64] Leong, K.W. et al., *J. Contr. Release* **53**, 183– 193, **1998**.
[65] Van de Wetering, P., Moret, E.E., Schuurmans-Nieuwenbroek , N.M., van Steenbergen, M.J. & Hennink, W.E., *Bioconjug. Chem.* **10**, 589–597, **1999**.
[66] Van de Woude, I.et al., *Proc. Natl. Acad. Sci. USA* **94**, 1160–1165, **1997**.
[67] Zhao, D. et al., *J. Pharmaceut*. **413**, 260-270, **2011**.
[68] Hartmann, L., and Boerner, H. G., *Adv. Mater*. **21**, 3425-3431, **2009**.
[69] Ernst, W., and Kloeckner, J., *Adv. Polym. Sci*. **192**, 135-173, **2006**.
[70] Jon, S. et al., *Biomacromolecules* **4**, 1759-1762, **2003**.
[71] Jones, D.H., Corris, S., McDonald, S., Clegg, J.C. & Farrar, G.H., *Vaccine* **15**, 814 –817, **1997**.

[72] Ando, S., Putnam, D., Pack, D.W.& Langer, R., *J. Pharm. Sci.* **88**, 126–130, **1999**.
[73] Wang, D., Robinson, D.R., Kwon, G.S. & Samuel, J., *J. Contr. Release* **57**, 9– 18, **1999**.
[74] Luo, D., Woodrow-Mumford, K., Belcheva, N. & Saltzman, W.M., *Pharm. Res.* **16**, 1300–1308, **1999**.
[75] Shea, L.D., Smiley, E., Bonadio, J.& Mooney, D.J., *Nat. Biotechnol.* **17**, 551–554, **1999**.
[76] Pannier, A. K., and Shea, L. D., Molecular Therapy, **10**, 19-26, **2004**.
[77] Mahor, S., Collin, E., Dash, B. C., and Pandit, A., *Curr. Drug Deliv*. **8**, 354-362, **2011**.
[78] Torchilin, V P., *Biopolymers* **90**, 604-610, **2008**.
[79] Wang, Q. et al., *Nat. Commun*. **4**, 1867, **2013**.
[80] Meng, F. et al., *materialstoday* **15**, 436-442, **2012**.
[81] Wijaya, A., Schaffer, S. B., Pallares, I. G., and Hamad-Schifferli, K., *ACS Nano*, **3**, 80-86, **2008**.
[82] Ghosh, P. S., Kim, C.-K., Han, G., Forbes, N. S., and Rotello, V. M., *ACS Nano*, **2**, 2213-2218, **2008**.
[83] Poon, L. et al., ACS Nano, **4**, 6395-6403, **2010**.
[84] Han, G. et al., *Angew. Chem. Int. Ed*., **45**, 3165-3169, **2006**.
[85] Yamashita, S. et al., *Bioorganic & Medicial Chemistry*, **19**, 2130-2135, **2011**.
[86] Takahashi, H., Niidome, Y., and Yamada, S., *Chem. Commun*., 2247-2249, **2005**.
[87] Barhoumi, A., Huschka, R., Bardhan, R., Knight, M. W., and Halas, N. J., *Chem. Phys. Lett*., **482**, 171-179, **2009**.
[88] Thibaudau, F., *J. Phys. Chem. Lett*., **3**, 902-907, **2012**.
[89] Huschka, R. et al., *J. Am. Chem. Soc*., **133**, 12247-12255, **2011**.
[90] Diaz, J. A., and Gibbs-Davis, J M., *Small*, **2013**.
[91] Sun, H., Zhu, X., Zhang, L., Zhang, Y., and Wang, D., *Mater. Sci. Eng. C*, **30**, 311-315, **2010**.
[92] Tanka, K., Narita, A., and Chujo, Y., *Composite Interfaces*, **20**, 27-32, **2013**.
[93] Leung, K. C., *Chem. Commun*. **49**, 549-551, **2013**.
[94] Salem, A. K., Searson, P. C., and Leong, K. W., *Nat. Mater*., **2**, 668-671, **2003**.
[95] De Puig, H. et al., *PLoS One* **8**, 68511, **2013**.
[96] Kah, J. C. Y. et al., *ACS Nano* **6**, 6730-6740, **2012**.
[97] Fukushima, H. et al., *Chem. Lett*. **41**, 711-712, **2012**.
[98] Huschka, R. et al., *J. Am. Chem. Soc* **133**, 12247-12255, **2011**.
[99] Wijaya, A. et al., *ACS Nano*, **3**, 80-86, **2009**.
[100] Chen, C.-C. et al., *J. Am. Chem. Soc* **128**, 3709-3715, **2006**.
[101] Takahashi, H., Niidome, Y., and Yamada, S., *Chem. Commun*. **17**, 2247-2249, **2005**.
[102] Wu. W., et al., *Angew. Chem. Int. Ed*., **44**, 6358-6362, **2005**.
[103] Cheung, W. et al., *Adv. Drug Deliv. Rev*. **62**, 633-649, **2010**.

[104] Kar, M et al., *Part. Part. Syst. Charact*. **30**, 166-179, **2013**.
[105] Hartono, S. B., *ACS Nano* **6**, 2104-2117, **2012**.
[106] Torney, F., Trewyn, B. G., Lin, V. S.-Y., and Wang, K., *Nat. Nanotechn*., **2**, 295-300, **2007**.
[107] Zhang, Y. et al., *Anal. Chem*., **84**, 1956-1962, **2012**.
[108] Climent, E. et al., *Angew. Chem. Int. Ed*., **122**, 7439-7441, **2010**.
[109] Calzaferri, G., Huber, S., Maas, H., Minkowski, C., *Angew. Chem. Int. Ed.* **42**, 3732-3758, **2003**.
[110] Albuquerque, R. Q., and Calzaferri, G., *Chem. Eur. J.* **13***,* 8939-8952, **2007**.
[111] Li, Z., Shuai, C., Li, X., Xiang, J., and Li, G., *J. Biomed. Mater. Res. A* **101**, 2846-2850, **2013**.
[112] Singh, H. D., Wang, G., Uludag, H., and Unsworth, L. D., *Acta Biomateria*, **6**, 4277-4284, **2010**.
[113] Kim, S. H., Jeong, J. H., Chun, K. W., and Park, T. G., *Langmuir* **21**, 8852-8857, **2005**
[114] Ren, K., Ji, J., and Shen, J., *Biomaterials* **27**, 1152-1159, **2006**.
[115] Kulkarni, S. A., and Feng, S. S., *Pharm. Res*. 30, 2512-2522, **2013**.
[116] Albanese, A., Chan, W., Warren, C. W., *ACS Nano* 5, 5478-5489, **2011**.
[117] Li, Z., Hüve, J., Krampe, C., Luppi, G., Tsotsalas, M., Klingauf, J., De Cola, L., Riehemann, L., *Small* 9, 1809-1820, **2013**.
[118] Salvati, A., et al., *Nanomedicine* **7**, 818-826, **2011**.
[119] Wang, F. et al., *Nanomedicine* **2013**, doi: 10.1016/j.nano.2013.04.010.
[120] Laskar, A., Ghosh, M. Khattak, S. I., Li, W., Yuan, X.-Y., *Nanomedicine* 7, 705-717, **2012**.

Zeolites as key-components for bio-medicine - Zeolite-L as a multifunctional PNA and drug delivery system

Abstract

This chapter describes the use of zeolite-L nanocrystals for an efficient PNA delivery into living cells. In the beginning a short overview over PNAs and a description of the different approaches to deliver these oligonucleotides to living cells will be given. After that the material preparation, in vitro experiments and their results will be described in detail.

Alessandro Bertucci, **Henning Luelf**, Dedy Septiadi, Alex Manicardi, Roberto Corradini*, Luisa De Cola*, *Adv. Healthcare Mater.*, 2013, submitted.

7.1. Introduction

In the previous chapter I have shown that zeolites can be used as a multifunctional DNA and drug delivery system. Now I describe the multifunctional delivery of peptide nucleic acids (PNAs) and a model drug into living cells.
PNAs have been proven to be a very powerful tool in biomedicine and gene therapy and there is great demand to efficiently deliver PNAs into living cells.

This project was carried out in cooperation with Professor Corradini from the University of Parma and in particular with Dr. Alex Manicardi and Mr. Alessandro Bertucci and Mr. Dedy Septiadi from the group of Professor De Cola (cell culture and confocal microscopy).

Peptide Nucleic Acids (PNAs)

Peptide Nucleic Acids (PNAs) are oligonucleotide (RNA and DNA) mimics where the sugar-phosphate backbone is replaced by a polyamide skeleton, which is composed of N-(2-aminoethyl)glycine units[1]. A comparison of the structures of RNA, DNA and PNA is shown below.

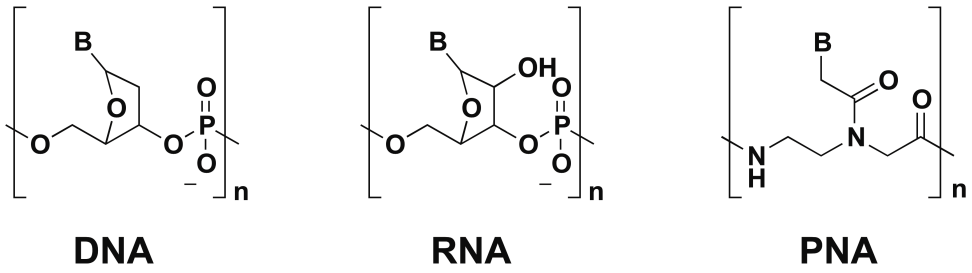

Figure 7.1. Structures of DNA, RNA and PNA

PNAs can bind to oligonucleotides according to standard Watson-Crick rules, but due to the lack of negatively charged phosphate groups in the backbone (and therefore electrostatic repulsion), PNA/oligonucleotide binding is significantly stronger than oligonucleotide/oligonucleotide binding, which is reflected in their increased thermal stability.
The binding is so strong that PNAs are able to dissociate DNA/DNA duplexes to form PNA/DNA pairs, which is called strand invasion[2]. Another interesting feature is the high selectivity in PNA/oligonucleotide binding. A single base-pair mismatch is much more destabilizing compared to oligonucleotide/oligonucleotide binding of the same length[3], which allows for very specific sequence recognition.
Above that, PNAs are highly stable towards enzymatic degradation of both nucleases and peptidases, because natural enzymes cannot recognize their unnatural backbone and especially due to their high stability in biological media PNAs have become a powerful tool in biochemistry, biomedicine and biotechnology[4].

PNAs have widely been applied as the functional unit in biosensors, like microarrays, electrochemical-, surface plasmon resonance (SPR)-biosensors, FISH and single molecule detection[5, 6, 7, 8].

7.2. Peptide Nucleic Acids in Gene Therapy

Although PNAs offer great potential for applications in biochemistry and biomedicine, a mayor drawback is their very poor membrane permeability, which makes practical applications very difficult.

During the years there has been a big effort done to overcome this problem, which was mostly resolved by conjugating the PNAs with different peptides or by directly modifying their backbone[9, 10, 11, 12, 13, 14, 15, 16, 17]. A very popular approach to increase membrane permeability is the conjugation of PNAs with membrane penetrating peptides (MPP), even though these PNA/MPP couples show just low abilities to escape from endosomes[10, 18].

Conjugates with arginine-rich peptides were for example used by Abes et al. to enter HeLa cells in absence of endosomolytic agents for sequence-specific interference with the nuclear pre-mRNA splicing machinery[11].

Arginine-based peptides were used also by Fabbri et al., showing that PNA conjugated with octaarginine at the carboxylic terminus was efficiently taken up by human leukemic K526 cells, inhibiting the activity of the target miRNA-210[12].

Lysine conjugates have also been used to deliver PNA in mice[19, 20]. Recently, Gait and coworker showed that the introduction of a terminal Cys residue further increased the cellular uptake of Cys-Lys-PNA-Lys_3 conjugate[13].

An alternative approach to enhance PNA cell uptake has been based on the direct modification of the PNA backbone, most of the times exploiting cationic modifications[21]. For example, C5-arginine-modified PNAs were successfully tested by Manicardi et al. to enter K526 cells and to inhibit the activity of the target miRNA-210[16]. Aminomethylene-modification is also reported by Mitra and Ganesh as a feasible candidate to improve PNA cellular uptake[17].

Very recently also first examples of using polymeric soft nanoparticles as PNA carrier moieties have been reported in the literature. Fang *et al.* reported an approach based on cationic shell-cross-linked knedel-like nanoparticles[22]. This is, together with the work of McNeer et al.[23] presenting the use of poly(lactic-co-glycolic acid) (PLGA) nanoparticles as nanocarriers for PNA oligonucleotide, one of the few examples in literature in which nanoparticles, more precisely soft polymeric, were thought as tools to facilitate PNA delivery into cells.

However, nothing is known of using hard and eventually highly porous nanoparticles, where the pores can additionally be used to add further functions to the system.

In biomedicine hard and porous nanoparticles have widely been used for drug delivery applications and to date mesoporous silica nanoparticles (MSNP) are the most used nanomaterials for this purpose[24, 25, 26]. Due to their high porosity and large surface area these species show great potentials in manufacturing tailor made multifunctional nanocarriers for transfection.
Very similar to MSNP are the crystalline zeolites. They are also silica-based materials, but contain a different silica/alumina ratio depending on the type of zeolite. This aluminosilicate are also highly porous, but, even though extremely popular in the areas e.g. of catalysis, dehydration and additive of detergent, they are much less studied in biomedicine. Preliminary *in vitro* and *in vivo* experiments for zeolite-L have been reported in the last years[27, 28, 29, 30, 31, 32] but none of them dealing with applications for transfection or gene therapy.
Furthermore it has been shown that soft materials like polymers can generally be used to increase the uptake of nanoparticles into cells[33, 34, 35, 36, 37, 38].

In this chapter the coupling of PNA to zeolites zeolite-L will be investigated for the first time, and proved that an efficient PNA delivery into living cells is possible.
The general strategy, depicted in figure 7.2, consists of a system designed in a way, that the PNA probes were covalently attached to the outer surface of the crystals and additionally the channels were filled with functional molecules. The entrapped molecules can be either fluorescent dye molecules to simply follow and localize the particles after cell uptake, or a model drug, which intracellular release can be monitored after cell uptake.
Due to the non-membrane permeable nature of the PNA probes, the bare PNA functionalized particles are expected to be very poorly uptaken (Figure 7.2.A).
To increase the cellular uptake, the system can further be coated with poly-L-lysine (PLL), which serves as a biodegradable uptake-enhancing compound. After cell uptake, the PLL degrades and leaves behind the active PNA/zeolite-L system (See figure 7.2.B).

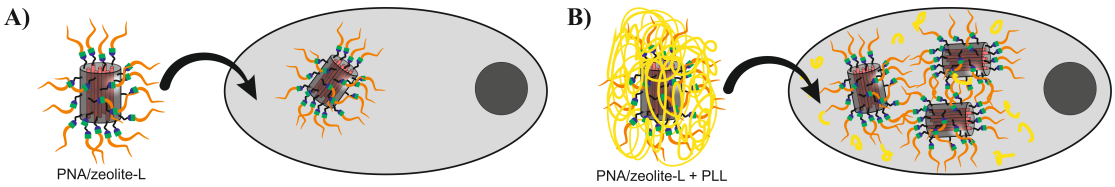

Figure 7.2. Schematic representation of the working paradigm. A) Uncoated PNA functionalized zeolites are poorly taken up into cells. B) PLL coating leads to an increased cell uptake. The PLL finally degrades inside the cells and a high amount of PNA/zeolite-L particles are taken up in this way.

In the next sections a detailed description of the experiments and results will be given.

7.3. Material preparation and characterization

The zeolite-L nanocrystals were synthesized as described in chapter 2 and analysis was done by TEM, DLS and zeta potential measurements.

The zeolites were obtained as monodisperse single crystals with a size of about 60 nm and show a zeta potential of –34.05 mV (in PBS buffer). In a next step the pores were filled with the dye or model drug.

The dye was chosen in the way, that a leaking from the pores into the culture media or cell is prevented. Therefore the water insoluble neutral dye DXP was incorporated in the pores as described in chapter 2. For the structure of DXP see figure 7.3.

After dye insertion, the nanoparticles have been amine functionalized with APTES. This functionalization has been chosen because the reaction can be followed by zeta potential measurements and the NH_2 can be easily tested by a positive ninhydrin test. Also the amino groups can then be easily converted into carboxylate functionalities. Amine functionalization has been confirmed by a zeta potential shift from -34.05 mV to +15.70 mV (in PBS buffer) and a positive ninhydrin test.

In a next step the amine groups were converted into carboxylic acid by reacting them with succinic anhydride, which leads to a decrease of the particle zeta potential to –37.37 mV.

Then the PNA was bound covalently to the surface of zeolite-L. To attach the PNA probes [H-$(AEEA)_2$-CTTTCCTTCACTGTT-NH_2 (AEEA = 2-(2-aminoethoxy)ethoxyacetyl spacer)], the carboxylic acids were first activated by converting them into NHS esters and the PNA probes were attached by coupling reaction. The remaining NHS ester groups were then quenched with ethanolamine.

After PNA binding the size increased to about 85 nm and the zeta potential shifted to –10.21 mV (in PBS buffer). The resulting slightly negative zeta potential is ascribed to the presence of remaining carboxylic acid functions and is very important for a later electrostatic PLL binding to the particles.

The particle preparation scheme and characterization is shown in figure 7.3.

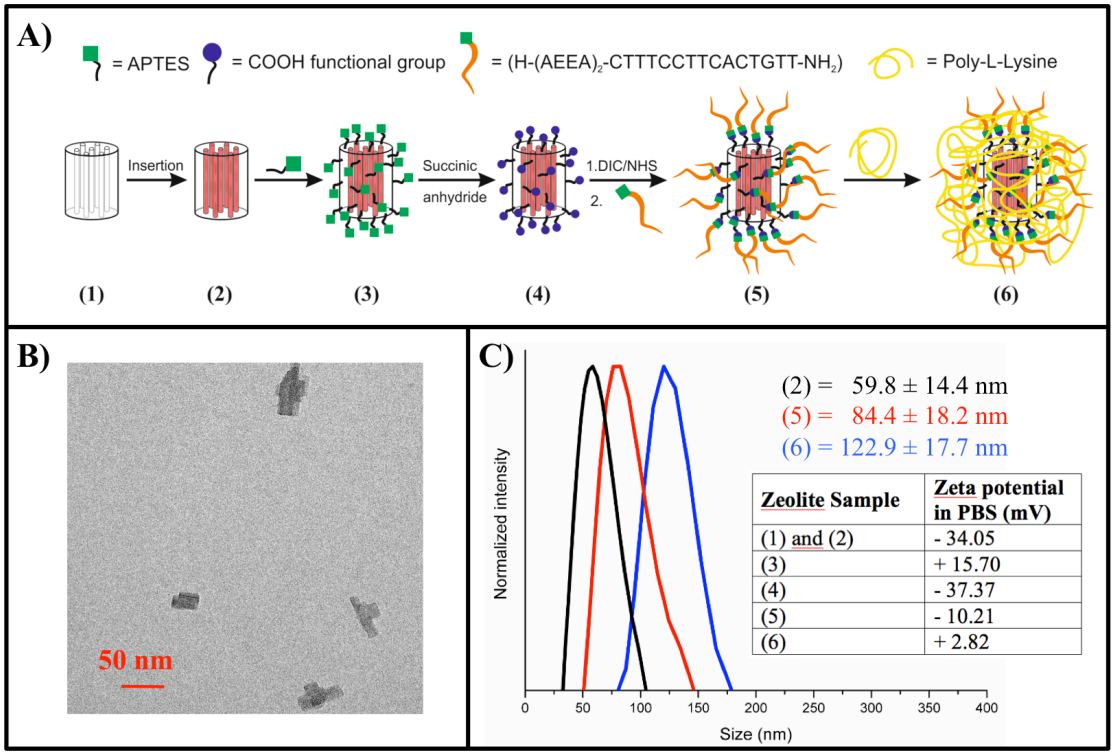

Figure 7.3. A) Functionalization scheme to obtain PNA functionalized zeolite-L nanoparticles. B) TEM images of zeolite-L nanoparticles. C) Size distribution of zeolite-L nanoparticles by DLS and zeta potential of every functionalization step (table).

The number of PNA probes attached to a single zeolite-L crystal was then determined.
Therefore the PNA has been labeled with a fluorescent dye (TAMRA), which was used for quantification by means of UV/Vis spectroscopy after the PNA functionalized particles have been dissolved in hydrofluoric acid (HF).
About **145** PNA molecules are attached to the surface of a single zeolite-L nanocrystal. For a detailed calculation see experimental section.

For following *in vitro* (and also *in vivo*) experiments it is crucial that the PNA maintains its biological activity even when its bound to the particles.
In order to prove that this is the case a hybridization test with a full match Cy3 labeled DNA strand was performed.
If the PNA probes maintain their activity, they should hybridize with the full match DNA oligonucleotide.
The zeolites were therefore filled with DAPI and functionalized with PNA. The particles were dispersed in PBS and a full complementary oligonucleotide sequence was added. Incubation was done for one hour at room temperature and the particles were washed with copious amounts of deionized water.
The co-localization of both dyes, the DAPI filled in the zeolites and the Cy3 attached to the DNA, was then used to confirm hybridization by using confocal microscopy. The results are shown in figure 7.4 A-C.

At the same time a control sample (DAPI filled zeolite-L without any further functionalization) was treated in the same way to prove that the DNA is indeed binding to the PNA probes and not just adsorbed on the particle surfaces (See figure 7.4 D-F).
Additionally a zeta potential shift to more negative potentials (-24.8 mV) after DNA binding confirms a successful binding. The negative shift is due to the negatively charged phosphate groups of the DNA.

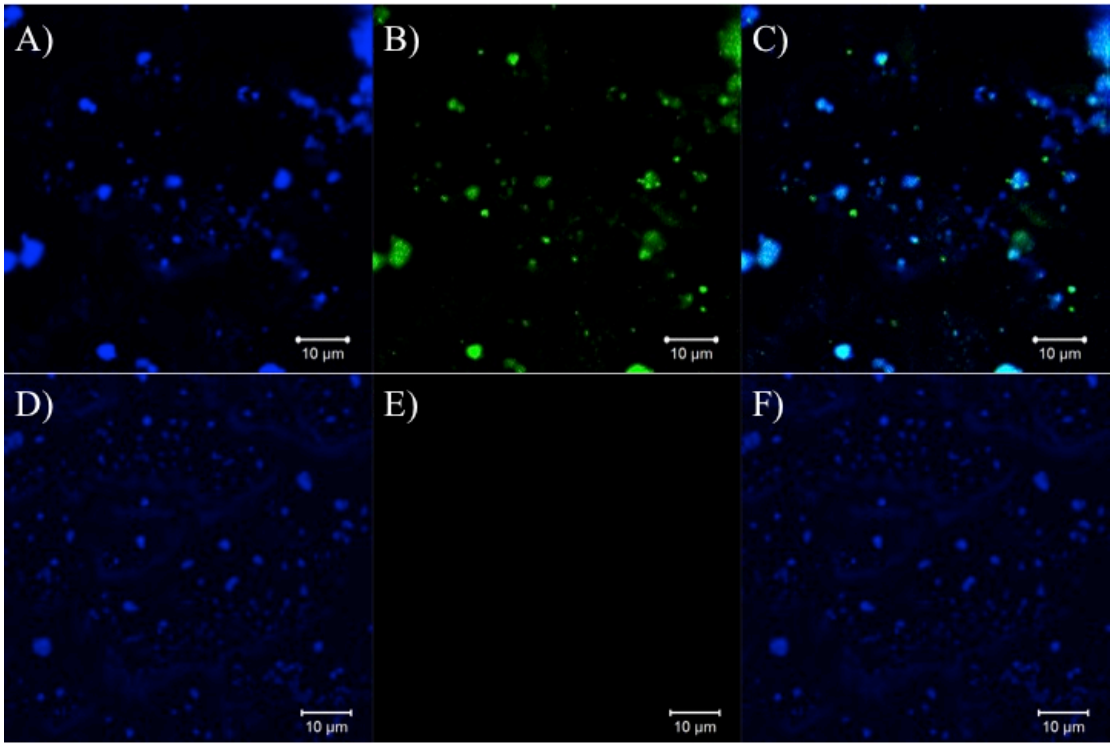

Figure 7.4. Confocal micrographs of PNA functionalized zeolites hybridized with full complementary Cy3-labeled DNA Oligonucleotide. A): DAPI signal (blue); B): Cy3 signal (green color); C): Overlay of A and B.

In a next step, it was determined whether the PNA remains its anti-sense biological activity, when bound to the zeolites.
Therefore 1 mg of PNA/zeolite-L particles were incubated with 3 different DNA oligonucleotide strands: a full match, a single mismatch, and a DNA strand showing 3 mismatch base pairs.
The DNA strands were labeled with Cy3 and no fluorescent dye label was present in the zeolite pores.
After incubation, the PNA/zeolite-L particles were washed with copious amounts of deionized water and then dissolved in hydrofluoric acid. The DNA concentration of each sample was then determined by UV/Vis spectroscopy using the Cy3 label. The exact DNA sequences, which were used, are summarized in table 7.1. The mismatches are underlined.

Table 7.1. Sequences of DNA-Oligonucleotide used for the hybridization tests.

Oligo	Sequence
DNA Full Match	Cy3-AACAGTGAAGGAAAG
DNA single mismatch	Cy3-AACAGTGGAGGAAAG
DNA 3-mismatches	Cy3-AAGAGTGGAGGGAAG

As it is shown in figure 7.5, a clear difference in DNA binding depending on the number of mismatches is obtained. The highest amount of DNA is bound to the PNA/zeolite-L particles if a full complementary DNA strand is added. The introduction of one mismatch in the DNA then leads to a significantly reduced binding, and finally no DNA is recognized by the PNA/zeolite-L particles if a 3-mismatch DNA strand is used.
These experiments clearly prove that the PNA remains its antisense activity even when bound to the surface of zeolite-L, which is very important when using this system *in vitro* or even *in vivo*.

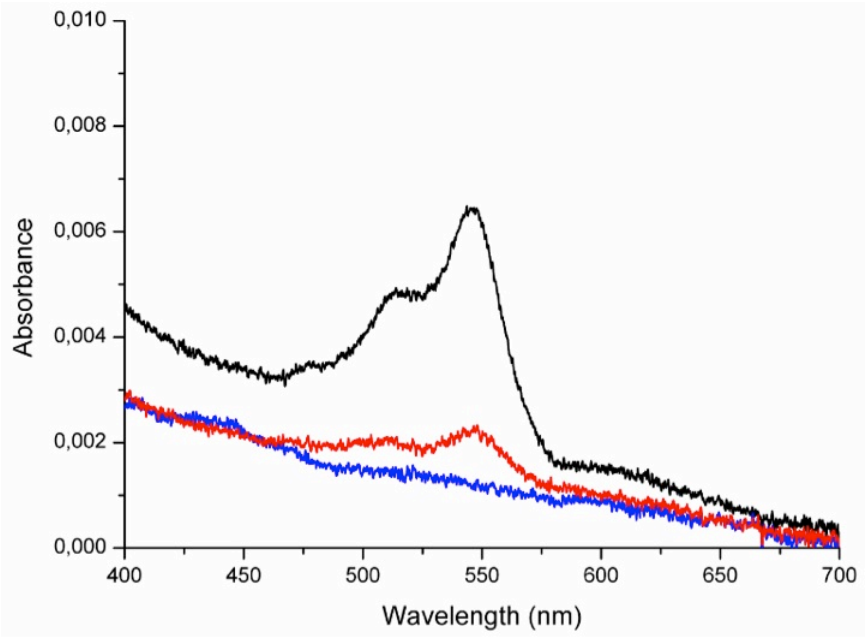

Figure 7.5. UV/Vis spectra of dissolved zeolite-L/PNA particles after hybridization with 3 different DNA strands. Black line: Full-match DNA strand; Red line: single mismatch DNA strand; Blue line: 3-mismatch DNA strand.

7.4. *In vitro* experiments with PNA functionalized zeolite-L

In a very first step it was confirmed that the zeolite-L/PNA particles are stable inside cells and that the PNA is not being detached from the particles.
The zeolite crystals and the PNA molecules were therefore labeled with fluorescent dye molecules and their co-localization after 24 hours incubation was confirmed by confocal microscopy.
In detail, the PNA was labeled with TAMRA and the PNA sequence which was used was H-TAMRA-(D-Lys)-GTAGATGA-NH_2. The zeolites were filled

with Ox170, since its emission is not overlapping with TAMRA or DAPI, which was used to stain the cell nucleus. The particles were coated with PLL to allow for a good cell uptake.
Finally, confocal microscopy was used to show a co-localization of the TAMRA and Ox170 emission, which proves that the PNA is still bound to the zeolites after 24 hours.

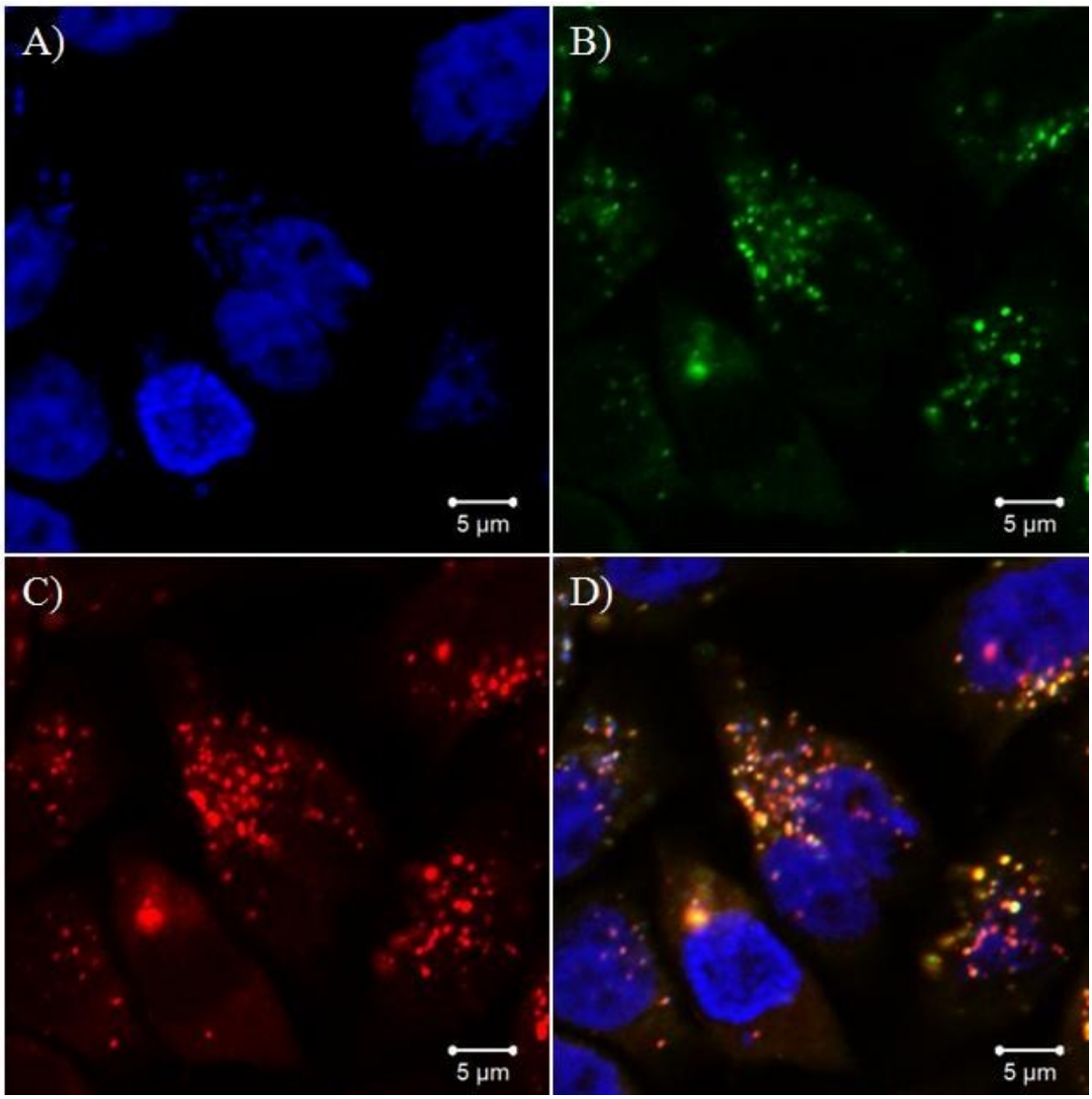

Figure 7.6. Confocal micrograph of HeLa Cells treated with PLL-(TAMRA)-PNA-Oxazine-zeolites after 24 hours of incubation using a 0.01 mg/ml concentration of the dispersion. A) fluorescent image of cell nuclei stained with DAPI; B) fluorescent image of TAMRA, showing the position of the labeled PNA probes; C) fluorescent image of Ox170. The same pattern for both Ox170 and TAMRA spots is the proof that PNA is still covalently bound to the zeolite surface and that the whole nanosystem is intact inside the cells; D) overlay of the previous pictures.

After the stability and the anti-sense activity of the PNA/zeolite-L particles have been proven, the cellular uptake was further determined, which is shown in the following.

In order to localize the zeolites inside cells, the pore system was first filled with the non-leaking dye DXP as described in chapter 2. After dye insertion, PNA probes were attached to the particles as described in chapter 7.3.
In vitro experiments were carried out by using human cervical cancer cells (HeLa) (50000 cells per well). Incubation was done for 1, 4 and 24 hours using a particle concentration of 0.01 mg/mL.
After incubation, the cells were fixed and analysed by confocal microscopy.
After 1 and 4 hours almost no particles are taken up by the cells and no flourescence signal can be recorded (Data not shown). Even after 24 hours just a very small number of PNA/zeolite-L particles is uptaken, which is confirmed by recording z-stacks (See figures 7.7 and 7.8).
The requirement of very long incubation times is most likely due to the non-membrane-permeable nature of PNAs.

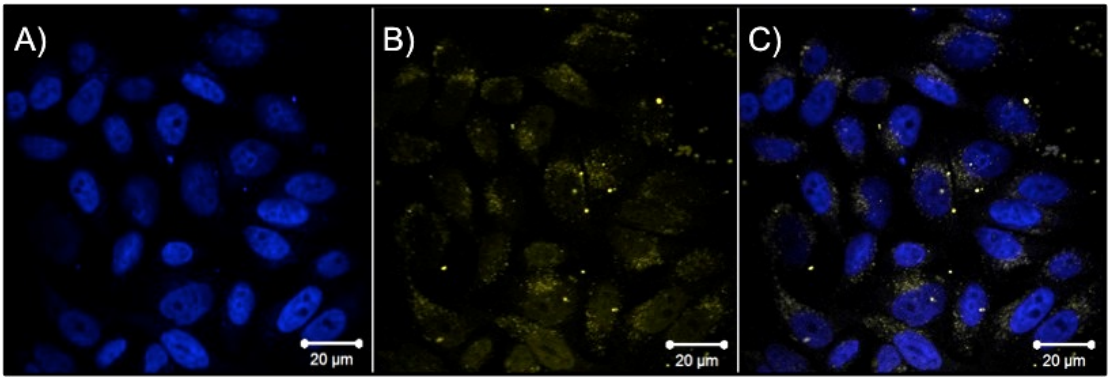

Figure 7.7. Confocal micrographs of HeLa Cells incubated with a 0.01 mg/mL dispersion of PNA/zeolite-L (DXP labeled) particles for 24 hours. The micrograph was recorded using laser excitation with wavelengths of 405 and 514 nm while the emission was collected in lambda mode acquisition. The recorded signals were unmixed by utilizing the linear unmixing tool, which is available in the Zeiss Zeon2011 software. A) DAPI signal; B) DXP signal, showing the presence of the nanoparticles inside the cells; C) overlay of A) and B).

That the zeolites are indeed taken up inside the cells after 24 hours incubation, has been confirmed by recording z-stacks, which is shown in figure 7.8.

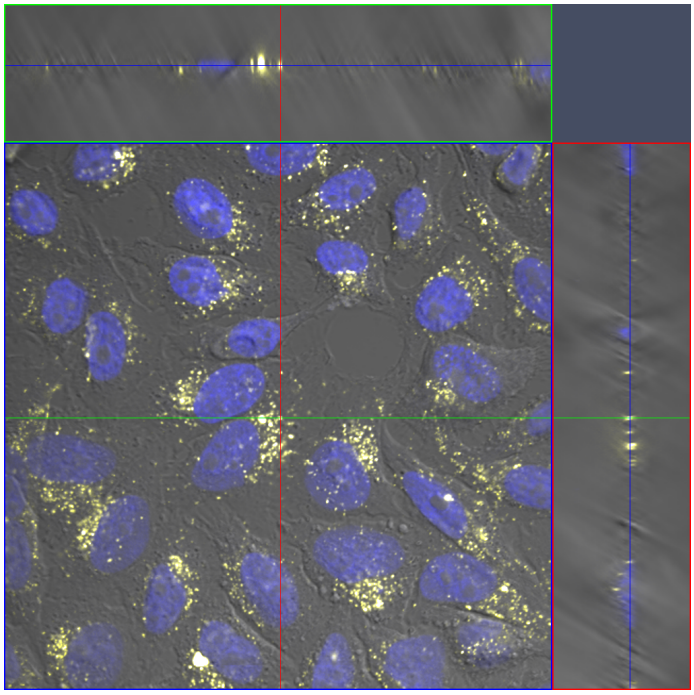

Figure 7.8. Orthogonal view of cells and zeolites taken up after 24 hours incubation.

In a next step the cytotoxicity of the PNA/zeolite-L particles was determined by performing a cell viability test.
The details can be found in the experimental part at the end of this chapter. The viability test shows, that indeed the zeolite-L/PNA particles are not toxic to cells (See figure 7.9.). As negative control, cells were incubated with 30% DMSO in culture media; as positive control, the cells were incubated with unmodified culture media.

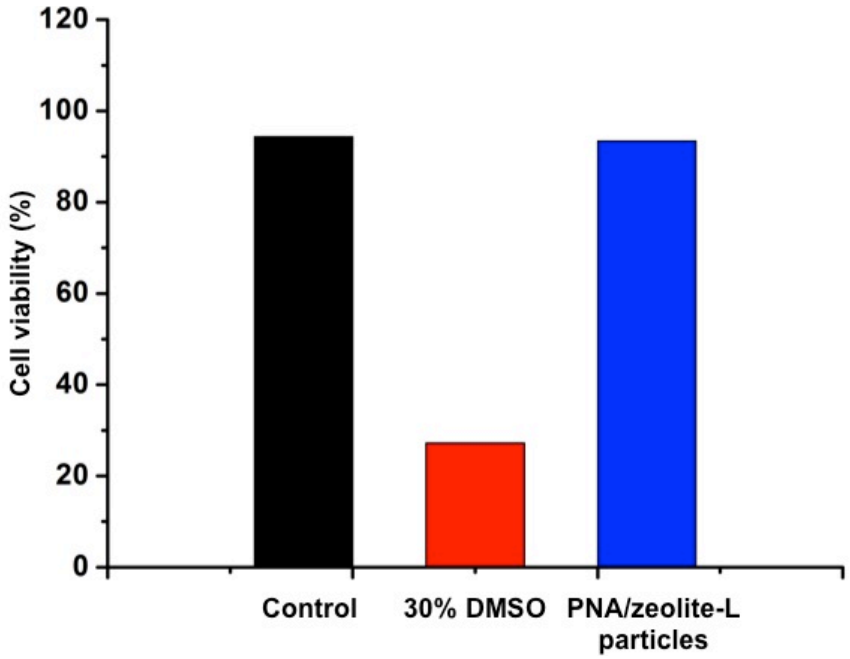

Figure 7.9. Viability study zeolite-PNA towards HeLa cells and its comparison to the negative (30 % DMSO inside culture media) and positive (without anything) control. The working concentration for zeolite-PNA is 0.01 mg/ml and the incubation was performed for 24 hours.

7.5. *In vitro* experiments with PLL coated and PNA functionalized zeolite-L

To overcome the problem of the very poor particle uptake, the PNA/zeolite-L particles were coated with a thin layer of PLL to increase the cellular uptake (See figures 7.2 and 7.3). The PLL degrades after cell uptake and does not affect the activity of the system itself.

Coating was done by incubating the zeolite-L/PNA particles in a 1% (wt/wt) aqueous solution of PLL and confirmed by a particle zeta potential shift to +2.82 mV (in PBS) and an increase in size to about 123 nm (by DLS), which is shown in figure 7.3c.

Indeed, it has been shown that biocompatible polymers can be used to increase the cellular uptake of nanoparticles. A variety of polymers have been used for this reason and PLL has been shown to be a good candidate to increase the cellular uptake[39].

Cell experiments were performed in the same conditions as described before (50000 cells per well, 0.01 mg/mL, 1, 4 and 24 hours incubation time). Figure 7.10. shows the confocal micrographs after 1, 4 and 24 hours incubation time.

It can be seen that a large number of particles is internalized already after just 1 hour incubation. Prolonging the incubation to 4 and 24 hours leads to an even higher amount of particles internalized inside the cells. The particles are localized in the cytoplasm of the cells.

These results confirm the possibility of using zeolite-L nanocontainers for an efficient PNA delivery into living cells.

Very remarkably, the zeolite-L/PNA system is efficiently taken into living cells without using any cell penentrating peptides, like it is usually used to deliver PNA to cells.

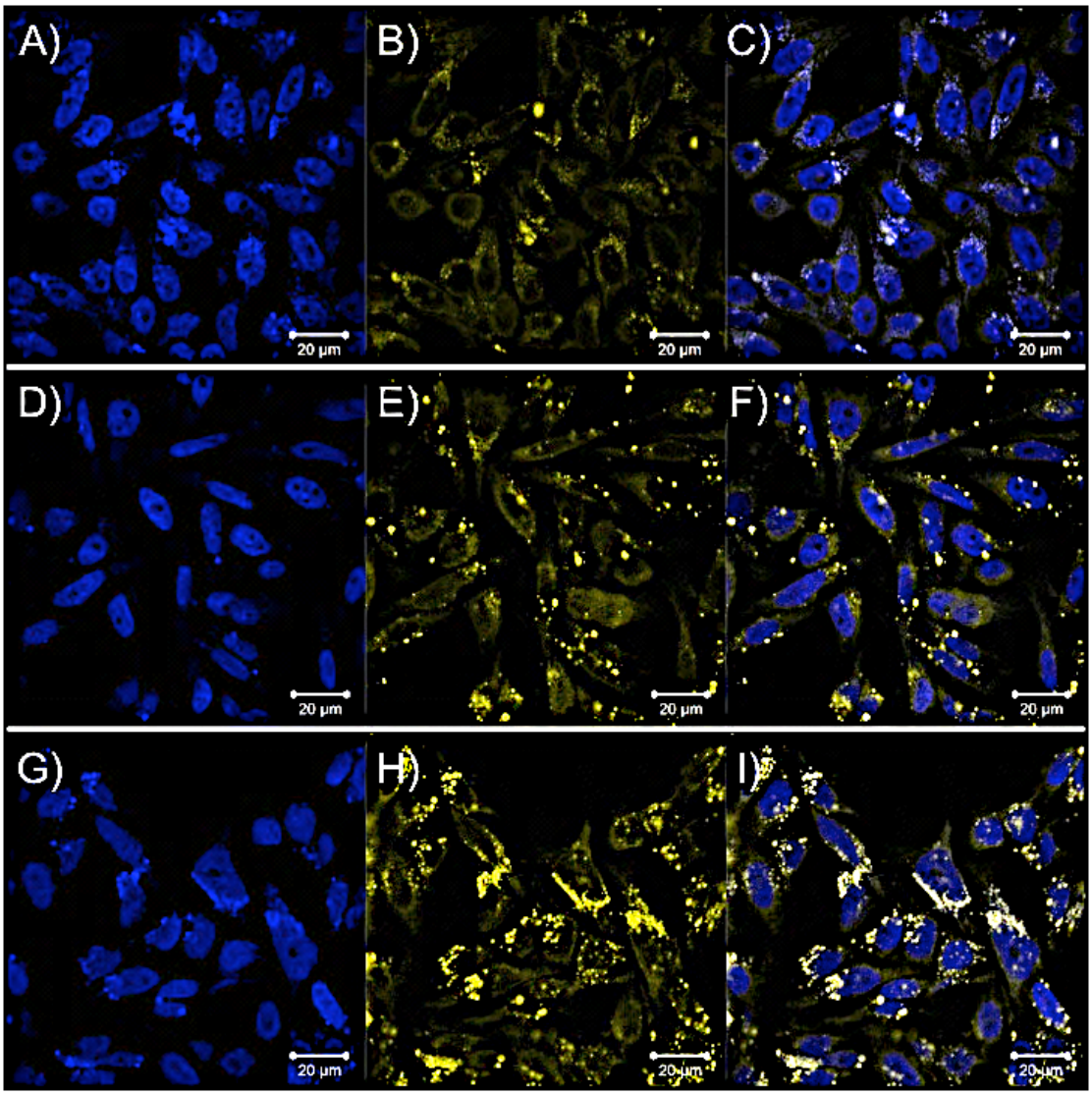

Figure 7.10. Confocal micrographs of HeLa Cells incubated with a 0.01 mg/ml dispersion of PLL-PNA-DXP-functionalized zeolites for 1 hour (A, B, C), 4 hours (D, E, F) and 24 hours (G, H, I). A,D,G) fluorescent image of cell nuclei stained with DAPI; B, E, H) fluorescent image of DXP, showing the presence of the nanoparticles inside cells; C, F, I) overlay of the previous pictures.

To prove that the particles are indeed located in the cytoplasm and not just adsorbed on the cell membrane, a z-stack was recorded after 1 hour of incubation (See figure 7.11.).

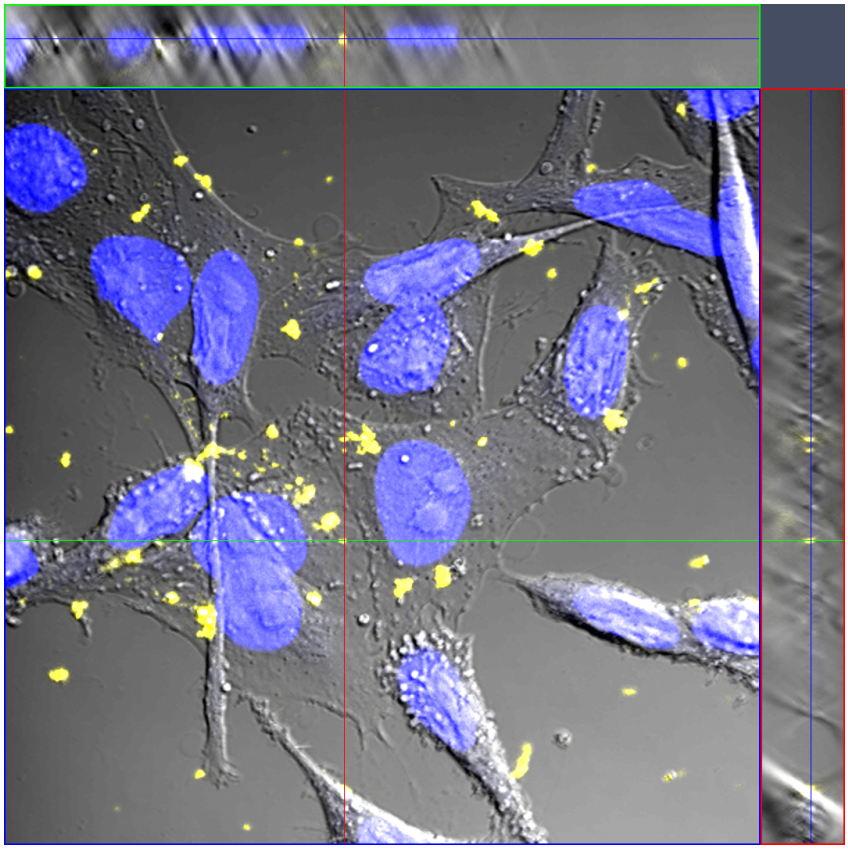

Figure 7.11. Orthogonal view of cells and zeolite taken by z-stack acquisition revealing the location of zeolites inside the cell. The picture refers to the sample incubated for 1 hour with PLL-PNA-nanoparticles.

7.6. Multifunctional PNA and model drug delivery to living cells

In a next step the possibility of using the described PNA/zeolite-L particles as a multifunctional PNA and drug delivery system was determined.
The pore system was therefore filled with a model drug (DAPI) and its release after cell uptake was recorded by confocal microscopy. The DAPI release should lead to a staining of the nucleus. DAPI itself is a non-membrane permeable molecule and a nucleus staining would therefore also confirm the particle uptake.
The zeolite pores have been loaded with DAPI as described in chapter 2 and the PNA probes were then attached to the zeolite outer surface as described before. To enhance the uptake (See chapter 7.5.), the particles were coated with PLL as described before.
Incubation was then done in analogy to the previous performed experiments for 1, 4 and 24 hours and the results are shown in figure 7.12.

Already after 1 hour, a high amount of particles is taken up, but the DAPI is still encapsulated inside the pores. The nucleus is not yet stained by the DAPI.
After 4 hours the amount of particles inside the cells is further increased and a blue staining of the nucleus can be observed, which is due to DAPI leaking from the pores.

A prolongation of the incubation time to 24 hours leads to a further increased particle uptake. At the same time a higher amount of DAPI is release, which can be seen from the bright blue staining of the cell nuclei.
The results are summarized in figure 7.12.

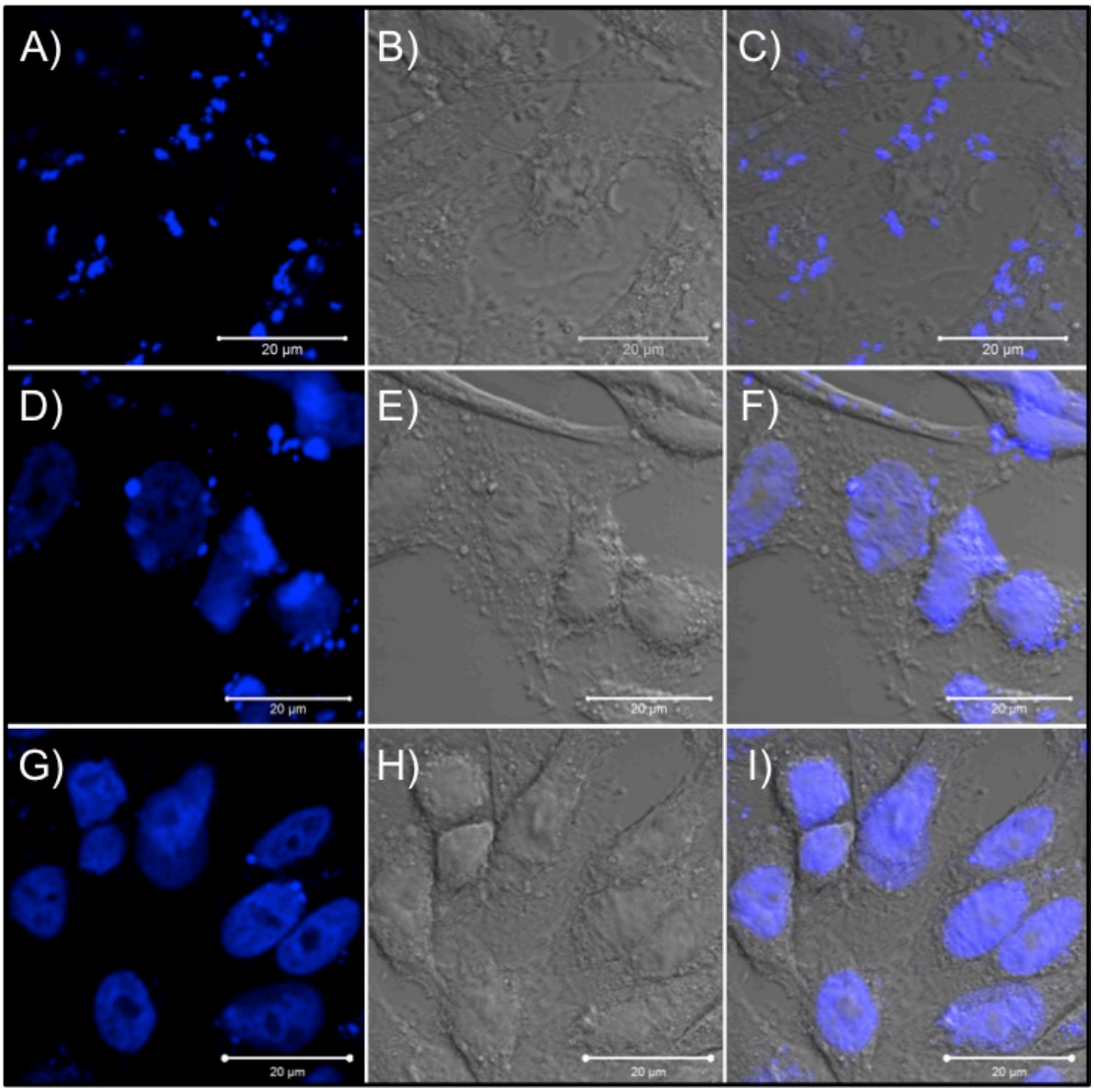

Figure 7.12. Confocal micrographs of HeLa cells incubated with a 0.01 mg/ml dispersion of PLL-PNA-DAPI-functionalized zeolites for 1 hour (A-C), 4 hours (D-F), 24 hours (G-I). A, D, G) Fluorescent image recorded monitoring DAPI signal; B, E, H) Bright field image; C, F, I) overlay of the previous ones.

7.7. Conclusion

In conclusion, a new hybrid nanosystem, which is able to vehicle PNA efficiently into the cells, was developed. For the first time inorganic nanoparticles were used for to achieve this goal.
Above that, the porous nature of the zeolite nanoparticles allows the design of a multifunctional PNA- and drug delivery system.
A very efficient and fast particle uptake can be achieved by coating the particles with a thin layer of PLL.

Remarkably it is possible to deliver high amounts of PNA to cells even after 1 hour. Increasing the incubation then leads to increasing concentrations of particles inside the cells.
Finally it has been shown that the system can not only be used to deliver PNA inside cells, but above that the pore system can be used to release molecules, in this case DAPI, inside cells.
Further applications towards bioimaging, drug delivery and gene therapy selecting specific PNA target sequences will be tested using these reported hybrid nanoparticles.

7.8. Experimental part

Chemicals

All reagents were purchased from commercial suppliers and used without further purification. Potassium hydroxide, Aluminium hydroxide, Dimethyl sulfoxide (DMSO), toluene, acetonitrile, sodium hydrogen carbonate, hydrochloric acid 37%, succinic anhydride, diisopropylcarbodiimide (DIC), N-hydroxysuccinimide (NHS), (3-aminopropyl)triethoxysilane (APTES), tris(hydroxymethyl)aminomethane (Tris), N,N'-bis(2,6-dimethylphenyl)perylene-3,4,9,10-tetracarbodiimide (DXP), poly-L-lysine hydrobromide (PLL) were all purchased from Sigma-Aldrich (France). Oxazine 170 perchlorate was provided by Acros Organics. Ethanol was purchased by Carlo Erba (Italy). Ethanolamine was purchased by Fisher Scientific (France). Cy3-labeled DNA Oligonucleotides were provided by Thermo Fisher Scientific (Germany). Fmoc-C(Bhoc)-OH, Fmoc-G(Bhoc)-OH, Fmoc-T-OH, Fmoc-AEEA-OH used for PNA synthesis were all purchased from ASM (Germany). Fmoc-A(Bhoc)-OH was purchased from Link Technologies (UK). HBTU was purchased from Matrix Innovation (Canada). Rink amide resin was provided by Merck (Italy). Aerosil Ox-50 was a gift from Evonik Industries. Ultra-pure water (Milli-Q Elememt, Millipore) was used for all the experiments.

PNA Oligomer synthesis

The solid-phase synthesis of PNA sequence H-$(AEEA)_2$-CTTTCCTTCACTGTT-NH_2 was performed as reported in [1] and that of labeled PNA sequence H-TAMRA-(D-Lys)-GTAGATGA-NH_2 was carried out as reported in [2].

Synthesis of nanozeolite-L

See chapter 2.

DAPI insertion in zeolite channels

Zeolite-L nanocrystrals (150 mg), were dispersed in 15 ml of a 0.3 mM aqueous solution of DAPI and stirred overnight at 50°C. The crystals were washed washed with deionized water until the supernatant did not show any fluorescence. A loading of 1.55 mg of DAPI per 100 mg zeolites was determined by means of TGA.

DXP insertion in zeolite channels

DXP insertion was done as described in chapter 2. An amount of 0.5 mg DXP per 100 mg zeolites was used.
A loading of 2.14 mg per 100 mg zeolites was determined by TG-analysis.

Insertion of Oxazine 170 in zeolite channels

Zeolite-L nanocrystals (500 mg) were dispersed in a 0.01 mmol solution of oxazine 170 perchlorate in water and refluxed overnight. The zeolites were then washed with deionized water until the supernatant did not show any fluorescence. A loading of about 2 mg of oxazine 170 per 100 mg of zeolites was determined by TGA.

Nanozeolites surface modification with PNA

In a first step the zeolites were amine-functionalized with APTES as described in chapter 2.

To obtain carboxylic acid-functionalized nanoparticles, 70 mg of the former NH_2 functionalized zeolites were dispersed in a succinic anhydride solution in DMSO (0.1 M in 10 mL) and, after 30 minutes of sonication, the mixture was stirred overnight at room temperature. The material was then centrifuged and washed three times with DMSO. After that, succinimidyl-functionalized nanozeolites were obtained by reaction of the former material (50 mg) with a solution of DIC and NHS (both 0.25 M) in dry DMSO. The nanoparticles were dispersed in 10 ml of the reactant solution and stirred overnight at room temperature under a nitrogen atmosphere. The final material was again recovered by centrifugation and washing with DMSO. PNA attachment was subsequently carried out by dispersing 5 mg of the activated-esters-modified-zeolites in 500 mL of a PNA solution 30 mM in a 100 mM carbonate buffer, H_2O:Acetonitrile 9:1, pH=9. The dispersion was stirred overnight at room temperature and PNA-zeolites were finally obtained by centrifugiation and washing three times with water. The final quenching step was performed by stirring the PNA-zeolites overnight at room temperature with a 100 mM solution of ethanolamine in Tris buffer (100 mM, pH = 9). The final material was recovered by centrifugation and washing three times with water.

Poly-L-lysine coating

Poly-L-lysine coating was always carried out by dispersing 1 mg of PNA-zeolites in a 1% w/v solution of poly-L-lysine hydrobromide in water and stirring the mixture at room temperature for 1 hour. The final material was recovered by centrifugation and washing with water.

Cell Culture

HeLa cells were cultured inside media which contain 88 % Dulbecco's Modified Eagle Medium (DMEM), 10 % Fetal Bovine Serum, 1 % Penicillin-Streptomycin and 1 % L-Glutamine 200mM (all material was purchased from Gibco) under 37^{o}C and 5% of CO2 condition for 48 hours until reaching 70 to 80 % cell confluency. Subsequently, the cells were washed twice with Phosphate Buffer Solution (PBS, Gibco), trypsinated and approximately 50,000 cells were reseeded on the monolayer glass cover slip inside 6 well plate cul-

ture dish. New culture media (2 ml) were added gently and the cells were grown overnight.

PNA/Zeolite-L Incubation

Working solutions of culture medium containing PNA-zeolites in 0.01 mg/mL concentration were added to the cells. After 1, 4 and 24 hour incubation, the media were removed and cells were washed with PBS twice. Cells were fixed with 4% paraformaldehyde (PFA) and the nuclei were stained with DAPI (4',6-Diamidino-2-Phenylindole). After staining, cells were washed once with PBS and then with water.

DNA:PNA-zeolites hybridization test

Zeolite-L/PNA (1 mg), were incubated at RT for 1 hour with 500 ml of 2 mM solutions of a Cy3-labelled full-match DNA-ON sequence, a single mismatch sequence and a three-mismatch sequence. After incubation, the material was recovered by centrifugation and washed 5 times with water (30 min, 6000 rpm). Every sample was then dissolved in 200 ml of HF and diluted with water to a final volume of 2.2 ml.

Calculation of PNA molecules bound to a zeolite-L crystal

1 mg zeolite-L/PNA were dissolved in 200 ml HF and the sample was diluted with water to a final volume of 2.2 ml. Finally, the sample was analyzed by UV/Vis spectroscopy and the amount of PNA molecules was calculated by the absorbance value of TAMRA dye (e_{555} = 65000 M^{-1} cm^{-1}). A rough estimate of the number of PNA molecules linked was obtained by the following calculations. From Abs_{555} = 0.027, we calculated that C_{TAMRA} = 0.42 mM; from this, the number of PNA molecules attached to 1 mg zeolites was evaluated to be 5.6E14. The following average dimensions were used for the Zeolite-L: diameter ≈ 50 nm; radius ≈ 25 nm; length ≈ 60 nm; mass = 0.001 g.

The number of parallel channels was calculated by:

$$n_{ch} = \frac{(r)(r)^2\pi}{|a|^2 \sin 60} = \frac{\pi}{2\sqrt{3}}\left(\frac{2r}{|a|}\right)^2 \quad (1)$$

with a: primitive vector perpendicular to the c-axis; r: zeolite-L diameter radius in nm

Equation (1) can be approximated as

$$n_{ch} = 1.104\, r^2 \quad (2)$$

Thus a zeolite-L crystal with a radius of 25 nm contains about 690 parallel channels.

The number (mol) of unit cells in one crystal was calculated from:

$$N_{ch} = n_{ch}\left(\frac{l}{N_A\,|c|}\right) \quad (3)$$

with l: length of zeolite crystal; |c|: primitive c-vector (0.75 nm)

Thus a zeolite L crystal with a length of 60 nm has 9.17E-20 mol unit cells.

The weight of one crystal is given as:

$$m_{Zeo} = N_{ch} * M_{u.c.} \quad (4)$$

with $M_{u.c.}$: molecular weight of one unit cell (2880 g/mol)

Thus the weight of one zeolite-L crystal is about 2.64E-16 g.

The number of crystals in 1 mg was calculated from:

$$N_{Zeo} = \frac{\text{Sample mass}}{m_{Zeo}} \quad (5)$$

Thus in 1 mg of zeolites there are 3.79E12 single crystals.

The amount of PNA molecules attached to one zeolite crystal was finally calculated as:

$$\frac{5.6E14}{3.79E12} \approx \underline{\mathbf{148}} \quad (6)$$

References

[1] Nielsen, P.E., Egholm, M., Berg, R.H., Buchardt, O., *Science*, **254**, 1497–1500, **1991**.
[2] Uhlmann E., Peyman A., Breipohl G., Will D. W. *Angew. Chem. Int. Ed.,* **37**, 2796-2823, **1998**
[3] Egholm, M., Buchardt, O., Christensen, L., Behrens, C., Freier, S.M., Driver, D.A., Berg, R.H., Kim, S.K., Norden, B., Nielsen, P.E., *Nature*, **365**, 566–568, **1993**
[4] Sahu, N., Shilakari, G., Nayak, A., Kohli, D.H., *Curr. Chem. Biol*. **2**, 110–121, **2008**.
[5] Zhang, N., Appella, D.H., *J. Infect. Dis*., **201**, S42–S45, **2010**.
[6] Sforza, S., Corradini, R., Tedeschi, T., Marchelli, R., *Chem. Soc. Rev*., **40**, 221–232, **2011**.
[7] D'Agata, R., Corradini, R., Grasso, G., Marchelli, R., Spoto, G., *Chembiochem*, **9**, 2067–2070, **2008**.
[8] D'Agata, R., Corradini, R., Ferretti, C., Zanoli, L., Gatti, M., Marchelli, R., Spoto, G., *Biosens. Bioelectron*., **25**, 2095–2100, **2010**.
[9] Rozners, E., *Journal of Nucleic Acids*, **2012**.
[10] Shiraishi, T., Nielsen, P. E., *Nature Protocols*, 1, 633-636, **2006**.
[11] Abes, S. et al., *Nucl. Acids Res*., **35**, 4495-4502, **2007**.
[12] Fabbri, E. et al., *ChemMedChem*, **6**, 2192-2202, **2011**.
[13] Torres, A. G. et al., *Nucl. Acids. Res*., **40**, 2152-2167, **2012**.
[14] Englund, E. A., and Appella, D. H., *Angew. Chem. Int. Ed*., **46**, 1414-1418, **2007**.
[15] Zhou, P. et al., *J. Am. Chem. Soc*., **125**, 6878-6879, **2003**.
[16] Manicardi, A. et al., *ChemBioChem*, **13**, 1327-1337, **2012**.
[17] Mitra, R., and Ganesh, K. N., *J. Org. Chem*., **77**, 5696-5704, **2012**.
[18] Hassane, F. S., Saleh, A.F., Abes, R., Gait, M.J., and Lebleu, B., *Cellular and Molecular Life Sciences*, **67**, 715–726, **2010**
[19] Wancewicz, E.V. et al., *Journal of Medicinal Chemistry*, **53**, 3919–3926, **2010**.
[20] Fabani, M. M. et al., *Nucleic Acids Research*, **38**, 4466–4475, **2010**.
[21] Koppelhus, U., Shiraishi, T., Zachar, V., Pankratova, S., and Nielsen, P. E., *Bioconjugate Chemistry*, **19**, 1526– 1534, **2008**.
[22] Fang, Zhang, K., Shen, K. L. Wooley, and Taylor, J. S. A., *Molecular Pharmaceutics*, **6**, 615–626, **2009**.
[23] McNeer, N. A. et al., Gene Therapy, 1-12, **2012**.
[24] Vallet-Regi, M., Balas, F., and Arcos, D. *Angew. Chem., Int. Ed.* **46**, 7548-7558, **2007.**
[25] Slowing, I. I., Trewyn, B. G., Giri, S., and Lin, V. S. Y. *Adv. Funct. Mater.* **17**, 1225-1236, **2007**.
[26] Lai, C. Y., Trewyn, B. G., Jeftinija, D. M., Jeftinija, K., Xu, S., Jeftinija, S., Lin, V. S., *J. Am. Chem. Soc*., **16**, 4451, **2003**.
[27] Li, Z. et al., *Small*, **9**, 1809-1820, **2013**.
[28] Tsotsalas, M., Kopka, K., Luppi, G., Wahner, S., Law, M. P., De Cola, L., Schaefers, M., *ACS Nano*, **4**, 2486, **2010**.
[29] Tsotsalas, M., Busby, M., Gianolio, E., Aime, S., De Cola, L., *Chem. Mater*., **20**, 5888-5893, **2008**.

[30] Popovic, Z., Otter, M., Calzaferri, G., De Cola, L., *Angew. Chem. Int. Ed*., **46**, 6188-6191, **2007**.
[31] Strassert, C. A., Otter, M., Albuquerque, R. Q., Hoene, A., Vida, Y., Maier, B., and De Cola, L., *Angew. Chem. Int. Ed*., **48**, 7928-7931, **2009.**
[32] Li, Z., et al., *Small*, **9**, 1809-1820, **2013**.
[33] Thiele, L. *et al. J Control Release* **76**, 59-71, **2001**.
[34] Brandhonneur, N. *et al. Eur J Pharm Sci* **36**, 474-485, **2009**.
[35] Liang, M., Ling, I. C., Whittaker, M. R., Minchin, R. F., Monteiro, M. J., and Toth, I., *ACS Nano*, **4**, 403-413, **2010**
[36] Stefanick, J. F., Ashley, J. D., Kiziltepe, T., Bilgicer, B., *ACS Nano*, **7**, 2935-2947, **2013**.
[37] Kantner, K., and Geidel, C., *ACS Nano*, **7**, 3253-3263, **2013**.
[38] Freese, C. *Biomacromolecules*, **13**, 1533-1543, **2012**.
[39] Ryser, H., and Wei-Chiang, S., *Proc. Natl. Acad. Sci. USA*, **75**, 3867-3870, **1978**.

Experimental and Instrumental Methods

Abstract

This chapter described the most important experimental and instrumental methods used in this thesis. All other experimental details can be found directly in the corresponding chapters.

8.1. Zeolite-L synthesis

Three different types of zeolite-L were used and synthesized in the context of this thesis:

1. Nanozeolite-L with a size of about 50 nm.
2. Disc-shaped zeolite-L with a diameter of about 200 nm and a height of about 50 nm
3. Microzeolite-L with a height and diameter of about 1 µm.

The zeolites have been synthesized according to literature protocols. The exact conditions and synthesis gel compositions can be found in chapter 2. All zeolites have been synthesized in hydrothermal conditions using a custom made oven and Teflon vessels (Figure 8.1). The Teflon vessels are hermetically sealed at crystallization conditions, which prevents an undesired water leaking. The Teflon vessels consist of 4 parts: The inner vessel (figure 8.1a), the outer vessel (figure 8.1b), the inner vessel cover (figure 8.1c), and the cap. The inner vessel is filled with the synthesis gel, placed in the outer vessel and tightly closed with the cover and cap. Crystallization was then done either in static or dynamic conditions in a custom made oven.

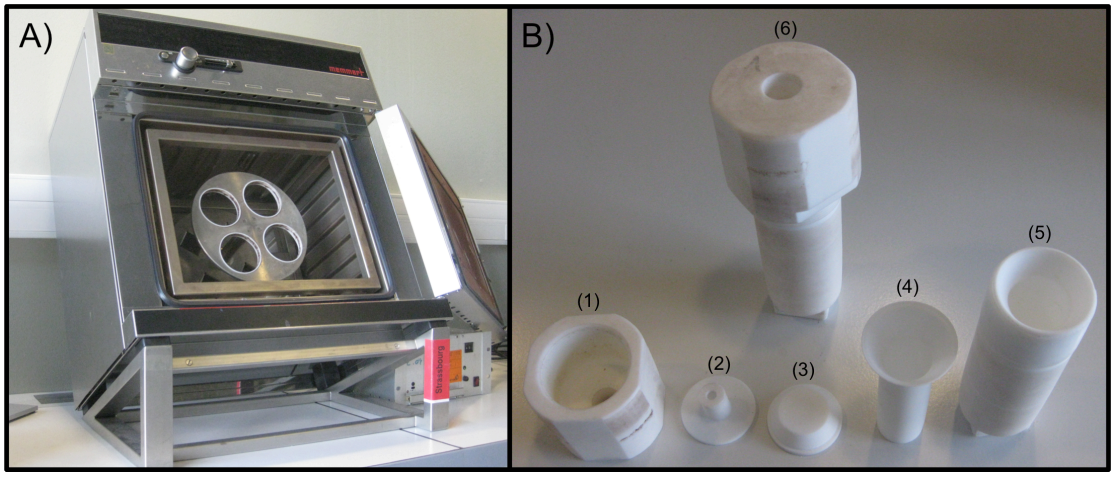

Figure 8.1. Equipment for zeolite-L synthesis. A) rotating oven. B) reaction vessel made of teflon. (1) final cap, (2) and (3) Inner vesser cover, (4) inner vesser, (5) main vessel, (6) assembled vessel..

8.2. Scanning electron microscopy (SEM)

The resolution of microscopes can be significantly increased by using a beam of electrons instead of light for imaging.

As shown by De Broglie, every moving particle has wave properties, with a certain wavelength. For a particle with the pulse p, the wavelength can be calculated according to

$$\lambda = \frac{h}{p}$$ (with h = 6.626E-34 Js).

The classical wavelength of an electron, which is accelerated in an electric field of 10 kV can be calculated as 0.012 nm, and therefore the resolution is practically no longer wavelength-limited.
The functionality of a SEM instrument with its key components will be discussed in the following.
Imaging in electron microscopy is done by scanning a beam of electrons over the surface of a sample. The high energy electrons, which are generated and focused in the electron column, interact with electrons in the sample and generate back scattered electrons, secondary electrons or x-rays, which can be used for imaging.
The electron beam is generated at the **electron source**, which is located at the top of the electron column. Two types of electron sources are basically used in SEM-instruments nowadays, Thermoionic-Sources and Field-Emission-Sources. Thermoionic-Sources use a thin V-shaped conductive wire, usually tungsten or lanthanhexaborid, which is heated to temperatures where the energy of the weakest bounded electrons exceeds the work function of the material. Field-Emission-Sources use high electric fields between a cathode (electron source) and an anode, which leads to a decrease of the work function of the cathode (Schottky-Effect). If the applied electric field is big enough, the work function vanished and electron emission is possible even at room temperature. This electron emission is a purely quantum mechanical phenomenon called tunneling. Because electrons are emitted in all directions, the electron source is surrounded by the **Wehnelt cap,** which focuses the electrons. Therefore the **Wehnelt Cap** is biased negatively in respect to the electron source, which causes a repulsive electric field and a condensation of the electrons.

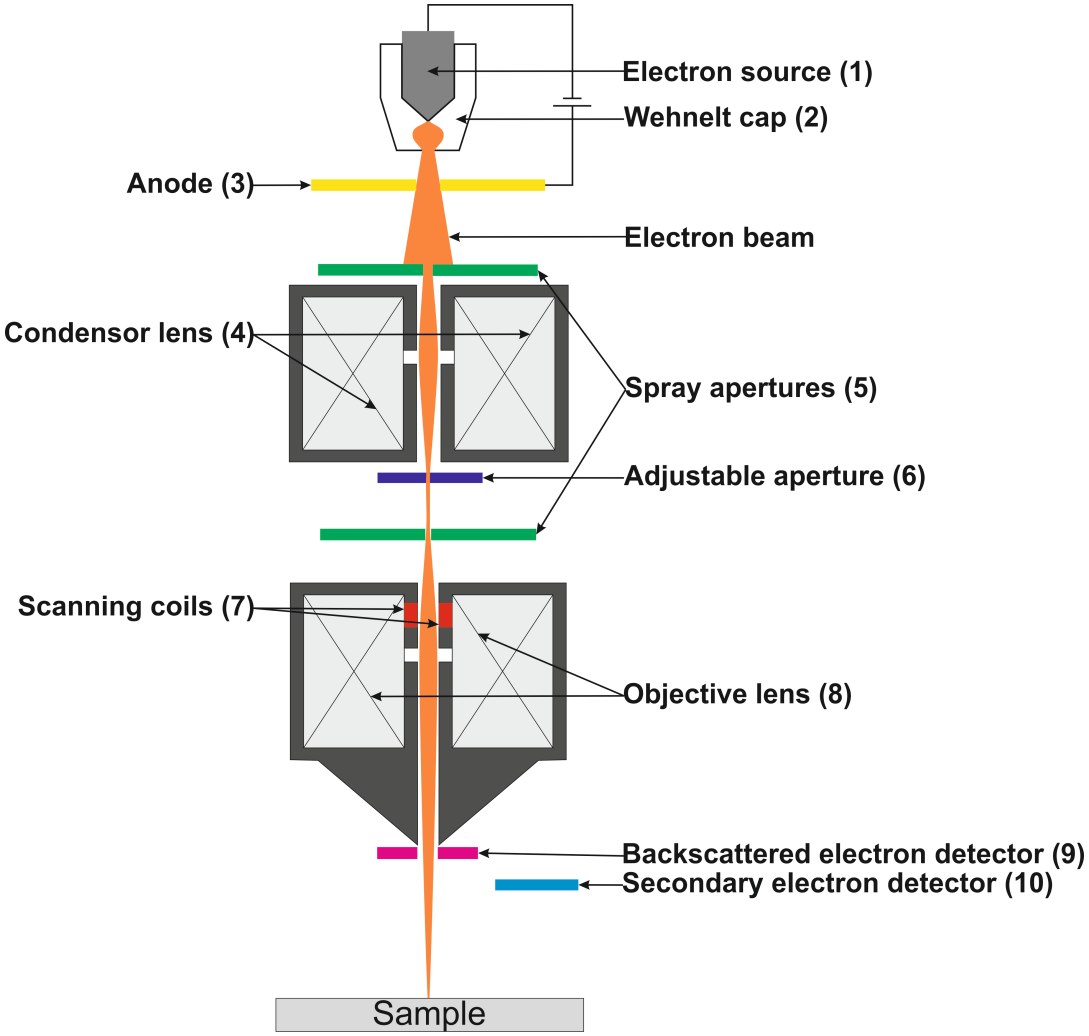

Figure 8.2. Schematic view of a SEM instrument.

The **Anode** serves the acceleration of the electrons down the electron column. Therefore the **anode** is biased +1 to +50 kV compared to the electron source. The voltage is adjustable by the user and is called the acceleration voltage.

In order to diminish spherical aberrations, the electron beam is confined to the center of the magnetic lenses, which is done by using so-called **spray apertures**.

The **condenser lens** focuses the electron beam on the aperture. Therefore the amount of current of the beam can be controlled. The sharper the focus on the aperture is, the less amount of the beam is intercepted by the aperture and the higher is the current of the beam.

After passing through the condenser lens, the beam is divergent and must be refocused on the sample. This is done by the **objective lens**, which is located just above the sample.

The **scanning coils** are located at the objective lens and are used to scan the over the sample surface.

After interaction of the beam with the sample, different kinds of electrons can be used for signaling. The most common imaging mode in electron microscopy uses **secondary electrons (SE)**. Secondary electrons originate when the incident electron beam excites an electron in the sample, which is then migrates to the surfaces and escapes from the sample, if it still has a certain amount of energy. Due to the very low energy, only secondary electrons near the surface (less than 10 nm) can leave the sample. The Volume in which secondary electrons are produced is relatively small, which leads to a high resolution (a few nm).
Backscattrered electrons (BSE) are another class of electrons that occur after interaction of the beam with the sample. They have energies of a few keV and the signal intensity depends on the atomic number of the material atoms. Heavy atoms cause a strong backscattering and the image appears brighter in these areas.

8.3. Transmission electron microscopy (TEM)

In analogy to SEM, also TEM uses a beam of accelerated electrons for imaging. But in contrast to SEM, which is based on scattered electrons, TEM is based on transmitted electrons. The electron beam is directly pointed towards the detector, placing the sample in between electron source and detector. The electrons that pass through the sample then cause bright parts in the image. While SEM gives information about the sample surface, TEM analyses what is beyond the surface or inside the sample.
In term of resolution and magnification TEM has advantages compared to SEM. While the typical resolution of SEM is about 0.4 nanometers, a TEM offer resolutions down to 0.5 angstroms. In terms of magnification SEM has a maximum of about 2 million, while modern TEM instruments allow a magnifications up to 50 million.
A typical TEM instrument consists of different components, which will be described in the following. A schematically view of the electron path in a TEM instrument is shown in figure 8.3.

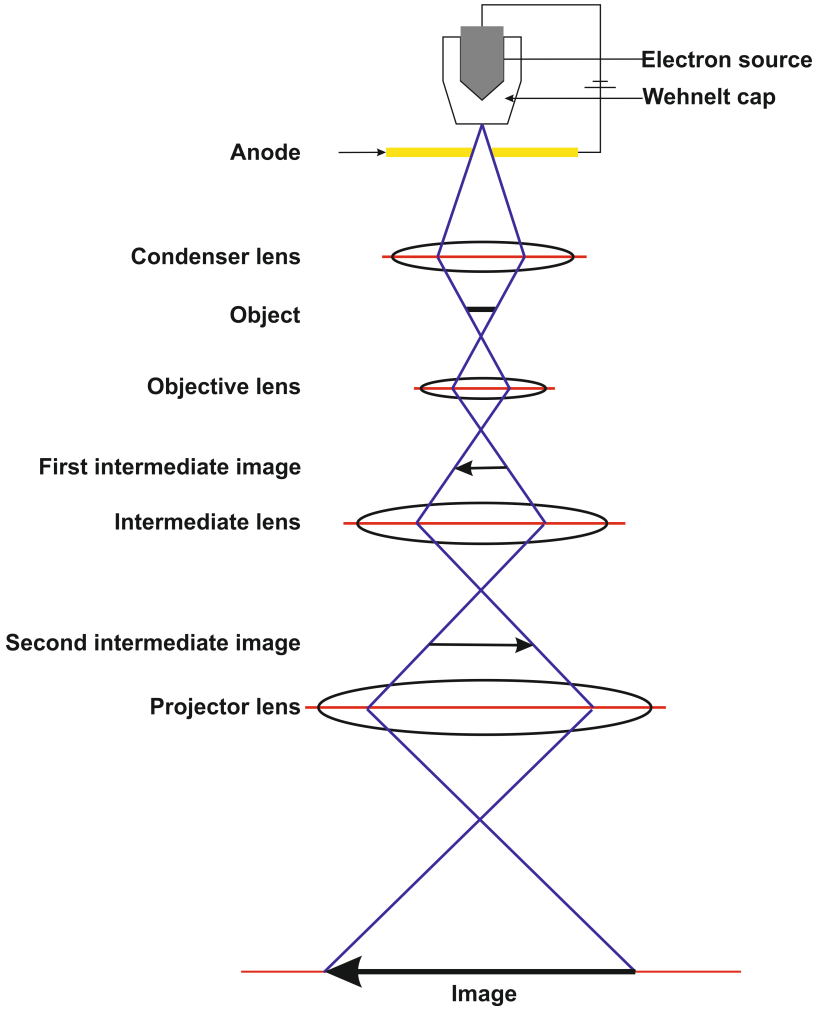

Figure 8.3. Intensity fluctuations aroused by big (top) and small particles (bottom)

The electron source works similar to those used for SEM, but TEM uses significantly higher accelerating voltages, typically between 80 kV and 400 kV. However, accelerating voltages below 200 kV are mostly used for biological or soft samples; in material science accelerating voltages of 200 kV and more are typically used.

The **condenser lens** is placed before the object and is used to form the beam and to limit the amount of current in the beam. The main purpose of the condenser lens is to focus the light onto the object and therefore it also controls the diameter of the electron beam. For lower magnification the beam is spread onto the object to illuminate a larger area; for high magnifications, the beam is strongly condensed onto the object.

Directly after the object one can find the **object lens**, which generates the first intermediate image, the quality of which determines the resolution of the final image. The intermediate is an inverted initial image, which then is subsequently magnified. The first magnification is done by the **intermediate lens** and produces a second intermediate image. The second intermediate image is the object for the **projector lens**, which forms a final image on a fluorescent screen or a recording device.

8.4. Dynamic light scattering (DLS)

Dynamic light scattering (DLS), also called photon correlation spectroscopy is widely used to determine the size of particles in dispersion. The size of many different kinds of particles and molecules, like nanoparticles, micelles, polymers, proteins, colloids and many more, can be determined by using DLS techniques.

Due to collisions with solvent molecules, dispersed particles are in a continuous random movement (Brownian motion). The magnitude of this random motion depends strongly on the size of the particles and the property, which is determined in first instance is the diffusion constant D. This is connected with the diameter of the particles by the Stokes Einstein equation:

$$D = \frac{k_B T}{3\pi\eta_0 d} \text{ where}$$

k_B is the Boltzmann constant, T is the temperature in Kelvin, η_0 is the viscosity of the solvent and d is the diameter of the particle.

Due to random motions of the particles, also the intensity of a scattered laser beam shows random fluctuations. The intensity fluctuates faster for smaller particles and slower for bigger particles.

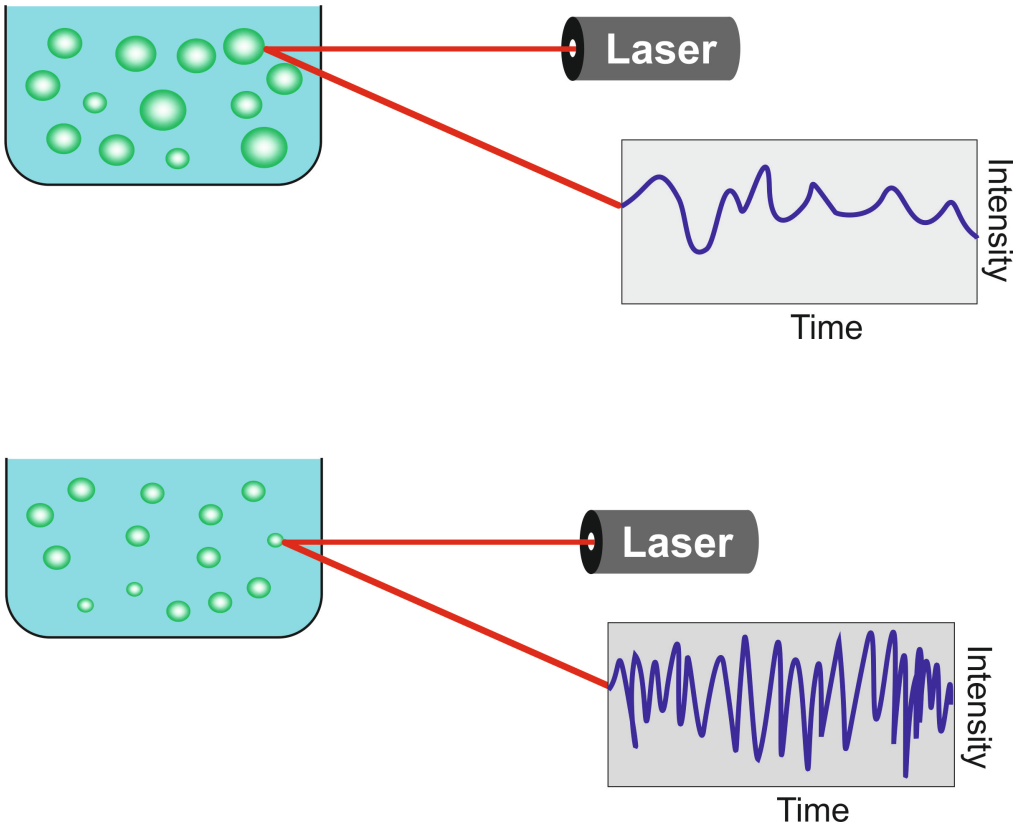

Figure 8.4. Representation of the intensity fluctuations obtained from a dispersion with big particles (top) and small particles (bottom).

The intensity fluctuations are collected and converted to an Autocorrelation Function (ACF) by using a digital correlator. The ACF is a function that decays as a function of delay time. The decay is fast for small particles and slow for bigger particles. The ACF is then used to calculate the diffusion coefficient and therefore also the size of the particles. The particle size is then given as statistical distribution sorted by scattering intensity, volume or number of particles. It should be noted that the directly measured parameter is the intensity distribution and the volume and number distributions are calculated from the intensity distribution by using Mie theory and by applications special mathematics. Therefore the most reliable results are obtained by using the intensity distribution.

Measurements in this thesis were carried out at room temperature (25 °C) using a Delsa Nano C setup by Beckmann Coulter. The light source is a 2 x 30 mW laser diode with a wavelength of 658 nm.

8.5. Zeta potential

When particles with a certain surface charge are dispersed in a liquid, ions from the media accumulate around the particle. In close proximity to the particle one can find ions that obtain the opposite charge than the particle surface. These ions are strongly bound to the particle and will stay close to the particle surface even the particle is in motion through the dispersion. This layer is called the Stern layer. Next to the stern layer one can find another layer of ions oriented around the particle. In this layer the ions are more diffuse and therefore it is called the Diffuse layer. Far away from the particle the ions are randomly oriented and it exists the same amount of positively and negatively charged particles.

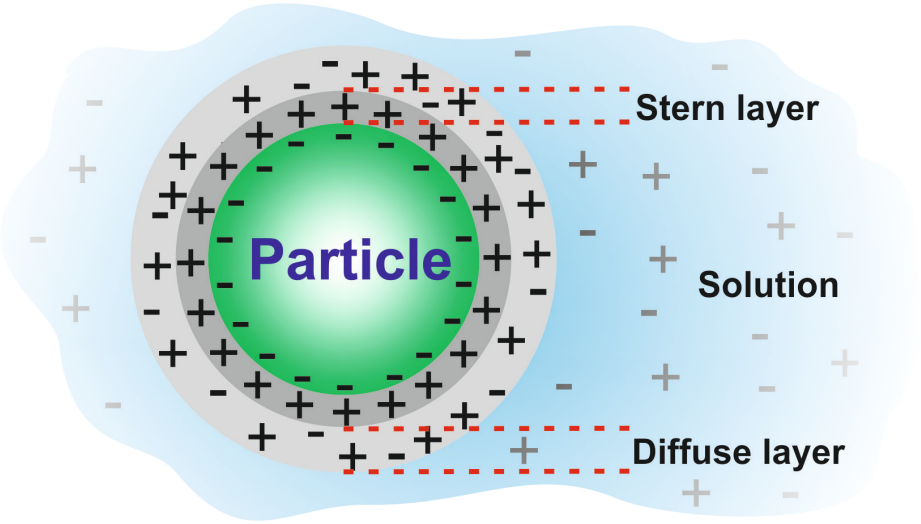

Figure 8.5. Stern and Diffusive layer around a particle dispersed in a media.

When these particles undergo Brownian motion in a media, the particle is moving together with the Stern layer and a part of the Diffusive layer. The boundary between moving and non-moving ions in the Diffusive layer is called the slipping plane. The zeta potential is defined as the potential at the slipping plane versus a point far away from the particle. Generally it is used as an index of surface charge and as an index of the tendency of particles to aggregate in suspension. The higher the surface charge, and therefore the zeta potential, is, the higher is the electrostatic repulsion between the particles, which avoids aggregation and leads to highly stable dispersions. As rule of thumb dispersion with zeta potentials below -30 mV or above +30 mV are considered to be stable.

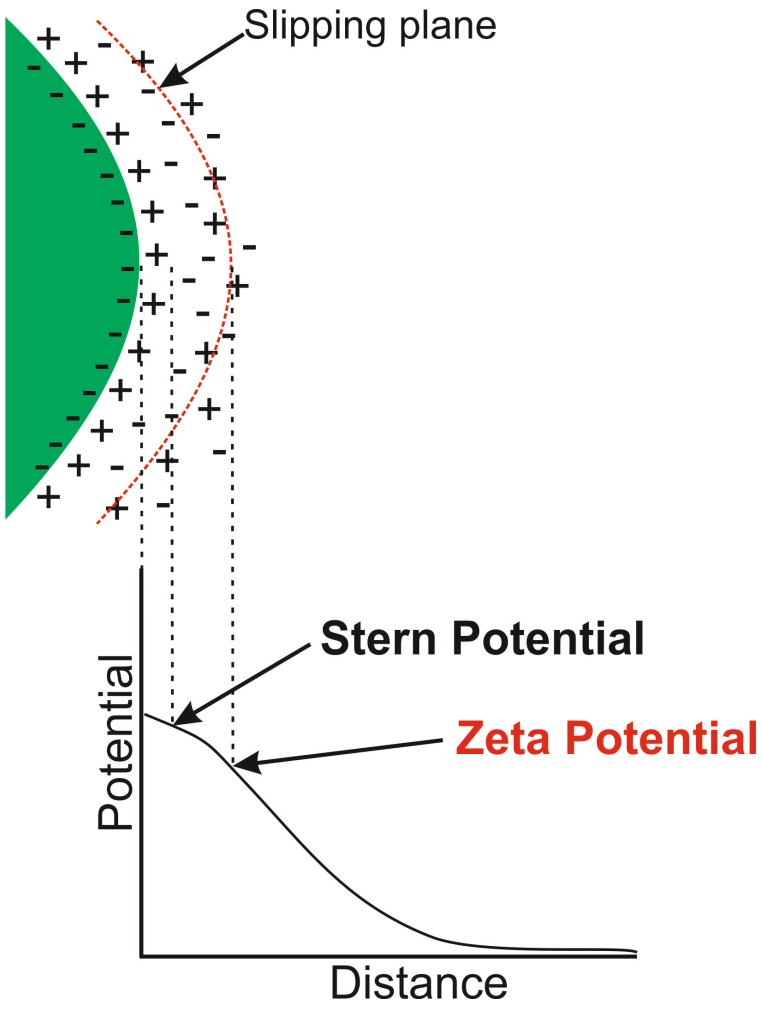

Figure 8.6. Potential in dependence of the distance from the particle surface.

When an electric field is applied to a dispersion of particles, the particles are moving towards the oppositely charged electrode. The speed with which the particles are moving is proportional to the surface charge of the particle and the zeta potential can be determined by measuring the speed of particles in an electric field. This is done by irradiating the moving particles with a light beam and comparing the scattered light to the incident light. Because the fre-

quency of the scattered light is shifted from the incident light in proportion of the particle speed, one can determine the particle speed by measuring the frequency shift between incident and scattered light. This method is based on the Doppler effect and is therefore called Laser Doppler Velocimetry (LDV).

The frequency shift v_D is related to the mobility of particles, U:

$$v_D = \frac{Uq}{2\pi}\cos\frac{\theta}{2} = \frac{Un}{\lambda}sin\theta \text{ where}$$

q is the scattering vector ($q=4\pi n\sin(\Theta/2)/\lambda$). λ is the wavelength, n is the refractive index oft he media and Θ is the scattering angle.

Measurements in this thesis were carried out at room temperature (25 °C) using a Delsa Nano C setup by Beckmann Coulter. The light source is a 2 x 30 mW laser diode with a wavelength of 658 nm.

8.6. UV/Vis spectroscopy

In UV/VIS spectroscopy light in the visible, near UV and near-infrared (NIR) region of the spectrum is used to electronically excite molecules. The Absorption (A), or better the molecular extinction coefficient (ε), at a given wavelength (λ) characterizes the efficiency of the transitions. UV/Vis spectroscopy is very often used to determine the concentration of an absorbing species in solution by applying the Lambert-Beer law:

$$\mathrm{A} = \log_{10}\left(\frac{\mathrm{I}_0}{\mathrm{I}}\right) = \varepsilon * \mathrm{c} * \mathrm{L}$$

where I_0 is the intensity of the incident light, I is the intensity of the transmitted light, c is the concentration, and L is the path length through the sample.
Figure shows a schematic view on a typical UV/Vis spectrometer. The incident light is split into two beams. One is directed on the sample and the second on a reference sample, which usually contains just the solvent. The final absorption is then obtained by subtracting the reference from the sample.

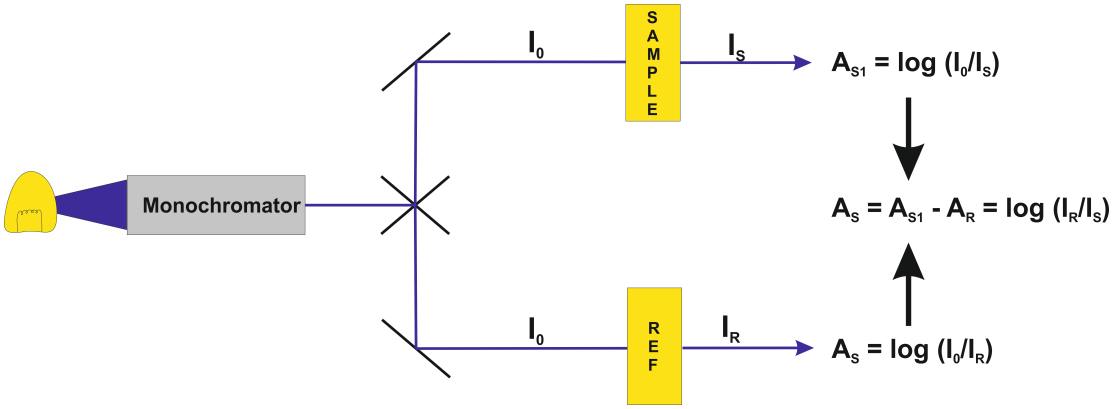

Figure 8.7. Schematic representation of a typical UV/Vis spectrometer.

If not indicated differently, measurements were carried out using a Shimadzu UV 3600 UV-Vis-NIR Spectrophotometer.

8.7. Steady state emission spectroscopy

In this technique the radiative decay from an excited state to the ground state of a molecule is recorded. The excitation light, which is usually emitted from a xenon lamp or a laser, passes first through a monochromator, before it reaches the beam splitter, where a few percent are reflected to a reference channel. The rest is directed to the sample. This light then excites the sample and its emission is usually recorded at 90° in respect to the excitation. It passes a second monochromator before it finally reaches the detector. The reference channel is used to correct for the wavelength intensity dependence of the excitation light. A schematic representation is shown in figure 8.8.

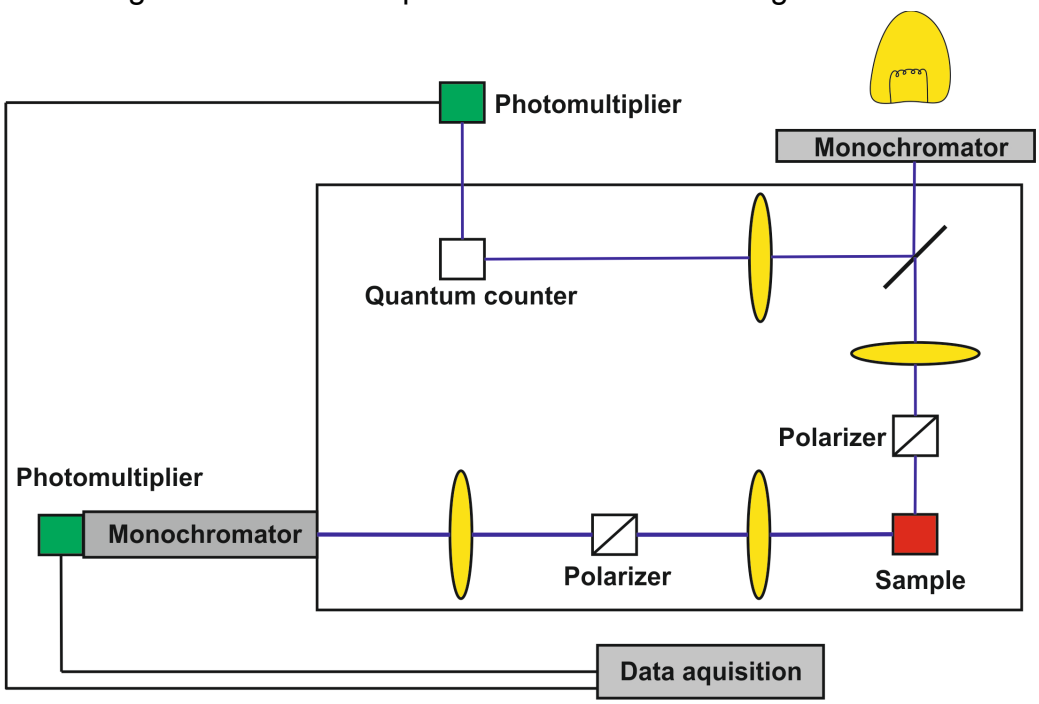

Figure 8.8. Scheme of a steady state emission spectrofluorometer.

If not indicated differently, emission spectra in this thesis were recorded using a HORIBA Jobin-Yvon IBH FL-322 Fluorolog 3 instrument equipped with a 450 W xenon arc lamp, double grating excitation and emission monochromators (2.1 nm/mm dispersion; 1200 grooves/mm) and a TBX-4-X single-photon-counting detector.

8.8. Confocal microscopy

Confocal microscopy is one of most widely used techniques in modern research. In contrast to epifluorescence microscopy, confocal microscopy uses point illumination and a pinhole in front of the detector to eliminate out-of-focus light. As only light coming from the focal plane of the specimen is detected, the optical resolution, particularly in the sample z-axis, is significantly improved. The principle is shown in figure 8.9.

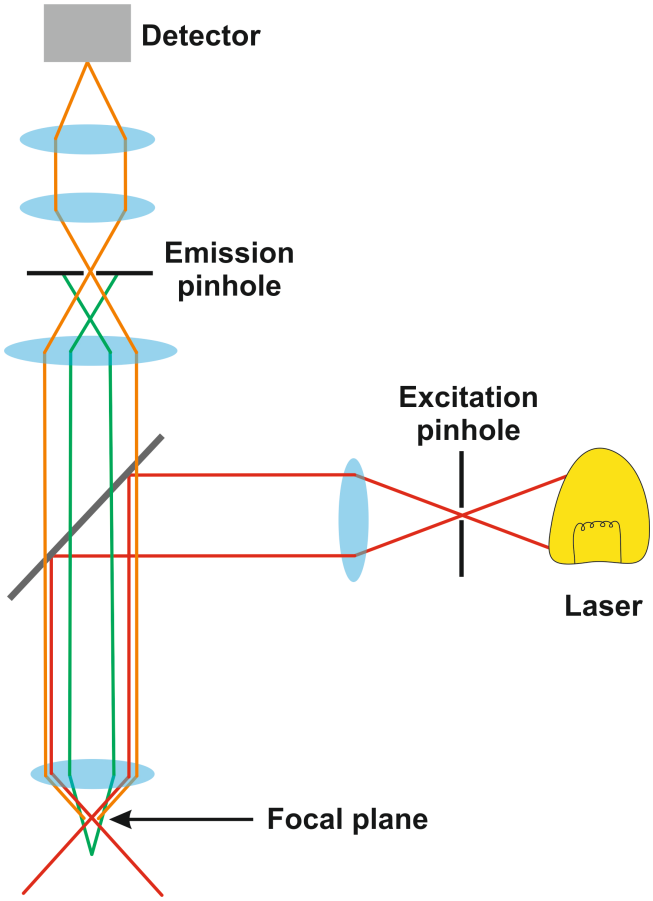

Figure 8.9. Scheme of a confocal microscope

If not indicated differently, a Zeiss LSM 710 confocal microscope system with 63X magnification, numerical aperture 1.3 of Zeiss LCI Plan-NEOFLUAR water immersion objective lens (Zeiss GmbH) was used in the frame of this thesis.

Summary

The aim of this thesis titled “Zeolites as key-components for electronics and biomedicine” is the synthesis, functionalization and applications of zeolite-L particles for applications in electronics and biomedicine.
This thesis is organized into 8 chapters, starting in chapter 1 with giving a general overview about nanotechnology and biomedicine. After that the concept of using nanocontainer in biomedicine are briefly discussed. In the following the nanocontainer zeolite-L is introduced and a summary of zeolite-L for applications in nanomedicine is given. Finally, the self-assembly of zeolites in monolayers and their further functionalization is discussed.

Chapter 2 describes the zeolite-L synthesis, functionalization and their assembly into functional materials in detail. Three different types of zeolite-L have been used in this thesis: Nanozeolite-L particles with a size of just a few tenths of nanometers, disc-shaped zeolite-L with a diameter of around 200 nm and micrometer sized crystals with a length of about 1000 nm.
Then different methods to functionalize the crystals with the desired groups and to obtain specific properties of the crystals are reported. In detail the exchange with different counter cations, the insertion of guest molecules and the functionalization of the external crystal surface are reported. Finally the assembly into monolayers and their further functionalization by soft lithography is discussed.

Chapter 3 deals with the growth of neuron cells on zeolite-L monolayers. The long-term goal is to pattern the surface with nanocontainers in order to address the cells in specific nanometer areas and to monitor the cell response.
In order to form the pattern, nanoparticles and self-assembled monolayers have been used in combination with proteins, as a kind of extracellular matrix mimics. The patterned surfaces have been generated on glass and neuron growth has been followed for several days in order to realize the formation of synapses. It is shown that a coating with special proteins can be used to allow for a neuron growth of at least 9 days

Chapter 4 then applies zeolites as key-components for electronics. It is shown that the per-se zeolite material can be rendered electrically conductive by filling the pore system with semiconducting organic molecules. Above that, these materials show extraordinary magnetoconductance properties at room temperature and just small magnetic fields. Indeed, the obtained results are the highest reported valued at room temperature so far, which makes this material very promising for further applications in nanoelectronic devices.

Chapter 5 describes a rather unexplored way of self-assembling functional organic molecules, perylene monoimide derivatives – by a direct self-assembly from the gas phase. A series of perylene monoimides has been synthesized and their self-assembly from solution and gas phase was studied.

The assembled systems present a morphology that is dependent on the nature of the functionalization introduced on the nitrogen and on the conditions the self–assembly has been performed (drop cast vs sublimation).

Chapter 6 describes the use of zeolite-L as a multifunctional DNA and drug release systems. It is shown that DNA functionalized zeolites can be used as a multifunctional DNA and drug release system in living cells. The release of DNA and a model drug (DAPI) in HeLa cells is shown and the particle uptake and kinetics of the DNA and DAPI release are investigated in detail. Finally, it is shown, that the particles are localized in the lysosomes and that the detached DNA is localized in the mitochondria.

Chapter 7 discusses the use of zeolite-L nanocrystals for an efficient PNA delivery into living cells. It is shown that high amounts of PNAs can be delivered to cells by binding them to zeolites and coating the particles with a thin layer of poly-L-lysine. Furthermore the pore system can be filled with a model drug, which is then released from the crystals after cell uptake.

In chapter 8 the main instrumental and experimental details are summarized.

In conclusion this thesis shows that zeolite-L is a very powerful platform for a variety of very different applications. Due to the easy functionalization of the pore system or the outer surface, the system can be tailor designed depending on the application.
Very promising first results for using zeolite-L for very different applications are presented. The crystals can be applied in the field of nanomedicine for applications ranging from tissue engineering up to gene therapy or even in the field of nanoelectronics to form organic wires with extraordinary and so far unknown properties.
In further experiments the system can be modified in order to allow for real applications in gene therapy or to design novel nanoelectronic devices.

Acknowledgements

This thesis would not have been possible with the help and support of so many people.
In the following pages I will try to acknowledge everybody who has done his or her part to make this thesis possible. I will try to remember everybody, but most probably I will forget a few people. So if you have given your precious time to support this work during the last 3.5 years, but your name is not there – don't take it personally.

First of all I want to say "thank you" to my supervisor **Luisa** for supporting me during my PhD (and also already during my "Diplomarbeit"). Thank you for giving me the opportunity to join this fantastic international group and for making it possible to spend so much time in this environment. I always enjoyed coming to the lab and spending my time there. Additionally I would like to say "thank you" for giving me these very interesting projects and for giving me the opportunity to follow some of my own ideas, which are now a part of this thesis.
At this point I would also like to thank the ERC (advanced grant award # 2009-247365) for financial support.

Secondly, I wish to thank the members of my jury (**Professor Dr. Gero Decher** from the University of Strasbourg, **Professor Dr. Luis M. Liz-Marzan** from the University of Vigo, and **Professor Dr. Christof Wöll** from the Karlsruhe Institue of Technology) for taking their time to read this thesis and to be present at my defense.

Now I would like to thank all my collaborators for their excellent work and enthusiasm.
Dank je wel, **Wilfred**. Our collaboration already started in the beginning of my PhD and I think it was a very fruitful time. I really liked (and I still like) our project and I hope some more nice results will come out in the future. I appreciated your very friendly nature and your incredible enthusiasm.
Robin, the same is for you. Thank you very much for doing such a good work in Twente. I really liked collaborating with you and visiting you in Twente.
Also I would like to thank all the other co-authors from the "Magnetoresistance project" for their excellent work: **M. H. Siekman**, **S. P. Kersten**, **P. A. Bobbert**, and **M. P. de Jong**.

Secondly I would like to thank **Dr. Frank Erdmann**, **Dr. Kay Jüngling** and **Professor Pape** for spending their time doing the neuron experiments for me.

For the DNA and PNA work I would like to thank **Professor Roberto Corradini**. It was great meeting you here in Strasbourg and collaborating with

you. I think we started a very nice project and I hope some very nice results will come out in the near future. **Bertucci** and **Dedy** – thanks for the great work.

Also I want to say Danke and Merci to the staff from Münster and Strasbourg: **Nicole**, **Judith**, **Bernhard**, **Claire**, **Fanny**, **Ines**. Thanks for all the work and organization you have done for all of us.

Céline, **Loïc**, **Youssef** and **Ricardo** for the translation of the Résumé.

I would also like to thank all the De Cola people I met during my time:
First of all I want to thank the nano-crew, who taught me the secrets and tricks of materials science: **André**, **Matthias**, **Seda**, **Cristian, Zhen** and…the only real nano-guy here…**Eko**. Thanks for always answering my questions and helping me out. You maybe have the biggest direct influence on this thesis.

Now is the time, where it could become a bit messy.
I want to thank **Jörn** (for spending a lot of time together with me in the good old ICB-lab). **Naveen 1 and Naveen 2** (I still have the pictures from Lviv. One day, when you are rich, I will use them to blackmail you ☺).
Eko (again) for being a "good" ☺ ping-pong buddy in Münster.
Edward for introducing me into the world of science and spending a lot of time with me in Münster, Hannover and everywhere else (We MUST go to amp again).
Matteo (thanks for always having time to help me with so many things).
Deanne (we must repeat the Kehl night ☺).
Amparo (for being a great office-buddy and for correcting a part of my thesis).
Valentin (for the move to Strasbourg/Karlsruhe). **Nadia** and **Chien-Wei** (good luck with your silicon particles. I hope one day you will find them).

And finally of course **Dedy**, **Bertucci**, **Longhi**, **Deanne** and **Materazzi** for all the great mornings, afternoons, evenings and nights.
Thanks for:
the numerous football-watching nights.
the Hamburg weekend (Btw…I still have the prince. You can always come to visit him ☺).
always going out for a beer, dinner or party.
the southside festival.
the Kehl night.
the Smurf night in Korrigan.
and of course everything I forgot.

Of course I would also like to say “thank you” to all the people I did not collaborate with:
Federica. **Dennis**. **Mydlak**. **Stephan**. **Cheng-Han**. **Jesus**. **Lola. Jan**. **Malte. Sebastian. Cristina**. **Mia**. **Aliprandi**. **Noviyan**. **Laura.**

I would also like to thank everybody I forgot and all my non-chemistry friends from Münster, Strasbourg and all around the world.

Finally I want to thank my family for all the help and support during the last years. Without knowing that there is always somebody in the background, my whole university time and especially this thesis would not have been possible.

Curriculum vitae

Personal Data

Name	Henning Lülf
Date of birth	23.04.1985
Place of birth	Steinfurt
Nationality	Deutsch
Email	henning@unistra.fr; HenningLuelf@gmx.de

Present status

Since December 2013	Patent attorney trainee Patentanwälte Uexküll & Stolberg Beselerstr. 4 D-22607 Hamburg

Education

August 2012 – December 2013	Ph.D. Student in chemistry. University of Strasbourg / (Institut de Science et d'Ingénierie Supramoléculaires (ISIS). Topic: **Zeolites as key-components for electronics and biomedics.** Supervisor: Professor Luisa De Cola
May 2010 – August 2012	Ph.D. at the University of Münster (Westfälische-Wilhelms-Universität Münster) Topic: **Zeolites as key-components for electronics and biomedics.** Supervisor: Professor Luisa De Cola

October 2009 – March 2010	Diplomarbeit University of Münster (Westfälische-Wilhelms-Universität Münster) Topic: **Luminescent metal complexes.** **Synthesis and photophysical properties.** Supervisor: Professor Luisa De Cola Grade: Sehr gut
October 2005 – October 2009:	Studies in chemistry. University of Münster (Westfälische-Wilhelms-Universität Münster)
1996 – June 2005	Kardinal-von-Galen Gymnasium, Münster-Hiltrup (Germany)
1992 – 1996	Kardinal-von-Galen Grundschule, Drensteinfurt (Germany)

Internships

28.04.2009 – 23.07.2009	Internship at the BASF in Guaratinguetá (Brazil); Topic: Method development and validation for the analysis of formulations via HPLC-UV/vis and HPLC-MS.
July 2004	Internship at Rottendorf Pharma GmbH, Ennigerloh (Germany).

Further education

26.06.2013 – 28.06.2013	Conference: “Supramolecular Functional Systems For Organic Electronics”, Strasbourg (France) Poster presentation Winner of “Best poster award”

27.05.2013 – 31.05.2013	EMRS 2013 Spring Meeting, Strasbourg (Frankreich) Oral presentation
22.11.2012 – 24.11.2012	ERC Grantees Conference 2012, Frontier Research in Chemistry, Strasbourg (France) Poster presentation
14.05.2012 – 18.05.2012	EMRS 2012 Spring Meeting, Strasbourg (France) Poster presentation
Wintersemester 2010/2011	Seminar for Ph.D. students "Innovationsmanagement"
06.10.2010 – 10.10.2010	3rd International Summer School "Supramolecular Systems in Chemistry and Biology", Lviv (Ukraine) Poster presentation
04.07.2010 – 09.07.2010	16th International Zeolite Conference joint with the 7th International Mesostructured Materials Symposium (IZC-IMMS 2010), Salerno (Italy)
02.07.2010 – 03.07.2010	Summer School of "16th International Zeolite Conference joint with the 7th International Mesostructured Materials Symposium", Sorrento (Italy)

Publications

H. Luelf, A. Devaux, E. Prasetyanto, L. De Cola in *Organic Nanomaterials Synthesis, Characterization, and Device Applications*, T. Torres, B. Bottari, Wiley 2013.

U. Hahn, **H. Luelf**, H. D. Winkler, C. A. Schalley, F. Vögtle, L. De Cola; *Chem. Eur. J.* **2012**, 18, 15424-15432.

R. N. Mahato, **H. Lülf**, M. H. Siekman, S. P. Kersten, P. A. Bobbert, M. P. de Jong, L. De Cola, W. G. van der Wiel, *Science* **341**, 257 (2013).

Henning Lülf, Alessandro Bertucci, Dedy Septiadi, Roberto Corradini, Luisa De

Cola, *Angew. Chem. Int. Ed*., 2013, submitted

Alessandro Bertucci, **Henning Luelf**, Dedy Septiadi, Alex Manicardi, Roberto Corradini*, Luisa De Cola*, *Adv. Healthcare Mater.*, 2013, submitted

Henning LÜLF

Zeolites as key-components for electronics and biomedicine

Résumé

La thèse intitulée « Zeolites as key-components for electronics and biomedicine » traite de travaux sur des cristaux de zéolite-L avec des tailles et des formes différentes pour des applications dans les domaines de l'électronique et de la biomédecine.

Il a été montré que, lorsque les monocouches de zéolites-L sont munies d'un biofilm, elles peuvent-être utilisées comme des substrats pour une croissance de longue durée de neurones primaires.

De plus, les pores des zéolites peuvent être remplies d'un spécial semi-conducteur organique, pour permettre un transport d'électrons à travers les canaux et, plus important, ces matériaux présentent une très haute magnétorésistance en y appliquant un champ magnétique externe.

Enfin, les monocristaux de zéolites-L peuvent être utilisés en tant que plateforme pour un oligo-nucléotide multifonctionnel et l'administration d'un médicament-modèle à l'intérieur de cellules vivantes. Les oligo-nucléotides sont attachés aux particules de la surface externe et le médicament-modèle est encapsulé dans les pores. Ces premières expériences-modèles confirment que ces systèmes offrent un grand potentiel dans le domaine de la thérapie génique.

En résumé, cette thèse montre que les cristaux de zéolites-L peuvent être appliqués avec succès dans des domaines très variés, de l'électronique à la biomédecine.

Résumé en anglais

The aim of this thesis titled "Zeolites as key-components for electronics and biomedicine" is the synthesis, functionalization and applications of zeolite-L particles for applications in electronics and biomedicine.

This thesis is organized into 8 chapters, starting in chapter 1 with giving a general overview about nanotechnology and biomedicine. After that the concept of using nanocontainer in biomedicine are briefly discussed. In the following the nanocontainer zeolite-L is introduced and a summary of zeolite-L for applications in nanomedicine is given. Finally, the self-assembly of zeolites in monolayers and their further functionalization is discussed.

Chapter 2 describes the zeolite-L synthesis, functionalization and their assembly into functional materials in detail. Three different types of zeolite-L have been used in this thesis: Nanozeolite-L particles with a size of just a few tenths of nanometers, disc-shaped zeolite-L with a diameter of around 200 nm and micrometer sized crystals with a length of about 1000 nm.

Then different methods to functionalize the crystals with the desired groups and to obtain specific properties of the crystals are reported. In detail, the exchange with different counter cations, the insertion of guest molecules and the functionalization of the external crystal surface are reported. Finally the assembly into monolayers and their further functionalization by soft lithography is discussed.

Chapter 3 deals with the growth of neuron cells on zeolite-L monolayers. The long-term goal is to pattern the surface with nanocontainers in order to ad-dress the cells in specific nanometer areas and to monitor the cell response.

In order to form the pattern, nanoparticles and self-assembled monolayers have been used in combination with proteins, as a kind of extracellular matrix mimics. The patterned surfaces have been generated on glass and neuron growth has been followed for several days in order to realize the formation of synapses. It is shown that a coating with special proteins can be used to allow for a neuron growth of at least 9 days

Chapter 4 then applies zeolites as key-components for electronics. It is shown that the per-se zeolite material can be rendered electrically conductive by filling the pore system with semiconducting organic molecules. Above that, these materials show extraordinary magnetoconductance properties at room temperature and just small magnetic fields. Indeed, the obtained results are the highest reported valued at room temperature so far, which makes this material very promising for further applications in nanoelectronic devices.

Chapter 5 describes a rather unexplored way of self-assembling functional organic molecules, perylene monoimide derivatives – by a direct self-assembly from the gas phase. A series of perylene monoimides has been synthesized and their self-assembly from solution and gas phase was studied. The assembled systems present a morphology that is dependent on the nature of the functionalization introduced on the nitrogen and on the conditions the self–assembly has been performed (drop cast vs sublimation).

Chapter 6 describes the use of zeolite-L as a multifunctional DNA and drug release systems. It is shown that DNA functionalized zeolites can be used as a multifunctional DNA and drug release system in living cells. The release of DNA and a model drug (DAPI) in HeLa cells is shown and the particle uptake and kinetics of the DNA and DAPI release are investigated in detail. Finally, it is shown, that the particles are localized in the lysosomes and that the de-tached DNA is localized in the mitochondria.

Chapter 7 discusses the use of zeolite-L nanocrystals for an efficient PNA de-livery into living cells. It is shown that high amounts of PNAs can be delivered to cells by binding them to zeolites and coating the particles with a thin layer of poly-L-lysine. Furthermore the pore system can be filled with a model drug, which is then released from the crystals after cell uptake.

In chapter 8 the main instrumental and experimental details are summarized.

In conclusion this thesis shows that zeolite-L is a very powerful platform for a variety of very different applications. Due to the easy functionalization of the pore system or the outer surface, the system can be tailor designed depend-ing on the application.

Very promising first results for using zeolite-L for very different applications are presented. The crystals can be applied in the field of nanomedicine for applications ranging from tissue engineering up to gene therapy or even in the field of nanoelectronics to form organic wires with extraordinary and so far unknown properties.

In further experiments the system can be modified in order to allow for real applications in gene therapy or to design novel nanoelectronic devices.